Engineering of Thin-Film Transistors for Chemical Sensing

MILLER, LAUREN,REBECCA

Engineering of Thin-Film Transistors for Chemical Sensing

Lauren R. Miller

A Thesis presented for the degree of
Doctor of Philosophy

Supervised by Prof Dagou Zeze, Dr Alejandro Galán-González &
Dr Mujeeb Chaudhry

Department of Engineering
University of Durham
United Kingdom

May 2025

Dedicated to

Ronald & Hazel Gould

"You know it makes sense."

Engineering of Thin-Film Transistors for Chemical Sensing

Lauren R. Miller

Submitted for the degree of Doctor of Philosophy
May 2025

Abstract

Semiconductor technologies underpin modern integrated circuit design. Among them, thin-film transistors (TFTs) play an increasingly significant role in emerging applications such as edge computing, the Internet of Things and healthcare. TFTs are especially valued in large-area electronics for their low-cost fabrication, straightforward processing and scalability with high device uniformity. They have also gained attention as next-generation, high-throughput chemiresistive gas sensors, with applications in medical diagnostics, defence and environmental monitoring. A notable example is their use in exhaled breath analysis.

This thesis focuses on fabricating high-performance TFTs using low-cost, solution-processable methods to support the development of a unified, portable diagnostic platform. Earth-abundant materials – ZnO, SnO_2 and Zn–Sn–O (ZTO) – are investigated as n-type semiconductors, offering economic and environmental advantages. The benefits of stacking alternating ZnO and ZTO layers via spin-coating are systematically evaluated. Each system is characterised in terms of morphology and surface chemistry using X-ray techniques to link material properties with key transistor performance metrics. The study is further extended to assess the chemiresistive response of the devices to volatile organic compounds, including methanol and acetone.

To address the unipolar nature of metal oxide TFTs and their reliance on highly doped silicon substrates with thermally grown dielectrics, water-gated TFTs (WG-TFTs) are investigated as an alternative architecture. These

devices integrate p-type organic semiconductors with n-type ZnO, mitigating limitations associated with all-organic channels. For the first time, this work explores how thermally-induced phase-separation in bulk heterojunction morphologies influences ambipolar charge transport – defined as the ability to support both electron and hole conduction under opposite gate biases within a single device. This ambipolarity enables inverter functionality and demonstrates strong potential for low-voltage operation and integration into clinical diagnostic technologies.

Declaration

The work presented in this thesis is based on research conducted at the Department of Engineering, Durham University, United Kingdom. No part of this thesis has been submitted elsewhere for any other degree or qualification.

All Thin-Film Transistors (TFTs) described in this work were fabricated by the author. Characterisation using Scanning Electron Microscopy (SEM), Transmission Electron Microscopy (TEM), and Energy-Dispersive X-ray Spectroscopy (EDX) was performed by the author with assistance from Leon Bowen, Department of Physics, Durham University. X-ray Diffraction (XRD) and X-ray Reflectivity (XRR) measurements were undertaken by Dr Ben Nicholson under Prof Del Atkinson, also from the Department of Physics. Atomic Force Microscopy (AFM) imaging was conducted by the author with support from Prof Richard Thompson, Department of Chemistry. Films for X-ray Photoelectron Spectroscopy (XPS) analysis were prepared by the author, with measurements carried out by Dr Guillaume Monier at the Institut Pascal, Aubière, Auvergne, France. Films used for Vapour Phase Infiltration (VPI) characterisation were prepared by Sasha Simotko from the Frey Group, and their wetting properties were analysed by Elena Prudnikov from the Pokroy Group, Department of Materials Science and Engineering, Technion – Israel Institute of Technology.

Acknowledgements

I would like to begin by thanking Dr Alejandro Galán-González. His guidance and friendship have not only made me a better researcher, but this thesis simply would not exist without him. I am also deeply grateful to Prof Dagou Zeze and Dr Mujeeb Chaudhry for giving me the opportunity to pursue a PhD and to those involved in my supervision. Dr Beth Barnes, thank you for letting me vent, cry and laugh – sometimes all at once – in your office. Thank you to my Israeli family for adopting me as one of your own – you are a canon!

To my best friend and twin sister, Tori – thank you for being my biggest fan and for helping me find Luke Miller. Mum, your resilience and drive have always inspired me and continue to shape everything I achieve – including this thesis. Ant – thank you for believing in my big brain. Dad – thank you for raising me to be a Liverpool fan. And thank you to Daniel, Sophie and all of my family for your love and support.

Ginge – you are family. Cai – thank you for introducing me to Rebecca Lucy Taylor and Inkscape. Emilia – thank you for being a constant ray of sunshine. Mana and Freddie – thank you for hugging me through every wobble. Paloma, your mentorship was instrumental in helping me find my place in academia. And Heather – thank you for always knowing what's best for me, especially when I'm too stubborn to see it for myself.

To Durham, thank you for being my home. And finally – cheers to me.

You'll Never Walk Alone

Contents

List of Figures

List of Tables

List of Publications

[1] L. R. Miller, R. J. Borthwick, P. L. dos Santos, and M. U. Chaudhry, "Detection of acetone vapours using solution-processed tin oxide thin-film transistors," *MRS Advances*, vol. 8, p. 440–445, 2023.

[2] L. R. Miller, A. Galán-González, B. Nicholson *et al.*, "Control Strategies for Solution-Processed ZTO-Based Thin-Film Transistors Tailored Toward Volatile Organic Compound Detection," *Advanced Electronic Materials*, vol. n/a, no. n/a, p. 2400810, 2025.

Acronyms

AFM	Atomic Force Microscopy.
BHJs	Bulk-Heterojunctions.
EDX	Energy-Dispersive X-ray Spectroscopy.
LED	Light-Emitting Diodes.
LEFET	Light-Emitting Field-Effect Transistors.
MOS	Metal-Oxide-Semiconductor.
MOSFET	Metal-Oxide-Semiconductor Field-Effect Transistors.
OLED	Organic Light-Emitting Diodes.
SEM	Scanning Electron Microscopy.
TEM	Transmission Electron Microscopy.
TFTs	Thin-Film Transistors.
VOCs	Volatile Organic Compounds.
VPI	Vapour Phase Infiltration.
WG-TFTs	Water-Gated Thin-Film Transistors.
XPS	X-ray Photoelectron Spectroscopy.
XRD	X-ray Diffraction.
XRR	X-ray Reflectivity.

Nomenclature

Symbol	Description	Unit
$I_{ds[max]}$	Maximum Drain Current	mA
$I_{ds[min]}$	Minimum Drain Current	mA
$I_{on/off}$	Current on/off Ratio	
S_{max}	Maximum Sensitivity	
S	Sensitivity	
V_{th}	Threshold Voltage	V
μ_{eff}	Effective Mobility	$\mathrm{cm^2\,V^{-1}\,s^{-1}}$
μ	Mobility	$\mathrm{cm^2\,V^{-1}\,s^{-1}}$

Chapter 1

Introduction

1.1 Background

The foundation of semiconductor technology dates back to the early nineteenth century and has since profoundly shaped modern electronics and society. [1, 2] In 1833, Faraday discovered that the electrical resistance of silver sulphide decreased with increasing temperature – an early observation of semiconducting behaviour. [3] The study of semiconductor materials progressed further with Braun, who in 1874 found that the resistance at a metal–semiconductor junction depended on both the magnitude and polarity of the applied bias, termed rectification. [4] In 1907, Round observed electroluminescence from a silicon carbide crystal under bias, noting the emission of yellow light – a phenomenon that underpins present-day Light-Emitting Diodes (LED). [5] These discoveries laid the groundwork for the development of semiconductor devices, including the point-contact transistor invented by Bardeen and Brattain in 1947 [6], followed by Shockley's report of the $p-n$ junction and bipolar junction transistor in 1949. [7] The silicon $p-n$ junction was later employed in the first solar cell, developed by Chapin *et al.* in

1954. [8]

Today, Metal-Oxide-Semiconductor Field-Effect Transistors (MOSFET) are the cornerstone of integrated circuit design. First reported by Kahng and Atalla in 1960 at Bell Labs, [9] the MOSFET brought about Moore's Law, proposed five years later, which states that the number of transistors on a microchip doubles approximately every two years while production costs decrease. [10] The MOSFET and related components constitute around 90 % of the semiconductor device market. [11] One prominent example is Thin-Film Transistors (TFTs), which have become increasingly vital in emerging applications such as edge computing, the Internet of Things and healthcare. [12] TFTs are particularly valued in large area electronics for their low-cost fabrication, ease of processing, and scalability with high device uniformity. A major breakthrough came in 1973, when Brody *et al.* successfully demonstrated the first active-matrix liquid crystal display (LCD) driven by cadmium selenide TFTs. [13] Since then, bulky, power-hungry cathode-ray tubes have been replaced by compact, energy-efficient display technologies such as LCDs and Organic Light-Emitting Diodes (OLED). More recently, the demand for flexible displays with enhanced brightness, contrast, and resolution has led to the development of increasingly sophisticated TFTs. These advances have enabled rapid row addressing and precise pixel control, allowing TFTs to replace traditional silicon-based circuitry.

Beyond displays, TFTs play critical roles in chemical sensing, X-ray imaging, and emerging flexible and wearable electronic systems. Their versatility and low-temperature processing make them compatible with a wide range of substrates, from rigid glass to flexible plastics and electronic skins. To fabricate these TFTs, semiconductor layers must be deposited using techniques such as chemical vapour deposition (CVD), atomic layer deposition (ALD), or solution-based methods like inkjet printing and spin-coating, with the latter being the focus of this thesis. [14]

While integrated circuit design has traditionally relied on silicon-based complementary metal–oxide–semiconductor (CMOS) technology – driven by

the pursuit of higher speed, improved energy efficiency, and greater integration density – limitations emerge in applications requiring mechanical flexibility and durability. Over the past six decades, MOSFET gate lengths have been scaled to below 20 nm; however, this miniaturisation is approaching fundamental limits, as short-channel effects degrade device performance. [15] Concurrently, there is growing demand for low-cost, ultra-thin, and recyclable electronic devices capable of withstanding repeated bending and deformation. [16] In particular, the realisation of disposable point-of-care testing and wearable technologies for biomarker detection – enabling rapid diagnosis and real-time health monitoring – has gained considerable attention for mitigating the spread of infectious diseases and reducing the burden on public health services. This demand has spurred the development of hydrogenated amorphous silicon (a-Si:H) and low temperature polysilicon (LTPS) TFTs. However, alternative material systems must be explored to deliver viable, scalable alternatives to silicon with low power requirements and diversify the global semiconductor supply chain. These include two-dimensional materials, [17, 18] amorphous oxide semiconductors (AOS) such as In_2O_3, Ga_2O_3, and ZnO, and organic semiconductors.

1.2 Research Motivation

The core objective of this thesis is the fabrication of high-performance TFTs using a low-cost, solution-processing method for the realisation of a unified, portable diagnostic platform. The incorporation of earth-abundant materials – ZnO, SnO_2 and Zn–Sn–O (ZTO) – for n-type transport offers significant economic and environmental benefits. The advantages of stacking these layers via spin-coating under varying processing conditions were systematically explored. Each material system was characterised with respect to its morphology and film composition to understand the origin of the resulting transistor performance metrics, namely the mobility (μ), threshold voltage (V_{th}) and current on/off ratio ($I_{on/off}$). This work is then extended to the

detection of Volatile Organic Compounds (VOCs), presenting a qualitative study of the TFTs' chemiresistive response.

Due to the unipolar nature of these metal oxide TFTs and their reliance on highly doped silicon substrates with thermally grown dielectric layers, an alternative transistor architecture was investigated: Water-Gated Thin-Film Transistors (WG-TFTs). These devices leverage the complementary properties of p-type organic semiconductors and n-type ZnO to address key limitations associated with all-organic Bulk-Heterojunctions (BHJs). In particular, this thesis explores, for the first time, the impact of thermally induced phase separation in BHJ morphologies on ambipolar charge transport – defined as the ability to support both p- and n-type conduction within a single TFT under opposite gate bias. This ambipolarity enables CMOS-like inverter functionality, offering strong potential for low-voltage operation and seamless integration into existing clinical diagnostic technologies.

Together, these two complementary sensing strategies – ZTO-based VOC detectors and WG-TFTs for aqueous biomarkers – enable the simultaneous analysis of breath and saliva, generating multimodal diagnostic signatures that enhance specificity and reliability. The novel combination of material systems, coupled with detailed analyses of their transistor and chemiresistive behaviours, establishes a blueprint for the future design of scalable, solution-processed thin film devices.

1.3 Thesis Structure

The thesis structure is as follows:

Chapter 2 provides a review of the fundamental principles of the semiconductor materials and an integrated discussion of state-of-the-art relevant to the operation of the devices studied in subsequent chapters: TFTs and WG-TFTs. The discussion begins with an overview of basic crystal structures and electronic band theory, focusing on the formation of energy bands and their relationship to electrical conduction in semi-

conductors. Building on this foundation, the concepts of intrinsic and extrinsic semiconductors are introduced. The chapter then explores charge carrier transport mechanisms – including drift under an electric field and diffusion due to concentration gradients – in homogeneous semiconductor materials. The operation principles of semiconductor devices based on $p-n$ junctions are then introduced. Their operating regimes and key performance parameters, such as V_{th} and μ, are described. An overview of the inorganic semiconductor materials used in this study is then presented, including ZnO, SnO_2 and ZTO. Their compatibility with solution-based fabrication techniques is also discussed. The focus then shifts to organic semiconductors, where the theory of charge transport in π-conjugated systems is outlined.

Chapter 3 offers a detailed account of the experimental methods and analysis techniques used throughout the thesis. Firstly, the preparation of different substrates and precursor solutions for solution-processing are described. This is followed by an overview of the thin film and electrode deposition methods, namely spin-coating and thermal evaporation. Next, microscopies for structural, morphological and chemical analyses are explained, including high-resolution Atomic Force Microscopy (AFM), Scanning Electron Microscopy (SEM) and Transmission Electron Microscopy (TEM). The working principles that underpin several X-ray techniques used in this work, X-ray Diffraction (XRD), X-ray Reflectivity (XRR), X-ray Photoelectron Spectroscopy (XPS) and Energy-Dispersive X-ray Spectroscopy (EDX) are also shown. Lastly, the measurement of the electronic properties of all transistor configurations is outlined.

Chapter 4 presents the first set of results, investigating single layer oxide TFTs and establishing a link between key transistor performance parameters, channel geometry and their sensitivity to VOCs. These metrics are then enhanced by examining multilayer systems based on

related oxides. The intercalation of a ZnO layer to construct ZTO-capped (ZTO-ZTO & ZTO-ZnO-ZTO) and ZnO-capped (ZTO-ZnO & ZTO-ZTO-ZnO) TFTs was explored. To investigate the clear differences in surface morphology and crystalline properties between the ZnO- and ZTO-capped TFTs, AFM, SEM, and XRD measurements were carried out. Moving on to film composition, TEM, XRR and XPS depth profiling analyses, were used to track the evolution of these components.

Chapter 5 builds on this by demonstrating the use of multilayer TFTs as chemiresistive gas sensors, with an emphasis on a qualitative assessment of their selectivity towards specific VOCs. To begin, XPS surface analyses was conducted to deconvolve the oxygen-related components and ascertain potential sites for the adsorption of VOCs. Secondly, the specificity of these TFTs was examined qualitatively by exposing them to a suite of VOCs with different functional groups and sizes, which included acetone, isopropanol (IPA) and toluene vapours. Next, the most responsive TFT was taken forward to examine the impact of channel geometry on the calculated responsivity obtained. To support the link between oxygen surface chemistry, morphology and TFT sensor performance, the ZTO-ZTO TFT was exposed to a smaller alcohol, methanol. Its reliability and reproducibility were evaluated by testing its dynamic response, with respect to methanol, and operation cycled three times following overnight, long and short exposure periods.

Chapter 6 introduces two novel WG-TFT designs that achieve ambipolar behaviour at low-voltage operation. First, the individual performances of the organic p-type and n-type semiconductors were evaluated as unipolar WG-TFTs. Subsequently, their ambipolar behaviour was examined by blending the two components into a single active layer using a BHJ structure. The amphiphilic fullerene, $PrC_{60}MA$, governed n-type transport and was individually blended with one of two polymers

– either P3HT or PCDTPT – to enable p-type transport. The blend composition, processing conditions, and thermal treatments were carefully controlled to tailor the morphology of the active layer, which was analysed using Vapour Phase Infiltration (VPI) and water contact angle measurements. Secondly, bilayer and hybrid (organic/inorganic) WG-TFTs were investigated to eliminate the effects of thermally induced phase separation between organic materials. To achieve this, an organic p-type polymer was deposited onto an n-type metal oxide underlayer.

Chapter 7 summarises the key findings and contributions of the thesis and outlines avenues for future research related to each of the results chapters. These include: a quantitative evaluation of the sensor response of both single- and multilayer TFTs; the demonstration of a WG-TFT based on a hybrid BHJ, in which ZnO is deposited using the same methodology as for VPI; and, finally, the optimisation and fabrication of Light-Emitting Field-Effect Transistors (LEFET) for remote chemical sensing applications.

References

[1] S. M. Sze, *Semiconductor Devices: Physics and Technology*, 2nd ed. John Wiley & Sons, 2001.

[2] S. M. Sze and K. K. Ng, *Physics of Semiconductor Devices*, 3rd ed. Wiley-Interscience, 2007.

[3] M. Faraday, "Experimental researches in electricity," *Proc. R. Soc. Lond.*, vol. 5, p. 592–595, 1851.

[4] F. Braun, "Ueber die Stromleitung durch Schwefelmetalle," *Annalen der Physik*, vol. 229, no. 12, pp. 556–563, 1875.

[5] H. J. ROUND, "A Note on Carborundum," in *Semiconductor Devices: Pioneering Papers*, 1991, pp. 879–879.

[6] J. Bardeen and W. H. Brattain, "The transistor, a semi-conductor triode," *Phys. Rev.*, vol. 74, pp. 230–231, Jul 1948.

[7] W. Shockley, "The Theory of p-n Junctions in Semiconductors and p-n Junction Transistors," *Bell System Technical Journal*, vol. 28, no. 3, pp. 435–489, 1949.

[8] D. M. Chapin, C. S. Fuller, and G. L. Pearson, "A New Silicon p-n Junction Photocell for Converting Solar Radiation into Electrical Power," *Journal of Applied Physics*, vol. 25, no. 5, pp. 676–677, 1954.

[9] M. M. Atalla and D. Kahng, "Silicon-silicon dioxide field induced surface devices," in *IRE-AIEE Solid-State Device Research Conference*, 1960.

[10] R. Schaller, "Moore's law: past, present and future," *IEEE Spectrum*, vol. 34, no. 6, pp. 52–59, 1997.

[11] R. A. Smith, *Semiconductors*, 2nd ed. Cambridge University Press, 1979.

[12] D. Geng, K. Wang, L. Li *et al.*, "Thin-film transistors for large-area electronics," *Nature Electronics*, vol. 6, pp. 963–972, 2023.

[13] T. P. Brody, J. A. Asars, and G. D. Dixon, "A new thin-film-display device," *IEEE Transactions on Electron Devices*, vol. 20, no. 11, pp. 995–1003, 1973.

[14] A. Yan, C. Wang, J. Yan *et al.*, "Thin-film transistors for integrated circuits: Fundamentals and recent progress," *Advanced Functional Materials*, vol. 34, no. 3, p. 2304409, 2023.

[15] G. Arutchelvan, Q. Smets, D. Verreck *et al.*, "Impact of device scaling on the electrical properties of MoS2 field-effect transistors," *Scientific Reports*, vol. 11, no. 1, p. 6610, 2021.

[16] W. Cao, H. Bu, M. Vinet *et al.*, "The future transistors," *Nature*, vol. 620, pp. 501–515, 2023.

[17] D. Wang, Y. Zhou, H. Zhang *et al.*, "Wafer-scale growth of pristine and doped monolayer mos films for electronic device applications," *Inorganic Chemistry*, vol. 59, no. 23, pp. 17 356–17 363, 2020.

[18] N. Li, Q. Wang, C. Shen *et al.*, "Large-scale flexible and transparent electronics based on monolayer molybdenum disulfide field-effect transistors," *Nature Electronics*, vol. 3, no. 11, pp. 711–717, 2020.

Chapter 2

Semiconductor Physics and Transistors

2.1 Chapter Overview

This chapter presents a review of the fundamental principles and an integrated discussion of the state-of-the-art relevant to semiconductor materials that underpin the operation of the devices studied in subsequent chapters: TFTs and WG-TFTs. The discussion begins with an overview of basic crystal structures and electronic band theory, focusing on the formation of energy bands and their relationship to electrical conduction in semiconductors. Building on this foundation, the concepts of intrinsic and extrinsic semiconductors are introduced, along with the role of doping in modulating carrier concentration under thermal equilibrium.

The chapter then explores charge carrier transport mechanisms – includ-

ing drift under an electric field and diffusion due to concentration gradients – in homogeneous semiconductor materials. This is followed by an examination of the behaviour of a semiconductor containing adjacent p- and n-type regions, forming a $p-n$ junction. The operation principles of semiconductor devices based on $p-n$ junctions are then introduced, including the Metal-Oxide-Semiconductor (MOS) capacitor and MOSFET. Their operating regimes and key performance parameters, such V_{th}, μ and $I_{on/off}$ are described.

An overview of the inorganic semiconductor materials used in this study is then presented, including ZnO, SnO_2 and Zn-Sn-O (ZTO). Their compatibility with solution-based fabrication techniques is also discussed. The focus then shifts to organic semiconductors, where the theory of charge transport in π-conjugated systems is outlined. The design of all-organic BHJs based on blends of an n-type small molecule ($PrC_{60}MA$) with p-type conjugated polymers (either P3HT or PCDTPT) is briefly discussed in the context of WG-TFTs and their ambipolar performance.

2.2 Semiconductor Physics

Semiconductor materials are categorised into two types: elemental and compound semiconductors. [1] Elemental semiconductors, such as Si and Ge, consist of single-element atoms and belong to Column IV. Compound semiconductors include binary, ternary and quaternary compounds composed of two or more different elements. Among these, binary compounds like GaAs are widely used in high-speed electronic and photonic applications. [2, 3]

2.2.1 Basic Crystal Structure

Solid-state materials are classified into three categories: insulators, semiconductors and conductors. The conductivity of a semiconductor can be adjusted for various applications in response to external stimuli, such as temperature changes or intentional doping. The inorganic semiconductor

materials studied here adopt a crystal structure: atoms are arranged in a periodic framework known as a lattice and remain fixed in position. The unit cell serves as the fundamental repeating component of the lattice, defining the overall properties of the crystal. Figure 2.1 illustrates this relationship, where the unit cell is defined by three vectors, a, b and c. These vectors do not necessarily have to be perpendicular to one another or equal in length. The position of any lattice point in the three-dimensional crystal can be expressed as:

$$R = m\mathbf{a} + n\mathbf{b} + p\mathbf{c}, \tag{2.2.1}$$

where m, n and p are integers. Figure 2.1(a) depicts a simple cubic (SC) crystal, where an atom occupies each corner of the cubic lattice, and each atom has six equidistant nearest neighbours. The body-centred cubic (BCC) structure, depicted in Figure 2.1(b), adds a single atom at the centre of the cube, giving each atom eight nearest neighbours. In contrast, the face-centred cubic (FCC) structure shown in Figure 2.1(c) features an atom at the centre

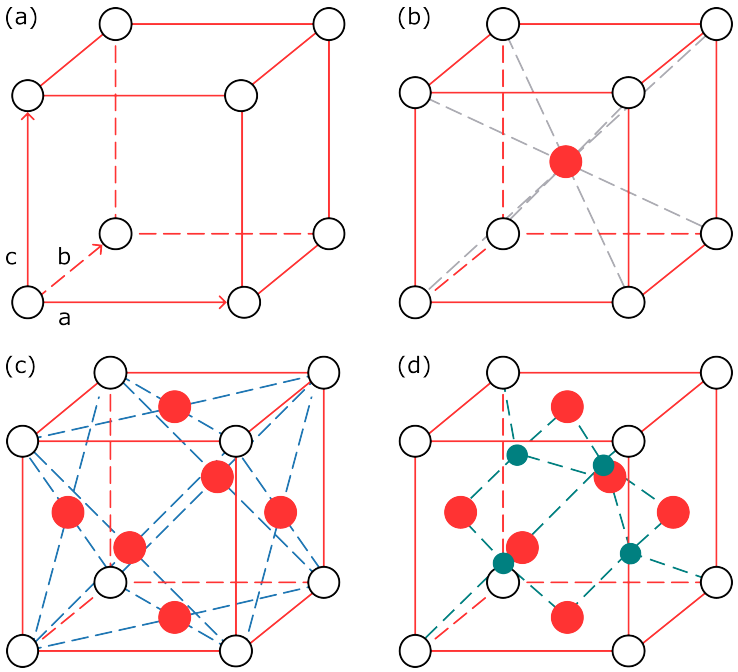

Figure 2.1: Four cubic-crystal unit cells. (a) Simple cubic. (b) Body-centred cubic. (c) Face-centred cubic. (d) Zincblende lattice.

of each of the six cube faces, resulting in twelve nearest neighbours per atom. The elemental semiconductors Si and Ge adopt a diamond cubic structure, which is derived from the FCC lattice. Each atom is surrounded by four equidistant nearest neighbours in a tetrahedral arrangement.

Compound semiconductors, such as gallium arsenide (GaAs), crystallise in the zincblende structure, illustrated in Figure 2.1(d). Zincblende is structurally identical to the diamond lattice, except that the two interpenetrating FCC sublattices consist of different elements – Group III (Ga) and Group V (As) atoms. Other compound semiconductors, such as gallium nitride (GaN), commonly crystallise in structures belonging to the hexagonal crystal family. Specifically, GaN adopts the wurtzite structure, comprising two interpenetrating hexagonal sublattices. In this arrangement, each Ga atom is tetrahedrally coordinated to four neighbouring N atoms, and vice versa.

In addition, the atomic arrangement within a crystal influences its properties along different crystallographic planes. For example, in Figure 2.2(b), the ABCD and ACEF planes contain four and five atoms, respectively, with different atomic spacing. These variations give rise to anisotropic physical and electronic characteristics, which can significantly impact device performance depending on the crystal orientation of the semiconductor. A widely used method for identifying these planes is the Miller indices notation, (hkl). [4] The (100), (110) and (111) planes for the SC family are illustrated in Figure 2.2(a)–(c), respectively.

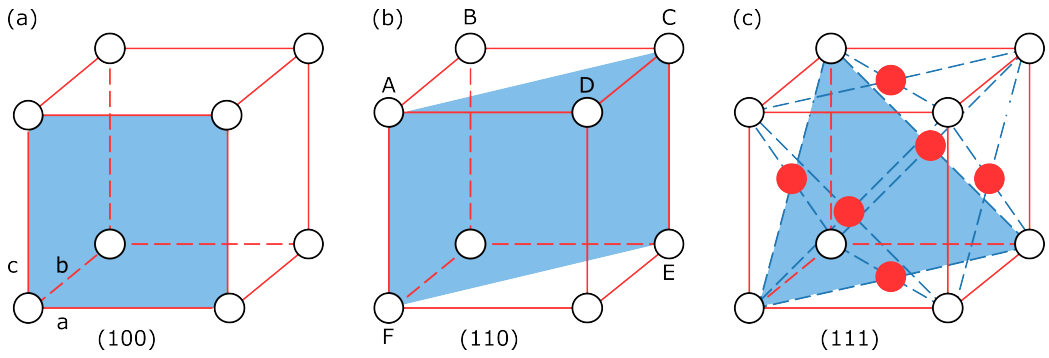

Figure 2.2: Miller indices of the (a) (100), (b) (110) and (c) (111) crystal planes.

2.2.2 Energy Bands

For an isolated atom, electrons occupy discrete energy levels determined by the Schrödinger equation. When extended to solids, this equation accounts for the periodic potential created by the atomic arrangement in the crystal lattice. The time-independent Schrödinger equation [5] for an electron in a potential $V(\mathbf{r})$ is given by:

$$\left[-\frac{\hbar^2}{2m_e}\nabla^2 + V(\mathbf{r})\right]\Psi(\mathbf{r}) = E\Psi(\mathbf{r}), \tag{2.2.2}$$

where $\hbar$ is the reduced Planck's constant, defined as $\hbar = h/2\pi$, m_e is the free electron mass, E is the energy of the system and ∇^2 is the Laplacian operator. The equation yields solutions for the wavefunction $\Psi(\mathbf{r})$, which describes the set of allowed energy levels for electrons to occupy. Assuming the potential energy of the electron is zero, the equation simplifies to:

$$-\frac{\hbar^2}{2m_e}\frac{\partial^2}{\partial r^2}\Psi(r) = E\Psi(r). \tag{2.2.3}$$

In a periodic crystal, Schrödinger's equation can be solved using Bloch's theorem, which states that the energy eigenstates for an electron in a crystal take the form:

$$\Psi_k(r) = e^{ikr}u_k(r), \tag{2.2.4}$$

where $u_k(r)$ is a periodic function with the periodicity of the crystal lattice. In the absence of a potential, $u_k(r)$ is a constant, reducing the wavefunction to:

$$\Psi_k(r) = e^{ikr}. \tag{2.2.5}$$

Taking the second derivative:

$$\frac{\partial^2}{\partial r^2}e^{ikr} = -k^2e^{ikr}. \tag{2.2.6}$$

Substituting this into Equation 2.2.3:

$$\frac{\hbar^2 k^2}{2m_e} e^{ikr} = E e^{ikr}. \tag{2.2.7}$$

Cancelling e^{ikr}:

$$E = \frac{\hbar^2 k^2}{2m_e}. \tag{2.2.8}$$

This result demonstrates the parabolic relationship between energy and the wave vector, k. The same relation can be derived using de Broglie's hypothesis, which states that the wavelength, λ, of an electron is related to its momentum, p, by:

$$\lambda = \frac{h}{p} = \frac{2\pi}{m_e v}, \tag{2.2.9}$$

where v is the velocity of the electron. Since the wave vector, k, is defined as:

$$k = \frac{2\pi}{\lambda}, \tag{2.2.10}$$

an electron in free space can also be described by k. Since there is no potential energy, the total energy of the electron is purely kinetic:

$$E = \frac{1}{2} m_e v^2 = \frac{p^2}{2m_e}. \tag{2.2.11}$$

Substituting the de Broglie relation, $p = \hbar k$, into Equation 2.2.11:

$$E = \frac{\hbar^2 k^2}{2m_e}. \tag{2.2.12}$$

This confirms that the energy of a free electron follows a quadratic dispersion relation with respect to the wave vector, k, resulting in a discrete set of allowed energy states. Figure 2.3 illustrates that electrons can only occupy certain energy levels, forming energy bands separated by forbidden energy gaps. At absolute zero ($T = 0\,\mathrm{K}$), electrons occupy the lowest available en-

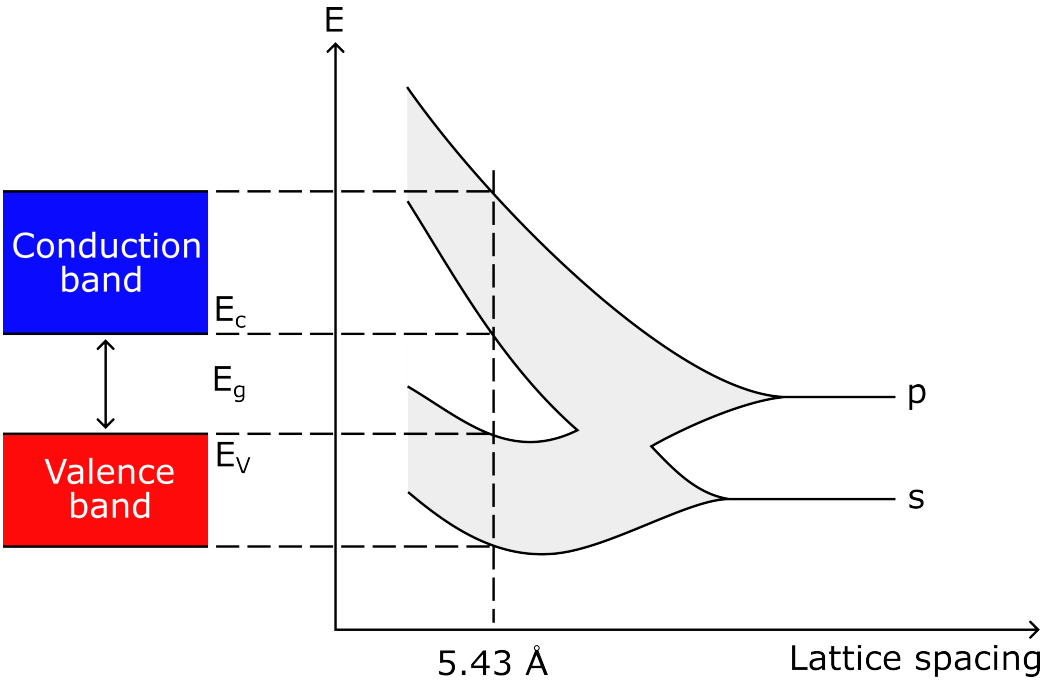

Figure 2.3: Energy band formation in a diamond lattice as two Si atoms are brought together.

ergy states, filling all states in the lower band, known as the valence band, while the next available upper band, the conduction band, remains unoccupied. The bandgap, E_g, refers to the energy difference between the lowest point of the conduction band and the highest point of the valence band. Although multiple valence and conduction bands exist due to the periodicity of the crystal lattice, only the first set is considered here.

At $T > 0\,\mathrm{K}$, electrons in the valence band can be thermally excited into the conduction band. These electrons can carry current, as there are empty available states in the conduction band under an applied electric field. The promotion of electrons leaves unoccupied states in the valence band, known as holes, which also contribute to electrical conduction. In a semiconductor crystal, an electron in the conduction band is relatively free to move within the lattice. However, due to the periodic potential of the nuclei, the free electron mass must be replaced by an effective mass, m_n. This effective mass is determined by taking the second derivative of Equation 2.2.11. The narrower the parabola (see Figure 2.4), corresponding to a larger second derivative, the smaller the effective mass. A similar expression applies to holes, with

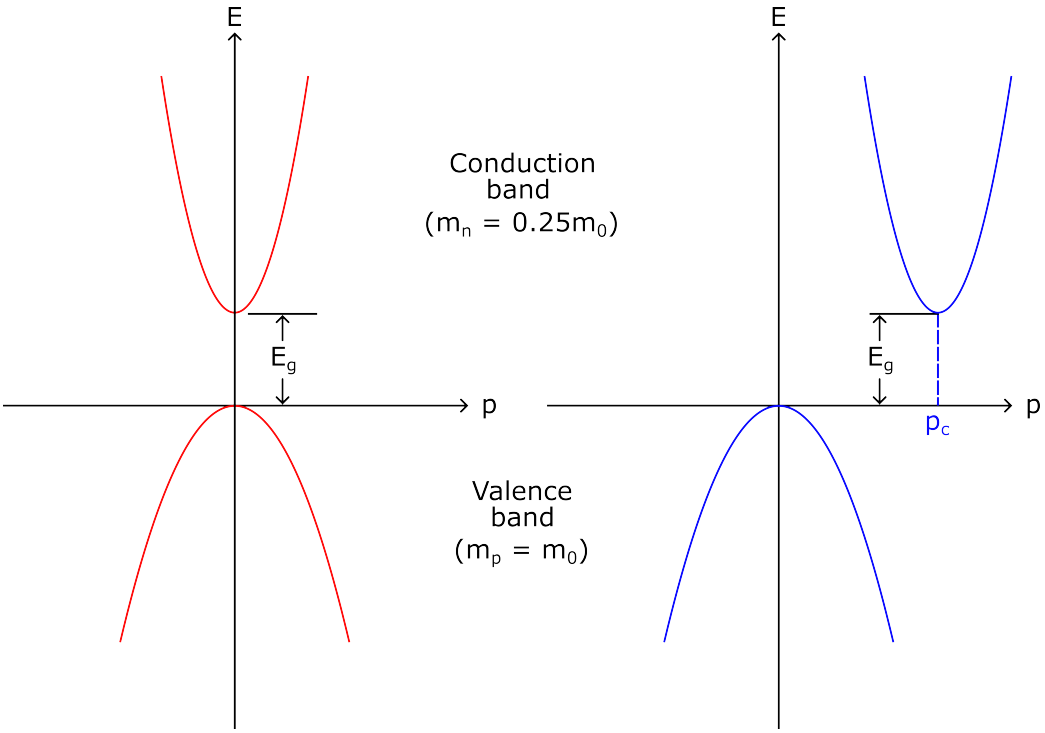

Figure 2.4: A schematic energy-momentum diagram with a direct (red) and indirect (blue) band gap , $m_n = 0.25m_0$ and $m_p = m_0$.

an effective mass denoted as m_p. The energy band diagrams Si and GasAs are more complex. In Si, the maximum of the valence band occurs at $p = 0$ while the minimum of the conduction band lies along the [100] direction at $p = p_c$. As a result, an electron transition requires not only an energy change ($\geq E_g$) but also a momentum change ($= p_c$). This makes silicon an indirect semiconductor. In contrast, GaAs is a direct semiconductor, as the maximum of the valence band and the minimum of the conduction band occur at the same momentum ($p = 0$). This allows an electron to transition between the valence and conduction bands without changing its momentum.

The variation in electrical conductivity among semiconductors, metals and insulators can be explained in terms of their energy bands. As shown in Figure 2.5(a), the conduction band of a metal is either partially filled or can overlap with the valence band, resulting in the absence of a bandgap, E_g. Consequently, the uppermost electrons in the partially filled band or those at the top of the valence band can easily transition to higher energy levels under an applied electric field. Since many unoccupied states are in close proximity

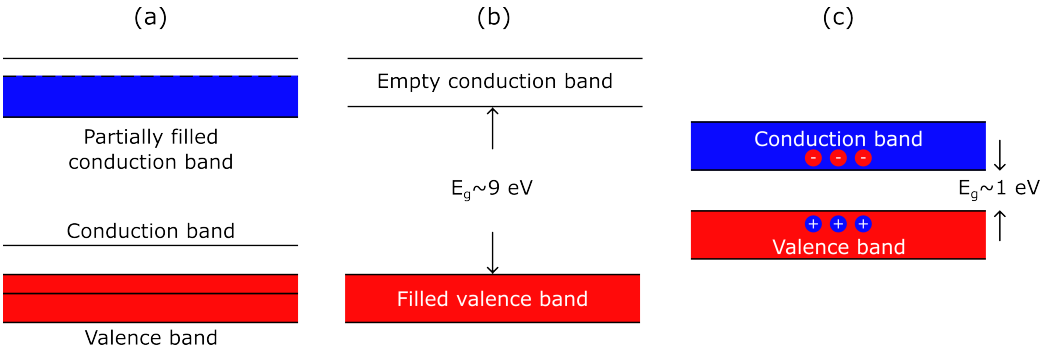

Figure 2.5: Illustration of (a) a conductor, with a partially filled conduction band or overlapping bands, (b) insulator and (c) semiconductor.

to the occupied states, electrons in metals can move freely with minimal applied bias, leading to very low resistivity. In an insulator, such as SiO_2, electrons form strong bonds between neighbouring atoms that are difficult to break. This results in a large E_g with all energy levels in the valence band occupied by electrons, while the conduction band remains empty (see Figure 2.5(b)). Since no free electrons are available for conduction, insulators exhibit high resistivity. Figure 2.5(c) shows that semiconductors have a much smaller bandgap, with Si and GaAs exhibiting E_g values of 1.12 eV and 1.42 eV, respectively. [6] At $T = 0$ K, all electrons reside in the valence band, and the conduction band remains empty. However, at room temperature, the thermal energy of electrons, kT, becomes a significant fraction of E_g, allowing a portion of electrons to gain enough energy to transition into the conduction band. Once there, the addition of a small potential can drive these free electrons into nearby unoccupied states within the conduction band, resulting in a measurable current.

2.2.3 Intrinsic Semiconductors

The carrier concentration at thermal equilibrium is referred to as the steady-state condition at a given temperature, where no external excitations, such as light or applied bias, are present. In this state, thermal excitation causes some electrons to move from the valence band to the conduction band. An intrinsic semiconductor is a material that contains only a small amount of

impurities relative to these thermally generated electrons and holes. To determine the number of electrons per unit volume in an intrinsic semiconductor, the electron density is evaluated over an energy range, dE. This density, $n(E)$, is given by the product of the density of states, $N(E)$ – the density of allowed energy states per energy range per unit volume including spin – by the probability, $F(E)$, of occupying that energy range. The electron density in the conduction band is thus given by:

$$n = \int_0^{E_{top}} n(E)dE = \int_0^{E_{top}} N(E)F(E)dE, \tag{2.2.13}$$

where n is in cm^{-3} and $N(E)$ is in $(\mathrm{cm}^3\,\mathrm{eV})^{-1}$. The probability that an electron occupies an electronic state with energy, E, is given by the Fermi-Dirac distribution function [3]:

$$F(E) = \frac{1}{1 + e^{\frac{E-E_F}{kT}}}, \tag{2.2.14}$$

where k is the Boltzmann constant, T is the absolute temperature in degrees Kelvin and E_F is the energy of the Fermi level. The Fermi level is the energy at which the probability of occupation by an electron is 50 % under thermal equilibrium. Equation 2.2.14 can be simplified to:

$$F(E) \cong e^{-\frac{E-E_F}{kT}} \text{ for } (E - E_F) > 3kT \tag{2.2.15}$$

for an electron, and

$$F(E) \cong 1 - e^{-\frac{E-E_F}{kT}} \text{ for } (E - E_F) < 3kT \tag{2.2.16}$$

for a hole. There are a large number of allowed states in the conduction band; however, in an intrinsic semiconductor, only a limited number of electrons occupy these states, making the probability of their occupation small. The same applies to the valence band, but in contrast, the probability of an electron occupying one of its states is nearly unity. By substituting $N(E)$ and Equation 2.2.15 into 2.2.13:

$$n = \frac{2}{\sqrt{\pi}} N_C (kT)^{-3/2} \int_0^{\infty} E^{1/2} e^{\frac{E_F - E}{kT}} dE, \tag{2.2.17}$$

where $E_{top} = \infty$, as $F(E)$ decreases when $(E - E_C) >> kT$ and E_F is located near the middle of E_g. If $x \equiv E/kT$ this becomes:

$$n = \frac{2}{\sqrt{\pi}} N_C e^{\frac{E_F}{kT}} \int_0^{\infty} x^{1/2} e^{-x} dx. \tag{2.2.18}$$

The integral is standard form and equals $\sqrt{\pi}/2$:

$$n = N_C e^{\frac{E_F}{kT}}. \tag{2.2.19}$$

Now, referring to the bottom of the conduction band as E_C instead of $E = 0$, the electron density in the conduction band is given by:

$$n = N_C e^{\frac{E_F - E_C}{kT}}, \tag{2.2.20}$$

where N_C is the effective density of states in the conduction band. Similarly, the hole density, p, in the valence band is given by:

$$p = N_V e^{\frac{E_V - E_F}{kT}}, \tag{2.2.21}$$

where N_V is the effective density of states in the valence band. For an intrinsic semiconductor, the number of electrons per unit volume in the conduction band is equal to the number of holes per unit volume in the valence band, that is $n = p = n_i$, where n_i is the intrinsic carrier density. By equating Equations 2.2.20 and 2.2.21:

$$E_F = E_i = \frac{E_C + E_V}{2} + \frac{kT}{2} \ln \frac{N_V}{N_C}. \tag{2.2.22}$$

At room temperature, the second term is much smaller than the bandgap, meaning the Fermi level, E_i, of an intrinsic semiconductor generally lies close to the middle of the bandgap. The intrinsic carrier density is given by the following equations:

$$\boldsymbol{np = n_i^2}, \tag{2.2.23}$$

which is known as the mass action law, where

$$n_i{}^2 = N_C N_V e^{\frac{-E_g}{kT}}, \tag{2.2.24}$$

$$n_i = \sqrt{N_C N_V} e^{\frac{-E_g}{2kT}}, \tag{2.2.25}$$

and $E_g \equiv E_C - E_V$. Hole concentration in a intrinsic semiconductor can be derived by substituting $E_F = E_i$ under these conditions into Equation 2.2.21 and rearranging for N_V:

$$N_V = n_i e^{\frac{E_i - E_V}{kT}}. \tag{2.2.26}$$

Substituting into Equation 2.2.21:

$$\boldsymbol{p = n_i e^{\frac{E_i - E_F}{kT}}}, \tag{2.2.27}$$

and similarly:

$$\boldsymbol{n = n_i e^{\frac{E_F - E_i}{kT}}}. \tag{2.2.28}$$

2.2.4 Extrinsic Semiconductors

A semiconductor becomes extrinsic when impurities are introduced into the crystal lattice to modify its electrical properties by increasing the density of free charge carriers, or by altering the energy levels within the band structure. As illustrated in Figure 2.6(a), when a Si atom is replaced by an As atom with five valence electrons, the As atom forms covalent bonds with its four neighbouring Si atoms. The fifth electron, being loosely bound to the As atom, can be ionised and contribute to conduction. This donated electron moves into the conduction band and As is therefore termed a donor. The doped Si is classified as an n-type semiconductor due to the introduction

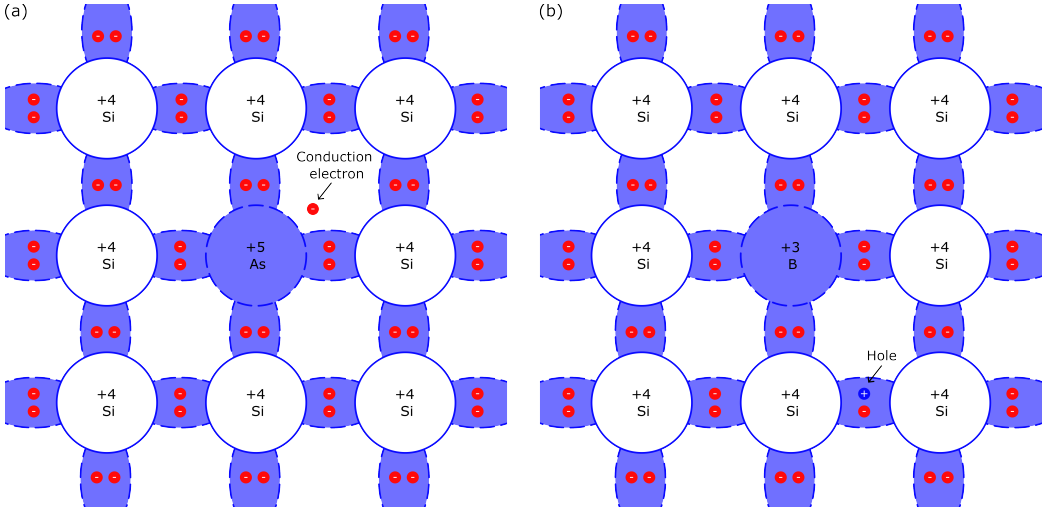

Figure 2.6: Bonding for (a) n-type Si with donor (As) and (b) p-type Si with acceptor (B).

of a negative charge carrier. As a result, E_F shifts above the mid-gap, E_i, since $n \gg p$, requiring the Fermi-Dirac function, $F(E)$, to move closer to the conduction band edge, to accommodate the change in carrier concentration. The relative position of E_F can be calculated using:

$$n = N_C e^{\frac{E_F - E_C}{kT}} \approx N_D, \tag{2.2.29}$$

$$E_C - E_F = kT \ln \frac{N_C}{N_D}. \tag{2.2.30}$$

This assumes that each donor impurity atom contributes one electron to the conduction band. As N_D increases, the logarithmic term decreases, causing E_F to move toward E_C. When $N_D > N_C$, the logarithmic term becomes negative and E_F moves into E_C, causing the semiconductor to behave similarly to a metal. This highly doped regime is referred to as a degenerate semiconductor.

Similarly, when a B atom with three valence electrons replaces a Si atom, an additional electron is accepted to form four covalent bonds, generating a positively charged hole in the valence band. This doped Si is now classified as a p-type semiconductor due to the removal of a negative charge carrier, with B acting as an acceptor (see Figure 2.6(b)). Consequently, E_F shifts

below E_i since $p \gg n$, requiring $F(E)$ to move closer to the valence band edge. As previously:

$$p = N_V e^{\frac{E_V - E_F}{kT}} \approx N_A, \tag{2.2.31}$$

$$E_F - E_V = kT \ln \frac{N_V}{N_A}. \tag{2.2.32}$$

2.2.5 Carrier Transport

Carrier mobility, μ, is a measure of how easily charge carriers move through the lattice under an applied electric field. As temperature increases, enhanced lattice vibrations lead to more frequent carrier scattering events, reducing mobility. Impurities within the material can also act as scattering centres, further influencing charge transport. The overall mobility is typically described as a combination of contributions from lattice and impurity scattering. The probability of a collision taking place in unit time is the sum of the probabilities of collisions due to the various scattering mechanisms:

$$\frac{1}{\tau_c} = \frac{1}{\tau_{c,lattice}} + \frac{1}{\tau_{c,impurity}}, \tag{2.2.33}$$

or

$$\frac{1}{\mu} = \frac{1}{\mu_L} + \frac{1}{\mu_I}, \tag{2.2.34}$$

where μ_L is the lattice-scattering term, which depends on temperature as $\mu_L \propto T^{-3/2}$, and μ_I is the impurity-scattering term, which depends on both carrier concentration and temperature as $\mu_I \propto \frac{T^{3/2}}{N_I}$. Carrier transport in semiconductors is governed by two key mechanisms: drift and diffusion. Drift refers to the motion of carriers under an electric field. At low fields, electron drift velocity is proportional to the electric field, subject to the proportionality constant, electron mobility:

$$\mu_n = \frac{q\tau_c}{m_n}, \tag{2.2.35}$$

where q is the elementary charge, τ_c is the mean free time between scattering events and m_n is the effective mass of electrons [2]. Diffusion results from the random thermal motion of carriers in the presence of a concentration gradient. When both an electric field and a concentration gradient are present, both drift and diffusion currents contribute to the total current flow. Thus, the total current density at any point is the sum of these two components:

$$J_n = q\mu_n\varepsilon + qD_n\frac{dn}{dx}, \tag{2.2.36}$$

where q is the charge of an electron, ε is the applied electric field in the x direction and D_n is the electron diffusion coefficient. A similar expression can be derived for hole current:

$$J_p = q\mu_p\varepsilon - qD_p\frac{dp}{dx}. \tag{2.2.37}$$

Thus, the total current density, valid for low electric fields, is given by:

$$J = J_n + J_p. \tag{2.2.38}$$

Understanding carrier transport is essential for analysing the behaviour of fundamental semiconductor components, particularly the p–n junction, which underpins devices such as the MOS capacitor and MOSFET. When p- and n-type semiconductors meet, the large concentration gradients at the junction cause carrier diffusion. Holes from the p-side diffuse into the n-side while electrons from the n-side diffuse into the p-side. As holes continue to diffuse, some acceptor ions ($N_A{}^-$) near the junction are left uncompensated, as they are fixed in place within the lattice. Similarly, donor ions ($N_D{}^+$) are also left behind to create a space-charge-limited region. Figure 2.7 shows that an electric field then forms, directed from the positive charge toward the negative charge, opposing the diffusion current for each type of charge carrier. At thermal equilibrium, the individual electron and hole currents flowing across the junction are zero. Therefore, the drift current due to

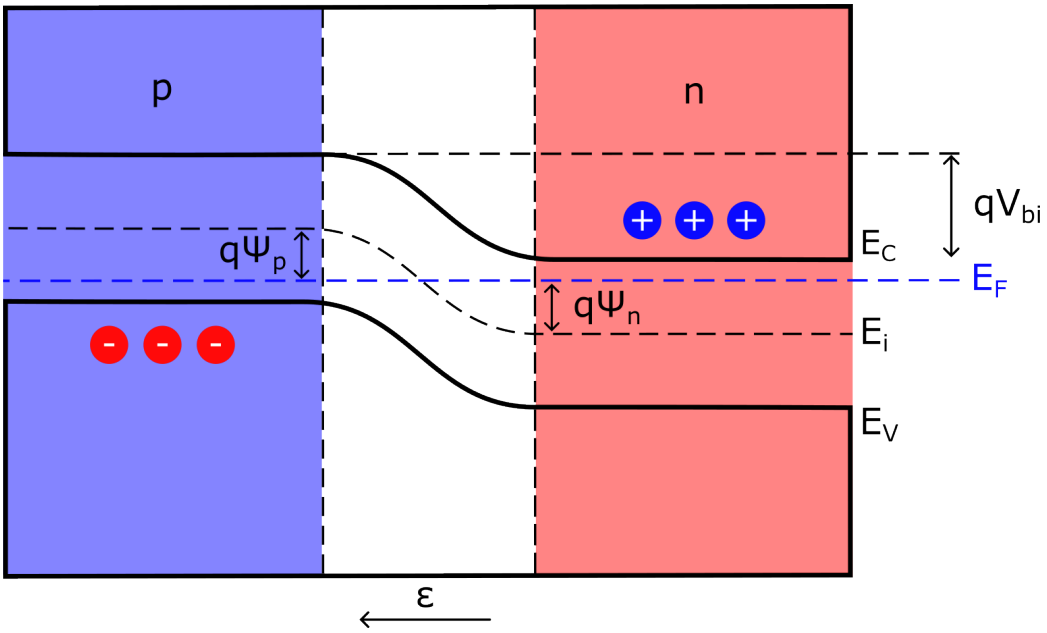

Figure 2.7: Energy band diagram of a $p-n$ junction at thermal equilibrium.

the electric field must cancel the diffusion current due to the concentration gradient for each type of carrier. By setting Equation 2.2.37 to zero:

$$q\mu_p p\left(\frac{1}{q}\frac{dE_i}{dx}\right) - kT\mu_p\frac{dp}{dx} = 0, \tag{2.2.39}$$

where $\varepsilon = \frac{1}{q}\frac{dE_i}{dx}$ and $D_p = (kT/q)\mu_p$ is termed the Einstein relation. Substituting $p = n_i e^{(E_i - E_F)/kT}$ and its derivative:

$$\frac{dp}{dx} = \frac{p}{kT}\left(\frac{dE_i}{dx} - \frac{dE_F}{dx}\right), \tag{2.2.40}$$

yields the hole current density:

$$J_p = \mu_p p\frac{dE_F}{dx} = 0. \tag{2.2.41}$$

Similarly for the net electron current density:

$$J_p = \mu_n n\frac{dE_F}{dx} = 0. \tag{2.2.42}$$

Therefore, under thermal equilibrium, the Fermi level remains constant and independent of x, resulting in a unique space charge distribution and

electrostatic potential, which can be described using Poisson's Equation. [6,7] Assuming complete ionisation of donors and acceptors, Poisson's equation is given by:

$$\frac{\boldsymbol{d^2\Psi}}{\boldsymbol{dx^2}} \equiv -\frac{\boldsymbol{d\varepsilon}}{\boldsymbol{dx}} = -\frac{\boldsymbol{\rho_s}}{\boldsymbol{\epsilon_s}} = -\frac{\boldsymbol{q}}{\boldsymbol{\epsilon_s}}(\boldsymbol{N_D - N_A + p - n}), \tag{2.2.43}$$

where ϵ_s is the semiconductor dielectric permittivity and ρ_s is the space charge density given by the algebraic sum of the charge carrier densities and ionised impurity concentration. In regions away from the metallurgical junction, charge neutrality is maintained and the total space charge density is zero. In these regions, $\frac{d^2\Psi}{dx^2} = 0$, simplifying Equation 2.2.43 to:

$$N_D - N_A + p - n = 0. \tag{2.2.44}$$

For the p-type region, where $N_D = 0$ and $p \gg n$, the electrostatic potential can be expressed in terms of E_F. Setting $N_D = n = 0$ and substituting $p = N_A$ into $p = n_i e^{(E_i - E_F)/kT}$ yields:

$$\Psi_p \equiv -\frac{1}{q}(E_i - E_F)\bigg|_{x \leq -x_p} = -\frac{kT}{q}\ln\left(\frac{N_A}{n_i}\right). \tag{2.2.45}$$

Similarly, for the n-type neutral region:

$$\Psi_n \equiv -\frac{1}{q}(E_i - E_F)\bigg|_{x \geq x_n} = -\frac{kT}{q}\ln\left(\frac{N_D}{n_i}\right). \tag{2.2.46}$$

The built-in potential, which represents the electrostatic potential difference between the neutral regions on the p- and n-sides at thermal equilibrium, is given by:

$$\boldsymbol{V_{bi} = \Psi_n - \Psi_p = \frac{kT}{q}\ln\left(\frac{N_D N_A}{{n_i}^2}\right)}. \tag{2.2.47}$$

The depletion region can be approximated as a rectangular charge distribution, as illustrated in Figure 2.8, where x_p and x_n denote the depletion layer widths on the p- and n-sides, respectively, with carrier concentrations

$p = n = 0$. In the depletion region, Poisson's Equation becomes:

$$\frac{d^2\Psi}{dx^2} = +\frac{qN_A}{\varepsilon_s} \tag{2.2.48}$$

for $-x_p \leq x < 0$, and

$$\frac{d^2\Psi}{dx^2} = -\frac{qN_D}{\varepsilon_s} \tag{2.2.49}$$

for $0 < x \leq x_n$. The overall space charge neutrality of the semiconductor requires that the total negative space charge per unit area in the p-side must equal the total positive space charge per unit area in the n-side:

$$N_A x_p = N_D x_n. \tag{2.2.50}$$

The total depletion layer width is shown by Figure 2.8

$$W = x_p + x_n. \tag{2.2.51}$$

The electric field is obtained by integrating Equations 2.2.48 and 2.2.49:

$$\varepsilon(x) = -\frac{d\Psi}{dx} = -\frac{qN_A(x + x_p)}{\epsilon_s} \tag{2.2.52}$$

for $-x_p \leq x < 0$, and

$$\varepsilon(x) = -\varepsilon_m + \frac{qN_D x}{\epsilon_x} = \frac{qN_D}{\epsilon_s}(x - x_n) \tag{2.2.53}$$

for $0 < x \leq x_n$, where ε_m is the maximum field that exists at $x = 0$, given by:

$$\varepsilon_m = \frac{qN_D x_n}{\epsilon_s} = \frac{qN_A x_p}{\epsilon_s}. \tag{2.2.54}$$

The total potential variation, namely, the built-in potential in terms of W:

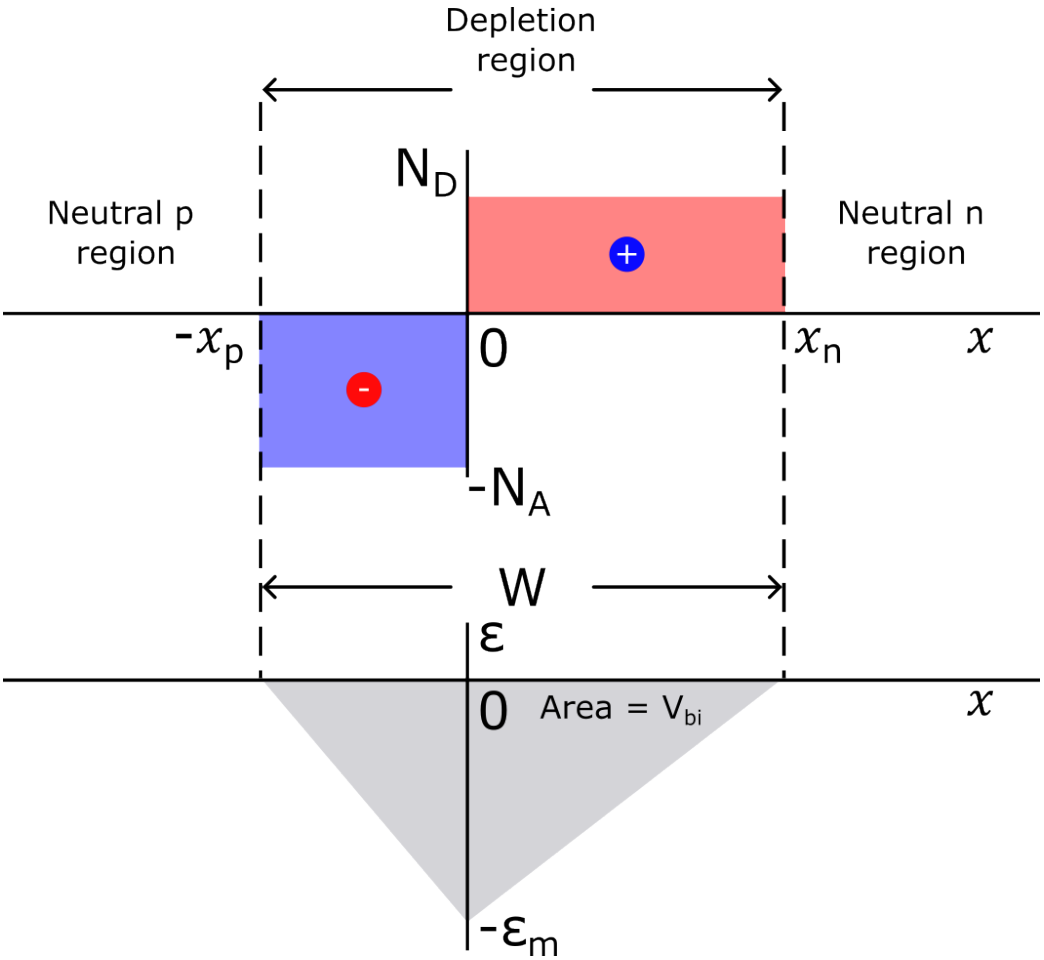

Figure 2.8: Space charge distribution in the depletion region. Electric field distribution with the grey area corresponding to the built-in potential.

$$V_{bi} = \int_{-x_p}^{x_n} \varepsilon(x)dx = -\int_{-x_p}^{0} \varepsilon(x)dx\Big|_{p-side} - \int_{0}^{x_n} \varepsilon(x)dx\Big|_{n-side} \tag{2.2.55}$$

$$= \frac{qN_A{x_p}^2}{2\varepsilon_s} + \frac{qN_D{x_n}^2}{2\varepsilon_s} = \frac{1}{2}\varepsilon_m W \tag{2.2.56}$$

Therefore, the total depletion layer width as a function of built-in potential is given by:

$$\boldsymbol{W = \sqrt{\frac{2\varepsilon_s}{q}\frac{N_A + N_D}{N_A N_D} V_{bi}}.} \tag{2.2.57}$$

For a one-sided abrupt junction ($p^+ - n$), $N_A >> N_D$. In this case the

depletion layer width of the p-side is much smaller than the n-side $x_p << x_n$ and the expression for W can be simplified:

$$\boldsymbol{W \cong x_n = \sqrt{\frac{2\varepsilon_s V_{bi}}{qN_D}}.} \tag{2.2.58}$$

Applying an external voltage to the p-n junction disrupts the balance between drift and diffusion currents. In thermal equilibrium, the mass action law (Equation 2.2.23) holds. However, when a forward bias is applied (positive voltage to the p-side), the electrostatic potential across the depletion region is reduced, diminishing the drift current relative to the diffusion current. The minority carrier concentration on either side of the junction increases due to carrier injection and the system is driven out of equilibrium such that $np > n_i^2$. As a result, current increases rapidly. Most semiconductor devices operate under these non-equilibrium conditions, where the interplay between carrier injection and recombination is fundamental to device performance. In contrast, reverse bias increases the electrostatic potential across the depletion region, suppressing the diffusion current. Consequently, only a small leakage current flows until the breakdown voltage is reached, beyond which a sudden and substantial increase in current – known as junction breakdown – occurs. The width of the depletion layer (W) varies with the square root of the total electrostatic potential across the junction, as described by Equation 2.2.59:

$$W = \sqrt{\frac{2\epsilon_s(V_{bi} - V)}{qN_D}} \tag{2.2.59}$$

Thus, forward bias (positive V) reduces the depletion width, while reverse bias (negative V) increases it.

2.3 Review of Metal-Oxide-Semiconductor (MOS) Devices

2.3.1 The Ideal MOS Capacitor

The metal-oxide-semiconductor (MOS) capacitor is the core building block of many semiconductor devices, including MOSFETs. The device structure shown in Figure 2.9 consists of an Al ohmic contact at the bottom of the substrate and a top contact on the Si – SiO_2 stack, forming a parallel-plate capacitor. With reference to the vacuum level (outside the material), the electron affinity, $q\chi$, of a semiconductor is defined as the energy difference between the conduction band minimum and the vacuum level. The work function, $q\phi$, is defined as the energy required to remove an electron from the Fermi level to the vacuum level. An ideal MOS capacitor is characterised by (i) the metal and semiconductor work functions are equal, $q\phi_m = q\phi_s$, meaning there is no barrier for charge injection. This condition, known as the flat-band condition, occurs in the absence of an applied voltage (see Equation 2.3.60), (ii) the only charges that exist in the capacitor are those confined in the semiconductor with equal and opposite polarities on the metal surface adjacent to the oxide, and (iii) there is no carrier transport through the oxide (leakage current).

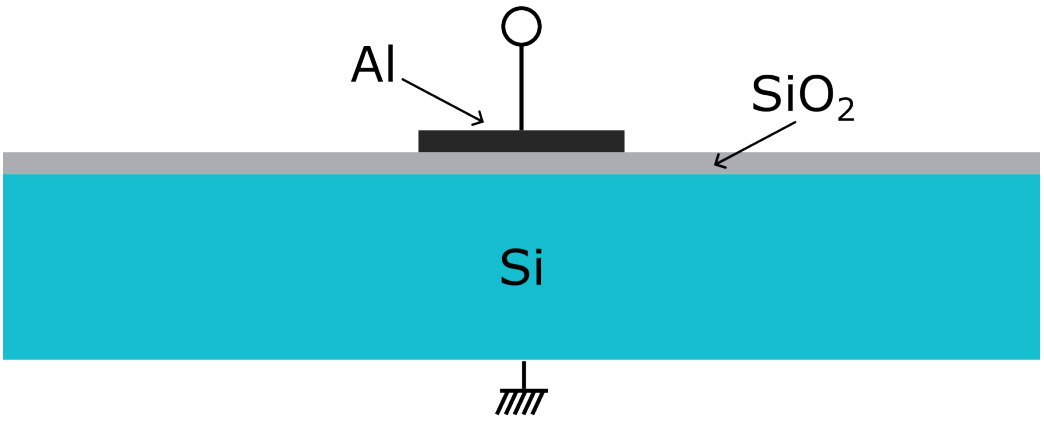

Figure 2.9: Diagram of a MOS capacitor.

$$q\phi_{ms} = q\phi_m - q\phi_s = q\phi_m - \left(q\chi + \frac{E_G}{2} + q\Psi_B\right) = 0 \tag{2.3.60}$$

With an applied bias, the MOS capacitor can operate in three distinct modes: accumulation, depletion and inversion. For a p-type semiconductor, under negative bias ($V < 0\,\mathrm{V}$), excess positive carriers (holes) accumulate at the oxide-semiconductor interface. This causes the energy bands near the semiconductor surface to bend upwards while E_F remains constant in the ideal case. The hole concentration depends exponentially on the energy difference between the intrinsic level and the Fermi level, given by:

$$p_p = n_i e^{\frac{E_i - E_F}{kT}}. \tag{2.3.61}$$

The upward bending increases $E_i - E_F$, leading to hole accumulation near the oxide-semiconductor interface. Conversely, under positive bias ($V > 0\,\mathrm{V}$), the bands bend downward, depleting holes and creating a space charge per unit area:

$$Q_{SC} = -qN_A W, \tag{2.3.62}$$

where W is the width of the depletion region. As the positive voltage increases, the bands bend further downward until E_i at the surface coincides with E_F, inducing negative charge carriers (electrons) at the oxide-semiconductor interface. The electron concentration follows:

$$n_p = n_i e^{\frac{E_F - E_i}{kT}}. \tag{2.3.63}$$

In this case, $E_F - E_i > 0$, meaning $n_p > n_i$ at the interface, while the hole concentration $p_p < n_i$ (from Equation 2.3.61). Since the number of electrons (minority carriers) at the surface exceeds that of holes (majority carriers), the surface becomes inverted. Initially, the surface enters a weak inversion regime, where n_p is small. As the bands bend further, the conduction band edge approaches E_F, leading to a strong inversion regime, when $n_p \approx N_A$.

Here, any additional negative charge accumulates as Q_n in the inversion layer over x_i ($0 \leq x \leq x_i$), which typically ranges from 1 nm to 10 nm. The total charge in the system is given by:

$$Q_s = Q_n + Q_{SC} = Q_n - qN_A W_m, \tag{2.3.64}$$

where W_m is the maximum depletion layer width under strong inversion. The electrostatic potential, Ψ, is defined as zero in the bulk of the semiconductor. At the surface, $\Psi = \Psi_S$, is termed the surface potential. The electron and hole concentration can be expressed in terms of Ψ:

$$n_p = n_i e^{\frac{q(\Psi - \Psi_B)}{kT}}, \tag{2.3.65}$$

$$p_p = n_i e^{\frac{q(\Psi_B - \Psi)}{kT}}, \tag{2.3.66}$$

where Ψ is positive when the band is bent downward. At the surface, the densities are:

$$n_s = n_i e^{\frac{q(\Psi_S - \Psi_B)}{kT}}, \tag{2.3.67}$$

$$p_s = n_i e^{\frac{q(\Psi_B - \Psi_S)}{kT}}, \tag{2.3.68}$$

The following regions of surface potential can be defined using 2.3.66 and 2.3.67:

$\Psi_S < 0$ Accumulation of holes (band bends upwards)

$\Psi_S = 0$ Flat band condition

$\Psi_S > 0$ Depletion of holes (band bends downwards)

$\Psi_S = \Psi_B$ Mid-gap with $n_s = n_p = n_i$

$\Psi_S > \Psi_B$ Inversion (band bends downwards)

The potential Ψ_S as a function of distance can be obtained by using the one-dimensional Poisson's Equation:

$$\frac{d^2\phi}{dx^2} = -\frac{\rho_s(x)}{\epsilon_s}, \tag{2.3.69}$$

where ρ_s is the charge density per unit volume at a position x and ϵ_x is the dielectric permittivity. Integration of Poisson's Equation gives the electrostatic potential distribution as a function of x in the surface depletion region:

$$\Psi = \Psi_S \left(1 - \frac{x}{W}\right)^2, \tag{2.3.70}$$

where $\rho_s = -qN_A$ and $\Psi_S = \frac{qN_AW^2}{2\epsilon_s}$ when the semiconductor is depleted to a width W identical to that obtained for a one-sided $n^+ - p$ junction.

The surface is inverted for $\Psi_S > \Psi_B$. For strong inversion, $n_s = N_A$, and $N_A = n_i e^{\frac{q\Psi_B}{kT}}$ (see Equation 2.3.67):

$$\Psi_S^{(\text{inv})} \cong 2\Psi_B = \frac{2kT}{q} \ln \frac{N_A}{n_i}. \tag{2.3.71}$$

Equation 2.3.71 states that a potential Ψ_B is required to bend the energy bands down to the intrinsic condition at the surface, $E_i - E_F$, and further bending by $q\Psi_B$ results in strong inversion. The surface depletion layer width reaches a maximum at strong inversion:

$$W_m = \sqrt{\frac{2\epsilon_s(2\Psi_B)}{qN_A}} = \sqrt{\frac{4\epsilon_s kT}{q^2 N_A} \ln \frac{N_A}{n_i}}, \tag{2.3.72}$$

and

$$Q_{SC} = -qN_AW_m = -\sqrt{2q\epsilon_s N_A(2\Psi_B)}. \tag{2.3.73}$$

In the absence of any work function differences, the applied voltage will appear partly across the oxide and semiconductor for an ideal MOS capacitor with band bending:

$$V = V_0 + \Psi_S, \tag{2.3.74}$$

where $V_0 = \frac{\epsilon_0}{d} = \frac{|Q_s|d}{\epsilon_{ox}} = \frac{|Q_s|}{C_0}$ is the potential across the oxide, ϵ_0 is the field in the oxide, Q_s is the charge per unit area in the semiconductor and $C_0 = \epsilon_{ox}/d$ is the capacitance per unit area. The total capacitance of the MOS capacitor is a series combination of the oxide capacitance, C_0, and that of the depletion layer, C_j:

$$C = \frac{C_0 C_j}{C_0 + C_j}, \tag{2.3.75}$$

where $C_j = \epsilon/W$, as in an abrupt p-n junction. Using Equations 2.3.70, 2.3.74 and 2.3.75, W can be eliminated to derive an expression for capacitance:

$$\frac{C}{C_0} = \frac{1}{\sqrt{1 + \frac{2\epsilon_{ox}^2 V}{qN_A\epsilon_s d^2}}}. \tag{2.3.76}$$

This equation predicts that capacitance decreases with increasing metal-plate voltage as the surface depletes. For $V < 0\,\mathrm{V}$, no depletion region forms, and instead, holes accumulate at the semiconductor surface, causing the total capacitance to almost equal the oxide capacitance. Under strong inversion ($\Psi_S = \Psi_S^{(\mathrm{inv})}$), the width of the depletion region does not exceed a maximum value even with further increases in bias. Substituting this condition into Equation 2.3.74 and noting that the charge per unit area is qN_AW_m, expresses the threshold voltage, V_T for strong inversion:

$$V_T = \frac{qN_AW_m}{C_0} + \Psi_S(inv) \cong \frac{\sqrt{2q\epsilon_s N_A(2\Psi_B)}}{C_0} + 2\Psi_B \tag{2.3.77}$$

Once strong inversion takes place, the total capacitance will reach a minimum value:

$$C_{min} = \frac{\epsilon_{ox}}{d + \left(\frac{\epsilon_{ox}}{\epsilon_s}\right) W_m}. \tag{2.3.78}$$

The analysis above describes the capacitance voltage behaviour of an ideal MOS capacitor, which assumes no work function difference and a perfect interface. In practice, the metal-SiO_2 capacitor is the most extensively studied, as its electrical characteristics closely resemble those of the ideal case. However, the work function difference, $q\phi_{ms}$, is generally not zero and various charges at the $Si-SiO_2$ interface can cause deviations from ideal MOS behaviour. The work function of a semiconductor, $q\phi_s$, varies with doping concentration. For a given metal with a fixed work function, $q\phi_m$, the work function difference therefore depends only on doping concentration. Common metal electrodes include Al and heavily doped n^+- and p^+-polysilicon, with work functions of $q\phi_m = 4.1\,\text{eV}$, $4.05\,\text{eV}$ and $5.05\,\text{eV}$, respectively. [3, 6]

2.3.2 Metal-Oxide-Semiconductor Field-Effect Transistors (MOSFETs)

The MOSFET integrates source and drain regions with the MOS structure to enable current modulation via the gate electrode. First demonstrated in 1960 by Kahng and Atalla at Bell Labs [8], the MOSFET is the most prevalent switching device in modern electronics. Figure 2.10 shows a schematic of an n-type MOSFET, which comprises a p-type substrate with two heavily doped n^+ regions (source and drain), a gate electrode separated by a thin oxide layer and a substrate contact serving as the fourth terminal. The distance between the two back-to-back metallurgical $n^+ - p$ junctions defines the channel length, L, and dielectric thickness, d.

MOSFETs can be classified into four types, depending on the type of inversion layer and the applied gate bias. In all cases, the source electrode typically serves as the voltage reference and is usually grounded. An n-channel MOSFET operating in enhancement mode is normally off at zero gate bias ($V_{gs} = 0\,\text{V}$), with only a small reverse-leakage current (I_{off}) flowing from source to drain. A sufficiently positive gate voltage must be applied to invert the surface region beneath the gate and create a conductive n-channel. In depletion mode, an n-channel MOSFET is normally on and a

negative gate voltage must be applied to deplete carriers. The remaining two types are p-channel MOSFETs in enhancement and depletion modes. In enhancement mode, a negative gate voltage is required to form a p-channel, while in depletion mode, the device conducts at zero bias and is turned off by applying a positive gate voltage.

The first type of measurement used to characterise the performance of a MOSFET is the output characteristic, which illustrates the evolution of drain-source current (I_{ds}) as the drain-source voltage (V_{ds}) increases, with each curve corresponding to an increment of V_{gs}. Figure 2.11(a) shows a typical output characteristic for an n-channel MOSFET that is normally-off at $V_{gs} = 0\,\mathrm{V}$, operating in enhancement mode. The output characteristics can be divided into two modes of operation: the linear regime ($V_{ds} < |V_{gs} - V_{th}|$) and the saturation regime ($V_{ds} > |V_{gs} - V_{th}|$). In the linear regime, I_{ds} increases linearly with V_{ds} and the MOSFET behaves as a gate voltage-controlled variable resistor. As V_{ds} approaches the saturation condition, the inversion layer near the drain ($y = L$) reduces to zero. This is known as pinch-off, where the channel is no longer continuous and the potential at this point becomes fixed by V_{gs} and V_{th}. Beyond pinch-off, I_{ds} remains constant

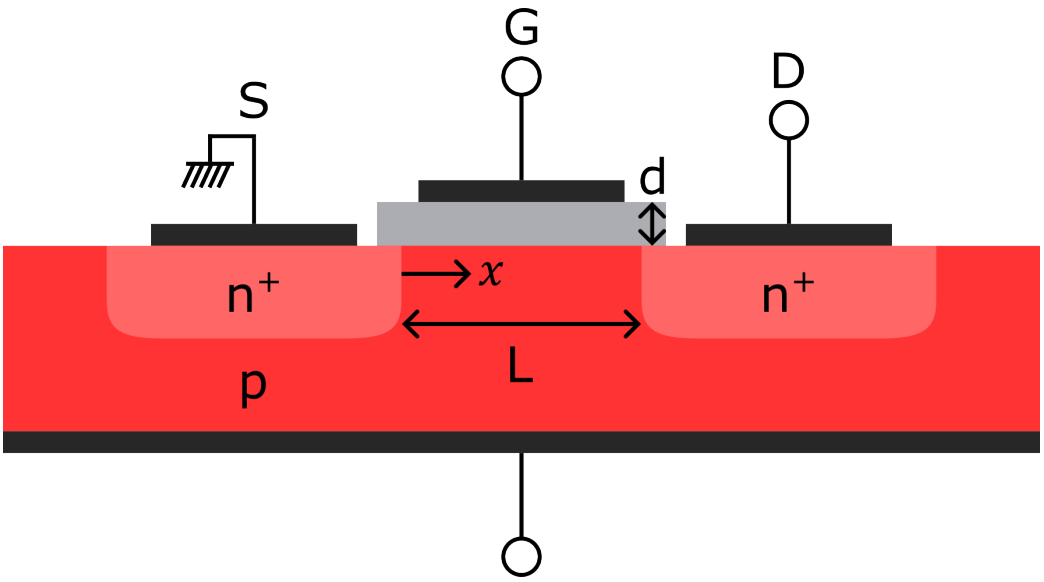

Figure 2.10: (a) Diagram of a MOSFET with source (S), drain (D) and gate (G) electrodes.

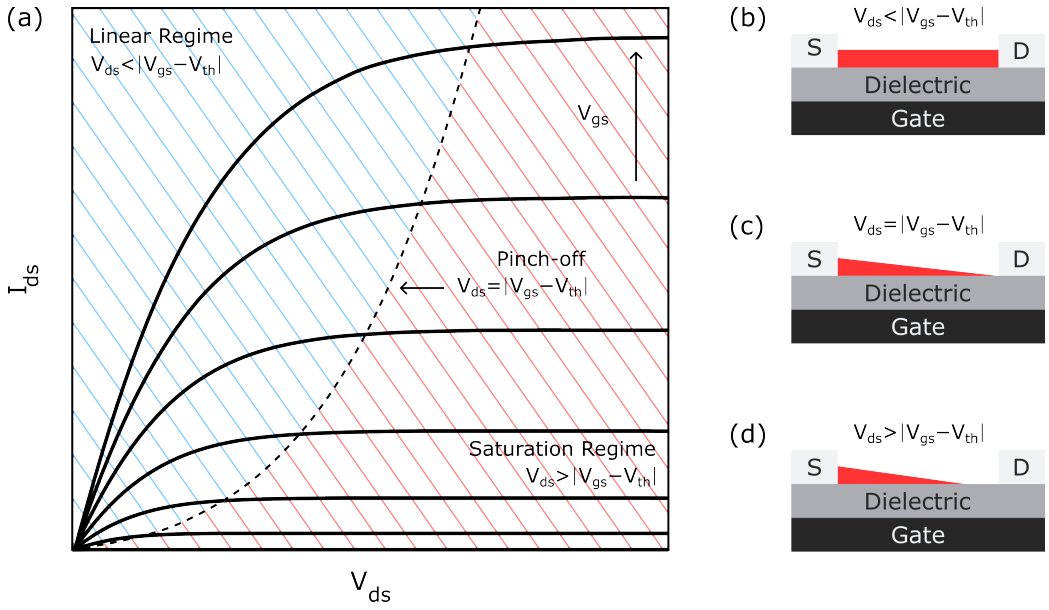

Figure 2.11: (a) Output curves illustrating the linear and saturation operation regimes. Charge distribution in the (b) linear regime (c) at pinch-off and (d) the saturation regime.

despite further increases in V_{ds}, as the depletion region extends further into the channel. This behaviour characterises the saturation regime of MOSFET operation.

The second type of measurement is termed a transfer characteristic (see Figure 2.12), where I_{ds} is plotted on a logarithmic scale against V_{gs} at a fixed V_{ds}. In this work, the approximation for I_{ds} was taken in the saturation regime. Key performance parameters, such as μ, are extracted from the transfer curves, with a detailed calculation provided in Chapter 3.10. The transfer characteristics also yield V_{th}, calculated by finding the intercept at $I_{ds} = 0\,\mathrm{A}$, as well as $I_{on/off}$ representing the difference between the minimum and maximum measured I_{ds} and quoted as a logarithmic value. In addition to the shift in V_{th}, evidence of charge trapping and de-trapping can be inferred from device hysteresis – observed as a significant difference in the measured I_{ds} between the forward and reverse voltage sweeps. The corresponding interface trap density, N_{trap}, can be estimated using:

$$N_{trap} = \frac{C_i \cdot \Delta V_{th}}{q}, \tag{2.3.79}$$

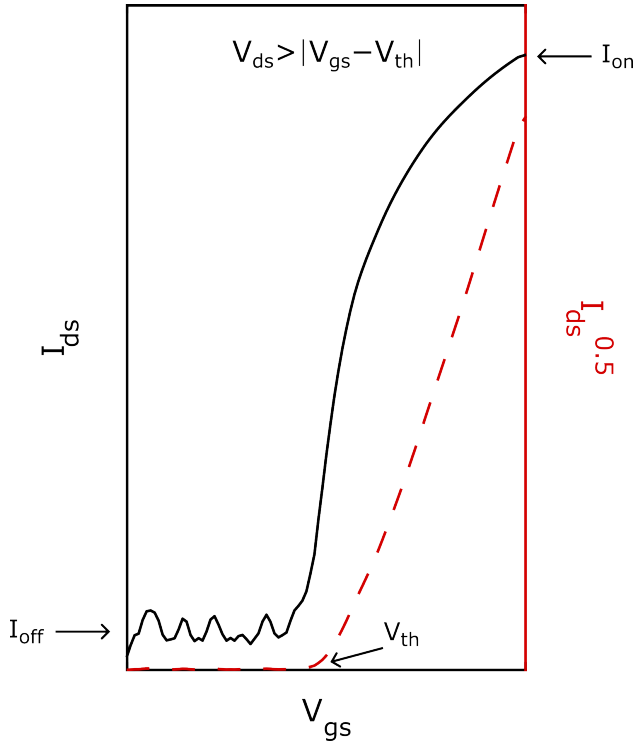

Figure 2.12: (a) Example transfer curves in the saturation regime, illustrating I_{on}, I_{off} and extraction of V_{th} from $\sqrt{I_{ds}}$. Forward V_{gs} sweep shown only.

where C_i is the gate dielectric capacitance per unit area, ΔV_{th} is the threshold voltage shift between forward and reverse sweeps and q is the elementary charge.

To analyse the electrical properties of a MOSFET, the gradual channel approximation is applied, assuming that the electric field between the source and gate electrodes is much greater than that between the source and drain electrodes. In general, d and L satisfy the relation $L/d \geq 10$, ensuring that short-channel effects are negligible. Within this model, the magnitude of V_{gs} governs the density of charge accumulation at the semiconductor-dielectric interface and the potential distribution can be approximated as one-dimensional across the channel. The total charge density is given by:

$$Q = -C_i V_{total}(x), V_{total}(x) = V_{gs} - V(x), \tag{2.3.80}$$

where x is the distance between source and drain electrodes and V_{total} is the total potential resulting from V_{ds} and V_{gs}. Now, taking into account that

an additional V_{th} is applied to fill possible charge traps at the semiconductor-dielectric interface before mobile carriers can accumulate:

$$Q_{mobile} = -C_i(V_{gs} - V(x) - V_{th}). \tag{2.3.81}$$

The mobile charges present along the x-direction create the drift current:

$$I_{ds} = \mu Q W E_x, E_x = -\frac{dV}{dx}, \tag{2.3.82}$$

where E_x is the electric field in the direction of current flow. Substituting Equation 2.3.81 into 2.3.82 retrieves:

$$I_{ds}dx = W\mu C_i(V_{gs} - V(x) - V_{th})dV, \tag{2.3.83}$$

assuming μ is constant with the applied potential, integrating Equation 2.3.83 along the channel from $x = 0$ to L, and from $V = 0$ to V_{ds} as such:

$$\int_0^L I_{ds}dx = W\mu C_i \int_0^{V_{ds}} (V_{gs} - V(x) - V_{th})dV, \tag{2.3.84}$$

results in

$$I_{ds[lin]} = \frac{W}{L}\mu C_i \left[(V_{gs} - V_{th})V_{ds} - \frac{V_{ds}^2}{2}\right]. \tag{2.3.85}$$

Equation 2.3.85 is valid only in the linear regime (Figure 2.11). To derive the corresponding expression for the saturation regime, the condition $V_{ds} = V_{gs} - V_{th}$ is substituted into Equation 2.3.85:

$$I_{ds} = \frac{W}{2L}\mu C_i(V_{gs} - V_{th})^2. \tag{2.3.86}$$

These expressions for I_{ds} in the linear and saturation regimes also underpin the operation of thin-film transistors (TFTs). Both MOSFETs and TFTs incorporate a gate electrode to generate a field-effect and modulate channel conductance. However, TFTs differ from MOSFETs as they do not rely on back-to-back p–n junctions and are fabricated on insulating substrates

– ranging from rigid glass to flexible plastics – due to their compatibility with low temperature processing. MOSFETs based on monocrystalline silicon, gallium nitride (GaN) or silicon carbide (SiC) continue to dominate high frequency and high voltage applications – such as power electronics, radio frequency design and computing – due to their stability and energy efficiency in harsh environments. However, these MOSFETs require high temperature processing and are thus limited to heat resistant substrates such as quartz.

2.3.3 Thin-Film Transistors (TFTs)

By contrast, TFTs are better suited to low frequency, large area and emerging flexible electronics to manufacture displays, wearable healthcare patches, digital microfluidics and more. They comprise multiple stacked layers, with the source and drain electrodes forming ohmic contacts directly with the semiconductor. Depending on the sequence of layer deposition, TFTs are categorised as either staggered or coplanar (Figure 2.13). In coplanar configurations, the source, drain and semiconductor lie in the same horizontal plane, whereas in staggered designs, the electrodes are vertically offset from the channel.

Depending on whether the channel is composed of a p- or n-type semiconductor, either holes or electrons accumulate at the semiconductor–dielectric interface in response to the applied gate bias. In the ideal case, no charge accumulation occurs at the semiconductor-dielectric interface when no V_{gs} is applied and the device is in an off-state. To turn the device on, an applied V_{gs} polarises the dielectric, causing charge carriers to accumulate. An applied V_{ds} then drives these accumulated carriers from the source to the drain electrode, at which point I_{ds} is measured. The charge density in the transistor channel – and therefore the current – are modulated by the magnitude of the applied field. In a real device, an additional V_{gs}, otherwise known as the V_{th}, is applied to fill possible charge traps at the semiconductor-dielectric interface before mobile carriers can accumulate.

Historically, most TFTs have been fabricated using hydrogenated amor-

phous silicon (a-Si:H) and low temperature polysilicon (LTPS). Despite the success of thin film Si, limitations such as high manufacturing costs and V_{th} instability have driven an intense search for new materials. Until around 2003, high performance TFTs – characterised by high μ, large $I_{on/off}$ and low V_{th} – were mainly based on binary amorphous oxide semiconductors (AOSs) such as In_2O_3, Ga_2O_3 and ZnO. However, early AOS-based devices suffered from long-term reliability issues. A major breakthrough came when Hosono *et al.* demonstrated the fabrication of single crystalline IGZO films and later optimised their method for near-room temperature deposition, achieving mobilities exceeding $10\,cm^2\,V^{-1}\,s^{-1}$. [9, 10] More recent efforts have focused on environmentally friendly, earth-abundant alternatives such as ZTO, which help reduce dependence on rare earth and toxic metals like indium and gallium. [11–13]

In the staggered bottom-gate configuration, TFTs have emerged as promising candidates for next-generation, high-throughput chemiresistive gas sensors, with applications spanning the medical, defence and environmental

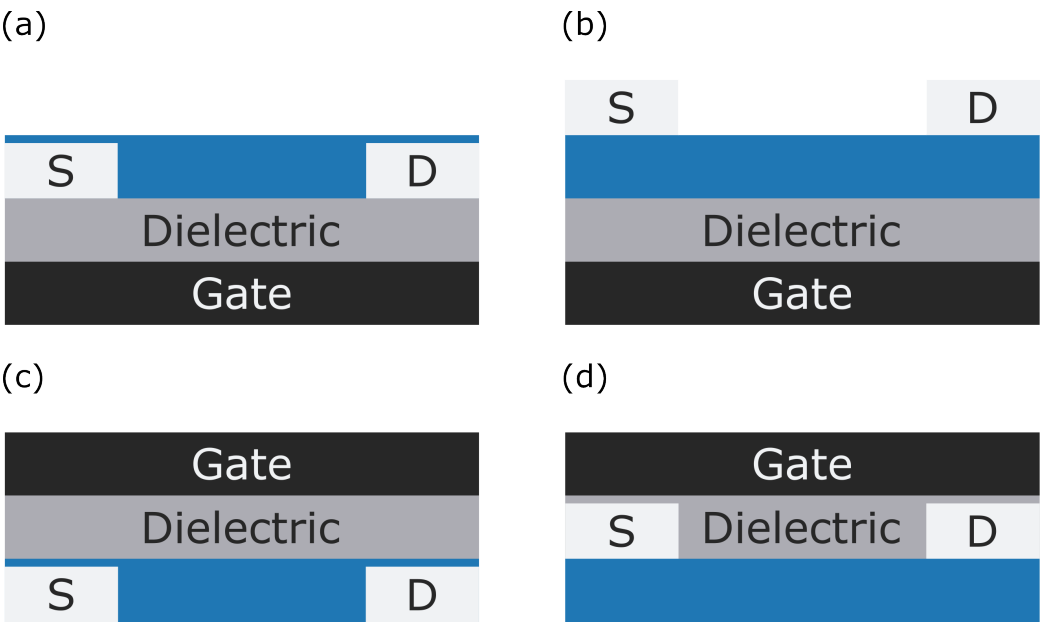

Figure 2.13: TFT architectures: (a) coplanar bottom-gate, (b) staggered bottom-gate, (c) staggered top-gate and (d) coplanar top-gate. S and D denote the source and drain, respectively. The semiconductor is shown by the blue area.

monitoring sectors. The origins of transistor-based gas sensing can be traced back to 1975, when Lundström *et al.* demonstrated a palladium-gated MOSFET for hydrogen detection. [14] Modern TFT-based gas sensors operate via a similar mechanism: the gate electrode modulates the conductivity of the semiconducting channel and variations in I_{ds} in response to gas exposure yield an amplified electrical signal at room temperature. [15–21]

2.3.4 TFTs as Chemiresistive Gas Sensors

Among emerging applications, one prominent example in the medical field is the use of TFT-based gas sensors for exhaled breath analysis. This area of research dates back to the 1970s, when Linus Pauling used gas chromatography to identify over two hundred VOCs in human breath. [22] In the decades since, specific VOCs such as acetone, methanol and isoprene have been correlated with various life-threatening conditions, serving as non-invasive biomarkers for early disease diagnosis. Breath testing offers numerous advantages over conventional diagnostic methods: it is painless, quick and does not require expert handling. However, its clinical adoption remains limited, largely due to challenges related to cross-sensitivity, selectivity and the miniaturisation required for portable, point-of-care devices. By leveraging the inherent amplification characteristics and versatility of TFTs, chemiresistive gas sensors based on this platform are well positioned to overcome these barriers and help transition breath diagnostics toward routine clinical use.

Among these, diabetes is of particular interest – a global health concern projected to affect 700 million people by 2045, according to the World Health Organization (WHO). [23] Early symptom recognition is crucial and can be facilitated by measuring acetone concentration in breath, ranging from 0.3 ppm to 0.9 ppm in healthy individuals but exceeding 1.8 ppm in cases of diabetic ketoacidosis. [24, 25] Another particularly relevant case is methanol poisoning from adulterated alcohol, which poses severe health risks, including organ failure, blindness and death, often overwhelming healthcare facilities in developing countries. [26–28] Detecting elevated methanol lev-

els in breath – above the normal 0.4 ppm – can enable rapid screening of contaminated beverages. However, laboratory-based techniques such as gas chromatography-mass spectrometry require long processing times, trained personnel and expensive equipment. [29, 30] Thus, the development of point-of-care sensors capable of detecting VOCs with high selectivity and specificity in humid environments holds significant societal benefits. [31]

Traditional two-terminal chemiresistive gas sensors incorporating highly abundant n-type metal oxides such as ZnO, SnO_2 and ZTO – along with their various crystal morphologies, including nanostructures, crystalline films and porous films – have been widely studied due to their high mobility, environmental stability and ease of fabrication. [32–36] Their working principle is simple and reversible, relying on changes in electrical resistance when exposed to different gas concentrations (see Equations 2.3.87 and 2.3.88). Many groups have developed highly sensitive exhaled breath sensors incorporating 1D nanostructures, which offer a high surface-to-volume ratio and open porosity. [24, 25, 28, 30, 31, 37] For instance, Shin *et al.* combined Pt catalytic nanoparticles with SnO_2 fibres, achieving short response (< 11 s) and recovery times (< 6 s) upon cyclic exposure to acetone and humid air. [31] Selectivity toward toluene was also observed with Pt decoration, whereas pure SnO_2 fibres showed no response. However, maximum sensitivity was achieved at elevated operating temperatures ($T > 300\,^{\circ}\mathrm{C}$), leading to high power consumption unsuitable for mobile applications.

The sensing mechanism for the detection of reducing vapours by TFTs is analogous to that of two-terminal devices. Acetone, for example, donates electrons to the channel and thereby reduces the film resistance – described by Equations 2.3.87 and 2.3.88. Due to its high electronegativity, oxygen adsorbed on the surface extracts electrons from the semiconductor, forming negatively charged oxygen species and increasing the channel resistance. [38, 39] Upon exposure to acetone, a redox reaction occurs with the adsorbed oxygen, releasing electrons back into the conduction band and thereby enhancing conductivity. [17, 40]

$$O_2(ads) + e^- \rightarrow {O_2}^-(ads) \tag{2.3.87}$$

$$C_3H_6O(ads) + 4\,{O_2}^-(ads) \rightarrow 3\,CO_2(ads) + 3\,H_2O(ads) + 4\,e^- \tag{2.3.88}$$

For TFTs, high sensitivity (S) at low-voltage operation is dictated by two key parameters, $I_{on/off} \geq 10^7$ and V_{th}, which should be near-zero to realise mobile applications with low power requirements. Zan *et al.,* showed that low $V_{th}(< 5\,V)$ and high $I_{on/off} > 10^6$ exhibited by amorphous IGZO TFTs capped with an organic sensing layer led to high sensitivity to acetone vapour with a limit of detection of 100 ppb (see Table 2.1). [41] Beyond medical diagnostics, TFT-based gas sensors have also been deployed for environmental monitoring and industrial safety, detecting hazardous gases such as NO_2. In contrast to two-terminal chemiresistors, TFT-based sensors can also exploit changes in other electrical parameters, such as μ and V_{th}. For example, Andringa *et al.* deposited ZnO thin films by spray pyrolysis, with source-drain electrodes patterned using photolithography, resulting in finger transistors. Unlike the redox reaction typically observed upon exposure to reducing vapours (Equations 2.3.87 and 2.3.88), the detection of NO_2 in these TFT-based sensors was based on a different mechanism: the interaction of NO_2 with the semiconductor led to charge trapping in the linear regime. I_{ds} decreased upon exposure to NO_2 and an applied positive bias ($V_{gs} > 0$), which caused a right-shift in V_{th} to $V_{gs} = 30\,V$ for concentrations as low as 10 ppb. [15] Mobile electrons became continuously trapped over time until the the gate bias was completely compensated by immobile trapped charges.

Various strategies have been employed to enhance the chemiresistive performance of metal oxide TFTs, including defect engineering and doping, which allow precise tuning of their electronic structure and surface morphology. In particular, the introduction of oxygen vacancies facilitates the chemisorption of oxygen species on the metal oxide surface, thereby improving sensitivity and reducing response times in VOC detection. [45] Sn doping, specifically, has been shown to create smooth films and offers advan-

tages in terms of large-area uniformity and potential for device miniaturisation. [12, 46] The origin of the electrical and chemiresistive properties of single layer TFTs is well understood. [17] However, detailed morphological and structural analyses of stacked and alternating layers remain limited. The design of multilayer channels that comprise different and complementary oxides has been shown to enhance both reliability and charge transport. [47–49] Lin *et al.* reported high-mobility thin-film transistors (TFTs) based on low-dimensional quasi-superlattices (QSLs), which were fabricated via sequential deposition and thermal treatment of In_2O_3, Ga_2O_3 and ZnO at low temperatures (180 °C to 200 °C). These QSL-based TFTs exhibited electron mobilities approximately ten times higher (25 $cm^2\,V^{-1}\,s^{-1}$ to 45 $cm^2\,V^{-1}\,s^{-1}$) than those of single oxide devices (2 $cm^2\,V^{-1}\,s^{-1}$ to 5 $cm^2\,V^{-1}\,s^{-1}$).

Despite significant advancements in AOS TFTs, oxide semiconductors remain predominantly n-type, limiting their application in gas sensing – sensitivity to both oxidising and reducing gases is essential – and hindering their integration into CMOS circuits, which require both n- and p-type transistors to form functional inverter branches. The development of reliable p-type

Table 2.1: Comparison of TFT-based gas sensors' performance at room temperature.

Sensor	Gas	S	C (ppm)	Response	Recovery	Ref.
IGZO	NO_2	1,330	5	3 min	3 min	[42][a]
	Ammonia	-	0.1	2 min	-	[41]
	Acetone	-	0.1	2 min	-	
ZTO	Acetone	9,326	-	24 h	1 h	[43][b]
	IPA	48,664	-	24 h	1 h	
	Methanol	1.08×10^6	-	24 h	15 min	
	Methanol	11,400	-	4 h	15 min	
	Methanol	400	-	1 h	15 min	
SnO_2	Acetone	1129	-	24 h	1 h	[44][b]
InNdO	Acetone	88	4	31 s	53 s	[17]

[a] Recovery by UV LED in N_2 purge.
[b] The longer response and recovery times reported here are attributed to differences in methodology, particularly the absence of a mass flow controller. These metrics relied on the diffusion of gas from a constant source.

oxide semiconductors is still in its early stages. In contrast, organic TFTs (OTFTs) have attracted considerable interest for this role, as their properties can be readily tuned through chemical synthesis or blending. [50] Smith *et al.* demonstrated solution-processed OTFTs based on phase-separated semiconducting blends, comprising a small molecule hole-transporting material and a conjugated amorphous polymer binder, which achieved performance metrics comparable to n-type AOS devices – including hole mobilities exceeding $5\,\mathrm{cm^2\,V^{-1}\,s^{-1}}$ and $I_{on/off} > 10^6$.

In terms of gas sensing, numerous studies on blend-based OTFTs have demonstrated advantages such as excellent electrical performance, good environmental stability and remarkable mechanical properties. Han *et al.* reported an NH_3 gas sensor using a polymer blend of poly(3-hexylthiophene) (P3HT) with polystyrene (PS). [51] Phase separation in the blend film led to a P3HT-enriched surface, facilitating effective interaction between the semiconductor and NH_3. The sensor exhibited saturation current responses of 52 % and 16 % under 50 ppm and 5 ppm NH_3, respectively. The same group then developed an OTFT gas sensor based on a P3HT/poly(9-vinylcarbazole) (PVK) blend. This device achieved a limit of detection of 300 ppb, with a fifteen-fold increase in response compared to P3HT-only TFTs. This enhancement was attributed to the hole-transporting and electron-blocking effects of PVK. [52]

However, a key limitation of conventional OFETs is their relatively high operating voltage, which arises from the low capacitance of typical gate dielectric layers, in the order of tens of $\mathrm{nF\,cm^{-2}}$. Several strategies have been reported to increase the capacitance of the gate dielectric layer, including the use of high dielectric constant (high-κ) materials such as HfO_2 and ZrO_x, [53–55] reducing dielectric thickness [56], or replacing conventional dielectric materials with ionically conductive electrolytes – water being the simplest example.

2.3.5 Water-Gated TFTs (WG-TFTs)

Under an applied bias, the random migration of ions and subsequent accumulation of charges at the water-semiconductor interface establish an electrical double layer (EDL), structured through the inner and outer Helmholtz planes in solution. The gating mechanism can be achieved using highly resistive, purified water. Under these conditions, rapid contamination by atmospheric carbon dioxide leads to the formation of HCO_3^- and H^+ ions, which migrate to the surface to facilitate p- and n-type gating. [57, 58] This interfacial coupling enables capacitance values exceeding $1\,\mu F\,cm^{-2}$ and supports low-voltage operation. [59] Furthermore, the use of aqueous electrolytes broadens the applicability of WG-TFTs in implantable electronics, as they can be seamlessly integrated into biological systems. Current modulation by the gate electrode enables the amplification of weak or noisy signals, which is particularly valuable in healthcare monitoring – for example in detecting trace concentrations of biomarkers in sweat. [60] The integration of recently developed high mobility, printable small molecules or polymers with flexible substrates further enhances the potential for cost-effective fabrication of integrated and wearable sensors [61–65].

These devices share similarities with organic electrochemical transistors (OECTs), in which ions from the electrolyte penetrate the channel and modulate its conductivity via volumetric doping. While PEDOT:PSS has been widely studied as an organic mixed ionic-electronic conductor (OMEIC), it requires an additional gate bias to de-dope and fully switch off the device. [66] Although new OMEIC materials continue to emerge [67, 68], their electrochemical and transistor performance remains highly sensitive to ionic properties – such as charge density, size and mobility – leading to increased hysteresis and degraded $I_{on/off}$ ratios. As such, this thesis focuses exclusively on WG-TFTs, where charge modulation occurs primarily at the interface, offering better control over switching characteristics for aqueous sensing applications.

Figure 2.14 shows a schematic of the bilayer WG-TFTs described in Chap-

ter 6, operating in the n-type regime. In this device, a positive gate bias ($V_{gs} > 0\,\mathrm{V}$) induces the accumulation of electrons at the water–semiconductor interface. This mechanism is analogous to the charge accumulation at the dielectric–semiconductor interface in conventional n-type TFTs and facilitates electron transport from the source to the drain electrode.

2.4 Review of Solution-Processable Materials

2.4.1 Inorganic Metal Oxides

The transistor technologies investigated in Chapters 4, 5 and 6 were fabricated using solution-based processing methods, with detailed fabrication procedures provided in Chapter 3. The deposition of the active semiconducting layer relied on materials compatible with solution-processing. In these formulations, the precursor powders consist of metal cations and organic anions that dissociate upon dissolution in a solvent and subsequently decompose at low temperatures through hydrolysis. For inorganic precursors, metal cations coordinated by water molecules react with OH^- or $O_2{}^-$ ions to form metal–hydroxide (M–OH) or metal–oxygen (M–O) bonds. Upon thermal treatment, condensation and dehydroxylation reactions eliminate residual impurities and drive the formation of extended metal–oxygen–metal (M–O–M) networks characteristic of metal oxide semiconductors. [43]

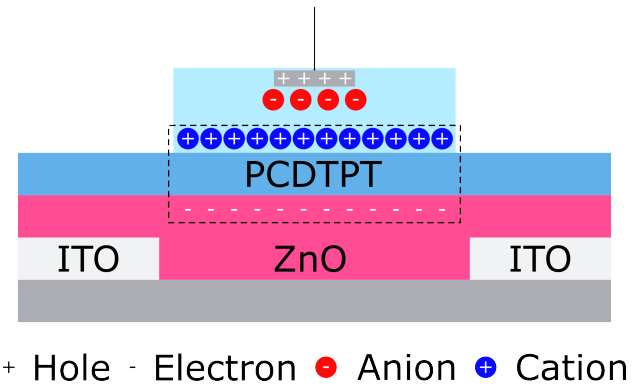

Figure 2.14: WG-TFT schematic illustrating accumulation of electrons under positive bias with a bilayer channels.

The inorganic semiconductors employed in this work include ZnO and SnO_2, combined in equal proportions to form ZTO. ZnO is a wide bandgap semiconductor with a hexagonal wurtzite structure, known for its piezoelectric properties and widespread use in optoelectronic applications. [69–71] Structurally similar to the zincblende lattice, each Zn atom in wurtzite ZnO is tetrahedrally coordinated to four neighbouring O atoms. ZnO exhibits high electron mobility and optical transparency in the visible range. Its ability to form diverse nanostructured morphologies further enhances electron injection, making it particularly suitable for thin-film applications such as solar cells, [72, 73] optoelectronic and chemical sensors. [15]

In contrast, SnO_2 adopts a rutile-type tetragonal crystal structure, similar to that of TiO_2. It is another transparent conducting oxide, characterised by a high density of oxygen vacancies, which contribute additional free carriers. [74] SnO_2 is also among the most widely used n-type semiconductors in two-terminal gas sensing devices. [75] The ZTO ternary system is one of the most promising examples of a heterometal-containing semiconducting material. Recent studies have reported solution-processed ZTO TFTs with electron mobilities of up to $33\,\mathrm{cm^2\,V^{-1}\,s^{-1}}$ and $I_{\mathrm{on/off}}$ ratios ranging from 10^3 to 10^8. [19,76,77] These properties are highly dependent on carrier concentration, which can increase with Sn content. This is because Sn has two more valence electrons than Zn and can act as a donor by substituting for Zn, occupying interstitial sites or promoting the formation of oxygen vacancies. Additionally, incorporating Sn can smoothen the film surface by reducing grain size. For example, Jeong *et al.* reported that the rms roughness decreased from 12.1 nm at 20 mol% Sn to 10.3 nm and 6.4 nm at 30 and 40 mol%, respectively. [78] In this work, the stoichiometric ratio between Zn and Sn was not explicitly controlled; instead, the stacking of multiple ZTO layers was used to influence the overall composition and resulting electronic properties (see Chapter 4.3).

2.4.2 Organic Semiconductors

In comparison to their inorganic counterparts, organic semiconductors offer the potential for large area deposition on flexible substrates due to their ability to be processed at significantly lower temperatures. These materials can be chemically tuned or functionalised for specific applications, making them attractive for use in displays, radio frequency tags, wearable sensors, logic circuits and solar cells. [79] Charge transport in organic semiconductors differs significantly from that observed in crystalline semiconductors due to the nature of their molecular structure and bonding. Organic materials exhibit much weaker intermolecular interactions – primarily van der Waals forces – and charge carriers typically move via hopping or tunnelling mechanisms between adjacent molecules, rather than through conventional band transport. The overlapping π-electron clouds in planar systems have been shown to give rise to hole mobilities greater than $4\,\mathrm{cm^2\,V^{-1}\,s^{-1}}$ in solution-processed devices. [80]

The band gap of an organic semiconductor is defined by the energy difference between the highest occupied molecular orbital (HOMO) and the lowest unoccupied molecular orbital (LUMO), which are analogous to the valence and conduction bands in inorganic semiconductors, respectively. Through molecular design, the band gap – and consequently the HOMO and LUMO energy levels– can be finely tuned. Unlike inorganic semiconductors, minor modifications to the chemical structure of organic materials can lead to significant changes in their electrical and optical properties.

Among small molecule semiconductors, polyacenes and heteroacenes are widely used as hole-transporting materials in OTFTs. Pentacene and rubrene, in particular, were extensively studied in the early 2000s and have since been modified to enhance their solubility. [81–83] Heteroacenes such as [1]benzothieno[3,2-b][1]benzothiophene (BTBT), which consist of fused thiophene rings in a ladder-type configuration, have demonstrated excellent p-type charge transport and environmental stability, due in part to their low-lying HOMO energy levels. [84]

The limited availability of low work function metals (2 eV to 3 eV) suitable for efficient electron injection has meant that most organic semiconductors naturally favour p-type transport. Furthermore, electrons – owing to their smaller effective mass (see Figure 2.4) – are more susceptible to trapping at the semiconductor-dielectric interface or at defect sites such as grain boundaries and other impurities. To address this, fullerene derivatives such as C_{60} and [6,6] phenyl-C_{61}-butyric acid methyl ester (PCBM) were developed with higher electron affinities to support n-type transport. [85] More recently, air stable and electrochemically active fullerenes such as fulleropyrrolidines with triethylene glycol monoethyl ether (TEG) side-chains (PTEG – 1) or C_{60},N,N,N -trimethyl-1-(2,3,4-tris(2-(2-methoxyethoxy)-ethoxy)-phenyl)-methanaminium monoadduct ($PrC_{60}MA$) have been employed in both OTFT and organic electrochemical transistor (OECT) architectures, and are investigated further in Chapter 6. [86–90]

Most solution-processable polymers used in OTFTs are based on alkyl-substituted polythiophenes, with poly(3-hexylthiophene) (P3HT) being the most prominent example. Few polymers have demonstrated n-type performance, however, poly(benzimidazobenzophenanthroline) (BBL) has been shown to exhibit electron mobilities of up to $0.1\,cm^2\,V^{-1}\,s^{-1}$. [80] Achieving ambipolar transport – where both electron and hole conduction occurs in the same material system – has often involved strategies inspired by organic photovoltaics (OPVs), such as employing a bulk heterojunction (BHJ) architecture. In such systems, blends of PCBM (n-type) and P3HT (p-type) are used to enable complementary charge transport. However, the microstructure and resulting device performance are highly sensitive to processing conditions, including blend ratio, solvent choice and thermal treatment. [91] This BHJ-based strategy is also adopted in Chapter 6.

2.5 Summary

In summary, this chapter presented the theoretical background and an integrated review of the state-of-the-art relevant to the materials and transistor architectures explored in Chapters 4, 5, and 6. It began with a discussion of basic crystal structure and electronic band theory, focusing on energy band formation and its influence on electrical conduction in intrinsic and extrinsic semiconductors. The operation of fundamental semiconductor devices based on $p-n$ junctions was then introduced, including the MOS capacitor and the MOSFET, alongside key performance metrics such as V_{th}, μ and $I_{on/off}$.

The chapter then transitioned to TFTs, discussing their operational principles and emerging role in remote chemical sensing, particularly for exhaled breath analysis. This included a brief overview of the limitations of traditional two-terminal chemiresistive sensors. The state-of-the-art in inorganic semiconductors – specifically ZnO, SnO_2 and ZTO – was reviewed in terms of their intrinsic properties and integration into TFTs. This discussion was then extended to organic semiconductors, with a focus on their application in both conventional TFTs and water-gated TFT technologies.

The following chapter outlines the fabrication methods and characterisation techniques employed in device preparation and evaluation.

References

[1] R. A. Smith, *Semiconductors*, 2nd ed. Cambridge University Press, 1979.

[2] R. F. Pierret, *Semiconductor Device Fundamentals*. Addison-Wesley, 1996.

[3] S. M. Sze, *Semiconductor Devices: Physics and Technology*, 2nd ed. John Wiley & Sons, 2001.

[4] C. Kittel, *Introduction to Solid State Physics*, 6th ed. John Wiley & Sons, 1986.

[5] D. J. Griffiths, *Introduction to Quantum Mechanics*, 2nd ed. Pearson Prentice Hall, 2005.

[6] S. M. Sze and K. K. Ng, *Physics of Semiconductor Devices*, 3rd ed. Wiley-Interscience, 2007.

[7] D. J. Griffiths, *Introduction to Electrodynamics*, 4th ed. Pearson, 2013.

[8] M. M. Atalla and D. Kahng, "Silicon-silicon dioxide field induced surface devices," in *IRE-AIEE Solid-State Device Research Conference*, 1960.

[9] K. Nomura, H. Ohta, K. Ueda *et al.*, "Thin-film transistor fabricated in single-crystalline transparent oxide semiconductor," *Science*, vol. 300, no. 5623, pp. 1269–1272, 2003.

[10] K. Nomura, H. Ohta, A. Takagi *et al.*, "Room-temperature fabrication of transparent flexible thin-film transistors using amorphous oxide semiconductors," *Nature*, vol. 432, no. 7016, pp. 488–492, 2004.

[11] R. D. Chandra, M. Rao, K. Zhang *et al.*, "Tuning Electrical Properties in Amorphous Zinc Tin Oxide Thin Films for Solution Processed Electronics," *ACS Applied Materials & Interfaces*, vol. 6, no. 2, pp. 773–777, 2014.

[12] L.-C. Liu, J.-S. Chen, J.-S. Jeng, and W.-Y. Chen, "Variation of Oxygen Deficiency in Solution-Processed Ultra-Thin Zinc-Tin Oxide Films to Their Transistor Characteristics," *ECS Journal of Solid State Science and Technology*, vol. 2, no. 4, p. Q59, 2013.

[13] S.-J. Seo, C. G. Choi, Y. H. Hwang, and B.-S. Bae, "High performance solution-processed amorphous zinc tin oxide thin film transistor," *Journal of Physics D: Applied Physics*, vol. 42, no. 3, p. 035106, 2008.

[14] I. Lundström, M. S. Shivaraman, C. Svensson, and L. Lundkvist, "A hydrogen-sensitive pd-gate mos transistor," *Applied Physics Letters*, vol. 26, no. 2, pp. 55–57, 1975.

[15] A.-M. Andringa, J. R. Meijboom, E. C. P. Smits *et al.*, "Gate-Bias Controlled Charge Trapping as a Mechanism for NO2 Detection with Field-Effect Transistors," *Advanced Functional Materials*, vol. 21, no. 1, pp. 100–107, 2011.

[16] K.-W. Kao, M.-C. Hsu, Y.-H. Chang *et al.*, "A Sub-ppm Acetone Gas Sensor for Diabetes Detection Using 10 nm Thick Ultrathin InN FETs," *Sensors*, vol. 12, no. 6, pp. 7157–7168, 2012.

[17] J. Li, L. Li, Q. Chen *et al.*, "Ultrasensitive room-temperature acetone gas sensors employing green-solvent-processed aligned InNdO nanofiber field-effect transistors," *Journal of Materials Chemistry C*, vol. 10, no. 3, pp. 860–869, 2022.

[18] L. Jiang, J. Li, K. Huang *et al.*, "Low-Temperature and Solution-Processable Zinc Oxide Transistors for Transparent Electronics," *ACS Omega*, vol. 2, no. 12, pp. 8990–8996, 2017.

[19] B. N. Pal, B. M. Dhar, K. C. See, and H. E. Katz, "Solution-deposited sodium beta-alumina gate dielectrics for low-voltage and transparent field-effect transistors," *Nature Materials*, vol. 8, no. 11, pp. 898–903, 2009.

[20] T. Kamiya, K. Nomura, and H. Hosono, "Present status of amorphous In–Ga–Zn–O thin-film transistors," *Science and Technology of Advanced Materials*, vol. 11, no. 4, p. 044305, 2010.

[21] ——, "Origins of High Mobility and Low Operation Voltage of Amorphous Oxide TFTs: Electronic Structure, Electron Transport, Defects and Doping," *Journal of Display Technology*, vol. 5, no. 7, pp. 273–288, 2009.

[22] L. Pauling, A. B. Robinson, R. Teranishi, and P. Cary, "Quantitative analysis of urine vapor and breath by gas-liquid partition chromatography," *Proceedings of the National Academy of Sciences*, vol. 68, no. 10, pp. 2374–2376, 1971.

[23] A. Sharma, W. S. AlGhamdi, H. Faber *et al.*, "Non-invasive, ultrasensitive detection of glucose in saliva using metal oxide transistors," *Biosensors and Bioelectronics*, vol. 237, p. 115448, 2023.

[24] S.-J. Choi, I. Lee, B.-H. Jang *et al.*, "Selective Diagnosis of Diabetes Using Pt-Functionalized WO3 Hemitube Networks As a Sensing Layer of Acetone in Exhaled Breath," *Analytical Chemistry*, vol. 85, no. 3, pp. 1792–1796, 2013.

[25] M. Righettoni, A. Tricoli, and S. E. Pratsinis, "Si:WO3 Sensors for Highly Selective Detection of Acetone for Easy Diagnosis of Diabetes by Breath Analysis," *Analytical Chemistry*, vol. 82, no. 9, pp. 3581–3587, 2010.

[26] Z. Nekoukar, Z. Zakariaei, F. Taghizadeh *et al.*, "Methanol poisoning as a new world challenge: A review," *Annals of Medicine and Surgery*, vol. 66, p. 102445, 2021.

[27] A. Mashallahi, M. Mohamadkhani, and A. Ostadtaghizadeh, "Methanol Poisoning Outbreaks in Southern Iran in 2018: A Lesson Learned," *Iranian Journal of Public Health*, vol. 50, no. 7, pp. 1502–1503, 2021.

[28] J. van den Broek, S. Abegg, S. E. Pratsinis, and A. T. Güntner, "Highly selective detection of methanol over ethanol by a handheld gas sensor," *Nature Communications*, vol. 10, no. 1, p. 4220, 2019.

[29] M. Phillips, K. Gleeson, J. M. B. Hughes *et al.*, "Volatile organic compounds in breath as markers of lung cancer: A cross-sectional study," *The Lancet*, vol. 353, no. 9168, pp. 1930–1933, 1999.

[30] G. Peng, U. Tisch, O. Adams *et al.*, "Diagnosing lung cancer in exhaled breath using gold nanoparticles," *Nature Nanotechnology*, vol. 4, no. 10, pp. 669–673, 2009.

[31] J. Shin, S.-J. Choi, I. Lee *et al.*, "Thin-Wall Assembled SnO2 Fibers Functionalized by Catalytic Pt Nanoparticles and their Superior Exhaled-Breath-Sensing Properties for the Diagnosis of Diabetes," *Advanced Functional Materials*, vol. 23, no. 19, pp. 2357–2367, 2013.

[32] K. S. Kim, C. H. Ahn, S. H. Jung *et al.*, "Toward Adequate Operation of Amorphous Oxide Thin-Film Transistors for Low-Concentration Gas Detection," *ACS Applied Materials & Interfaces*, vol. 10, no. 12, pp. 10 185–10 193, 2018.

[33] Y. Shimizu, A. Jono, T. Hyodo, and M. Egashira, "Preparation of large mesoporous SnO2 powder for gas sensor application," *Sensors and Actuators B: Chemical*, vol. 108, no. 1, pp. 56–61, 2005.

[34] N. Barsan and U. Weimar, "Conduction Model of Metal Oxide Gas Sensors," *Journal of Electroceramics*, vol. 7, no. 3, pp. 143–167, 2001.

[35] G. Korotcenkov, "Metal oxides for solid-state gas sensors: What determines our choice?" *Materials Science and Engineering: B*, vol. 139, no. 1, pp. 1–23, 2007.

[36] S. J. Patil, A. V. Patil, C. G. Dighavkar *et al.*, "Semiconductor metal oxide compounds based gas sensors: A literature review," *Frontiers of Materials Science*, vol. 9, no. 1, pp. 14–37, 2015.

[37] N.-H. Kim, S.-J. Choi, D.-J. Yang *et al.*, "Highly sensitive and selective hydrogen sulfide and toluene sensors using Pd functionalized WO3 nanofibers for potential diagnosis of halitosis and lung cancer," *Sensors and Actuators B-Chemical*, vol. 193, pp. 574–581, 2014.

[38] H. Windischmann and P. Mark, "A Model for the Operation of a Thin-Film SnO x Conductance-Modulation Carbon Monoxide Sensor," *Journal of The Electrochemical Society*, vol. 126, no. 4, pp. 627–633, 1979.

[39] Y. Chen, H. Qin, Y. Cao *et al.*, "Acetone Sensing Properties and Mechanism of SnO2 Thick-Films," *Sensors*, vol. 18, no. 10, p. 3425, 2018.

[40] J. Lee, Y. Choi, B. J. Park *et al.*, "Precise control of surface oxygen vacancies in ZnO nanoparticles for extremely high acetone sensing response," *Journal of Advanced Ceramics*, vol. 11, no. 5, pp. 769–783, 2022.

[41] H.-W. Zan, C.-H. Li, C.-C. Yeh *et al.*, "Room-temperature-operated sensitive hybrid gas sensor based on amorphous indium gallium zinc oxide thin-film transistors," *Applied Physics Letters*, vol. 98, no. 25, p. 253503, 2011.

[42] M. T. Vijjapu, S. G. Surya, S. Yuvaraja *et al.*, "Fully Integrated Indium Gallium Zinc Oxide NO2 Gas Detector," *ACS Sensors*, vol. 5, no. 4, pp. 984–993, 2020.

[43] L. R. Miller, A. Galán-González, B. Nicholson *et al.*, "Control Strategies for Solution-Processed ZTO-Based Thin-Film Transistors Tailored Toward Volatile Organic Compound Detection," *Advanced Electronic Materials*, vol. n/a, no. n/a, p. 2400810, 2025.

[44] L. R. Miller, R. J. Borthwick, P. L. dos Santos, and M. U. Chaudhry, "Detection of acetone vapours using solution-processed tin oxide thin-film transistors," *MRS Advances*, vol. 8, p. 440–445, 2023.

[45] H. Yuan, S. A. A. A. Aljneibi, J. Yuan *et al.*, "ZnO Nanosheets Abundant in Oxygen Vacancies Derived from Metal-Organic Frameworks for ppb-Level Gas Sensing," *Advanced Materials*, vol. 31, no. 11, p. 1807161, 2019.

[46] S. Ruzgar and M. Caglar, "The effect of Sn on electrical performance of zinc oxide based thin film transistor," *Journal of Materials Science: Materials in Electronics*, vol. 30, no. 1, pp. 485–490, 2019.

[47] K. Hu, Z. Guo, J. Wang *et al.*, "Tri-Layer Heterostructure Channel of a-IGZO/a-ITZO/a-IGZO Toward Enhancement of Transport and Reliability in Amorphous Oxide Semiconductor Thin Film Transistors," *Advanced Electronic Materials*, p. 2400266, 2024.

[48] W. Cai, M. Li, S. Lu *et al.*, "Heterojunction Channel Engineering in Performance Enhancement of Solution-Processed Oxide Thin-Film Transistors," *IEEE Transactions on Electron Devices*, vol. 70, no. 6, pp. 3085–3091, 2023.

[49] Y. Lin, H. Faber, J. G. Labram *et al.*, "High Electron Mobility Thin-Film Transistors Based on Solution-Processed Semiconducting Metal Oxide Heterojunctions and Quasi-Superlattices," *Advanced Science*, vol. 2, no. 7, p. 1500058, 2015.

[50] J. Smith, W. Zhang, R. Sougrat *et al.*, "Solution-processed small molecule-polymer blend organic thin-film transistors with hole mobility greater than 5 cm^2/vs," *Advanced Materials*, vol. 24, no. 18, pp. 2441–2446, 2012.

[51] S. Han, X. Zhuang, W. Shi *et al.*, "Poly(3-hexylthiophene)/polystyrene (P3HT/PS) blends based organic field-effect transistor ammonia gas sensor," *Sensors and Actuators B: Chemical*, vol. 225, pp. 10–15, 2016.

[52] S. Han, Z. Yang, Z. Li *et al.*, "Improved Room Temperature NO2 Sensing Performance of Organic Field-Effect Transistor by Directly Blending a

Hole-Transporting/Electron-Blocking Polymer into the Active Layer," *ACS Applied Materials & Interfaces*, vol. 10, no. 44, pp. 38 280–38 286, 2018.

[53] J. Chung, Y. J. Tak, W.-G. Kim *et al.*, "Low-temperature fabrication of solution-processed hafnium oxide gate insulator films using a thermally purified solution process," *Journal of Materials Chemistry C*, vol. 6, no. 18, pp. 4928–4935, 2018.

[54] M. U. Chaudhry, K. Tetzner, Y.-H. Lin *et al.*, "Low-Voltage Solution-Processed Hybrid Light-Emitting Transistors," *ACS Applied Materials & Interfaces*, vol. 10, no. 22, pp. 18 445–18 449, 2018.

[55] J. Zhang, M. Jia, M. G. Sales *et al.*, "Impact of ZrO2 Dielectrics Thickness on Electrical Performance of TiO2 Thin Film Transistors with Sub-2 V Operation," *ACS Applied Electronic Materials*, vol. 3, no. 12, pp. 5483–5495, 2021.

[56] M. J. Panzer and C. D. Frisbie, "Exploiting ionic coupling in electronic devices: Electrolyte-gated organic field-effect transistors," *Advanced Materials*, vol. 20, no. 16, pp. 3177–3180, 2008.

[57] R. Porrazzo *et al.*, "Water-gated n-type organic field-effect transistors for complementary integrated circuits operating in an aqueous environment," *ACS Omega*, vol. 2, pp. 1–10, 2017.

[58] M. J. Panzer, C. R. Newman, and C. D. Frisbie, "Low-voltage operation of a pentacene field-effect transistor with a polymer electrolyte gate dielectric," *Applied Physics Letters*, vol. 86, no. 10, p. 103503, 2005.

[59] S.-H. Kim, J.-H. Yun, H.-L. Park, and S.-H. Lee, "Neuromorphic motor control with electrolyte-gated organic synaptic transistors," *Advanced Electronic Materials*, vol. n/a, no. n/a, p. e00359.

[60] B. Wang, C. Zhao, Z. Wang *et al.*, "Wearable aptamer-field-effect transistor sensing system for noninvasive cortisol monitoring," *Science Advances*, vol. 8, no. 1, p. eabk0967, 2022.

[61] M. Hamedi *et al.*, "Fiber-embedded electrolyte-gated field-effect transistors for e-textiles," *Adv. Mater.*, vol. 21, pp. 573–577, 2009.

[62] S. H. Kim *et al.*, "Electrolyte-gated transistors for organic and printed electronics," *Adv. Mater.*, vol. 25, pp. 1822–1846, 2013.

[63] P. Harikesh *et al.*, "Organic electrochemical neurons and synapses with ion mediated spiking," *Nat. Commun.*, vol. 13, p. 901, 2022.

[64] Y. Lee, A. Carnicer-Lombarte, S. Han *et al.*, "Tunable Organic Active Neural Probe Enabling Near-Sensor Signal Processing," *Advanced Materials*, vol. 35, no. 38, p. 2301782, 2023.

[65] S. Chai, Y. Lee, R. M. Owens *et al.*, "Dynamic monitoring of a 3D-printed airway tissue model using an organic electrochemical transistor," *Biomaterials*, vol. 314, p. 122806, 2025.

[66] C.-Y. Lo, Y. Wu, E. Awuyah *et al.*, "Influence of the molecular weight and size distribution of PSS on mixed ionic-electronic transport in PEDOT:PSS," *Polym. Chem.*, vol. 13, no. 19, pp. 2764–2775, 2022.

[67] E. Stein, O. Nahor, M. Stolov *et al.*, "Ambipolar blend-based organic electrochemical transistors and inverters," *Nature Communications*, vol. 13, no. 1, p. 5548, 2022.

[68] B. D. Paulsen, K. Tybrandt, E. Stavrinidou, and J. Rivnay, "Organic mixed ionic–electronic conductors," *Nature Materials*, vol. 19, no. 1, pp. 13–26, 2020.

[69] J. Yoo, K. Lee, U. J. Yang *et al.*, "Highly efficient printed quantum dot light-emitting diodes through ultrahigh-definition double-layer transfer printing," *Nature Photonics*, vol. 18, no. 10, pp. 1105–1112, 2024.

[70] A. Galán-González, P. Pander, R. C. I. MacKenzie *et al.*, "Nanostructured Channel for Improving Emission Efficiency of Hybrid Light-Emitting Field-Effect Transistors," *ACS Photonics*, vol. 10, no. 12, pp. 4315–4321, 2023.

[71] Özgür, D. Hofstetter, and H. Morkoç, "Zno devices and applications: A review of current status and future prospects," *Proceedings of the IEEE*, vol. 98, no. 7, pp. 1255–1268, 2010.

[72] J. Huang, Z. Yin, and Q. Zheng, "Applications of ZnO in organic and hybrid solar cells," *Energy & Environmental Science*, vol. 4, no. 10, pp. 3861–3877, 2011.

[73] E. Mazzolini, J. Faria, D. Pugliese *et al.*, "Discerning blend microstructure and charge recombination for stable biorenewable-based organic photovoltaics," *Advanced Energy Materials*, vol. n/a, no. n/a, p. 2405635, 2025.

[74] Y. Wang, Y. Zhang, H. Li *et al.*, "Fully-printed flexible n-type tin oxide thin-film transistors and logic circuits," *Journal of Materials Chemistry C*, vol. 9, pp. 11 662–11 670, 2021.

[75] P. Raju and Q. Li, "Review—Semiconductor Materials and Devices for Gas Sensors," *Journal of The Electrochemical Society*, vol. 169, no. 5, p. 057518, 2022.

[76] Y. Zhao, G. Dong, L. Duan *et al.*, "Impacts of Sn precursors on solution-processed amorphous zinc–tin oxide films and their transistors," *RSC Advances*, vol. 2, no. 12, pp. 5307–5313, 2012.

[77] M. G. Kim, M. G. Kanatzidis, A. Facchetti, and T. J. Marks, "Low-temperature fabrication of high-performance metal oxide thin-film electronics via combustion processing," *Nature Materials*, vol. 10, pp. 382–388, 2011.

[78] S. Jeong, Y. Jeong, and J. Moon, "Solution-Processed Zinc Tin Oxide Semiconductor for Thin-Film Transistors," *The Journal of Physical Chemistry C*, vol. 112, no. 30, pp. 11 082–11 085, 2008.

[79] J. Rivnay, S. C. B. Mannsfeld, C. E. Miller *et al.*, "Quantitative determination of organic semiconductor microstructure from the molecular to device scale," *Chemical Reviews*, vol. 112, pp. 5488–5519, 2012.

[80] Z. A. Lamport, H. F. Haneef, S. Anand *et al.*, "Tutorial: Organic field-effect transistors: Materials, structure and operation," *Journal of Applied Physics*, vol. 124, no. 7, p. 071101, 2018.

[81] O. D. Jurchescu, J. Baas, and T. T. M. Palstra, "Effect of impurities on the mobility of single crystal pentacene," *Applied Physics Letters*, vol. 84, pp. 3061–3063, 2004.

[82] M. M. Payne, J. H. Delcamp, S. R. Parkin, and J. E. Anthony, "Robust, soluble pentacene ethers," *Organic Letters*, vol. 6, no. 10, pp. 1609–1612, 2004.

[83] O. D. Jurchescu, S. Subramanian, R. J. Kline *et al.*, "Organic single-crystal field-effect transistors of a soluble anthradithiophene," *Chemistry of Materials*, vol. 20, no. 21, pp. 6733–6737, 2008.

[84] E. K. Lee, M. Y. Lee, C. H. Park *et al.*, "Toward environmentally robust organic electronics: Approaches and applications," *Advanced Materials*, vol. 29, no. 44, p. 1703638, 2017.

[85] J. E. Anthony, A. Facchetti, M. Heeney *et al.*, "N-type organic semiconductors in organic electronics," *Advanced Materials*, vol. 22, no. 34, pp. 3876–3892, 2010.

[86] C. Li, X. Liu, H. Liu *et al.*, "A julolidine functionalized benzimidazoline n-dopant: optimizing molecular doping in fullerene derivatives by modulating miscibility," *Journal of Materials Chemistry C*, vol. 11, no. 26, pp. 8381–8389, 2023.

[87] T. D. Anthopoulos, C. Tanase, S. Setayesh *et al.*, "Ambipolar organic field-effect transistors based on a solution-processed methanofullerene," *Advanced Materials*, vol. 16, no. 23-24, pp. 2174–2179, 2004.

[88] J. Liu, L. Qiu, and S. Shao, "Emerging electronic applications of fullerene derivatives: an era beyond OPV," *Journal of Materials Chemistry C*, vol. 9, no. 45, pp. 16 143–16 163, 2021.

[89] X. Qiu, V. Ivasyshyn, L. Qiu *et al.*, "Thiol-free self-assembled oligoethylene glycols enable robust air-stable molecular electronics," *Nature Materials*, vol. 19, no. 3, pp. 330–337, 2020.

[90] N. Moscovich, S. Simotko, E. Reyn *et al.*, "Balanced ambipolar oects through tunability of blend microstructure," *ACS Applied Materials & Interfaces*, vol. 17, no. 30, pp. 43 327–43 338, 2025.

[91] J. Rivnay, S. C. B. Mannsfeld, M. F. Toney *et al.*, "Quantitative determination of organic semiconductor microstructure from the molecular to device scale," *Chemical Reviews*, vol. 113, no. 4, pp. 1784–1799, 2013.

Chapter 3

Methodology

3.1 Chapter Overview

This chapter details the fabrication techniques utilised for specimen preparation as well as the morphological and structural analyses of the material systems detailed in this work. Firstly, the preparation of different substrates and precursor solutions for solution-processing are described. This is followed by an overview of the thin film and electrode deposition methods, namely spin-coating and thermal evaporation. The control parameters and condi-

tions are given for the device architectures detailed in Chapter 2, specifically, TFTs and WG-TFTs.

Next, microscopies for structural, morphological and chemical analyses are explained, including high-resolution atomic force microscopy (AFM), scanning electron microscopy (SEM) and transmission electron microscopy (TEM). The working principles that underpin several X-ray techniques used in this work, X-ray diffraction (XRD), X-ray reflectivity (XRR), X-ray photoelectron spectroscopy (XPS) and energy-dispersive X-ray spectroscopy (EDX) are also shown. Lastly, the measurement of the electronic properties of all transistor configurations is outlined as well as the chemiresistive behaviour of metal TFTs. The methods explained here serve as the foundation to understand the results shown in Chapters 4, 5 and 6.

3.2 Preparation of Substrates

Different types of substrates were used in this work depending on the transistor technology and characterisation technique applied. Bottom gate top contact TFTs were fabricated using diced substrates (20 mm × 20 mm), consisting of a 400 nm SiO_2 dielectric on a highly doped Si wafer, which acted as the back gate. Two types of substrates were used for the fabrication of water-gated FETs: unpatterned ultra-flat quartz-coated glass (15 mm × 20 mm, rms = 1 nm, Ossila) and pattered indium tin oxide (ITO) source-drain electrodes on glass (20 mm × 20 mm). Finally, glass substrates with a 300 nm-thick and 4 mm-wide centred ITO strip, were used for the fabrication of hole-transporting diodes.

All substrates were cleaned by sonication in acetone and IPA ($\geq$ 99.5% from Sigma-Aldrich) separately for 15 min to remove debris, fibres or inorganic contaminants and blow-dried with N_2. The Si- and ITO-based substrates were placed in a UV ozone cleaner (Novascan) for 1 h and 30 min, respectively, to remove oils, fingerprints or organic contaminants. This process also increased the wettability of the substrates prior to spin-coating

and ensured that a uniform layer of material was deposited with the desired thickness.

3.3 Preparation of Precursor Solutions

The precursor solutions were prepared using the solution-processable materials detailed in Chapter 2.4. Inorganic precursor solutions were prepared under a fume hood. $ZnCl_2$ and $SnCl_2$ (150 mM, anhydrous, 99.999 % from Sigma-Aldrich) were dissolved in 2-methoxyethanol (anhydrous, 99.999 % from Sigma-Aldrich) separately and sonicated for 15 min. The ZTO solution was prepared by mixing equal amounts of $ZnCl_2$ and $SnCl_2$ (1:1) precursor solutions and aged under stirring for 24 h at room temperature.

Organic precursor solutions were prepared in a N_2 glovebox. P3HT (5 mg mL^{-1}, 4002-E from Rieke Metals, regioregular) and $PrC_{60}MA$ (10 mg mL^{-1}, $>$ 99 % from Lumtec) solutions were prepared by using chloroform as the solvent (anhydrous, contains amylene as stabiliser, $\leq$ 99 % from Sigma-Aldrich), while PCDTPT (10 mg mL^{-1}, CAS No. 1334407-47-4 from 1-Material) powder was dissolved in chlorobenzene (anhydrous, 99.8 % from Sigma-Aldrich).

For blend preparation, $PrC_{60}MA$:P3HT mixtures were prepared at percentage ratios of 95:5 and 99:1, with a total concentration of 5 mg mL^{-1}. $PrC_{60}MA$ was also blended with PCDTPT at percentage ratios of 90:10 and 95:5, using the same concentration. All blend solutions were stirred at room temperature for 3 h prior to use.

3.4 Vapour Phase Infiltration (VPI)

VPI is a solvent-free technique that utilises atomic layer deposition (ALD) to introduce inorganic materials into a polymer matrix. At low ALD processing temperatures, organic films can be safely exposed to organometallic precursor molecules, which diffuse into the polymer and convert *in-situ* into

the corresponding metal oxide. [1] A typical VPI process includes (i) sorption of gas phase precursors into the polymer matrix, (ii) diffusion of the precursors within the polymer, and (iii) entrapment and subsequent conversion of the precursors into the respective metal oxide. The distribution of ALD-deposited metal oxides within the polymer can be readily visualised using SEM with a back-scattered electrons (BSE) detector, due to the high contrast between the organic matrix and accumulated inorganic phase. Details of the microscopy techniques used for morphological analysis, including SEM, are provided in §3.6.

Herein, the disordered domains in $PrC_{60}MA$:P3HT blend films are studied via sub-surface ALD of ZnO. Prior to examining the blend films, their individual components were subjected to the VPI process separately. P3HT and $PrC_{60}MA$ films were exposed to a VPI process using diethylzinc (DEZ) and deionised (DI) water vapours. The ZnO precursors selectively infiltrate different phases of the organic films, resulting in Z-contrast. This process was performed in an ALD system (Savannah® S200, Veeco Instruments Inc.) in a pulse-exposure-purge sequence. The cycle was repeated forty times with N_2 (99.99 %) as the carrier and purging gas. During each cycle, the specimens were exposed to the DEZ pulse for 180 s, followed by a purge process lasting 300 s. After the DEZ pulses, the specimens were exposed to a single H_2O pulse, followed by another purge process lasting 900 s.

The reaction chamber was heated to 60 °C with a base N_2 flow rate of 20 sccm. Thicker P3HT, $PrC_{60}MA$ and $PrC_{60}MA$:P3HT blend films (15 mg mL^{-1}) were span onto cleaned SiO_2 substrates for characterisation. High-resolution cross-sectional images of the films were recorded using a Zeiss Ultra-Plus Field Emission Scanning Electron Microscope (FESEM) operated at 1.5 keV, equipped with a BSE detector to observe the Z-contrast between the as-deposited ZnO and the polymer matrix. The BSE images reveal a clear contrast between the bright regions of ZnO and the darker areas corresponding to the organic film.

3.5 Thermogravimetric Analysis (TGA)

TGA monitors the mass loss of a specimen in the solid or liquid phase as a function of temperature or time while it is heated at a fixed rate in a controlled atmosphere. It can be used to assess the thermal stability and decomposition behaviour of precursors during solution processing, providing insight into how temperature influences the properties of the resulting thin films [2]. In this work, the thermal behaviour of the metal chlorides, $ZnCl_2$ and $SnCl_2$, was examined using TGA (PerkinElmer Pyris 1 TGA) at a heating rate of $10\,^{\circ}\mathrm{C}\,\mathrm{min}^{-1}$ from $30\,^{\circ}\mathrm{C}$ to $500\,^{\circ}\mathrm{C}$ in air. The upper temperature limit of $500\,^{\circ}\mathrm{C}$ was selected to align with the constraints of the fabrication process, as the films were treated on a hot plate up to $500\,^{\circ}\mathrm{C}$ to maintain low-cost processing and avoid the use of a furnace that was unsafe to operate. Data analysis was performed using the Pyris™ software package.

3.6 Microscopies for Structural & Morphological Analyses

Three different microscopy techniques were employed to provide in-depth structural and morphological analyses of the single and multilayer metal oxide films based on ZnO, SnO_2 and ZTO. AFM and SEM were used to characterise the film surface morphology and topography at different magnifications, while, TEM was used to study the composition of cross-sectional specimens with complementary elemental mapping.

3.6.1 AFM

AFM is a high-resolution form of scanning probe microscopy used to characterise film surfaces. [3] An atomic force microscope consists of a sharp probe tip mounted on a flexible cantilever, positioned parallel to the specimen surface and oscillating at a frequency determined by the selected measurement mode (Figure 3.1). The lateral forces between the tip and the specimen –

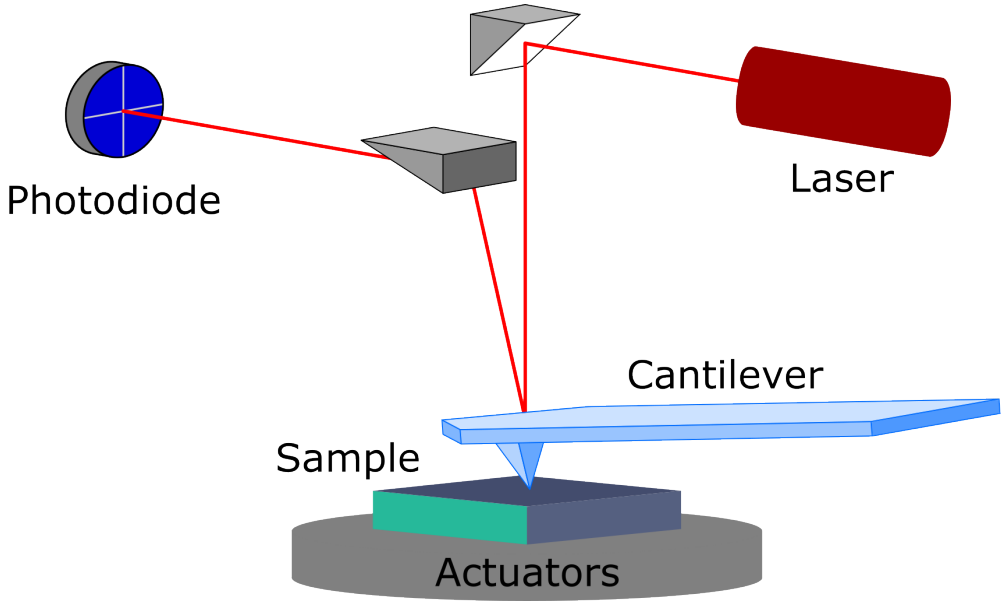

Figure 3.1: Schematic of a typical atomic force microscope.

governed by Hooke's Law – are monitored to study the surface morphology. As these forces can dull or damage the tip, depending on the nature and hardness of the specimen, AFM instruments are capable of operating in different measurement modes. The most common is contact mode, which records interactions between the specimen and the probe tip by tracking the tip's deflection during raster-scanning, using a laser and photodiode. The tip is brought into direct contact with the surface and an electronic feedback loop maintains constant deflection, allowing surface topography to be mapped as a function of vertical displacement. While contact mode can provide high spatial resolution, it can also cause damage to softer materials, such as organic samples, or to the AFM tip itself due to sustained contact between the tip and the surface. Therefore, a more flexible cantilever with a lower spring constant and resonant frequency is typically used in tapping mode, as discussed below.

An alternative measurement mode is tapping mode, illustrated in Figure 3.2, in which the cantilever is vibrated near its resonant frequency, causing the probe tip to oscillate at a fixed rate. The tip makes intermittent contact with the specimen surface, and interactions between the probe and the specimen are measured as changes in oscillation amplitude. Other AFM

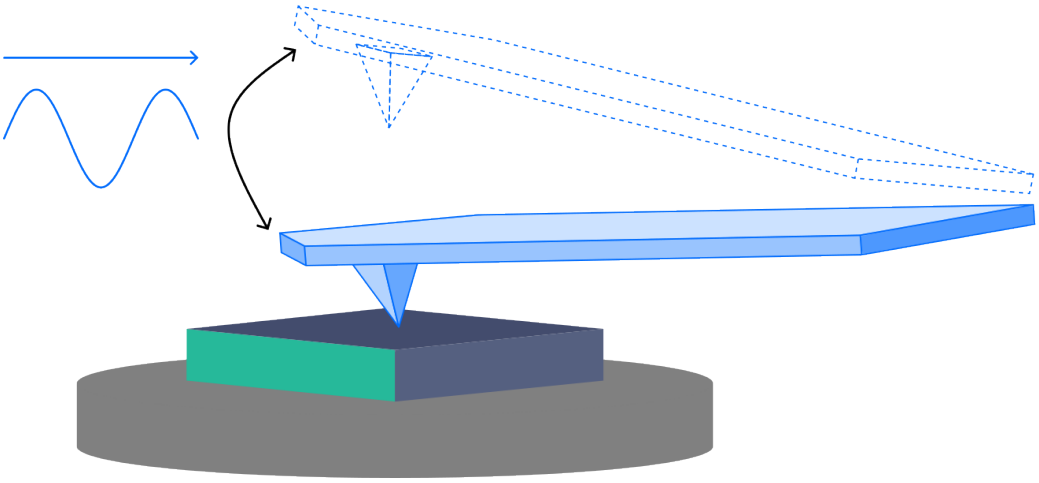

Figure 3.2: Illustration of tapping mode AFM.

measurement modes and metrics exist, such as non-contact mode; however, these are beyond the scope of this work. [4] In this thesis, only tapping mode AFM is employed in an Asylum Research MFP-3D Infinity instrument to examine the surface morphology and topography of metal oxide thin films, and generate images with 1 µm × 1 µm scan area. Image processing and analysis were performed using the open-source software Gwyddion.

3.6.2 SEM

SEM is an imaging technique that uses a focused electron beam to scan the specimen surface under an inert atmosphere. The electron beam can be generated by different sources such as a thermionic filament or a field emission (FE) gun. The source brightness is the key performance metric that differentiates between them since it represents the electron count per unit area. Therefore, FE guns are preferred as they produce higher brightness, which translates to an improved signal-to-noise ratio and image resolution. A series of magnetic lenses and apertures are used to focus and correct the beam, so that a spot size appropriate to resolve nanometric features is obtained. A schematic of a SEM column is shown in Figure 3.3.

The electron beam then scans the surface in a raster pattern and the impinging radiation interacts with the electron cloud created by atoms within

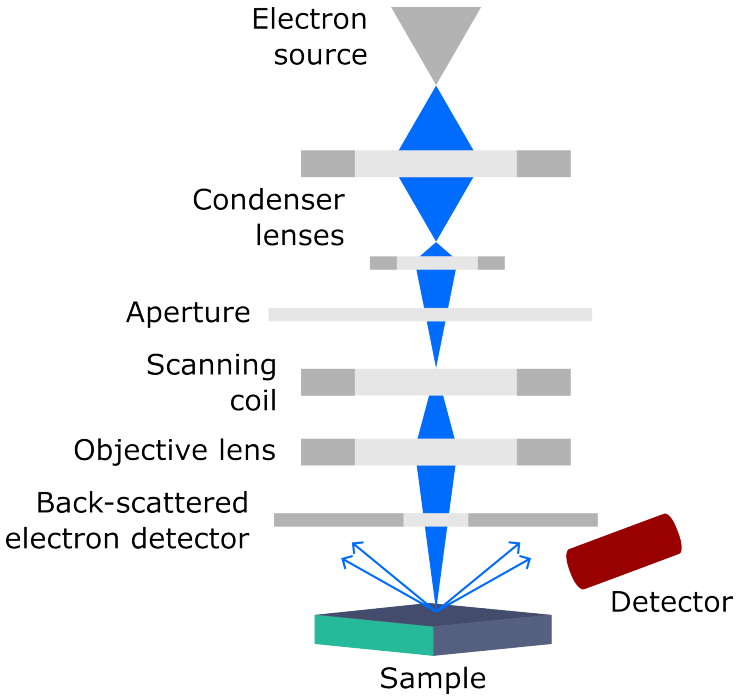

Figure 3.3: Schematic of a scanning electron microscope column, including the electron beam source, lenses and apertures.

the specimen to release different signals such as secondary electrons (SE), BSE or characteristic X-rays that correspond to the certain elements present in the specimen. Low energy SE ($< 50\,\text{eV}$) emitted from the material originate from elastic interactions with the primary electron beam and are of particular interest as these provide topographical information of the specimen in terms of their energy, which is directly translated to a spatial grayscale map of the surface. High energy ($> 50\,\text{eV}$) BSE generated from inelastic interactions with the primary electron beam also provide additional qualitative analysis relating to average atomic number of the specimen, which yields a Z-contrast across the scanned region.

A FEI Helios Nanolab 600 equipped with a FE gun at 15 kV with 2 nm resolution was used to study the trilayer metal oxide TFTs. SEM images of the P3HT, $PrC_{60}MA$ and $PrC_{60}MA$:P3HT blend films as-cast and after annealing were recorded using a Zeiss Ultra-Plus Field Emission Scanning Electron Microscope (FESEM) operated at 1.5 keV, equipped with a BSE detector to observe the Z-contrast between the as-deposited ZnO and the polymer matrix.

3.6.3 TEM

TEM is a type of electron microscopy used herein to produce cross-sectional images of thin films (thickness $< 300\,\text{nm}$) by transmitting an electron beam through the specimen. [5] A field emission (FE) gun generates electrons via an applied electric field, which are then focused into a narrow beam by condenser magnetic lenses to probe the specimen, as illustrated in Figure 3.4. TEM images are formed from electrons transmitted through the film, which are focused by the objective lens and collected by a charge-coupled device (CCD) camera. This results in a grayscale map, where intensity corresponds to the number of electrons transmitted. Darker regions indicate lower electron transparency, typically associated with higher material density (e.g., higher atomic number, Z).

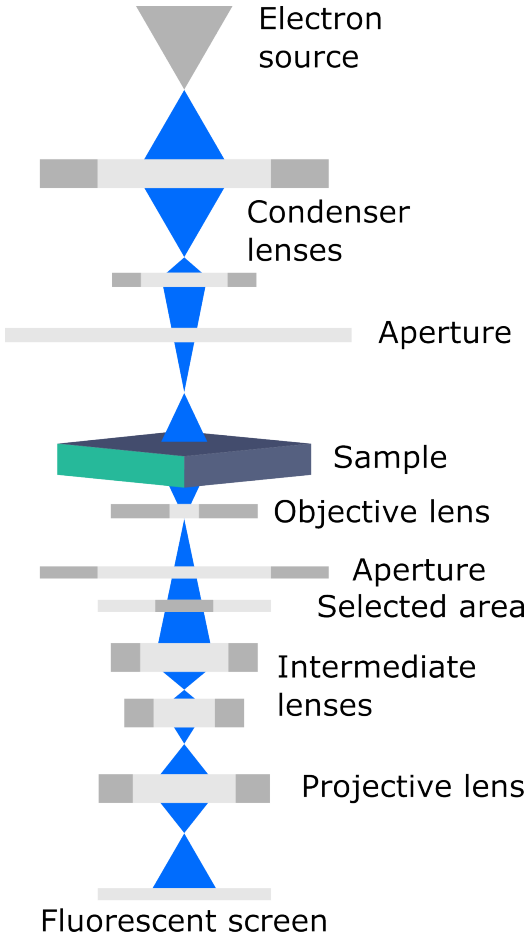

Figure 3.4: Schematic of a transmission electron microscope column, including the electron beam source, lenses and apertures.

Additional apertures and condenser lenses can be introduced within the column to block high-angle electrons and resolve atomic features, termed high-resolution TEM. This uses transmitted and scattered electrons in-tandem to create the phase contrast required to achieve atomic resolution. In addition to transmission mode, the microscope can be operated in scanning TEM (STEM) mode, which focuses the beam to a fine spot at the nanometric scale and uses a set of scanning coils to probe the surface of the films in a raster motion, akin to the working mechanism of SEM. The entirety of the specimen is imaged simultaneously, in contrast to SEM, in which different regions are scanned over time. In this work, TEM was carried out in a JEOL 2100F equipped with a FE gun at 200 kV. The cross-sectional specimens were prepared in the FEI Helios Nanolab 600 SEM system previously described, equipped with a Ga focused ion beam (FIB) source. Pt was deposited on the films prior to FIB milling to ensure a smooth and clean cross-section was obtained.

3.7 X-ray Techniques

Four different X-ray techniques were used to probe the structural, crystalline and chemical properties of the metal oxide thin films, namely XRD, XRR, XPS and EDX and corroborate findings made from the previously described imaging techniques.

3.7.1 XRD

XRD is a versatile, non-destructive analytical technique used to examine the morphological properties and crystal structure of a specimen. X-rays produced by the source illuminate the specimen and cause constructive and destructive interferences due to its atomic arrangement. Figure 3.5 shows that the theoretical basis of XRD stems from Bragg's Law and the diffraction angle, 2θ, is defined as the angle between the incident and diffracted beams. Assuming that the incident X-ray beam is a plane wave with wave-

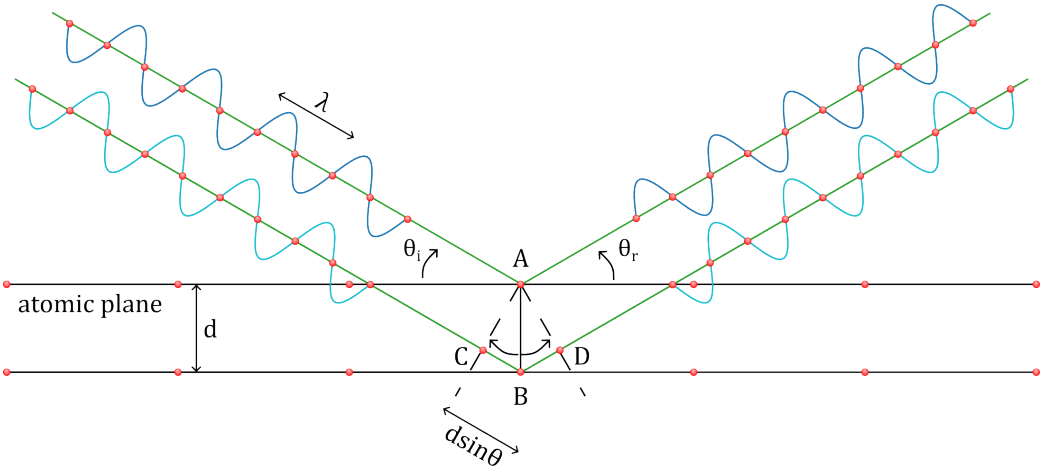

Figure 3.5: Schematic of Bragg's Law according to Equations 3.7.1 & 3.7.2

length λ, it will be scattered by the lattice planes of the specimen under test arranged at a certain inter-planar distance $d_{h,k,l}$, The incoming wave can be scattered destructively or constructively, and the latter will occur only if the scattered waves are in phase, given that the difference in their path length is proportional to a positive integer, n. The scattered beam will undergo constructive interference at a Bragg angle θ, described by Equation 3.7.1.

$$2d_{h,k,l} \sin\theta = n\lambda, \tag{3.7.1}$$

where $d_{h,k,l}$ is the inter-planar spacing of the lattice, expressed as:

$$d_{h,k,l} = \frac{a_0}{\sqrt{h^2 + k^2 + l^2}}. \tag{3.7.2}$$

The lattice parameter for the crystalline direction, h, k, l, is given by a_0. An X-ray diffractometer measures the intensity of constructive interference of the scattered waves described by Bragg's Law as a function of the scattering angle. Hence, sharp diffraction peaks are observable at different θ angles assignable to individual crystal planes corresponding to the lattice structure of the specimen. XRD (Bruker AXS D8 Advance GX003410) was used to assess the crystallinity of the metal oxide thin films studied in Chapter 4. The origin of increased surface roughness and micron-sized features on the surface were supported by crystallographic data obtained from XRD analysis.

3.7.2 XRR

XRR is an analytical technique used to characterise thin films based on the reflection of an incident X-ray beam at grazing angle, θ. [6] The reflected X-ray intensity is measured by a detector as a function of θ, which is varied close to the critical angle, θ_c, for total external reflection. At higher angles, part of the incident beam will propagate ($\theta = \theta_c$) or refract ($\theta > \theta_c$) inside the film. For an ideal system, the reflected X-rays will be a specular image of the impinging X-rays, and thus, their incidence angle will be equal. In practice, the surface of a specimen will not be perfectly smooth and flat, henceforth, the incidence angle and intensity of the reflected X-rays will deviate from the initial beam, according to Fresnel's Law. [7] A schematic of the working principle of XRR is shown in Figure 3.6(a) for a multilayer thin film.

The reflectivity profile in Figure 3.6(b) shows oscillations caused by X-ray interference that were first observed by Kiessig in 1931. The onset of these fringes i.e., critical angle for total reflection, provides information on the density of the films. At higher angles, the position of the critical angle indicates denser films. The amplitude of the oscillation influences the shape of the critical angle, which depends on the difference between the film density and Si substrate.

The period of these Kiessig fringes is related to differences in film thickness

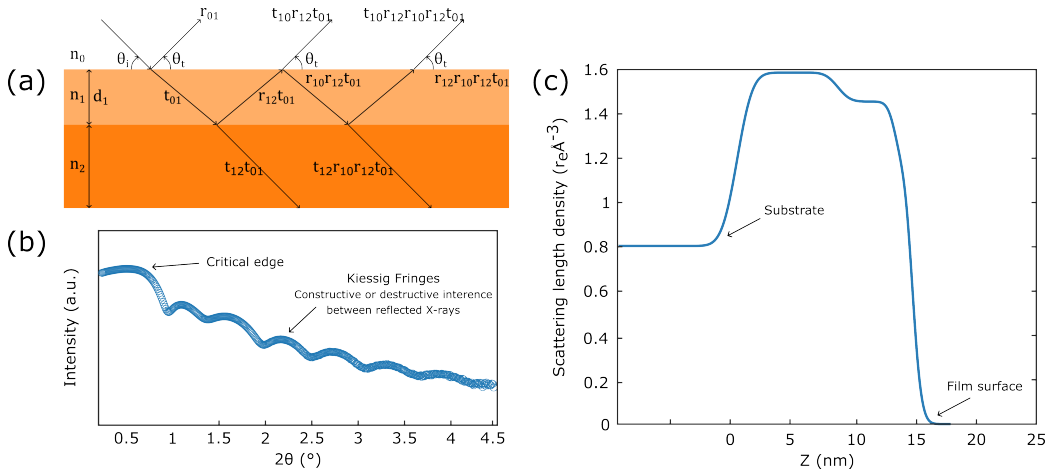

Figure 3.6: (a) Working principle behind XRR, (b) example XRR spectra and (c) extracted SLD versus depth profile.

– a thicker film results in a shorter period. The variation in total interface width considers both topographical roughness and chemical intermixing of the interference between layers. The oscillation decay rate and drop-off in fringe amplitude at higher angles is related to surface or interface roughness, while the latter considers surface roughness only.

The experimental data are fitted to an iterative best-fit model of the specimen, which uses a set of control parameters – such as film thickness, total interface width and electron density – as inputs. The number of possible interfaces increases with the number of layers present in the stack, thereby requiring greater computational resources to achieve convergence. The best-fitting simulations of the XRR results are used to extract the scattering length density (SLD) as a function of specimen thickness, as shown in Figure 3.6(c). The rising and falling edges in the SLD profile provide insight into the film composition and allow distinction between different layers in the stack, such as the substrate, semiconductor and metallic electrodes.

In this thesis, XRR was used to examine the total interface width, thickness and effective density of multilayer metal oxide thin films, in order to understand the physical basis for the enhanced electronic functionality of the fabricated TFTs. These metal oxide systems were modelled assuming smooth and continuous surfaces. XRR analysis was employed alongside AFM and cross-sectional TEM to verify film thickness and surface roughness. Furthermore, variation in the SLD profile as a function of specimen depth was compared with the evolution of specific peak intensities obtained through XPS depth profiling, since the constituent elements exhibit different material densities.

3.7.3 XPS

XPS is based on the photoelectric effect and is widely used to determine the elemental composition of a material, as well as the chemical state of its elements, the overall electronic structure and the density of electronic states. [8] The working principle of XPS is illustrated by Figure 3.7: when a

specimen is illuminated by incident X-rays, the absorbed energy may exceed the binding energy of core electrons bound to the atoms. In such cases, electrons are ejected from the material and the excess energy contributes to the kinetic energy of the emitted electrons (E_k). If the incident energy is insufficient to overcome the binding energy, it is re-emitted instead.

Since the binding energy of an electron is specific to each element, the kinetic energy measured by the detector will correspond to a discrete signal assigned to that element (see Figure 3.8). Given that the binding energy is characteristic of different atomic orbitals, their contribution can be directly obtained from the survey analysis. The intensity of a signal for an element is correlated against the total number of electrons. During XPS, electrons are only ejected by the photoelectric effect in the first few nanometres of the specimen. Therefore, monotonic depth profiling using an ion beam to etch layers of a specimen can be utilised to reveal subsurface information. XPS can be combined with a sequence of ion gun etch cycles to track the evolution of certain signals throughout the bulk of a specimen and confirm layer thicknesses against other X-ray techniques in addition to depth-dependent compositional information.

Herein, the chemical states of the multilayer metal oxide films were examined using XPS surface and depth profiling analyses. XPS measurements

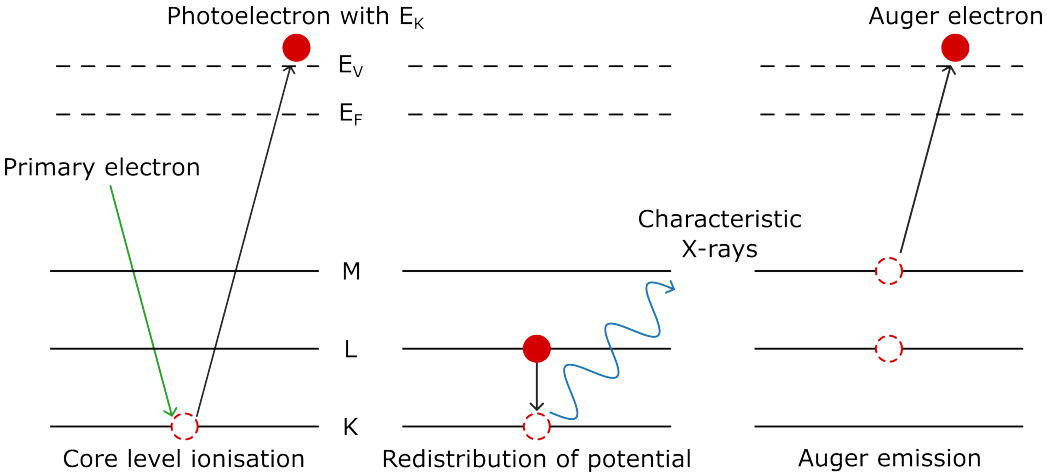

Figure 3.7: Schematic of the Auger effect and emission of characteristic X-rays.

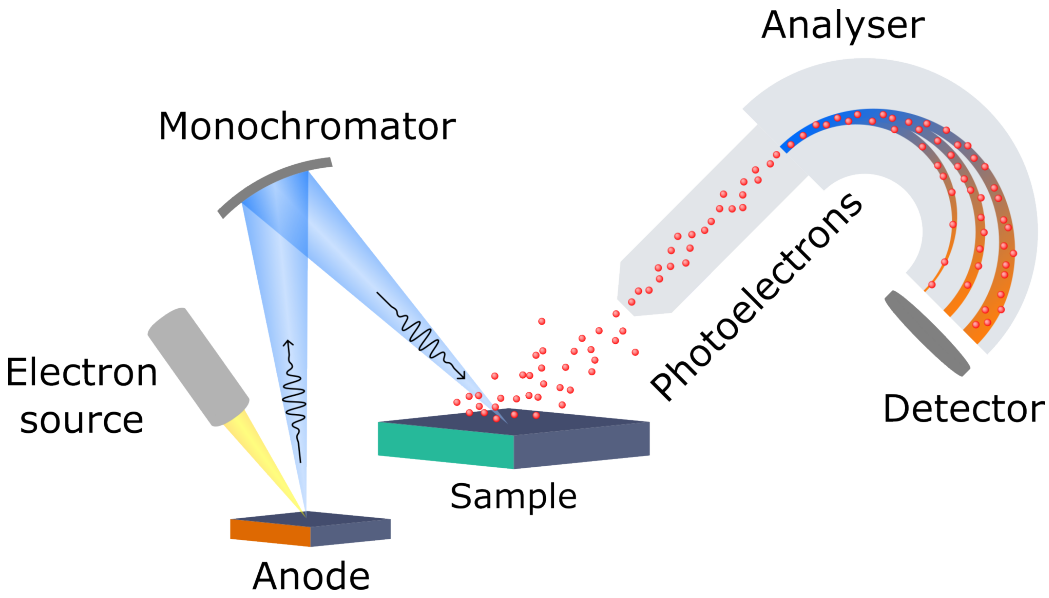

Figure 3.8: Schematic of an X-ray photoelectron spectrometer, including the electron source, monochromator, generation of photoelectrons and hemispherical analyser.

were carried out in a SPECS ProvenXPS system equipped with a PHOIBOS 150 2D-CMOS hemispherical analyser and a monochromatic X-ray source FOCUS 500. The Al Kα X-ray source (1486.6 eV) operated at 400 W and was separated from the analyser by 55°. A medium magnification mode and constant pass energy of the analyser equal to 20 eV were used for analysis. Photoelectron data were recorded at a take-off angle of 90° (normal detection). The survey spectrum and the high-resolution spectra were recorded with an energy step of 0.5 eV over 1400 eV and 0.1 eV, respectively. Binding energies, line widths and areas of the different XPS peaks were obtained by a weighted least-squares fitting of a Gaussian-Lorentzian model curve to the experimental data using the program CasaXPS. For depth profiling analyses, the specimens were etched using an Ar ion gun at 2 keV with a specimen current density of 0.5 µA cm^{-2}. The etch cycle duration was 60 s and etch rate was approximated as 0.025 ± 0.05 nm s^{-1}. Etch cycle zero corresponded to the film surface, and the etching was considered complete when the main signals present were the Si 2 s, Si 2 p and O 1 s peaks of the substrate, from etch cycle ten to twenty depending on the thickness of the film.

3.7.4 EDX

EDX is a technique for elemental and compositional analysis of materials examined by SEM or TEM, based on the information from the X-rays produced by electron irradiation. X-rays are emitted during the transfer of an electron from the outer to the inner shell of a constituent atom, as illustrated by Figure 3.7, and their energy of is characteristic of these orbital transitions, which allows the elemental identification of the constituents of the specimen. The intensity of these characteristic X-rays can be plotted versus position to measure the content of each element or overlapped with an electron microscope image to analyse segregation within the field of view. [9]

EDX was used in this work to study the trilayer ZTO-based films shown in Figure 3.9 and assess the distribution of the Zn and Sn contents throughout the TFTs. EDX was carried out alongside the previously described TEM analysis (see §3.6.3) using the Oxford Instruments Aztec microanalysis system. The microscope was operated in STEM mode to obtain an elemental map superimposed on the image generated by secondary electrons. Figure 3.9 shows the individual elemental analysis (Pt, Sn, Zn, O and Si) for a TEM image of a ZTO-based film.

3.8 Water Contact Angle Measurements

Water contact angle measurements are employed to assess the wettability of a surface by determining the angle formed between a water droplet and the surface of the specimen. This measurement provides insight into the

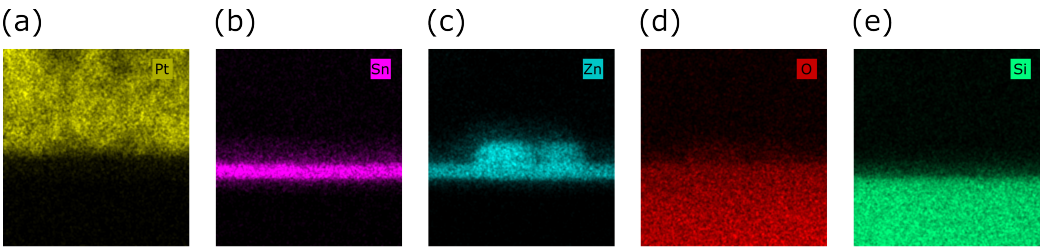

Figure 3.9: Individual elemental mapping of the (a)-(e) ZTO-ZTO-ZnO film showing the Pt, Sn, Zn, O and Si components from left to right.

hydrophilicity and surface energy of the material under investigation. [10] A water contact angle, $\theta_w < 90°$, indicates a hydrophilic surface with higher surface energy, whereas $\theta_w > 90°$ signifies a hydrophobic surface with lower surface energy (Figure 3.10).

In this work, water contact angle measurements were conducted to determine the hydrophilicity of P3HT, $PrC_{60}MA$ and $PrC_{60}MA$:P3HT blend films. These films were prepared from solutions with a concentration of 15 mg mL^{-1} and cast onto Si substrates for characterisation, in the same manner as for VPI (see §3.4). The wetting properties of the film surfaces were characterised using contact angle measurements performed at the Department of Materials Science and Engineering, Technion – Israel Institute of Technology, employing an Attension Theta Lite tensiometer and high-purity water droplets of 7 µL volume.

3.9 Transistor Fabrication

This work employs two low-cost, high-throughput and scalable techniques for device fabrication, that is, spin-coating and thermal evaporation. Spin-coating is used to prepare thin-films by direct deposition of a solution and subsequent thermal treatment. [11] A fixed volume of the precursor solution is span at high speed and the centrifugal force creates a uniform layer of material. The spin duration can be adjusted to improve the homogeneity of the thin film, depending on the vapour pressure of the organic solvent and processing conditions, in air or N_2 atmosphere, while spin speed defines the range of thicknesses that can be achieved from a given precursor solu-

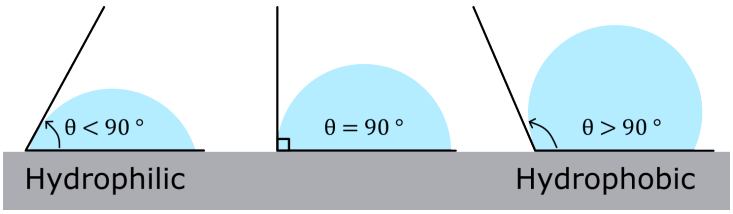

Figure 3.10: Schematic of water contact angles for a hydrophilic and hydrophobic film.

tion. During spin-coating, most of the precursor solution is expelled from the substrate, depending on the spin speed. After spinning, the substrate is thermally treated to evaporate the residual organic solvent and anneal the as-cast film.

Thermal evaporation is a common physical vapour deposition method that uses resistive heating under high vacuum to evaporate the source material. [12] The sources are held in a crucible, boat or coil, which are heated slowly by a direct current to evaporate the material at a certain rate and achieve a predefined layer thickness on the specimen, which is held directly above the source. During evaporation, the substrate can be rotated to eliminate shadow effects and the deposition of a uniform layer of material.

In this work, all thin films were spin-coated and thermally treated on a hot plate at different temperatures, depending on the nature of the deposited material and the specific transistor architecture, as discussed in the following sections. The precursor solutions were cast onto static, cleaned substrates (following the procedure described in §3.2) and the spin-coating parameters are specified for each transistor configuration below. Following thin-film deposition and subsequent thermal treatment, all source–drain electrodes were thermally evaporated under vacuum ($\approx 6 \times 10^{-6}$ mbar) using a thermal evaporation system integrated within a N_2 glovebox.

3.9.1 TFTs

For the fabrication of metal oxide TFTs, ZnO, SnO_2 and ZTO precursor solutions were spin-coated under a fume hood at 5000 rpm for 30 s onto cleaned substrates consisting of a 400 nm SiO_2 dielectric on a highly doped Si wafer. The multilayer films were grown by the sequential deposition and thermal treatment of ZTO and ZnO at temperatures in the range of 300 °C to 500 °C. After deposition and thermal treatment, Al source electrodes were deposited on top of the metal oxide films (50 nm at $\approx 2\,\text{Å}\,\text{s}^{-1}$) using the source-drain electrode masks shown in Figure 3.11, without rotation.

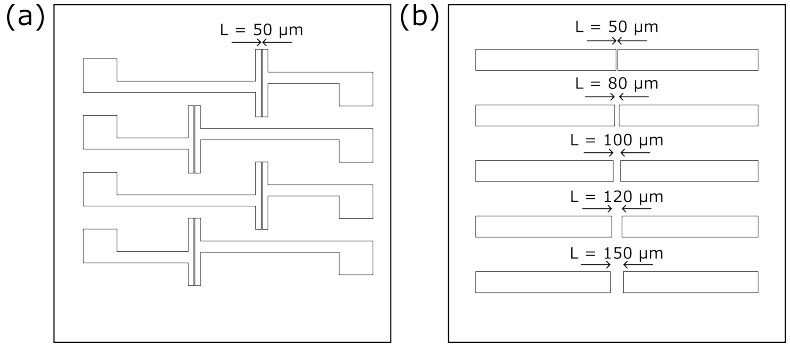

Figure 3.11: Schematics of (a) fixed channel length source-drain, (b) variable channel length source-drain electrode shadow masks.

3.9.2 Water-Gated TFTs

Two types of substrates were used for the fabrication of water-gated TFTs: unpatterned ultra-flat quartz-coated glass (15 mm × 20 mm) for P3HT-based devices and patterned ITO source-drain electrodes on glass (20 mm × 20 mm) for PCDTPT- and ZnO-based devices.

The quartz-coated glass substrates were placed in an OFET shadow mask (E291, Ossila) with a channel width (W) and length (L) of 1000 µm and 30 µm, respectively. 5 nm/50 nm-thick Cr/Au source-drain electrodes were then thermally evaporated following the methodology outlined in §3.9. After deposition, the substrates were cleaned again following the same procedure outlined in §3.2. P3HT, $PrC_{60}MA$ and $PrC_{60}MA$:P3HT blend solutions were spin-coated at room temperature inside a N_2 glovebox at 1000 rpm for 60 s followed by 3000 rpm for 10 s. PCDTPT, $PrC_{60}MA$ and $PrC_{60}MA$:PCDTPT blend solutions were spin-coated onto cleaned patterned ITO source-drain electrodes on glass following UV ozone treatment using the same parameters and conditions as for the P3HT-based devices. After deposition, the films were left inside a N_2 glovebox at room temperature for 1 h to allow the solvent to evaporate slowly. Secondly, P3HT- and PCDTPT-based films were annealed at 120 °C for 20 min and 150 °C for 30 min, respectively.

Conversely, ZnO was spin-coated onto ITO substrates under a fume hood in air at 5000 rpm for 30 s and thermally treated at 500 °C for 1 h. Bilayer films were prepared by spin-coating and annealing ZnO as the underlayer,

followed by the deposition and thermal treatment of PCDTPT as the overlayer. The as-cast and thermally treated films were dry-wiped using a cotton bud to remove them from the contacts and minimise crosstalk between pixels. Finally, Kapton® tape was used to isolate the channel area and avoid contact between the electrolyte and metal during electrical characterisation.

3.10 Electrical Characterisation

The electronic properties of all transistor configurations were measured using a dual-channel source measurement unit (SMU, B2902A, Keysight Technologies) with a dedicated software (EasyExpert).

3.10.1 TFTs

For the electrical characterisation of metal oxide TFTs fabricated on Si substrates, output and transfer curves were acquired using a double-sweep measurement, with the maximum applied gate bias fixed at 40 V. In electron accumulation mode, output characteristics were measured at $V_{gs} = 0$ V to 40 V in 5 V steps and $V_{ds} = 0$ V to 40 V in 0.1 V steps. The corresponding n-type transfer characteristics were recorded at $V_{ds} = 40$ V, with $V_{gs} = -40$ V to 40 V in 0.5 V steps.

3.10.2 WG-TFTs

For the electrical characterisation of WG-TFTs, a Ag/AgCl pellet electrode (E206, Warner Instruments) was used as the gate, submerged in a 200 µL drop of DI water (see Figure 3.12), without making direct contact with the substrate. Output and transfer curves were acquired with a double-sweep measurement and the applied gate bias did not exceed 1 V to prevent water electrolysis and faradaic reactions. In hole accumulation mode, output curves were obtained at $V_{gs} = 0$ V to -0.7 V in steps of -50 mV and $V_{ds} = 0.05$ V to -0.6 V in steps of -13 mV. The accompanying p-type transfer characteristics were recorded at $V_{ds} = -0.6$ V and $V_{gs} = 0.05$ V to -0.7 V in steps of -1 mV.

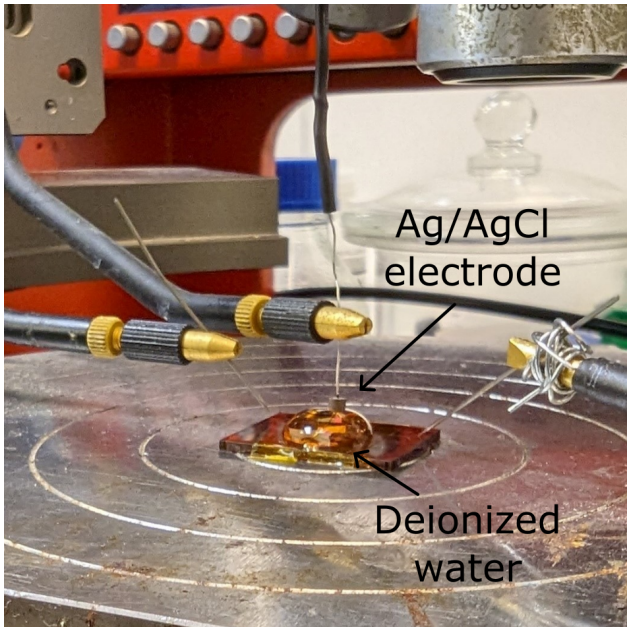

Figure 3.12: Probe station for electrical characterisation of water-gated FETs.

In electron accumulation mode, output curves were obtained at $V_{gs} = 0.4\,\mathrm{V}$ to $1\,\mathrm{V}$ in steps of $50\,\mathrm{mV}$ and $V_{ds} = -0.05\,\mathrm{V}$ to $0.6\,\mathrm{V}$ in steps of $13\,\mathrm{mV}$. The accompanying n-type transfer characteristics were recorded at $V_{ds} = 0.6\,\mathrm{V}$ and $V_{gs} = 0.4\,\mathrm{V}$ to $1\,\mathrm{V}$ in steps of $1\,\mathrm{mV}$.

3.10.3 Calculation of Saturation & Effective Mobility

Assuming that charge carrier mobility (μ) is independent of applied gate bias (V_{gs}) and neglecting short channel effects, drain-source current (I_{ds}) in the saturation regime is given by Equation 3.10.3 [13]:

$$I_{ds} = \frac{W}{2L}\mu C_i (V_{gs} - V_{th})^2, \tag{3.10.3}$$

where $\frac{W}{L}$ is the channel width-to-length ratio, C_i is the capacitance per unit area of the dielectric layer and V_{th} is the threshold voltage. μ is obtained by taking the derivative with respect to V_{gs}. Rearranging the resulting equation yields Equation 3.10.4:

$$\mu = \frac{2L}{WC_i}\left(\frac{\partial\sqrt{I_{ds}}}{\partial V_{gs}}\right)^2. \tag{3.10.4}$$

$\frac{\partial\sqrt{I_{ds}}}{\partial V_{gs}}$ can be extracted by plotting $\sqrt{I_{ds}}$ against V_{gs} and finding the gradient. Ideal transfer characteristics are linear and hence $\frac{\partial\sqrt{I_{ds}}}{\partial V_{ds}}$ is constant. In practice, external factors such as contact resistance can produce curved plots, which has resulted in several erroneous reported mobilities, particularly for OFETs. [14] The reliability factor (r) given in Equation 3.10.5, accounts for nonlinearities in transfer characteristics [13]. It is defined as the ratio (expressed in %) of the maximum channel conductivity experimentally achieved in a FET to that calculated in an equivalent ideal FET:

$$r = \frac{\left(\frac{\sqrt{|I_{ds}|^{max}}-\sqrt{|I_{ds}|^{0}}}{|V_{gs}|^{max}}\right)^2}{\left(\frac{WC_i}{2L}\mu\right)^2_{claimed}}, \tag{3.10.5}$$

where $\left(\frac{WC_i}{2L}\mu\right)^2_{claimed}$ accounts for the claimed device parameters and mobility in the saturation regime. $|I_{ds}|^{max}$ is the experimental maximum drain current reached at the maximum gate voltage, $|V_{gs}|^{max}$. $|I_{ds}|^0$ is the drain current at $V_{gs} = 0$. Effective mobility, μ_{eff}, is thus given by:

$$\mu_{eff} = r \times \mu. \tag{3.10.6}$$

Hereafter, the mobility values quoted in this thesis are effective mobility, unless otherwise stated.

3.10.4 Calculation of TFT Sensitivity (S)

The chemiresistive responses of the TFT gas sensors described in Chapters 4 and 5 were measured using a sealed, custom-built testing rig, shown in Figure 3.13, operated without a mass flow controller. Chapter 4 focuses on the chemiresistive response of single layer SnO_2 TFTs exposed to acetone vapour overnight, while Chapter 5 investigates bilayer ZTO- and ZnO-capped TFTs exposed to a range of volatile organic compounds (VOCs).

For testing, the TFT was placed upside down, with the metal electrodes aligned to the appropriate pins corresponding to each channel length. A baseline response was first recorded. An open 3 mL vial containing the solvent

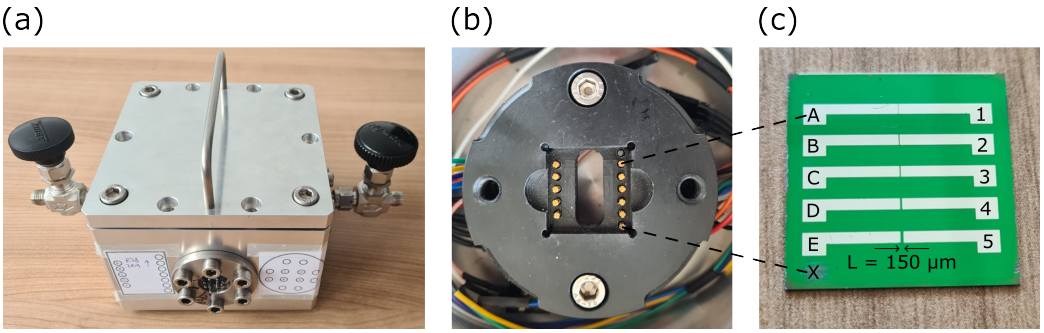

Figure 3.13: (a) Bespoke testing chamber with (b) device stage illustrations corresponding to (c) source-drain electrodes. The source contact pins were listed from one to five with complementary drain contact pins from A to E. The largest channel length (L = 150 µm) corresponded to contacts five and E. The substrate was lightly scratched with a diamond tip pen below pin E to access the gate electrode at pin X and flipped prior to testing.

under investigation was then placed inside the chamber adjacent to the device stage. The chamber was sealed and allowed to reach vapour saturation over short (1 h), long (4 h) or overnight exposure periods. Following the exposure period, the device was re-tested. The chamber was subsequently opened inside a fume cupboard, the vial and TFT were removed, and the TFT was heated at 100 °C for either a short (15 min) or long (1 h) recovery period to restore I_{ds}. A final electrical test was then performed to measure the post-recovery I_{ds}, establishing a new baseline for repeated exposure testing.

The sensitivity (S) of the TFT gas sensors was calculated using Equation 3.10.7, based on the comparison between baseline and post-exposure I_{ds} characteristics: [15, 16]

$$S = \frac{\Delta I_{ds}}{I_{ds}[0]} = \frac{I_{ds}[gas] - I_{ds}[0]}{I_{ds}[0]}, \tag{3.10.7}$$

where ΔI_{ds} is the change in I_{ds} before ($I_{ds}[0]$) and after ($I_{ds}[gas]$) exposure to reducing vapours. A negative S indicates a decrease in I_{ds}, while a positive S indicates an increase following exposure.

3.11 Summary

This chapter has detailed the experimental and characterisation methodologies used for specimen preparation and analysis. The preparation of various substrates and precursor solutions, including TGA, was first outlined, followed by the deposition of thin films and metal contacts via spin-coating and thermal evaporation, respectively, with the specific control parameters provided for each transistor configuration. Structural and morphological characterisation techniques were then introduced, including AFM, SEM and TEM. This was followed by a description of the X-ray techniques employed to examine the crystalline properties (XRR and XRD) and the chemical composition and environment (XPS and EDX) of the thin films. Additionally, the intrinsic properties of all-organic blend films used in low-voltage WG-TFTs were characterised via VPI and water contact angle measurements. Finally, the electrical characterisation procedures and sweep settings applied to all transistor configurations were described.

References

[1] S. Obuchovsky, M. Levin, A. Levitsky, and G. L. Frey, "Morphology visualization of P3HT:Fullerene blends by using subsurface atomic layer deposition," *Organic Electronics*, vol. 49, pp. 234–241, 2017.

[2] J. W. Park, B. H. Kang, and H. J. Kim, "A Review of Low-Temperature Solution-Processed Metal Oxide Thin-Film Transistors for Flexible Electronics," *Advanced Functional Materials*, vol. 30, no. 20, p. 1904632, 2020.

[3] N. Jalili and K. Laxminarayana, "A review of atomic force microscopy imaging systems: application to molecular metrology and biological sciences," *Mechatronics*, vol. 14, no. 8, pp. 907–945, 2004.

[4] T. R. Ramachandran, C. Baur, A. Bugacov *et al.*, "Direct and controlled manipulation of nanometer-sized particles using the non-contact atomic force microscope," *Nanotechnology*, vol. 9, no. 3, p. 237, 1998.

[5] D. B. Williams and C. B. Carter, "The Transmission Electron Microscope," in *Transmission Electron Microscopy: A Textbook for Materials Science*, D. B. Williams and C. B. Carter, Eds. Boston, MA: Springer US, 1996, pp. 3–17.

[6] K. N. Stoev and K. Sakurai, "Review on grazing incidence X-ray spectrometry and reflectometry," *Spectrochimica Acta Part B: Atomic Spectroscopy*, vol. 54, no. 1, pp. 41–82, 1999.

[7] J. Daillant and A. Gibaud, *X-ray and Neutron Reflectivity: Principles and Applications*. Springer, 2008.

[8] R. H. PRATT, A. RON, and H. K. TSENG, "Atomic Photoelectric Effect Above 10 keV," *Reviews of Modern Physics*, vol. 45, no. 2, pp. 273–325, 1973.

[9] M. Scimeca, S. Bischetti, H. K. Lamsira *et al.*, "Energy Dispersive X-ray (EDX) microanalysis: A powerful tool in biomedical research and diagnosis," *European Journal of Histochemistry*, vol. 62, no. 1, 2018.

[10] N. Fumeaux, C. P. Almeida, S. Demuru, and D. Briand, "Organic electrochemical transistors printed from degradable materials as disposable biochemical sensors," *Scientific Reports*, vol. 13, no. 1, p. 11467, 2023.

[11] L. L. Hench and J. K. West, "The sol-gel process," *Chemical Reviews*, vol. 90, no. 1, pp. 33–72, 1990.

[12] Z. Dai, Z. Pan, and Z. Wang, "Novel Nanostructures of Functional Oxides Synthesized by Thermal Evaporation," *Advanced Functional Materials*, vol. 13, no. 1, pp. 9–24, 2003.

[13] H. H. Choi, K. Cho, C. D. Frisbie *et al.*, "Critical assessment of charge mobility extraction in FETs," *Nature Materials*, vol. 17, no. 1, pp. 2–7, 2018.

[14] M. Nikolka, I. Nasrallah, B. Rose *et al.*, "High operational and environmental stability of high-mobility conjugated polymer field-effect transistors through the use of molecular additives," *Nature Materials*, vol. 16, no. 3, pp. 356–362, 2017.

[15] J. Li, L. Li, Q. Chen *et al.*, "Ultrasensitive room-temperature acetone gas sensors employing green-solvent-processed aligned InNdO nanofiber field-effect transistors," *Journal of Materials Chemistry C*, vol. 10, no. 3, pp. 860–869, 2022.

[16] M. T. Vijjapu, S. G. Surya, S. Yuvaraja *et al.*, "Fully Integrated Indium Gallium Zinc Oxide NO2 Gas Detector," *ACS Sensors*, vol. 5, no. 4, pp. 984–993, 2020.

Chapter 4

Characterisation of Metal Oxide TFTs

4.1 Chapter Overview

This chapter presents the systematic design of metal oxide TFTs for applications in VOC detection using a low-cost, high-throughput and fully solution-processed method. The incorporation of highly abundant, non-toxic metal chloride precursors, $SnCl_2$ and $ZnCl_2$, offered substantial economic and environmental benefits. Thermal analysis of the precursors provided an indication of the influence that temperature had on the properties of the metal-oxide films during their thermal treatment. To begin, the electronic functionality of single oxide SnO_2 TFTs treated at 350 °C and 450 °C was studied. Their transistor performance was heavily influenced by several factors, including surface morphology and crystalline properties, which were examined using AFM and XRD measurements, respectively. Furthermore,

their source-drain electrode geometry was varied to assess the impact of channel resistance on I_{ds} as a result of increased W/L. Finally, their chemiresistive response was qualitatively assessed following exposure to acetone vapour in ambient conditions to provide proof-of-concept.

Next, SnO_2 was blended with ZnO in equal proportions to prepare ZTO TFTs. The electrical performance of multilayer devices – fabricated by depositing alternating layers of ZnO and ZTO – was subsequently evaluated. A handful of reports have highlighted the benefit of stacking metal oxide layers via spin-coating, which includes enhanced charge transport and reliability for optoelectronic applications. Therefore, the primary objective of this study was to improve upon the key metrics used to quantify the electronic performance of single layer TFTs studied previously, namely μ_{eff}, V_{th} and $I_{on/off}$, by identifying a suitable material system. Firstly, the impact of the precursor concentration was assessed to highlight the benefit of layering metal oxide films treated at the optimal temperature. On the basis of these successful results, the intercalation of a ZnO layer to construct ZTO-capped (ZTO-ZTO & ZTO-ZnO-ZTO) and ZnO-capped (ZTO-ZnO & ZTO-ZTO-ZnO) TFTs was explored. To investigate the clear differences in surface morphology and crystalline properties between the ZnO- and ZTO-capped TFTs, AFM, SEM, and XRD measurements were carried out. Moving on to film composition, TEM, XRR and XPS depth profiling analyses, were used to track the evolution of these components. The best performing transistors are taken forward in the next chapter and discussed relative to the their chemiresistive functionality.

4.2 Single Layer SnO_2 TFTs

4.2.1 Structural Characterisation of SnO_2 Films

A schematic of the TFT employed here is shown in Figure 4.1(a) following the description of the different transistor architectures given in Chapter 2.3.3. The channel comprised a single layer SnO_2 film prepared from the $SnCl_2$

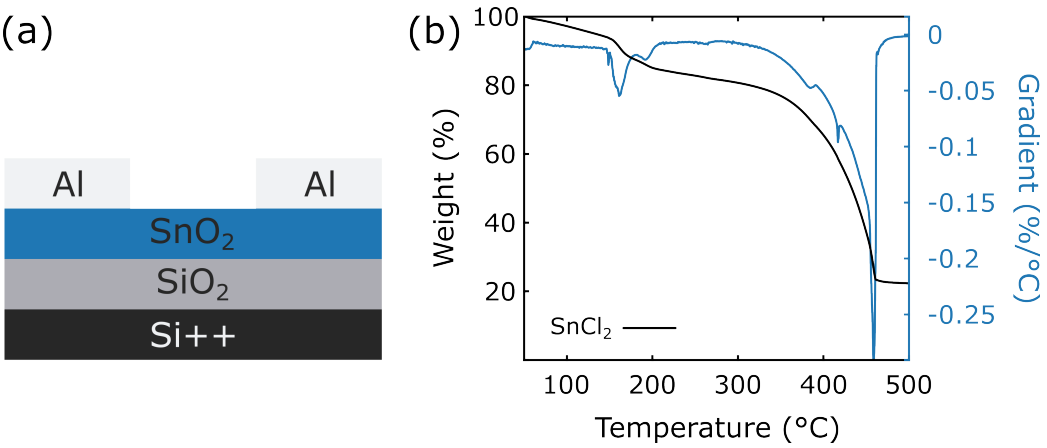

Figure 4.1: (a) Device schematic. (b) TGA curve for $SnCl_2$ powder with the first derivative.

precursor described in Chapter 3.2. The result obtained from the TGA of $SnCl_2$ and calculated first derivative plotted in Figure 4.1(b) identified the temperatures at which the films were treated following deposition, and the details behind these solution-processing techniques were provided in Chapter 3.9.1. Figure 4.1(b) shows a two-step thermal degradation process in which the $SnCl_2$ precursor had lost 9 % and 60 % of its total weight at around 160 °C and 457 °C, respectively. The onset, peak and endset temperatures of the first process occurred at 145 °C, 160 °C and 210 °C. This was likely attributed to the desorption and removal of moisture, as it is well known that $SnCl_2$ is hygroscopic. [1] The second process revealed a phase transition from $SnCl_2$ to SnO_2 between 277.1 °C and 486.4 °C with the maximum derivative weight loss at 456.9 °C. No further weight loss was recorded after 490 °C, which suggests that the hydrolysis and condensation reactions were complete. The remaining mass was calculated as just over 20 %, which was significantly lower than the expected value, given that the molar mass of SnO_2 is approximately 79.5 % of $SnCl_2$. This discrepancy is consistent with previous observations by Zhao *et al.* and is likely due to loss of volatiles containing Sn. [1] Previous studies have also reported that low treatment temperatures, such as 250 °C, result in electronically inactive TFTs due to incomplete decomposition of the metal chloride precursor, leaving residual impurities that inhibit the formation of a continuous metal oxide lattice. [2] Furthermore, the thermal

processing temperature was limited to 500 °C by the hot plate used in this study. Therefore, SnO_2 films were treated at 350 °C and 450 °C to ensure sufficient thermal decomposition while avoiding the need for a furnace. The spin-coating parameters were maintained at 5000 rpm for 30 s to ensure long-range film homogeneity.

The effect of annealing SnO_2 films at increasing temperatures was assessed using AFM. The AFM scans were performed in 1 µm by 1 µm regions to ensure that the features on the surface of the thin films could be resolved and evaluate the long-range homogeneity of the TFTs. Figure 4.2 shows clear differences in surface morphology. The AFM image of the sample treated at 350 °C (Figure 4.2(a)) displays a smooth film with surface roughness comparable to the substrate (0.340 nm), while, the sample treated at 450 °C shows increased surface roughness (1.28 nm) as a result of small crystallites dispersed on the surface (Figure 4.2(b)).

Considering now their crystalline properties, Figure 4.3 shows the XRD measurements of both films. XRD indicates that the film treated at 350 °C was amorphous as the shape of the plot was broad with no sharp diffraction peaks assignable to a crystalline phase, which concurred with AFM analysis. The peak at $2\theta = 33°$ was attributed to reflections related to the Si substrate (dashed green lines). [3] Conversely, the film treated at 450 °C shows two small halos at $2\theta = 26.6°$ and 33.9° ascribed to the (110) and (101) crystalline phases of SnO_2, respectively. [4] It was also inferred that this film was thicker

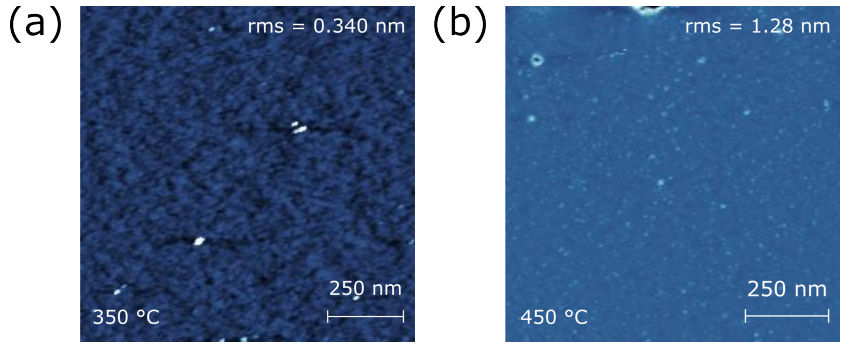

Figure 4.2: AFM images (1 µm^2 scan area) of SnO_2 films treated at (a) $T = 350$ °C and (b) $T = 450$ °C with calculated rms surface roughness.

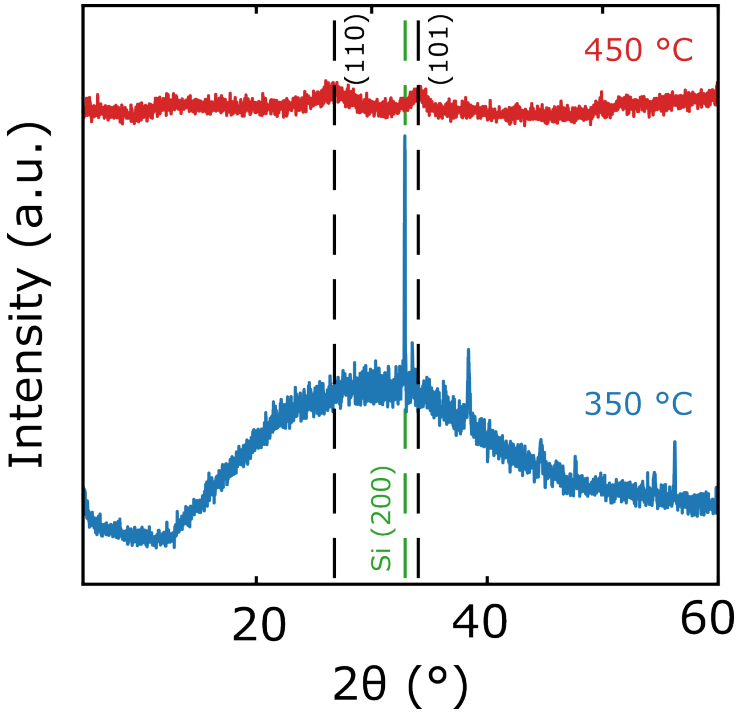

Figure 4.3: XRD measurements for $2\theta = 10°$ to $60°$.

than that treated at 350 °C as the Si (200) peak was no longer visible.

4.2.2 Electrical Properties of SnO_2 TFTs

Having previously studied the morphological and structural behaviour of the SnO_2 films treated at 350 °C and 450 °C, their electronic functionality was tested. The employment of a staggered bottom-gate transistor architecture helped to minimise contact resistance as the source-drain electrodes were deposited directly on top of the metal oxide. The key metrics used in this work to evaluate the performance of TFTs were $I_{ds[max]}$, μ_{eff}, V_{th} and $I_{on/off}$, described in Chapters 2 and 3.10. Source-drain electrode geometry was varied from $L = 80\,\mu m$ to $120\,\mu m$ and $W = 1\,mm$ to assess the impact of channel resistance on these parameters. μ_{eff} and V_{th} were extracted using Equations 3.10.3–3.10.6, from the I_{ds} against V_{gs} transfer characteristics presented in Figure 4.4.

Figure 4.4(a) shows that $I_{ds[max]}$, attained by SnO_2 TFTs treated at 350 °C, halved with increasing L – from 0.04 mA at $L = 80\,\mu m$ to 0.02 mA at $L = 120\,\mu m$. Simultaneously, V_{th} shifted towards more positive bias, from

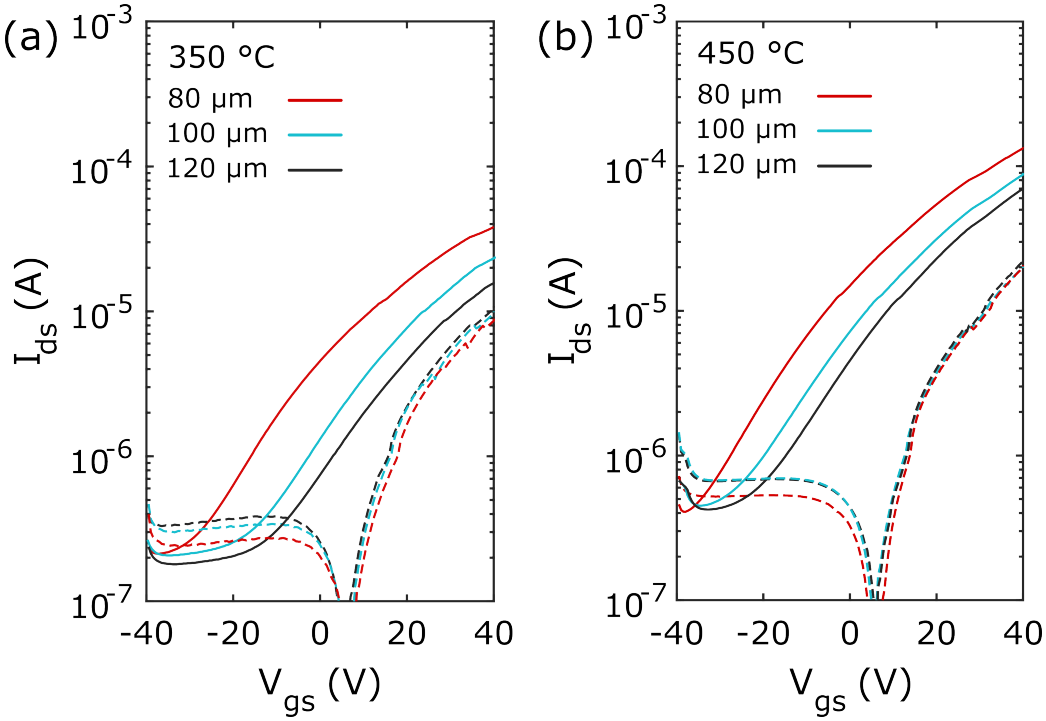

Figure 4.4: Transfer characteristics in the saturation regime at $V_{ds} = 40$ V, $V_{gs} = -40$ V to 40 V for the SnO_2 TFTs thermally treated at (a) 350 °C and (b) 450 °C with I_{gs} (dashed lines). The red, cyan and black lines correspond to $L = 80$ µm, 100 µm and 120 µm, respectively.

−19.0 V to −8.36 V, which resulted in a flattened $I_{ds[min]}$ response. In the ideal case, V_{th} is independent of channel geometry (see Equation 3.10.3). Therefore, the observed shift in V_{th} was inferred to originate from increasing channel resistance with L. [5] The extracted effective mobilities listed in Table 4.1 accounted for these non-idealities and showed minimal variation with L – $\mu_{eff} = 0.0797 \pm 0.0063\,cm^2\,V^{-1}\,s^{-1}$ and $0.292 \pm 0.024\,cm^2\,V^{-1}\,s^{-1}$ for the TFTs treated at 350 °C and 450 °C, respectively.

The SnO_2 TFT treated at 450 °C showed a similar trend, with $I_{ds[max]}$ decreasing from 0.13 mA to 0.07 mA as L increased from 80 µm to 120 µm (see Figure 4.4(b)). V_{th} again shifted towards more positive bias from −18.6 V to −11.8 V. For all L, both V_{th} and $I_{ds[max]}$ were higher in the 450 °C TFT, indicating enhanced conductivity due to increased crystalline size and a higher proportion of Sn^{4+} ions. The Sn^{2+} from the $SnCl_2$ precursor likely oxidised to Sn^{4+} in the SnO_2 films during thermal treatment in air, with Sn^{4+} being the primary contributor to n-type conduction. [6,7] The device treated

Table 4.1: $I_{on/off}$, μ_{eff}, $I_{ds[max]}$ and V_{th} of SnO_2 TFTs.

T (°C)	L (µm)	μ_{eff} ($cm^2\,V^{-1}\,s^{-1}$)	$I_{on/off}$	$I_{ds[max]}$ (A)	V_{th} (V)
350	80	0.0685	10^2	3.83×10^{-5}	-19.0
	100	0.0902	10^2	2.36×10^{-5}	-10.4
	120	0.0802	10^2	1.59×10^{-5}	-8.36
450	80	0.246	10^2	1.33×10^{-4}	-18.6
	100	0.301	10^2	8.97×10^{-5}	-14.2
	120	0.329	10^2	7.17×10^{-5}	-11.8

at 450 °C showed significantly better electronic performance, with μ_{eff} more than three times higher than that of the 350 °C-treated device at $L = 80$ µm. The extracted electronic parameters are summarised in Table 4.1.

The sol-gel process is a solution preparation technique based on the hydrolysis and condensation of molecular precursors such as metal chlorides. It is well-known that these reactions are very fast and residual organic species such as Cl^- ligands are suppressed during high temperature thermal treatment. [8] The previously discussed TGA result shows that the oxidation of SnO_2 was incomplete at 350 °C, as the calculated weight loss between 350 °C and 450 °C was 40.6 %. During this interval, the slope of the TGA curve increased. Therefore, it is inferred that the suppression of residual chloride species and surface crystallisation, as evidenced by AFM and XRD analyses, during the phase transitions of the precursor solution could have led to the remarkable enhancement of device performance with increasing temperature from 350 °C to 450 °C.

Finally, the I_{ds} versus V_{ds} output characteristics plotted in Figure 4.5 further demonstrate non-ideal behaviour. Both TFTs exhibited a rightward shift from the origin ($V_{gs}, V_{ds} = 0$ V) with increasing V_{gs}, likely due to elevated I_{gs}, particularly at low V_{gs}. This may have originated from (i) leakage through the gate dielectric, (ii) parasitic leakage outside the channel region, (iii) contributions from minority carriers, and (iv) increased channel resistance. [9] As shown in Figure 4.4, I_{gs} exceeded I_{ds} at $V_{gs} < V_{th}$, suggesting that fewer charges were able to accumulate at the semiconductor–dielectric

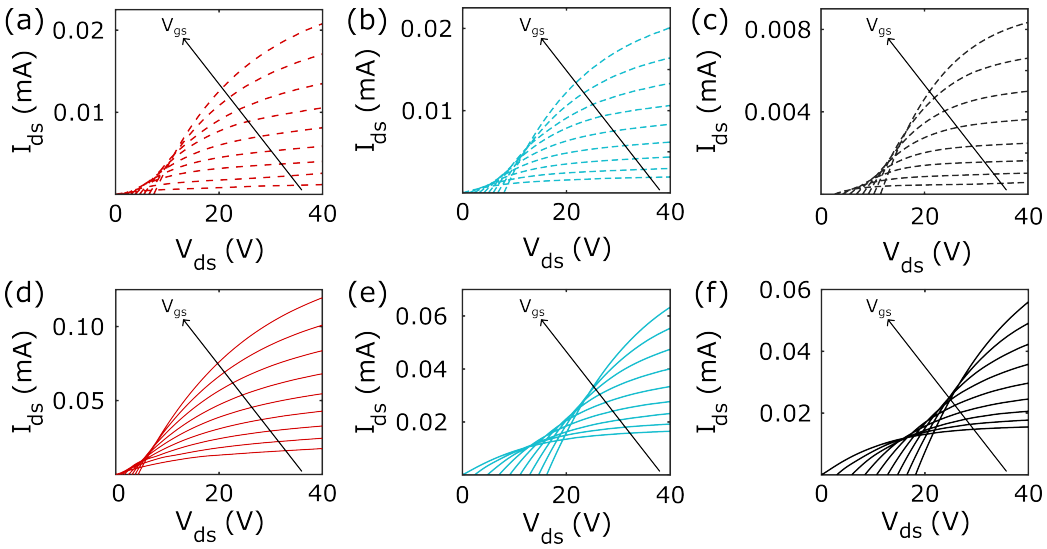

Figure 4.5: Output characteristics of SnO_2 TFTs thermally treated at (a)-(c) 350 °C (dashed lines) and (d)-(f) 450 °C (solid lines), measured at V_{gs} = 0 V to 40 V in 5 V steps. Channel lengths: (a), (d) L = 80 µm; (b), (e) L = 100 µm; (c), (f) L = 120 µm.

interface and contribute to the measured I_{ds}. Longer channels may have also exacerbated differences in morphology and trap density.

These key performance parameters were extracted using a gated two-probe (2P) method, which relies on the gradual channel approximation and assumes that both V_{th} and μ remain constant. However, in solution-processed systems, these parameters may vary with V_{gs} and L due to non-idealities, which may compromise the method's accuracy. Gated four-point probe (4PP) measurements could be employed to extract V_{th} and μ more reliably – two additional voltage-sensing electrodes are used to probe the potential drop along the channel. This approach is proposed as part of future work in Chapter 7.3.

4.2.3 Chemiresistive Properties of SnO_2 TFTs

To correlate these differences with their chemiresistive sensor response in ambient conditions, both TFTs were exposed to acetone vapour as described in Chapter 3.10.4. These experiments were conducted in a maintained clean-room environment under controlled conditions (Class 1000, RH = 45.5 %,

T = 19.2 °C) in the air i.e., not inside a N_2 glovebox. Most importantly, their open channel configuration permitted the adsorption and desorption of vapour on the surface. The effect of source-drain electrode geometry on their electrical and chemiresistive properties was explored to deepen the understanding of the sensitivity obtained. Changes in I_{ds} were monitored from $V_{gs} = -40$ V to 40 V and their transfer characteristics are shown in Figure 4.6.

Figure 4.6(a) shows that V_{th} and $I_{ds[max]}$ of the TFT treated at 350 °C increased after exposure to acetone vapour, which suggested a decrease in the electrical resistance of the film during adsorption of the vapour on the surface. The transistor did not fully switch off within the V_{gs} sweep (−40 V to 40 V), which led to a reduction in $I_{on/off}$ by over two orders of magnitude, as I_{off} and I_{on} were taken at the limits of the sweep. The $I_{ds[max]}$ achieved by this TFT increased by two orders of magnitude from 0.04 mA to 1.62 mA after exposure for $L = 80$ µm. As it can be observed, the recovery of the device (dashed grey lines) with heat treatment for 1 h was almost complete after desorption of acetone vapour on the surface, since all of the metrics returned to values close to those prior to exposure (see Table 4.2). There

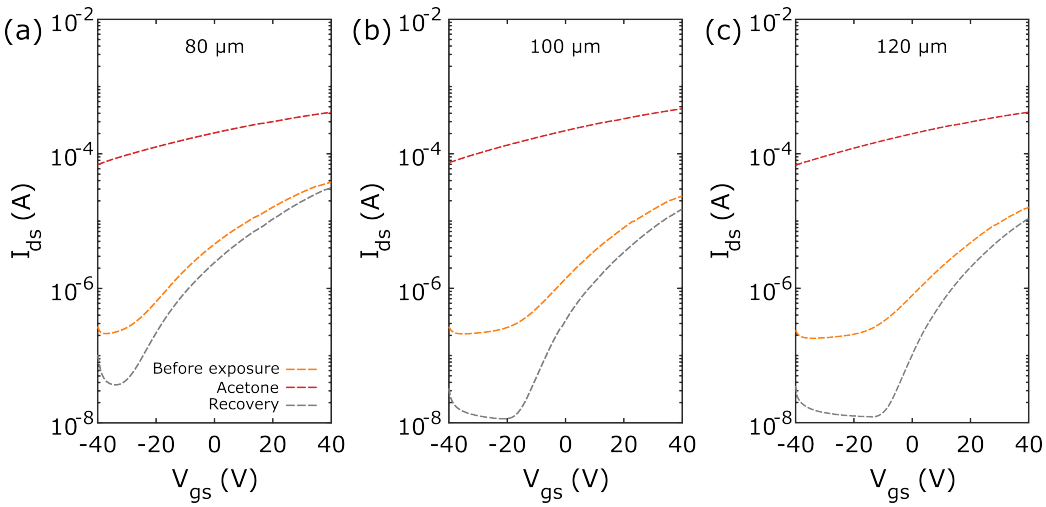

Figure 4.6: Transfer characteristics in the saturation regime at $V_{ds} = 40$ V, $V_{gs} = -40$ V to 40 V for the SnO_2 TFTs thermally treated at 350 °C following exposure to acetone vapour and recovery in air at $L =$ (a) 80 µm, (b) 100 µm and (c) 120 µm.

was negligible difference in μ_{eff} before exposure ($0.069\,cm^2\,V^{-1}\,s^{-1}$) and after recovery ($0.068\,cm^2\,V^{-1}\,s^{-1}$), while $I_{on/off}$ was maintained at 10^2. However, V_{th} shifted to positive bias after recovery from $-19.0\,V$ to $-12.8\,V$. SnO_2-based films are well known to contain oxygen-related defects that provide additional charge carriers, therefore, these defects could have been filled by free oxygen due to the dynamic energy of atoms when the temperature was elevated, which caused the aforementioned V_{th} shift to $V_{gs} = 0$. [10] At $L = 100\,\mu m$, a similar increase in V_{th} and $I_{ds[max]}$ of the TFT treated at 350 °C was observed after exposure, from $-10.4\,V$ and $0.02\,mA$ to $-87.8\,V$ and $0.42\,mA$, respectively. This caused a reduction in $I_{on/off}$ analogous to that at $L = 80\,\mu m$, due to the increased conductivity of the channel following a redox reaction between acetone and adsorbed oxygen on the SnO_2 surface, as described in Chapter 2.3.4. $I_{ds[min]}$ was estimated as $\approx 10^{-8}$ from the recovered transfer characteristics for $L = 100\,\mu m$. This was an order of magnitude lesser than that attained by the as-prepared TFT treated at 350 °C ($\approx 10^{-7}$). V_{th} also moved closer to $V_{gs} = 0$ from $-10.4\,V$ to $-3.87\,V$. These metrics suggest that oxygen readsorbed to the film surface and its resistance increased after recovery. Thirdly, Figure 4.6(c) shows that the transfer characteristics recorded for $L = 120\,\mu m$, after the TFT treated at 350 °C was exposed to acetone, were comparable to that plotted for $L = 80\,\mu m$ and $100\,\mu m$. Instead, changes in L influenced the recovery of I_{ds}, as $V_{th} \approx 0\,V$ for $L = 120\,\mu m$.

Moving on to the TFT treated at 450 °C, V_{th} increased after exposure by over $100\,V$ to $\approx -140\,V$, which caused a reduction in $I_{on/off}$ by almost three orders of magnitude at $L = 80\,\mu m$, in comparison with the as-prepared TFT. Figures 4.7(a)-(c) additionally show that the transfer characteristics obtained for this TFT were almost identical after exposure, measured within the high-voltage sweep for V_{gs}, as L increased from $80\,\mu m$ to $120\,\mu m$. For all L, $I_{ds[max]} > 1\,mA$. After recovery, V_{th} returned to $5.8\,V$, $2.3\,V$ and $1.7\,V$ for $L = 80\,\mu m$, $100\,\mu m$ and $120\,\mu m$, respectively. The shift in V_{th} to $V_{gs} = 0\,V$ with increasing L was minimised. This suggests that this

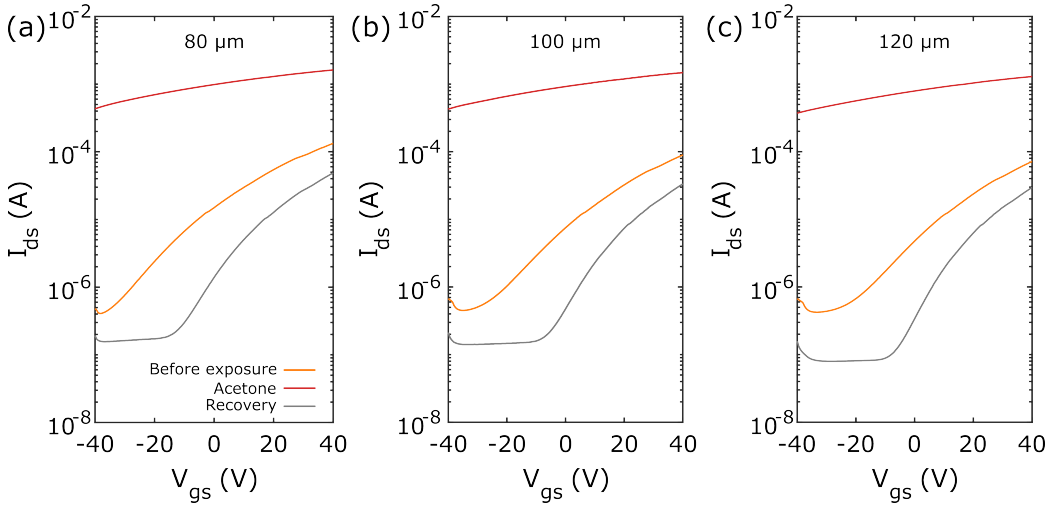

Figure 4.7: Transfer characteristics in the saturation regime at $V_{ds} = 40$ V, $V_{gs} = -40$ V to 40 V for the SnO_2 TFTs thermally treated at 450 °C following exposure to acetone vapour and recovery in air at $L =$ (a) 80 µm, (b) 100 µm and (c) 120 µm.

TFT was more responsive to acetone vapours, which was governed by the larger difference in $I_{on/off}$. Therefore, the difference in the channel resistance following the redox reaction given in Equations 2.3.87-2.3.88 had a greater impact on its functionality versus increased L. The electronic parameters for the as-prepared TFTs as well as after exposure and recovery with heat treatment are summarised in Table 4.2.

The chemiresistive sensor responses of the TFTs were calculated by measuring the relative change in I_{ds} after exposure to acetone vapour (Equation 3.10.7). Changes in the position and magnitude of maximum sensitivity, S_{max}, were governed by the V_{gs} at $I_{ds[min]}$, and $I_{on/off}$ of the as-prepared TFTs, respectively. Starting with the TFT treated at 350 °C, Figure 4.8 shows that S_{max} increased from 381.2 at $V_{gs} = -33$ V to 517.5 at 22.5 V and 588.3 at −18.5 V for $L = 80$ µm, 100 µm and 120 µm, respectively. The reduction of $I_{ds[min]}$ with L (Figure 4.4, dashed black lines), discussed in §4.2.2, and the near identical transfer characteristics obtained after this TFT was exposed to acetone vapour meant that $I_{on/off}$ and hence S were maximised at $L = 120$ µm. The position of S_{max} also shifted towards positive bias, which matched well with the movement of V_{th} with increasing L of the as-prepared

Table 4.2: $I_{on/off}$, μ_{eff}, $I_{ds[max]}$ and V_{th} of SnO_2 TFTs before exposure, after exposure and recovery.

SnO_2 TFTs						
T (°C)		L (µm)	μ_{eff} ($cm^2\,V^{-1}\,s^{-1}$)	$I_{on/off}$	$I_{ds[max]}$ (A)	V_{th} [a] (V)
350	As-prepared	80	0.0685	10^2	3.83×10^{-5}	-19.0
		100	0.0902	10^2	2.36×10^{-5}	-10.4
		120	0.0802	10^2	1.59×10^{-5}	-8.36
	Acetone	80	0.153	10^0	4.15×10^{-4}	-94.6
		100	0.303	10^0	4.67×10^{-4}	-87.8
		120	0.330	10^0	4.15×10^{-4}	-89.2
	Recovery	80	0.0677	10^2	3.12×10^{-5}	-12.8
		100	0.0730	10^2	1.51×10^{-5}	-3.87
		120	0.0749	10^3	1.10×10^{-5}	-0.799
450	As-prepared	80	0.246	10^3	1.33×10^{-4}	-18.6
		100	0.301	10^2	8.97×10^{-5}	-14.2
		120	0.329	10^2	7.17×10^{-5}	-11.8
	Acetone	80	0.329	10^0	1.62×10^{-3}	-142
		100	0.443	10^0	1.48×10^{-3}	-149
		120	0.512	10^0	1.29×10^{-3}	-143
	Recovery	80	0.140	10^2	4.86×10^{-5}	-5.79
		100	0.173	10^2	3.34×10^{-5}	-2.28
		120	0.201	10^2	2.96×10^{-5}	-1.67

[a] The values of V_{th} outside the sweep range of $V_{gs} = -40\,V$ to $40\,V$ were extrapolated.

TFT treated at 350 °C. In addition, the shape around S_{max} broadened with increasing L, which suggests that $I_{ds[min]}$ of the as-prepared TFT treated at 350 °C was stable across a larger V_{gs} window within the subthreshold regime ($V_{gs} < V_{th}$).

For the TFT treated at 450 °C, S_{max} of 1130 at $V_{gs} = -37.5$ was achieved. This value decreased slightly to 1106 at $-33\,V$ and 1070 at $30\,V$ for $L =$ 80 µm, 100 µm and 120 µm, respectively. Likewise the shape around S_{max} broadened with increasing L. However, the impact of channel geometry was less noticeable for this TFT, due to the enhanced $I_{ds[max]}$ and μ_{eff} of the as-prepared devices, in contrast with those treated at lower temperature. The TFT treated at 450 °C exhibited S_{max} approximately twice that of the device treated at 350 °C. This enhancement may have been attributed to the increased crystallinity of the SnO_2 thin films annealed at the higher temper-

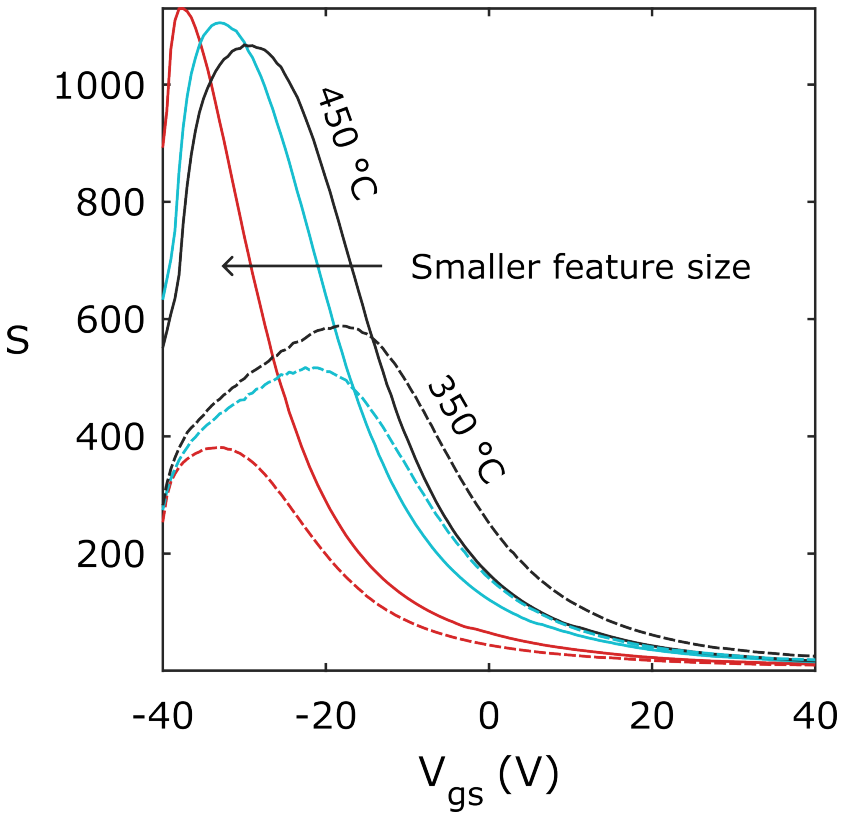

Figure 4.8: Calculated sensitivity for the SnO_2 TFTs treated at 350 °C (dashed lines) and 450 °C (solid lines). The red, cyan and black lines correspond to $L = 80\,\mu m$, $100\,\mu m$ and $120\,\mu m$, respectively.

ature, which likely promoted more effective acetone adsorption. As shown in the AFM image (Figure 4.2(b)), the surface of the SnO_2 film treated at 450 °C featured a homogeneous distribution of particulates. This rougher morphology may have provided a greater number of adsorption sites for acetone molecules, thereby enhancing the chemiresistive response.

Finally, Figure 4.9 shows the chemiresistive response at fixed V_{gs} and V_{ds} of the TFT treated at 450 °C for the smallest channel length (L =80 µm), as this was found to be the most sensitive to acetone vapours. S was calculated at V_{gs} = 15 V, 25 V and 35 V in the linear (V_{ds} = 10 V) and saturation (V_{ds} = 40 V) regimes. In both cases, S was maximised as V_{gs} approaches the V_{th} of the as-prepared TFT following exposure to acetone. In the linear regime, S decreased from 14.7 to 8.4 and 3.9 for V_{gs} = 15 V, 25 V and 35 V, respectively. A similar trend was observed in the saturation regime, with S = 26.4, 18.0 and 12.9 in order of increasing bias. The SnO_2 TFT was

clearly more sensitive to acetone vapour in the saturation regime, governed by Equation 3.10.3.

The V_{gs} at which S_{max} was achieved and the shape of the curve around this point was dictated by the position of $I_{ds[min]}$ for the as-prepared TFTs. $I_{ds[min]}$ relied on V_{th}, which shifted right towards $V_{gs} = 0$ with $L = 80\,\mu m$, $100\,\mu m$ and $120\,\mu m$. The SnO_2 TFT treated at 450 °C was more responsive to the presence of acetone vapour than the TFT treated at 350 °C across the whole bias range attributed to two factors (i) surface crystallisation, and (ii) greater difference in $I_{on/off}$ before and after exposure to acetone vapour. The former could have favoured the adsorption of acetone and the nanofeatures may have served as specific adsorption sites. Furthermore, the difference in $I_{on/off}$ at the V_{gs} of S_{max} was 10^2 versus 10^3 for the TFTs treated at 350 °C and 450 °C, respectively. Recovery of I_{ds} following heat treatment

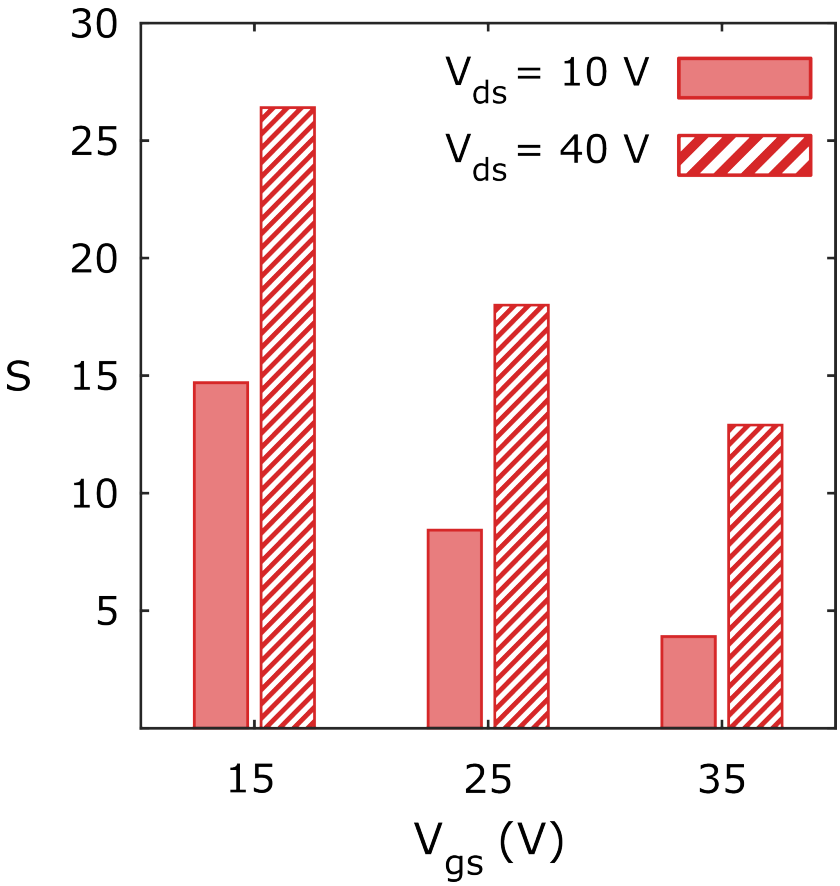

Figure 4.9: Calculated sensitivity for the TFT treated at 450 °C and $L = 80\,\mu m$ in the linear ($V_{ds} = 10\,V$) and saturation regimes ($V_{ds} = 40\,V$).

was possible due to the increased channel resistance caused by re-exposure to the air and desorption of acetone. The following study will build upon these findings by engineering the electronic functionality of metal oxide TFTs prepared by depositing alternating layers of ZTO and ZnO to improve upon that achieved by the single layer TFTs presented thus far.

4.3 Multilayer ZTO-based TFTs

4.3.1 Thermal Treatment of ZTO-ZTO TFTs

The thermal treatment of ZTO-ZTO bilayer films was first assessed by annealing two stacked ZTO layers at increasing temperatures. Figure 4.10(a) shows a schematic of the device and Figure 4.10(b), the TGA for the $ZnCl_2$ precursor in addition to that provided for $SnCl_2$ in §4.2.1. There was a similar weight reducion of 26 % between 30 °C and 200 °C that was attributed to the desorption and removal of moisture as with $SnCl_2$. In contrast, the second stage of thermal degradation was less pronounced, as gradual changes were still observed between 420 °C and 500 °C (solid pink curve), with a total weight loss of just over 12 %, as indicated by the shallow derivative peak in Figure 4.10(c). This is consistent with previous works that report a maximum derivative weight loss at 510 °C for $ZnCl_2$. [11] Therefore, the films were treated at temperatures from 300 °C to 500 °C to assess the impact of thermal treatment on the properties of ZTO-based TFTs. The temperature of the hot plate did not exceed 500 °C to ensure that the fabrication process remained low-cost, and avoided the use of a furnace. Figure 4.11(a) presents the I_{ds} against V_{gs} transfer characteristics used to extract μ_{eff} and V_{th} (see Equations 3.10.3 –3.10.6). Source-drain geometry was fixed at $W = 1\,\text{mm}$ and $L = 80\,\mu\text{m}$. The spin-coating parameters were maintained at 5000 rpm for 30 s to provide a one-to-one comparison between the multilayer and single layer TFTs.

To begin, the first and second ZTO depositions were treated at 300 °C and 400 °C in-line with previous works. [12] The thermal treatment of each

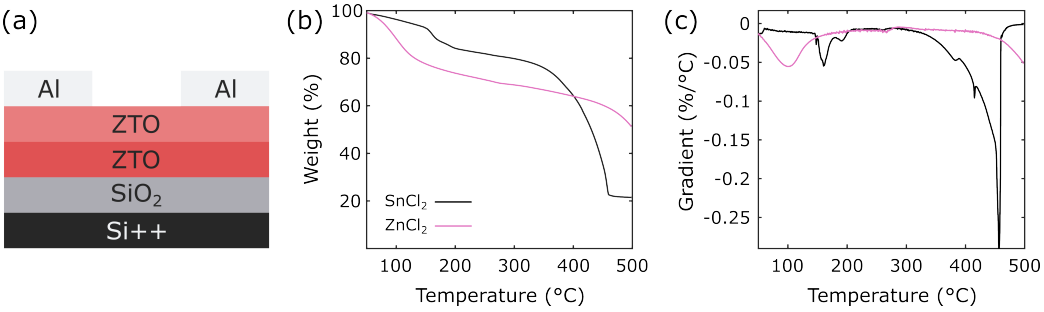

Figure 4.10: (a) Device schematic of ZTO-ZTO TFT. (b) TGA curves for the $SnCl_2$ and $ZnCl_2$ powders and (c) calculated deriative.

layer was then incremented by steps of 50 °C up to 500 °C. Figure 4.11(a) shows that $I_{on/off}$ was largely determined by the position of V_{th}, which shifted gradually towards positive bias with increasing temperature – from −45.4 V for the TFT treated at 300 °C – 400 °C (denoted as 300 – 400 in Table 4.3) to a near-zero value of 2.20 V at 500 °C. This shift led to a drastic enhancement in $I_{on/off}$ from 10^2 to 10^7, suggesting that the switching speed and energy efficiency of the TFT treated at 500 °C far surpassed those treated at lower temperatures. The output characteristics plotted in Figures 4.11(b)–(c) exhibit a sharp turn-on at $V_{ds}, V_{gs} = 0$ V, with both the 450 °C and 500 °C TFTs achieving comparable $I_{ds[\max]} \approx 2$ mA. However, despite the 450 °C device demonstrating $I_{on/off} > 10^6$ and efficient electron transport ($\mu_{eff} = 9\,\mathrm{cm^2\,V^{-1}\,s^{-1}}$), its $V_{th} = -13.6$ V remained too negative to enable low-power operation (< 5 V). In contrast, the TFT treated at 500 °C combined excellent switching behaviour, high on-current, and a near-zero V_{th} – making it the most promising candidate for energy-efficient applications.

Table 4.3: Electrical properties obtained from ZTO-ZTO TFTs treated at temperatures from 300 °C to 500 °C.

Temperature (°C)	μ ($\mathrm{cm^2\,V^{-1}\,s^{-1}}$)	μ_{eff} ($\mathrm{cm^2\,V^{-1}\,s^{-1}}$)	$I_{on/off}$	V_{th} (V)
300 – 400	9.42	9.33	10^2	-45.4
350 – 450	10.6	10.5	10^4	-27.8
450	9.39	9.00	10^6	-13.6
500	10.2	9.49	10^7	2.20

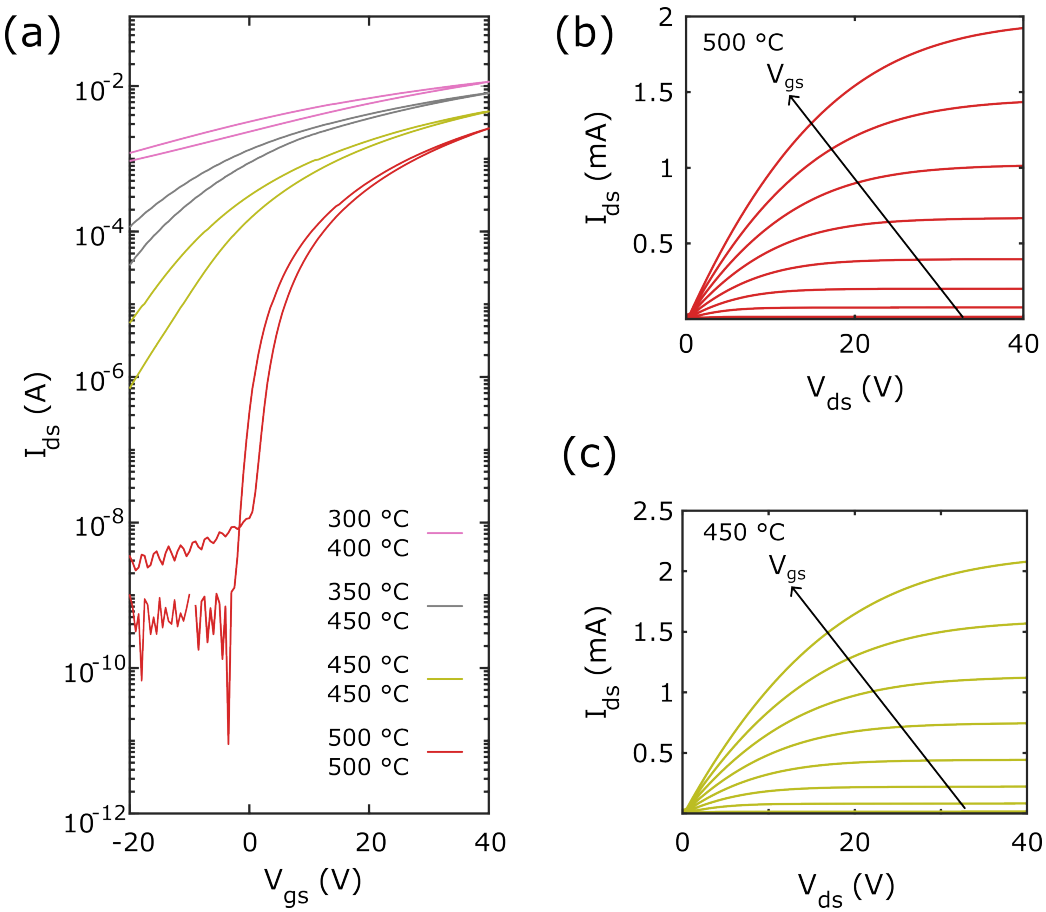

Figure 4.11: (a) Transfer characteristics in the saturation regime at $V_{ds} = 40\,\text{V}, V_{gs} = -20\,\text{V}$ to $40\,\text{V}$ for the ZTO-ZTO TFTs treated at temperatures from 300 °C to 500 °C. Output characteristics at $V_{ds}, V_{gs} = 0\,\text{V}$ to $40\,\text{V}$ and for ZTO-ZTO TFTs treated at (b) 500 °C and (c) 450 °C.

4.3.2 Impact of Precursor Concentration

To highlight the benefit of controlling film thickness and morphology via the sequential spin-casting and thermal treatment of metal oxide layers, the electronic performance of a single layer ZTO TFT prepared from a precursor solution with double the concentration (0.3 M) was compared against the stacked ZTO-ZTO TFT analysed in §4.3.1. This would equate to the same amount of metal oxide content as the two stacked ZTO layers prepared from a concentration of 0.15 M. The single layer film was treated at the optimal temperature of 500 °C and a summary of the electrical parameters is given in Table 4.4.

It is well-known that the electrical properties of solution-processed oxide

TFTs prepared from metal chlorides, specifically μ_{eff} and V_{th}, are strongly affected by the precursor and solvent choices. More precisely, the addition of more material is known to create large aggregates during the spin-coating procedure. In turn, this leads to a more heterogeneous morphology, which increases the concentration of trap-related defects. [13] Table 4.4 confirms that the ZTO TFT ($C = 0.3\,\mathrm{M}$) exhibited limited electron transport in comparison to the bilayer ZTO-ZTO material system as $\mu_{eff} = 0.16\,\mathrm{cm^2\,V^{-1}\,s^{-1}}$ and $9.49\,\mathrm{cm^2\,V^{-1}\,s^{-1}}$, respectively. The mobility difference can be related to the average time between scattering events using Equation 2.2.33:

$$\frac{\mu_1}{\mu_2} = \frac{\tau_1}{\tau_2} = \frac{10.2}{0.172} \approx 59.3, \tag{4.3.1}$$

indicating that carriers in the ZTO-ZTO TFT experience scattering approximately sixty times less frequently than in the ZTO TFT. The large hysteresis observed in Figure 4.12(a) for the ZTO TFT caused a V_{th} shift from 4.84 V (forward) to 8.55 V (reverse). The corresponding interface trap density was estimated using Equation 2.3.79 and $C_i = 15\,\mathrm{nF\,cm^{-2}}$, giving $N_{trap} \approx 3.48 \times 10^{11}\,\mathrm{cm^{-2}}$. This high trap density likely contributed to the reduced mobility and electrical instability, which suggests that the resulting thicker film was more defective and possessed a non-uniform conductivity. In contrast, the bilayer ZTO-ZTO TFT demonstrated excellent stability and a smaller V_{th} shift – from 2.20 V to 3.84 V – with a lower $N_{\mathrm{trap}} \approx 1.54 \times 10^{11}\,\mathrm{cm^{-2}}$. The improved performance is attributed to the compaction and passivation resulting from the second layer's deposition and thermal treatment, which likely enhanced film uniformity and promoted efficient charge percolation pathways between the source and drain electrodes.

Table 4.4: Electrical properties obtained from ZTO-based TFTs treated at 500 °C and prepared from 0.15 M and 0.3 M precursor solutions.

Device	C (M)	μ ($\mathrm{cm^2\,V^{-1}\,s^{-1}}$)	μ_{eff} ($\mathrm{cm^2\,V^{-1}\,s^{-1}}$)	$I_{on/off}$	V_{th} (V)
ZTO-ZTO	0.15	10.2	9.49	10^7	2.20
ZTO	0.3	0.172	0.159	10^6	4.84

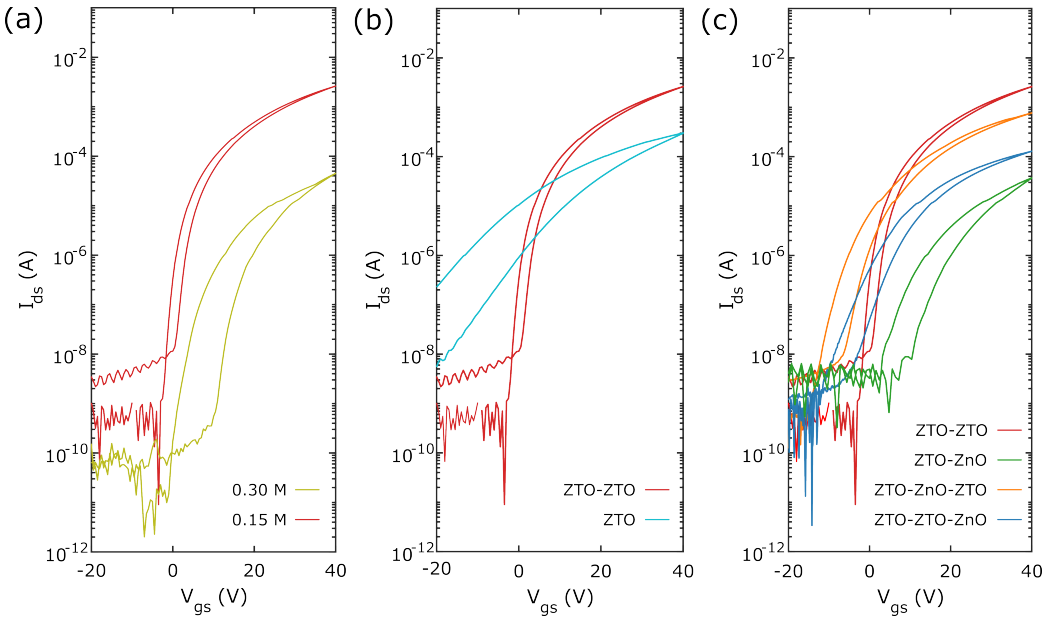

Figure 4.12: Transfer characteristics in the saturation regime at $V_{ds} = 40\,\text{V}$, $V_{gs} = -20\,\text{V}$ to $40\,\text{V}$ for the (a) ZTO-based TFTs prepared from 0.15 M and 0.30 M sol-gels, (b) ZTO and ZTO-ZTO TFTs & (c) bilayer and trilayer TFTs treated at 500 °C.

It is worth noting that the estimate for N_{trap} did not account for other factors that can degrade mobility, such as deeper, slow-release traps in the bulk or variations in film morphology.

4.3.3 Layering of ZnO-based TFTs

Having carefully established the correct processing conditions for the best performing ZTO-based TFTs, the electrical performance of monolayer TFTs prepared from a precursor solution with a concentration of 0.15 M and treated at 500 °C was also compared against the benchmark ZTO-ZTO TFT. A typical transfer characteristic is shown in Figure 4.12(b). Electronically, the ZTO TFT performed poorly owing to large hysteresis in the $I_{ds} - V_{gs}$ measurement, which led to a large V_{th} shift from $-7.44\,\text{V}$ to $2.31\,\text{V}$ for the forward and backward sweeps of V_{gs}, respectively. Electron transport was also adversely affected as μ_{eff} decreased to $1\,\text{cm}^2\,\text{V}^{-1}\,\text{s}^{-1}$, which was just under ten-fold lower than that listed previously for the ZTO-ZTO TFT.

Given that the bilayer ZTO-ZTO exhibited a dramatic improvement over

the monolayer ZTO TFT, a multilayer approach was explored by intercalating a ZnO layer to construct bilayer and trilayer TFTs. ZnO was chosen due to its well-documented ability to enhance electron injection in other solution-processed devices, particularly when ZnO nanostructures are grown on the surface of ZTO. [12] The resulting multilayers were treated at 500 °C following the previously discussed results, and their transfer characteristics are presented in Figure 4.12(c). The electrical properties of the ZnO-capped TFTs were inferior to those of the ZTO-capped TFTs. The ZnO-capped bilayer TFT exhibited significant hysteresis and poor carrier mobility ($\mu_{eff} = 0.14\,\mathrm{cm^2\,V^{-1}\,s^{-1}}$). Furthermore, as shown in Table 4.5, its $I_{on/off} < 10^4$, dropping by a factor of 10^3 compared to the ZTO-capped bilayer TFT. These results suggest that the ZnO capping layer had a detrimental impact on electron transport and switching behaviour in bilayer TFTs.

A similar trend was observed in trilayer TFTs, where the ZnO-capped device demonstrated a mobility of $\mu_{eff} = 0.42\,\mathrm{cm^2\,V^{-1}\,s^{-1}}$ – significantly lower than the $2.32\,\mathrm{cm^2\,V^{-1}\,s^{-1}}$ measured for the ZTO-capped counterpart. This decline in performance confirmed that the final ZnO deposition hindered electron transport between the source-drain electrodes, leading to reduced mobility and degraded switching properties.

4.3.4 Surface Properties of ZTO-based TFTs

To understand the physical basis of the enhanced electronic functionality of ZTO-capped TFTs described in §4.3, a detailed morphological investigation

Table 4.5: Electrical properties obtained from monolayer and multilayer metal oxide TFTs treated at 500 °C.

Device	μ ($\mathrm{cm^2\,V^{-1}\,s^{-1}}$)	μ_{eff} ($\mathrm{cm^2\,V^{-1}\,s^{-1}}$)	$I_{on/off}$	V_{th} (V)
ZTO	0.775	0.741	10^6	-7.44
ZTO-ZnO	0.148	0.135	10^4	-5.36
ZTO-ZTO	10.2	9.49	10^7	2.20
ZTO-ZnO-ZTO	2.55	2.32	10^6	-1.74
ZTO-ZTO-ZnO	0.458	0.417	10^5	-0.91

of the multilayer TFTs was undertaken. The effect of inserting a ZnO layer on the surface properties of the ZTO-based TFTs was investigated using AFM. First, the AFM images of the monolayer and bilayer material systems are shown in Figure 4.13. The ZTO-capped films displayed a very smooth surface morphology with roughness values of 0.37 nm and 0.66 nm for the monolayer and bilayer TFTs, respectively, which were comparable to that of the Si substrates (< 5 Å). Meanwhile, the ZnO-capped bilayer TFT clearly showed crystalline features that contributed to a rougher surface (rms = 8.13 nm). [12] To further investigate the differences in surface morphology between the ZnO- and ZTO-capped TFTs, SEM and AFM analyses were carried out on the trilayer devices.

The AFM image shown in Figure 4.14(a) of the ZTO-capped trilayer TFT presents a rather smooth film consistent with what was observed previously for the monolayer and bilayer ZTO-capped TFTs, with an identical surface roughness of 0.66 nm. This morphology was confirmed over a larger area by the SEM image of the same TFT in Figure 4.14(b). In contrast, the ZnO-capped trilayer TFT (Figure 4.14(c)) exhibited increased surface roughness (rms = 10.2 nm) due to ZnO nanoparticles grown on the surface, reaching sizes of up to 50 nm. These nanoparticles aggregated into larger clusters, measuring between 200 nm and 300 nm, as evidenced by the texture in the AFM image. The corresponding SEM image (Figure 4.14(d)) revealed that there was more aggregation at lower magnification and these Zn aggregates were distributed randomly across the film. This morphological analysis sug-

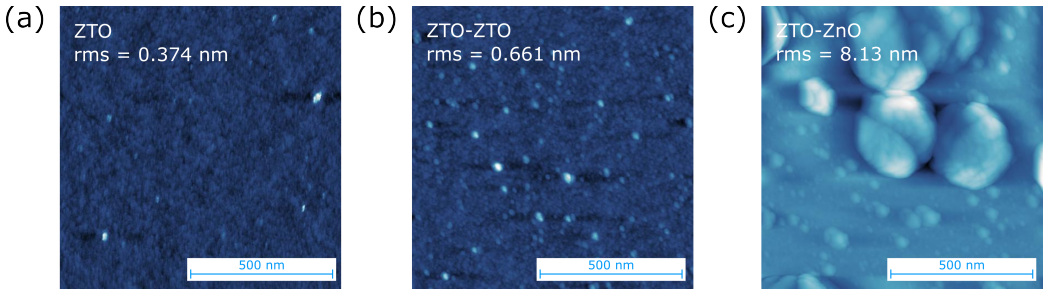

Figure 4.13: AFM images of (a) ZTO (b) ZTO-ZTO and (c) ZTO-ZnO films with calculated rms surface roughness.

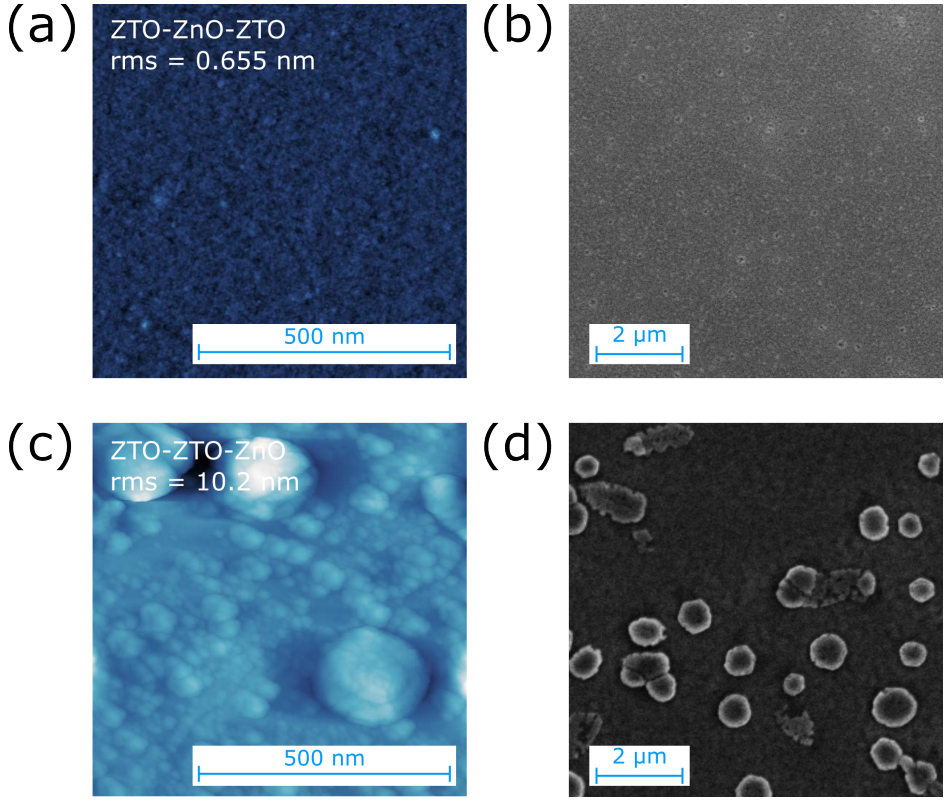

Figure 4.14: AFM images of (a) ZTO-ZnO-ZTO and (c) ZTO-ZTO-ZnO films with calculated rms surface roughness. SEM images of (b) ZTO-ZnO-ZTO and (d) ZTO-ZTO-ZnO films.

gests that the final ZTO layer may have contributed to planarizing the film surface, enabling cleaner deposition of source-drain electrodes and ultimately enhancing the electrical performance of the ZTO-capped TFTs.

Considering now the effect of inserting a ZnO layer on the crystalline properties of the ZTO-based films, XRD was carried out to confirm the amorphous nature of the ZTO-capped films and identify the crystalline features on the ZnO-capped film surface. XRD indicated that the ZTO-capped films were amorphous as they did not exhibit sharp diffraction peaks assignable to a crystalline phase (Figure 4.15). The sharp peak at $2\theta = 33°$ was attributed to reflections related to the Si substrate, as discussed in §4.2.1. These results are comparable with those of solution-processed films prepared using metal chlorides dissolved in 2-methoxyethanol at similar conditions reported in the literature. [14–18] Conversely, the ZnO-capped films showed a small halo at $2\theta \approx 34.4°$, ascribed to the hexagonal wurtzite structure of ZnO (002). [19]

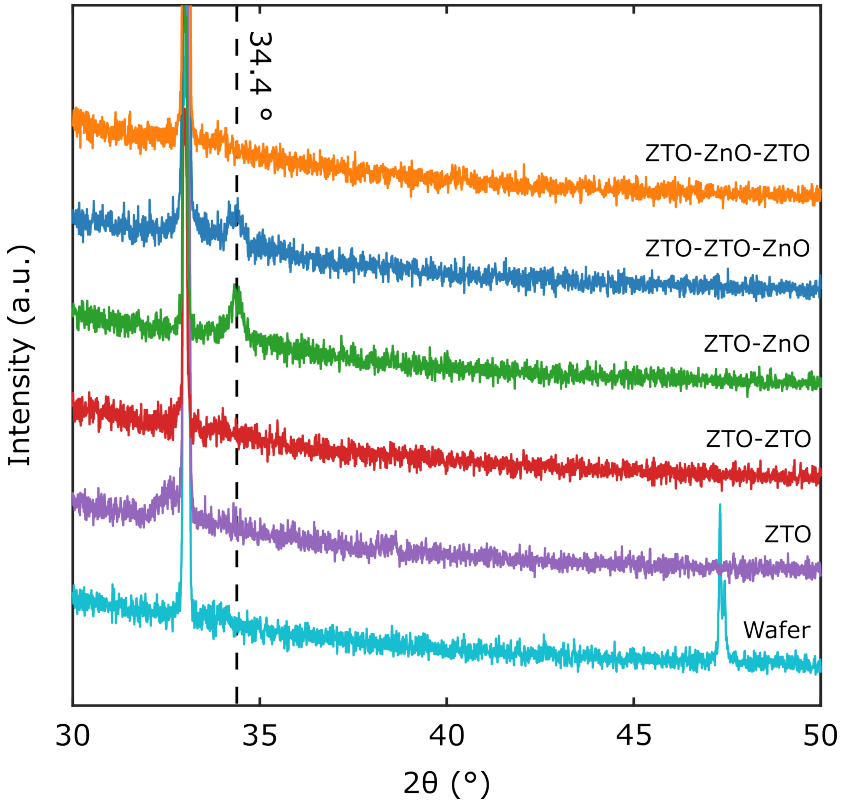

Figure 4.15: XRD measurements for $2\theta = 30°$ to $50°$.

This peak is ascribed to the as-grown and aggregated ZnO nanoparticles observed in the AFM and SEM micrographs, which were responsible for the increased surface roughness and the degradation of electrical performance in ZnO-capped TFTs inferred previously.

4.3.5 Cross-Sectional Analyses

Up until now, surface analyses of the ZTO- and ZnO-capped films showed that the worsened performance of the multilayer metal oxide TFTs can be partly attributed to the rougher active layer surface and larger particle size caused by the growth and aggregation of ZnO nanoparticles, which heavily impacted the charge transport between source-drain electrodes. However, despite these results, it was still difficult to independently identify the changes in the physical properties throughout the film responsible for the improved electrical performance of the TFTs. To confirm the presence of ZnO nanoparticles, TEM coupled with EDX was conducted to create cross-sectional im-

ages of the ZTO- and ZnO-capped trilayers shown in Figures 4.16(a)-(c) and (d)-(f), respectively.

The high-magnification TEM image (Figure 4.16(a)) of the ZTO-capped trilayer film shows a homogenous film that has a thickness between 18 nm and 20 nm over a substantial region of the TFT (Figure 4.16(b)). Complementary elemental mapping (Figure 4.16(c)) suggest that Zn and Sn components were well mixed throughout the entire film. The TEM images of the ZnO-capped trilayer film confirmed the growth of nanoparticles, composed primarily of Zn. More specifically, Figures 4.16(d)-(e) show that two of these nanoparticles, measuring 35 nm and 50 nm in diameter, respectively, aggregated and fused together in accordance with the AFM images shown previously. As previously mentioned, these nanoparticles were responsible for the small halo observed in the XRD analysis at $2\theta \approx 34.4°$, which corresponded to the (002) reflection

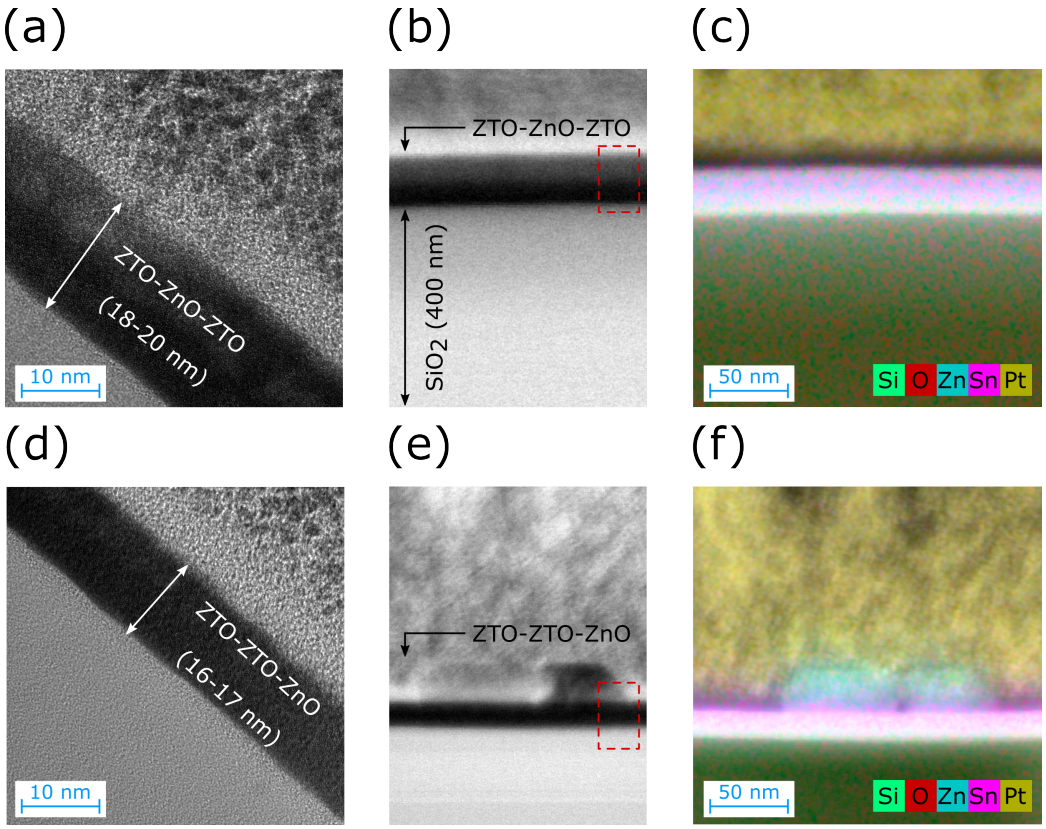

Figure 4.16: Cross-sectional analyses of the (a)-(c) ZTO-ZnO-ZTO and (d)-(f) ZTO-ZTO-ZnO films. (a), (d) High- and (b), (e) low-magnification TEM images (red dashed square). (c), (f) Elemental mapping.

of the hexagonal wurtzite ZnO structure.

Additionally, XRR results helped to correlate the growth of these ZnO nanoparticles with interface width, film thickness and density of the metal oxide systems. The reflectivity profile in Figure 4.17 shows oscillations caused by X-ray interference that were first observed by Kiessig in 1931. The onset of these fringes i.e., critical angle for total reflection, provided information on the density of the films. At higher angles, the position of the critical angle indicated denser films. The amplitude of the oscillation influenced the shape of the critical angle, which depended on the difference between the film density and Si substrate.

The period of these Kiessig fringes was related to differences in film thickness – a thicker film resulted in a shorter period. The variation in total interface width with sample depth considered both topographical roughness and chemical intermixing of the interference between layers, as discussed in Chapter 3.7.2. The oscillation decay rate and drop-off in fringe amplitude at higher angles were related to to surface or interface roughness, while the latter considered surface roughness only. [20, 21]

The sharp critical angle of the monolayer ZTO film was analogous with that of the reference substrate at $2\theta = 0.5°$, which pointed to a less dense film. The larger period of the Kiessig fringes for the monolayer compared to the ZTO-capped bilayer and trilayer systems, were well represented by the best fitting simulations (solid black lines), indicating that the monolayer was a thinner film. The position of the critical angle for the ZTO-capped films also shifted to higher angles and approached $2\theta = 1°$, which suggests an increase in density after the second and third layers were spin-coated and thermally treated. The curve shape around the critical angle broadened as additional layers were added to the ZTO-capped multilayer stacks, suggesting that the film density was not uniform throughout the bulk of the bilayer and trilayer structures. Furthermore, Kiessig fringes were observed at higher angles ($2\theta > 3.5°$), which further supported the presence of a smooth surface, as indicated by the AFM and SEM images.

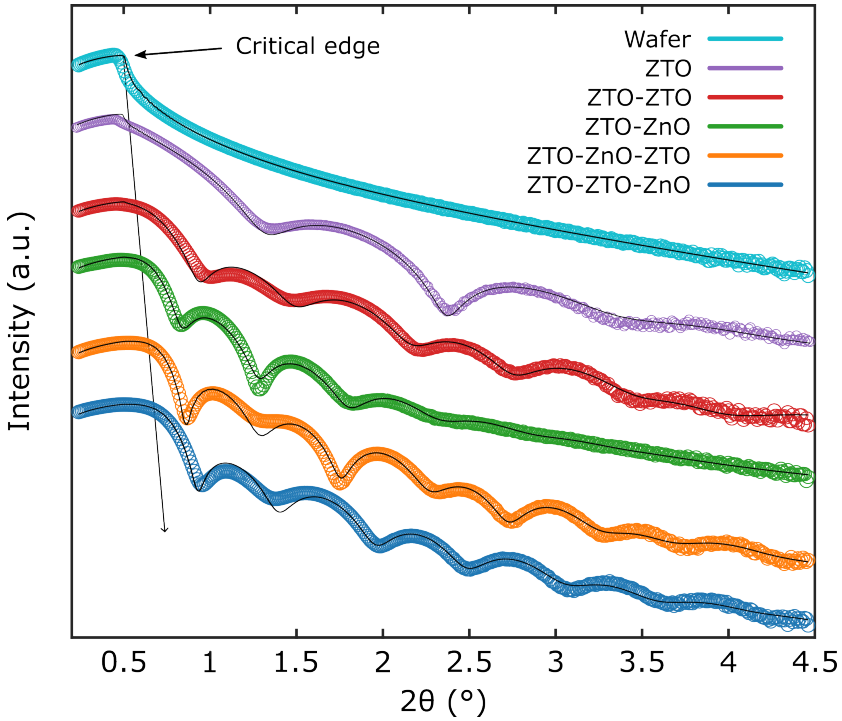

Figure 4.17: Measured (symbols) and calculated (solid black lines) XRR spectra obtained from single, bilayer and trilayer metal oxide systems.

For the ZnO-capped films, the critical angle of the ZnO-capped bilayer sample was $2\theta \approx 0.7°$. The oscillation period was short, and the amplitude decayed rapidly after $2\theta = 2°$, eventually forming a flat line – indicative of a rougher film surface and a non-uniform interface between the first ZTO and second ZnO layers. This is also consistent with the observations of ZnO nanoparticles and aggregates grown on the film surface, as seen in the microscopy analyses. The shift of the critical angle to higher values in the ZnO-capped trilayer film (darker blue circles) suggests that this system had the highest film density. However, significant density variations were observed, as evidenced by the broadening of the critical angle in this material system. Surprisingly, Kiessig fringes for the ZnO-capped trilayer film appeared at higher angles ($2\theta > 4.5°$), suggesting improved film coverage on the substrate surface compared to the ZnO-capped bilayer sample due to the addition of more material. The bilayer stack likely contained structural defects, such as pores or pin holes, resulting from volatilisation during the high-temperature annealing process. [22] These defects can easily trap

organic residues, introducing impurities into the thin-film bulk. Such impurities can weaken the lattice, ultimately degrading charge carrier mobility, as evidenced in §4.3.

A comparison of the ZTO- and ZnO-capped bilayer films indicates that they had similar densities, as the critical angle was positioned at 2θ just beyond 0.5°. Furthermore, the shorter oscillation period in the latter suggests a thicker film. The XRR results align with the AFM and SEM images of the ZTO- and ZnO-capped bilayer TFTs, as Kiessig fringes were observed up to $2\theta = 2°$ with a constant amplitude, indicating a smoother film surface due to the ZTO capping layer. In general, the ZTO- and ZnO-capped trilayer films exhibited similar XRR profiles, with oscillations observed up to $2\theta = 4°$ and roughly the same amplitude. However, the critical edge of the ZTO-capped trilayer sample was shifted to lower angles compared to the ZnO-capped system, indicating differences in film density. Additionally, the period of the Kiessig fringes for the ZnO-capped sample was longer, suggesting a thinner film. The films were prepared using identical metal chlorides and solvent, therefore, differences in the film density were predominantly caused by the addition of more material, order of deposition and final ratio of Sn to Zn (Sn/Zn). The best-fitting simulations of the XRR results were used to determine the scattering length density (SLD), which is plotted in Figure 4.18 against sample depth. From these results, the thickness of the monolayer ZTO film was estimated to be approximately 8 nm, which increased to over 15 nm for the ZTO-capped trilayer film. This is consistent with the increased periodicity of the Kiessig fringes and TEM analysis. For the monolayer ZTO film, the effective density increased from approximately $0.8\,\mathrm{re\,Å^{-3}}$ to approximately $1.15\,\mathrm{re\,Å^{-3}}$ at the substrate ($Z \approx 0\,\mathrm{nm}$). The film density remained constant before reaching the ZTO film surface, suggesting that this system primarily contained Zn or Sn.

In contrast, the ZTO-capped bilayer film exhibited a peak effective density of $1.3\,\mathrm{re\,Å^{-3}}$, followed by a clear drop of approximately $0.2\,\mathrm{re\,Å^{-3}}$ to $1.1\,\mathrm{re\,Å^{-3}}$. A similar behaviour was observed for the ZTO-capped trilayer

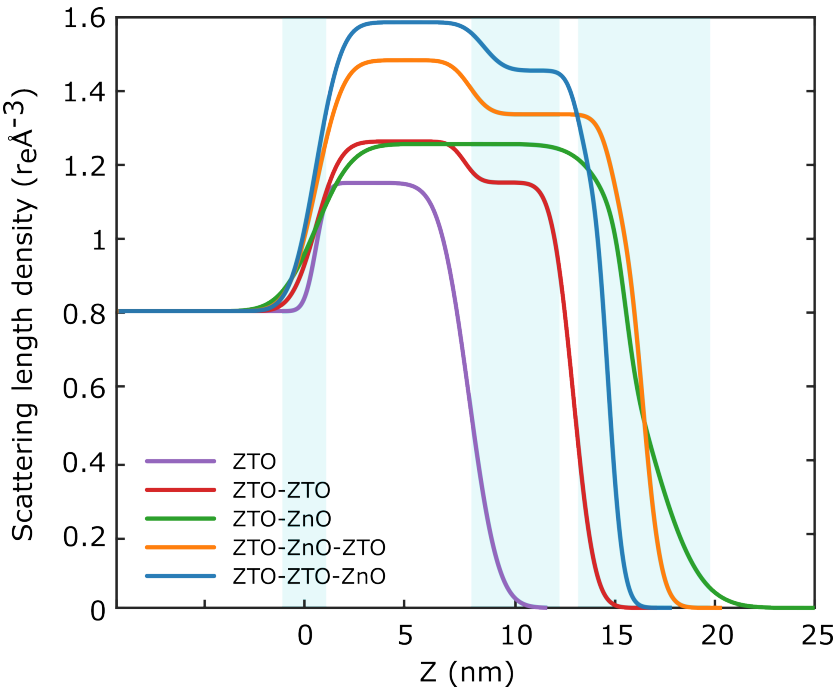

Figure 4.18: Extracted SLD versus depth profile (Z) for $2\theta = 0°$ to $4.5°$.

system, where the film depth approached 10 nm (shown by the shaded areas of Figure 4.18), in agreement with the broadening around the critical angle, from 1.5 re Å^{-3} to 1.3 re Å^{-3}. The ZTO-capped trilayer film also exhibited a higher SLD compared to the monolayer and bilayer systems, indicating a denser film due to the additional layer deposition.

Considering now the ZnO-capped films, the bilayer stack exhibited a peak SLD value of 1.3 re Å^{-3}, which remained constant before reaching the film surface at $Z > 20$ nm. The gradual and non-uniform decrease in effective density, along with Kiessig fringes appearing only at lower angles and producing a more pronounced tail ($2\theta < 2.5°$), suggested a significantly rougher and more defective surface morphology compared to the ZTO-capped bilayer film. This was attributed to the presence of ZnO nanoparticles observed in Figure 4.13(c). The ZnO-capped trilayer stack exhibited the highest SLD value of 1.6 re Å^{-3}, in agreement with the right-most position of its critical angle shown in the XRR spectrum and addition of the third layer. Unlike the ZnO-capped bilayer film, this decreased to 1.4 re Å^{-3} at just over $Z = 10$ nm. Therefore, it is inferred that the spin-coated films were not organised in a

traditional layer-by-layer heterostructure system with a single uniform interface. Instead, the first layer was compacted by the addition and thermal treatment of the second or third ZTO layer, giving rise to two distinct regions with different film densities. The ZnO-capped bilayer TFT maintained a constant film density, possibly due to the ZnO nanoparticles on the surface.

4.3.6 XPS Depth Profiling

Finally, XPS depth profiling was conducted to track the evolution of the Zn 2 $p_{3/2}$ and Sn 3 d peak intensities and assess the possible gradients or migration of either component in the TFTs. Etch cycle zero corresponded to the film surface, and the etching was considered complete when the main signals present were the Si 2 s, Si 2 p and O 1 s peaks of the substrate, from etch cycle ten to twenty depending on the thickness and surface morphology of the films. First, Figure 4.19 confirms that the intensities of the Si 2 s, Si 2 p and O 1 s components were amplified moving from etch cycle zero to twenty (see Figure 4.19(a) & (b), respectively) as the ion beam approached the surface of the substrate. Very little chlorine, which is a residue of the precursors, was present, which suggests that film treatment by thermal annealing at 500 °C was sufficient. This is supported by the low interfacial trap density calculated in §4.3.2.

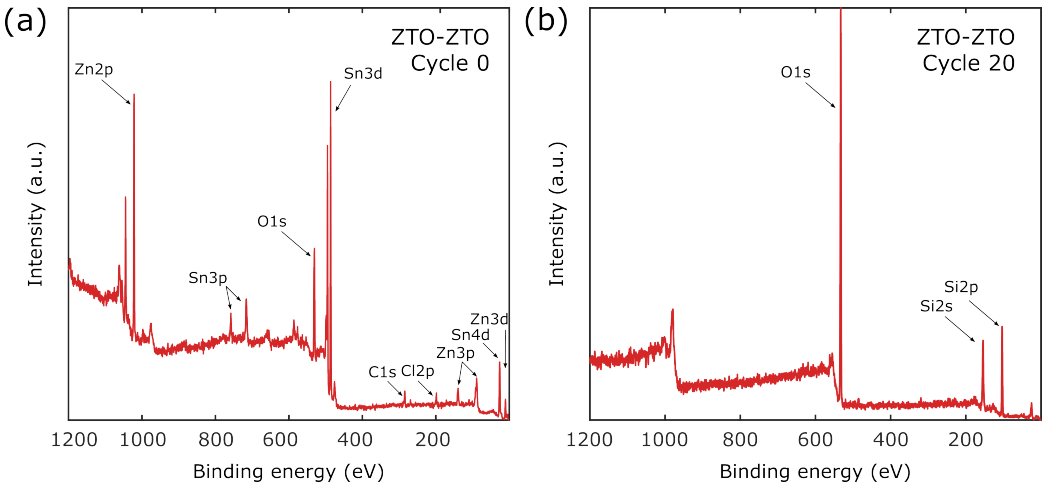

Figure 4.19: XPS wide scan of ZTO-ZTO films at etch cycles (a) zero and (b) twenty.

Starting with the ZTO-capped bilayer system, this TFT comprised a film homogeneous in thickness and Sn/Zn distribution on the surface of the substrate, as the Zn 2 $p_{3/2}$ and Sn 3 d signals diminished after the eighth etch cycle (see Figure 4.20(a)). The Zn 2 $p_{3/2}$ and Sn 3 d signals reached a plateau at maximum intensity around etch cycle five, aligning with the two distinct regions of film density observed in XRR analysis. Figure 4.20(b) shows that the ZTO-capped trilayer TFT exhibited a similar plateau at maximum intensity; however, the Zn 2 $p_{3/2}$ and Sn 3 d signal intensities began to decline slightly later, following the eleventh etch cycle, due to the deposition of the third layer that resulted in a denser film, as shown in the XRR results of Figure 4.18.

Secondly, there were clear differences in Zn and Sn composition for the

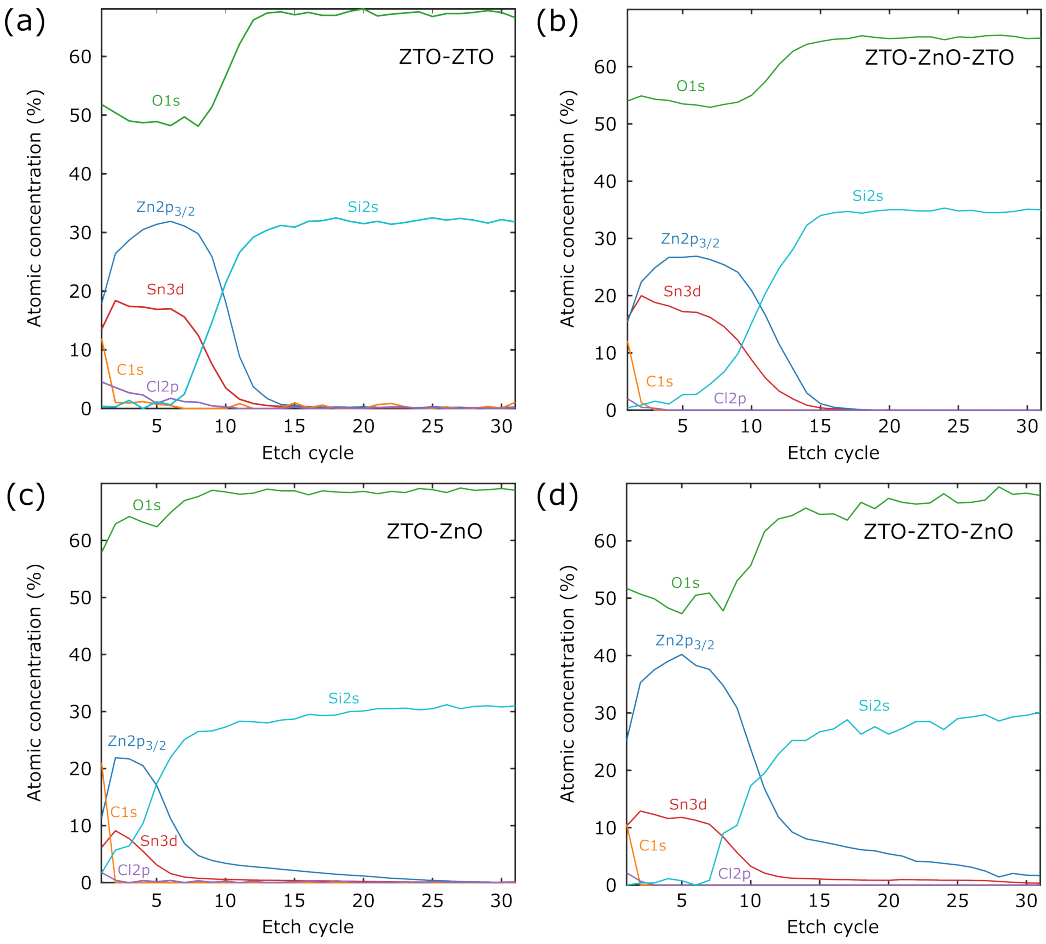

Figure 4.20: XPS depth profile of (a) ZTO-ZTO (b) ZTO-ZnO-ZTO (c) ZTO-ZnO and (d) ZTO-ZTO-ZnO films.

ZnO-capped bilayer TFT. Figure 4.20(c) shows that the Zn 2 $p_{3/2}$ signal was still prominent beyond etch cycle twenty-five for the ZnO-capped bilayer sample due to the presence and aggregation of ZnO nanoparticles. Furthermore, the Sn 3 d signal rose sharply before reaching its maximum intensity but was markedly weaker compared to the Zn 2 $p_{3/2}$ signal in the ZnO-capped bilayer sample. This observation aligned well with the XRD results, which – together with the TEM analysis – confirmed the formation of ZnO nanoparticles alongside the intended material. The film density of the ZnO-capped bilayer sample also remained constant throughout the bulk of the film, indicative of a single layer film that was majority Zn. It was also noticeably easier to etch through the ZnO-capped bilayer film as the O 1 s and Si 2 s signals relating to the substrate reached a plateau around cycle eight, which suggests that the distribution of ZnO nanoparticles and film coverage was not uniform.

Similarly, the Zn 2 $p_{3/2}$ signal was still detected beyond cycle thirty, reflecting a greater presence of ZnO nanoparticles on the surface of the ZnO-capped trilayer film (see Figure 4.20(d)). The Sn 3 d signal was also just over a quarter of the Zn 2 $p_{3/2}$ signal. Conversely, it took longer to etch through the ZnO-capped trilayer film, as the substrate-related signals, O 1 s and Si, reached a plateau around etch cycle fifteen – albeit with increased noise due to the random distribution of ZnO nanoparticles. This suggests improved film coverage on the substrate surface compared to the ZnO-capped bilayer sample, owing to the addition of more material, consistent with the presence of Kiessig fringes at higher angles in XRR analysis.

Proceeding to the quantitative analysis of the film composition, the atomic concentrations described by Table 4.6 were taken at etch cycles zero and five as the Zn 2 p and Sn 3 d signals were most obvious, while the C 1 s and Cl 2 p signals were diminished in all cases after etching. It was confirmed that the ZTO-capped films comprised the highest Sn content at cycle zero, calculated as 13.5 % and 16.0 %, respectively, for the bilayer and trilayer TFTs (Table 4.6). A similar trend was observed at cycle five, calculated as 16.9 %

Table 4.6: Atomic concentration (%) and calculated composition ratios at etch cycles zero and five following XPS depth profiling of bilayer and trilayer films.

Cycle 0				
Film	O 1 s (%)	Sn 3 d (%)	Zn 2 $p_{3/2}$ (%)	Sn/Zn
ZTO-ZTO	51.8	13.5	17.9	0.75
ZTO-ZnO	57.9	6.2	11.4	0.54
ZTO-ZnO-ZTO	54.0	16.0	15.4	1.04
ZTO-ZTO-ZnO	51.7	10.3	25.2	0.41
Cycle 5				
Film	O 1 s (%)	Sn 3 d (%)	Zn 2 $p_{3/2}$ (%)	Sn/Zn
ZTO-ZTO	48.9	16.9	31.4	0.54
ZTO-ZnO	62.4	3.1	17.0	0.18
ZTO-ZnO-ZTO	53.5	17.2	26.7	0.64
ZTO-ZTO-ZnO	47.3	11.8	40.2	0.29

and 17.2 %. The high metallic content recorded for the ZTO-capped films may have explained the superior electronic performance of the ZTO-capped TFTs. As alluded to in §4.3.4 and literature survey, Junk *et al.* demonstrated that increasing Sn content in blend films improves the device performances, reaching a fivefold on-current (I_{on}) improvement over standard Ge devices for 11 at.% Sn content. [23]

In contrast, the ZnO-capped bilayer film contained the lowest Sn content at cycles zero (6.2 %) and five (3.1 %). The Sn/Zn ratios were calculated from the atomic concentrations listed as 0.41, 0.54, 0.75 and 1.04 at cycle zero for the ZTO-ZnO, ZTO-ZTO-ZnO, ZTO-ZTO and ZTO-ZnO-ZTO TFTs, in increasing order. Similar values were obtained at cycle five, calculated as 0.18, 0.29, 0.54 and 0.64 for the ZTO-ZnO, ZTO-ZTO-ZnO, ZTO-ZTO and ZTO-ZnO-ZTO TFTs, in ascending order, responsible for the exceptionally low mobility calculated for the ZnO-capped bilayer TFT. This also correlates well with XRR analysis (Figure 4.17(b)), which showed that film density was constant before reaching the ZnO-capped bilayer film surface, due to very little contribution from Sn.

Lastly, distinguishing between the film and the substrate was challenging, as a higher percentage of O 1 s (62.4 %) was calculated at cycle five for the ZnO-capped bilayer stack. This supports the conclusion that the film coverage was poor and that the film contained more organic chemical-induced species, which contributed to the significantly lower SLD observed in XRR analysis. In contrast, the ZnO-capped trilayer stack had the lowest O 1 s percentage (47.3 %) at cycle five, aligning well with XRR analysis, as this film exhibited the highest effective film density.

4.4 Summary

In summary, beginning with the single layer SnO_2 TFTs, surface crystallisation – evidenced by AFM and XRD analyses – significantly enhanced device performance as the annealing temperature increased from 350 °C to 450 °C. The TFT treated at 450 °C showed a stronger chemiresistive response to acetone vapour across the entire bias range than the device treated at 350 °C, due to this improved surface crystallinity, which likely promoted acetone adsorption at nanoscale surface features and thus a greater change in $I_{on/off}$ upon exposure.

The electronic performance of monolayer ZTO TFTs was also markedly improved by stacking multiple ZTO layers. Introducing a ZnO capping layer strongly influenced the crystalline and morphological characteristics. While ZTO-capped devices delivered enhanced electrical performance, the ZnO capping layer led to nanoparticle formation, which increased surface roughness and degraded source–drain contact quality. Notably, the ZTO-ZTO TFT achieved near-zero threshold voltage ($V_{th} = 2.20\,\mathrm{V}$), excellent switching ($I_{on/off} = 10^7$), and high mobility ($\mu_{eff} \approx 10\,\mathrm{cm^2\,V^{-1}\,s^{-1}}$). The ZTO-ZnO-ZTO TFT also performed well, with $V_{th} = -1.74\,\mathrm{V}$, $I_{on/off} = 10^6$, and $\mu_{eff} \approx 3\,\mathrm{cm^2\,V^{-1}\,s^{-1}}$. Their low surface roughness ($< 1\,\mathrm{nm}$) and high Sn content ($Sn/Zn = 0.75$ and 1.04, respectively) contributed to strong current driveability.

The next chapter explores the chemical environment of these materials in greater detail, linking oxygen vacancy content to their electronic properties. The interplay between electronic and chemiresistive behaviour in both ZTO- and ZnO-capped TFTs is then assessed following exposure to various VOCs with different functional groups. As sensor reliability and reproducibility are critical for point-of-care applications, their response is evaluated through repeated cycling between exposure and recovery states.

References

[1] Y. Zhao, G. Dong, L. Duan *et al.*, "Impacts of Sn precursors on solution-processed amorphous zinc–tin oxide films and their transistors," *RSC Advances*, vol. 2, no. 12, pp. 5307–5313, 2012.

[2] S. Jeong, J.-Y. Lee, S. S. Lee *et al.*, "Impact of Metal Salt Precursor on Low-Temperature Annealed Solution-Derived Ga-doped In2O3 Semiconductor for Thin-Film Transistors," *The Journal of Physical Chemistry C*, vol. 115, no. 23, pp. 11 773–11 780, 2011.

[3] P. Zaumseil, "High-resolution characterization of the forbidden Si 200 and Si 222 reflections," *Journal of Applied Crystallography*, vol. 48, no. 2, pp. 528–532, 2015.

[4] G. Huang, L. Duan, G. Dong *et al.*, "High-Mobility Solution-Processed Tin Oxide Thin-Film Transistors with High- Alumina Dielectric Working in Enhancement Mode," *ACS Applied Materials & Interfaces*, vol. 6, no. 23, pp. 20 786–20 794, 2014.

[5] Y. Zhang, S. Pecorario, X. W. Chua *et al.*, "Critical assessment of contact resistance and mobility in tin perovskite field-effect transistors," *Advanced Electronic Materials*, vol. n/a, no. n/a, p. e00924.

[6] M. Lei, L. Guo, C. Wang *et al.*, "Analysis of the valence state of tin in ZnSnOx thin-film transistors," *Journal of Materials Science: Materials in Electronics*, vol. 33, no. 32, pp. 24 785–24 793, 2022.

[7] G. Gordillo, L. C. Moreno, W. de la Cruz, and P. Teheran, "Preparation and characterization of SnO2 thin films deposited by spray pyrolysis from SnCl2 and SnCl4 precursors," *Thin Solid Films*, vol. 252, no. 1, pp. 61–66, 1994.

[8] V. Rohnacher, F. Ullrich, H. Eggers *et al.*, "Analytical Study of Solution-Processed Tin Oxide as Electron Transport Layer in Printed Perovskite

Solar Cells," *Advanced Materials Technologies*, vol. 6, no. 2, p. 2000282, 2021.

[9] H. E. Kaden, "Transistor Leakage Currents," in *Transistors Applied*, H. E. Kaden, Ed. London: Macmillan Education UK, 1965, pp. 104–113.

[10] L. R. Miller, A. Galán-González, B. Nicholson *et al.*, "Control Strategies for Solution-Processed ZTO-Based Thin-Film Transistors Tailored Toward Volatile Organic Compound Detection," *Advanced Electronic Materials*, vol. n/a, no. n/a, p. 2400810, 2025.

[11] M. K. Trivedi *et al.*, "A comprehensive physicochemical, thermal, and spectroscopic characterization of zinc (ii) chloride using x-ray diffraction, particle size distribution, differential scanning calorimetry, thermogravimetric analysis/differential thermogravimetric analysis, ultraviolet-visible, and fourier transform-infrared spectroscopy," *Int J Pharm Investig.*, vol. 7, pp. 33–40, 2017.

[12] A. Galán-González, P. Pander, R. C. I. MacKenzie *et al.*, "Nanostructured Channel for Improving Emission Efficiency of Hybrid Light-Emitting Field-Effect Transistors," *ACS Photonics*, vol. 10, no. 12, pp. 4315–4321, 2023.

[13] K.-H. Lim, J. Lee, J.-E. Huh *et al.*, "A systematic study on effects of precursors and solvents for optimization of solution-processed oxide semiconductor thin-film transistors," *Journal of Materials Chemistry C*, vol. 5, no. 31, pp. 7768–7776, 2017.

[14] S.-J. Seo, C. G. Choi, Y. H. Hwang, and B.-S. Bae, "High performance solution-processed amorphous zinc tin oxide thin film transistor," *Journal of Physics D: Applied Physics*, vol. 42, no. 3, p. 035106, 2008.

[15] P. K. Nayak, M. N. Hedhili, D. Cha, and H. N. Alshareef, "Impact of Soft Annealing on the Performance of Solution-Processed Amorphous Zinc

Tin Oxide Thin-Film Transistors," *ACS Applied Materials & Interfaces*, vol. 5, no. 9, pp. 3587–3590, 2013.

[16] M.-G. Kim, H. S. Kim, Y.-G. Ha *et al.*, "High-Performance Solution-Processed Amorphous ZincIndiumTin Oxide Thin-Film Transistors," *Journal of the American Chemical Society*, vol. 132, no. 30, pp. 10 352–10 364, 2010.

[17] Y. J. Kim, B. S. Yang, S. Oh *et al.*, "Photobias Instability of High Performance Solution Processed Amorphous Zinc Tin Oxide Transistors," *ACS Applied Materials & Interfaces*, vol. 5, no. 8, pp. 3255–3261, 2013.

[18] D. Ho, H. Jeong, H.-B. Park *et al.*, "Solution-processed amorphous zinc indium tin oxide thin-film transistors with high stability under AC stress," *Journal of Materials Chemistry C*, vol. 11, no. 39, pp. 13 395–13 402, 2023.

[19] Y. Zhou, S.-T. Han, L. Zhou *et al.*, "Flexible organic/inorganic heterojunction transistors with low operating voltage," *Journal of Materials Chemistry C*, vol. 1, no. 42, pp. 7073–7080, 2013.

[20] Y. Lin, H. Faber, J. G. Labram *et al.*, "High Electron Mobility Thin-Film Transistors Based on Solution-Processed Semiconducting Metal Oxide Heterojunctions and Quasi-Superlattices," *Advanced Science*, vol. 2, no. 7, p. 1500058, 2015.

[21] C. Swindells, H. Głowiński, Y. Choi *et al.*, "Proximity-induced magnetism and the enhancement of damping in ferromagnetic/heavy metal systems," *Applied Physics Letters*, vol. 119, no. 15, p. 152401, 2021.

[22] J. M. Kwon, J. Jung, Y. S. Rim *et al.*, "Improvement in Negative Bias Stress Stability of Solution-Processed Amorphous In–Ga–Zn–O Thin-Film Transistors Using Hydrogen Peroxide," *ACS Applied Materials & Interfaces*, vol. 6, no. 5, pp. 3371–3377, 2014.

[23] Y. Junk, O. Concepción, M. Frauenrath *et al.*, "Enhancing Device Performance with High Electron Mobility GeSn Materials," *Advanced Electronic Materials*, vol. n/a, no. n/a, p. 2400561.

Chapter 5

Chemiresistive Properties of ZTO-based TFTs

5.1 Chapter Overview

This chapter aims to enhance the sensitivity of single layer SnO_2 TFTs by exploring multilayer ZnO-based material systems, as prepared in Chapter 4, for VOC detection. The chemiresistive responses of the best and worst performing transistors analysed in Chapter 4.2.1, namely the ZTO-ZTO and ZTO-ZnO TFTs, were compared. Differences in their chemical environment and surface morphology heavily influenced their electronic and thus chemiresistive functionality. To begin, XPS surface analyses was conducted to deconvolve the oxygen-related components and ascertain potential sites for the adsorption of VOCs. Secondly, the specificity of these TFTs was examined qualitatively by exposing them to a suite of VOCs with different functional groups and sizes, which included acetone, isopropanol (IPA) and toluene

vapours. Next, the most responsive TFT was taken forward to examine the impact of channel geometry on the calculated responsivity obtained. To support the link between oxygen surface chemistry, morphology and TFT sensor performance, the ZTO-ZTO TFT was exposed to a smaller alcohol, methanol. Its reliability and reproducibility were evaluated by testing its dynamic response, with respect to methanol, and operation cycled three times following overnight, long and short exposure periods.

5.2 Analysis of the Surface Chemistry

The surface chemistry of TFT gas sensors based on metal oxides plays a crucial role in their chemiresistive functionality. Therefore, the elemental composition of the ZTO- and ZnO-capped films presented in Chapter 4 was examined by XPS surface analysis. Figure 5.1 shows the XPS spectra for the Zn 2 $p_{3/2}$ and Sn 3 d components, which were calibrated against the C 1 s peak centred at 284.6 eV to adjust for any charging induced shift during testing. The slight shift of Zn 2 $p_{3/2}$ peak to lower binding energy points to increased oxygen vacancy content, commonly regarded as a major factor in the generation and separation of charge carriers within ZnO-based films [1].

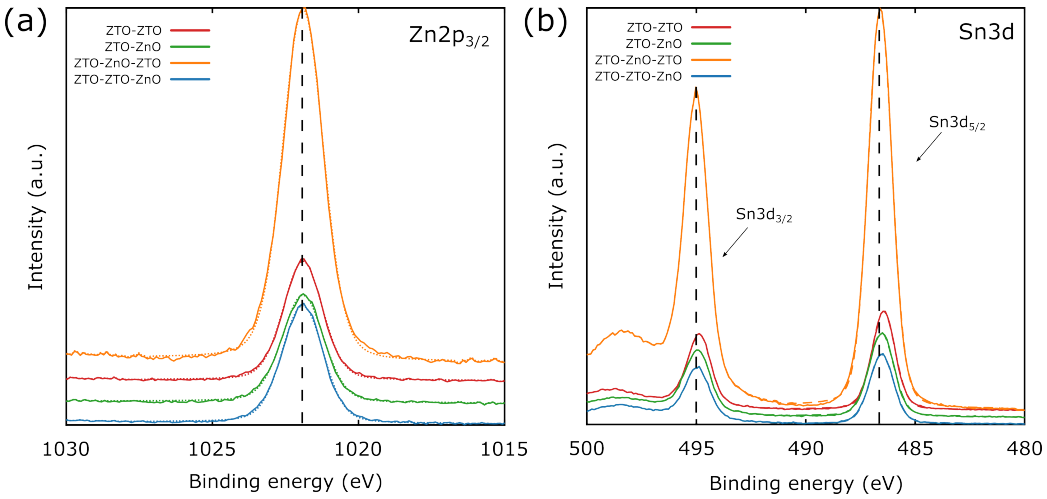

Figure 5.1: XPS core level spectra of (a) Zn 2 $p_{3/2}$ and (b) Sn 3 d. The dashed lines are centred at 1021.4 eV, 486.5 eV and 495 eV for the Zn 2 $p_{3/2}$ and Sn 3 d peaks respectively.

Table 5.1: Binding energies of Zn 2p, Sn 3d and O 1s film components.

Film	Zn 2p (eV)	Sn 3d (eV)	O 1s (eV)
ZTO-ZTO	1021.4	486.4	530.4
ZTO-ZnO	1021.5	486.5	530.5
ZTO-ZnO-ZTO	1021.5	486.5	530.5
ZTO-ZTO-ZnO	1021.7	486.7	530.7

As shown in Table 5.1, the ZTO-capped bilayer film likely exhibited the highest proportion of oxygen vacancies, followed by the ZTO-capped trilayer, ZnO-capped bilayer, and finally the ZnO-capped trilayer films. This trend is reflected in the Zn $2\,p_{3/2}$ peak positions, which were centred at 1021.4 eV, 1021.5 eV, 1021.5 eV, and 1021.7 eV, respectively.

The binding energies at 486.5 eV and 495 eV, separated by 8.5 eV, were assigned to the Sn $3\,d_{5/2}$ and Sn $3\,d_{3/2}$ core levels, respectively, indicating the presence of Sn^{4+} oxidation states. [2] This confirms that the Sn^{2+} in the $SnCl_2$ precursor was oxidised to Sn^{4+} in the ZTO films upon thermal treatment at 500 °C in air – Sn^{4+} being the dominant contributor to n-type conduction. [3,4] The incorporation of Sn has been shown to increase carrier density and reduce electron scattering, owing to the similar ionic radii of Zn^{2+} (0.074 nm) and Sn^{4+} (0.069 nm). [2,5] Consistent with this, XPS depth profiling in Chapter 4.3.6 confirmed that the ZnO-capped films contained significantly less Sn than the ZTO-capped films. This reduction was attributed to the addition of the ZnO top layer and correlated with both the degraded electrical performance and the formation of a rough, particulate surface morphology.

The clear shift of the Zn $2\,p_{3/2}$ peak to lower binding energy pointed to increased oxygen vacancy content. Interestingly, high oxygen vacancy content in metal oxides can promote the adsorption of relevant gases and accommodate more chemisorbed oxygen species that enhance sensitivity and shorten the response time for VOC detection. [6,7] Therefore, robust analysis of the O 1 s peak in the ZTO- and ZnO-capped TFTs was conducted to couple oxygen vacancy content with their electronic properties, so that the most appropriate TFTs could be taken forward as chemiresistive gas sen-

sors. The O 1 s peak was deconvolved into three components through Gaussian–Lorentzian fitting, as described in Chapter 3.7.3 and shown in Figure 5.2. The lower binding energy component at 530.3 eV was associated with the oxygen bonded to metal atoms (M-O), [3] while the higher binding energy component at 531.5 eV corresponded to an oxygen-deficient region, related to oxygen vacancy content (V_O) in the metal oxide thin films. [8] Finally, the component centred at 533.4 eV was ascribed to the presence of loosely bound oxygen, such as hydroxide (M-OH). [9]

The ZTO- and ZnO-capped trilayer films contained the largest proportion of M-O = 70.1 % and 68.2 %, (Table 5.2), responsible for the high density observed from XRR analysis (Chapter 4.3.5), while the ZTO- and

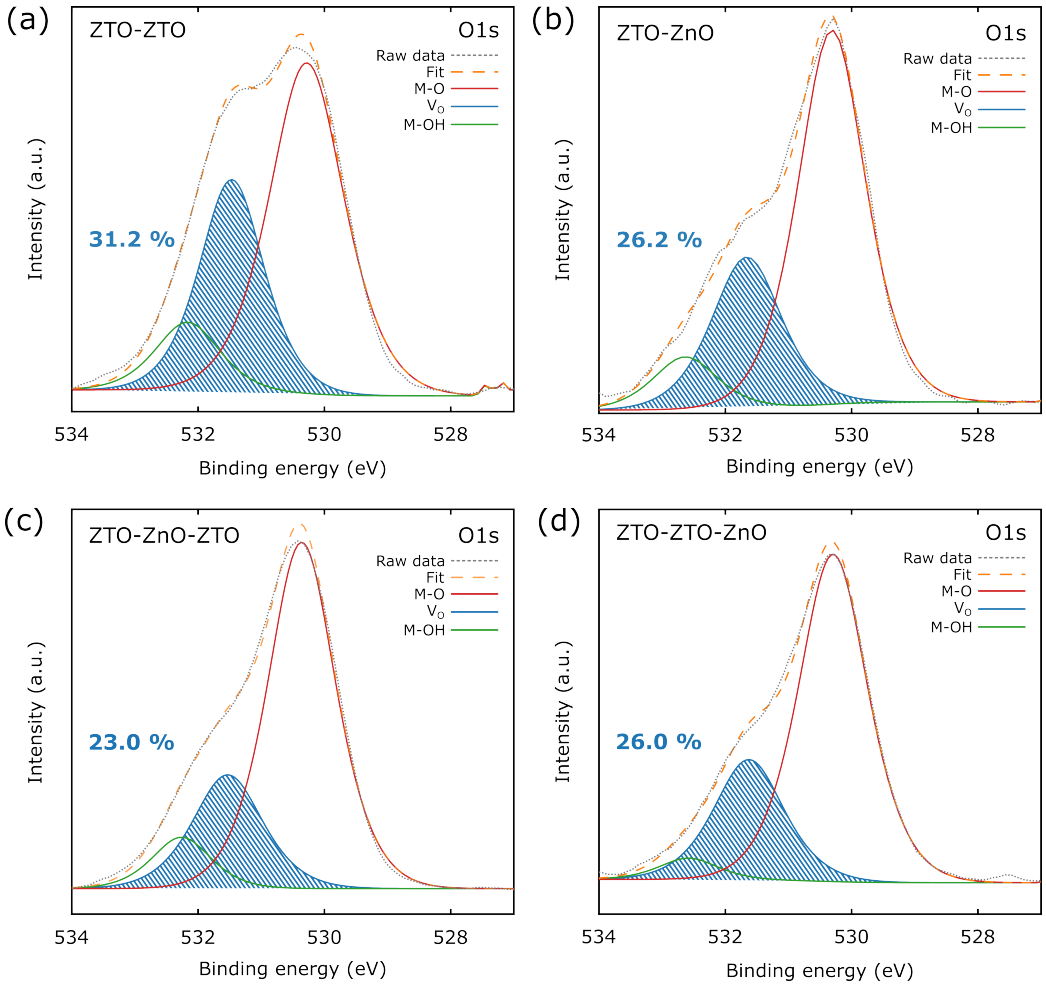

Figure 5.2: XPS core level spectra of O 1 s for (a) ZTO-ZTO, (b) ZTO-ZnO, (c) ZTO-ZnO-ZTO & (d) ZTO-ZTO-ZnO films.

Table 5.2: Percentage contents and position of O 1s components for bilayer and trilayer films. M-O, V_O and M-OH denote metal-oxygen, oxygen vacancy and metal-hydroxide contents, respectively.

Film	M-O		V_O		M-OH	
	(%)	(eV)	(%)	(eV)	(%)	(eV)
ZTO-ZTO	57.8	530.3	31.2	531.5	11.4	532.1
ZTO-ZnO	64.4	530.3	26.2	531.6	9.4	532.6
ZTO-ZnO-ZTO	70.1	530.3	26.0	531.6	3.9	532.3
ZTO-ZTO-ZnO	68.2	530.4	23.0	531.5	8.8	532.3

ZnO-capped bilayer films contained the lowest percentage of M-O = 57.8 % and 64.4%, respectively. However, Figure 5.2(a) shows that the O 1 s envelope for the ZTO-capped bilayer film had a distinct shape compared to the other systems, with a pronounced shoulder attributed to the oxygen vacancy fraction. [10] This film exhibited the highest proportion of oxygen vacancies ($V_O = 31.2\%$), whereas the ZnO-capped bilayer system contained a lower proportion ($V_O = 26.2\%$), explaining its positive threshold voltage ($V_{th} > 1\,\mathrm{V}$), as the film was less conductive. The ZTO- and ZnO-capped trilayers followed with V_O = 26.0 % and 23.0 %, respectively, consistent with the previously discussed trend in the Zn 2 $p_{3/2}$ peak shift toward lower binding energy.

From these results, it is clear that the substantial M-O content of the ZnO-capped bilayer film did not translate to improved charge transport due to the much rougher film surface with worsened source-drain contacts. In addition, Table 5.2 further lists that the ZTO-capped bilayer film comprised the largest proportion of M-OH = 11.4 %, which could act as additional adsorption sites. On the other hand, the ZTO-capped trilayer film, comprised little M-OH = 3.9 %. The low off-current ($I_{ds[min]} \approx 10^{-10}$) and near-zero V_{th} of the ZTO-capped bilayer (2.20 V) and trilayer TFTs (−1.74 V) reported in Chapter 4.3 make them ideal candidates for VOC detection within a low-voltage window. Furthermore, their oxygen environment, described in §5.2, is expected to play a major role in their chemiresistive functionality.

5.3 Selection of the Optimal TFT sensor

5.3.1 ZnO-capped Bilayer TFTs

To establish the correlation between the oxygen environment, electronic functionality, and sensing performance – and thus identify the best-performing TFT chemiresistive sensor – the ZTO-ZnO TFT was exposed to three VOCs: acetone, IPA, and toluene vapours. This choice was based on the ZnO-capped bilayer film's reduced V_O (26.2 %) compared to the ZTO-capped equivalent system (Figures 5.2(a),(b)). These experiments were conducted under a controlled environment as specified in Chapter 4.2.3. Figure 5.3(a) shows that there was a small V_{th} shift to negative bias, by $\approx 6\,\text{V}$, following exposure to acetone (solid red lines). $I_{ds[min]}$ also rose by tenfold, which caused a subsequent reduction in $I_{on/off}$ from 10^3 to 10^2. These changes were consistent with a slight decrease in the electrical resistance of the ZTO-ZnO film.

Unlike the chemiresistive response observed for the single layer SnO_2 TFTs (Chapter 4.2.2), $I_{ds[max]}$ did not increase accordingly. This suggests that acetone was less prone to adsorption and desorption on the ZTO-ZnO surface. The ZTO-ZnO film surface was significantly rougher (8.12 nm) compared to the SnO_2 system (1.28 nm), as the Sn nanoparticles were smaller and

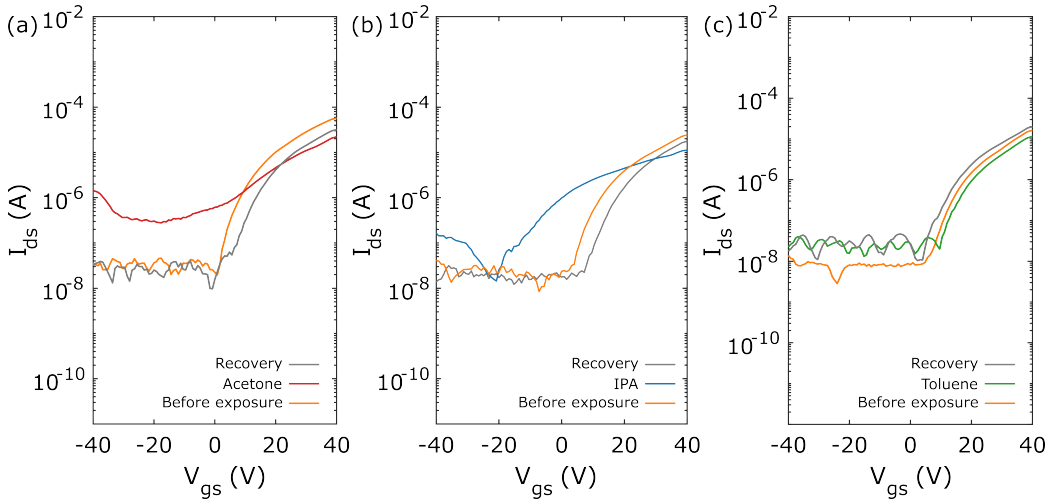

Figure 5.3: Transfer characteristics for the ZTO-ZnO TFTs treated at 500 °C in the saturation regime at $V_{ds} = 40\,\text{V}$, $V_{gs} = -40\,\text{V}$ to 40 V following overnight exposure to (a) acetone, (b) IPA and (c) toluene vapours.

more uniformly distributed. The larger Zn aggregates described in Chapter 4.3.4 reduced the number of active sites due to the decreased surface area, resulting in a less pronounced decrease in the electrical resistance of the ZTO-ZnO film. As it can be seen, the recovery of the ZTO-ZnO TFT (solid grey lines) with heat treatment was sufficient since $I_{on/off}$ returned to 10^3. There was a slight positive shift in V_{th} from 3.0 V to 4.7 V, and similar reduction in $I_{ds[max]}$ after re-adsorption of oxygen in ambient conditions.

Figure 5.3(b) displays a different response following exposure to IPA, as $I_{ds[min]}$ and therefore $I_{on/ff}$ were maintained. There was a much larger V_{th} shift to negative bias from 5.7 V to −17.1 V compared with acetone. This suggests that IPA adsorbed on the ZTO-ZnO surface more easily due to differences in the polarity of the alcohol (−OH) and carbonyl (C=O) groups. This film also contained a moderate amount of M-OH = 9.4 %, which could have acted as specific adsorption sites for IPA. [11] In addition, Table 5.3 shows that this TFT recovered well as V_{th} = 3.5 V and returned to positive bias ($V_{gs} > 0$) after heat treatment.

Toluene, a subclass of VOCs with aromatic rings, serves as an important biomarker for cancer. Elevated toluene concentrations have been observed in the exhaled breath of lung cancer patients compared to healthy non-smokers. [12] The high specificity of a sensor for aromatic compounds

Table 5.3: $I_{on/off}$, μ, μ_{eff} and V_{th} of ZTO-ZnO TFTs before exposure, after exposure and recovery.

	$I_{on/off}$	μ ($cm^2\,V^{-1}\,s^{-1}$)	μ_{eff} ($cm^2\,V^{-1}\,s^{-1}$)	V_{th} (V)
As-prepared	10^3	0.23	0.22	2.96
Acetone	10^2	0.62	0.61	-2.82
Recovery	10^3	0.14	0.12	4.73
As-prepared	10^3	0.08	0.07	5.74
IPA	10^3	0.02	0.02	-17.1
Recovery	10^3	0.10	0.10	3.53
As-prepared	10^3	0.06	0.06	5.92
Toluene	10^3	0.05	0.04	5.87
Recovery	10^3	0.08	0.07	5.74

like toluene primarily depends on the chemical environment of the sensing material, the decomposition rate of the adsorbed molecule on the surface, and the operating temperature. Figure 5.3(c) shows that the relative change in I_{ds} after overnight exposure to toluene at room temperature was negligible. Furthermore, Table 5.3 shows that $I_{on/off}$, μ_{eff}, and V_{th} remained largely unchanged after exposure, with values of approximately 10^3, $0.1\,\mathrm{cm^2\,V^{-1}\,s^{-1}}$, and 6 V, respectively. This suggests that toluene vapour – specifically the methyl group ($-CH_3$) – did not adsorb onto the ZTO-ZnO surface as effectively as the other reducing vapours. This may be attributed to molecular size, as toluene has an estimated kinetic diameter of 0.59 Å, compared to acetone (0.46 Å) and IPA (0.47 Å). [13, 14] Additionally, hydroxyl and carbonyl groups interact more readily with the oxygen-active sites than methyl groups.

The calculated sensitivities (S) of the ZTO-ZnO TFTs following exposure to acetone, IPA and toluene vapours are plotted against $V_{gs} = -40$ V to 40 V at a fixed $V_{ds} = 40$ V, shown by the solid red, blue and green lines, respectively (see Figure 5.4(a)). For acetone, the maximum sensitivity ($S_{max} = 41.0$) occurred at -38.4 V, influenced by a slight rise in the tail of $I_{ds[min]}$ at the beginning of the V_{gs} sweep. Following exposure to IPA, $S_{max} = 90.3$ at 4.8 V, nearly double that observed for acetone. This increase was due to the combined effect of retained $I_{on/off}$ and a much larger shift in V_{th} toward negative bias, resulting in a difference of just over 10^2 versus 10^1 for acetone in I_{ds} at the V_{gs} corresponding to S_{max}. Lastly, the poor responsivity of the ZTO-ZnO TFT to toluene – particularly the $-CH_3$ group attached to its benzene ring – is evident from $S_{max} < 10$.

Finally, Figures 5.4(b) and (c) show the chemiresistive response at fixed V_{gs} and V_{ds} of ZTO-ZnO TFTs. Sensitivity (S) was calculated at $V_{gs} = 15$ V, 25 V, and 35 V in both the linear ($V_{ds} = 10$ V) and saturation ($V_{ds} = 40$ V) regimes. Following exposure to IPA vapour, an increase in I_{ds} was easily distinguishable from the as-prepared measurements, even at positive bias. In this case, S was maximised as V_{gs} approached the V_{th} of the as-prepared

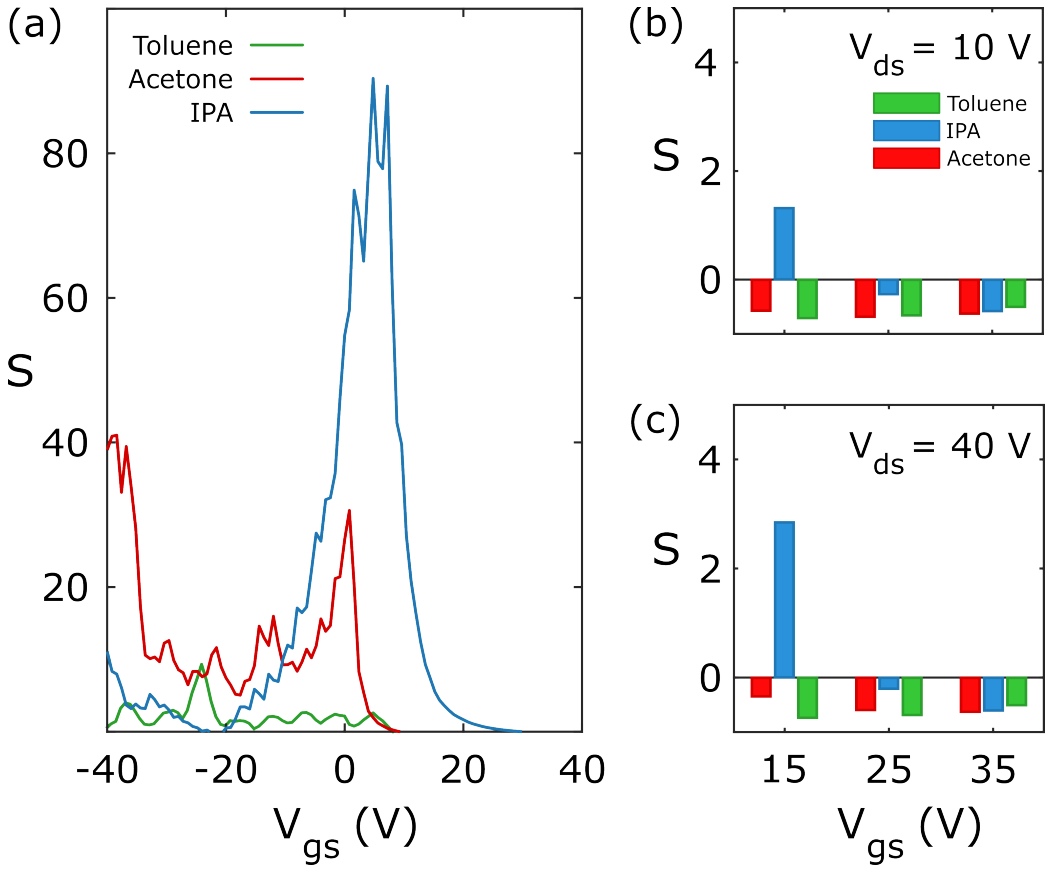

Figure 5.4: (a) Calculated sensitivity for ZTO-ZnO TFT following exposure to acetone, IPA and toluene vapours (b) at fixed V_{gs} in the linear (V_{ds} = 10 V) and (c) saturation regimes (V_{ds} = 40 V).

ZTO-ZnO TFT in both the linear and saturation regimes. In the linear regime, S decreased from 1.3 to -0.3 and -0.6 for V_{gs} = 15 V, 25 V, and 35 V, respectively. A similar trend was observed in the saturation regime, with S = 2.8, -0.2, and -0.6 in the order of increasing bias. The ZTO-ZnO TFT was clearly more sensitive to IPA vapour in the saturation regime, governed by Equation 3.10.3, consistent with the observations in Chapter 4 for single layer SnO_2 TFTs for acetone.

The presence of ZnO nanoparticles grown on the ZTO-ZnO surface impeded the clean deposition of source-drain contacts and thus weakened electron transport. These nanoparticles aggregated into larger Zn clusters that reduced the number of active sites due to the decreased surface area, resulting in poor sensitivity to the VOCs under test. However, there were measurable differences in the transfer characteristics following exposure to acetone, IPA

and toluene, relative to those extracted for the as-prepared ZTO-ZnO TFTs. This suggests that there is some specificity to alcohol vapours due to comparably high M-OH content of this material system.

5.3.2 ZTO-capped Bilayer TFTs

To further investigate the role of high M-OH and V_O contents in enhancing sensitivity, particularly to alcohol vapours, the ZTO-ZTO TFT was exposed to acetone, IPA, and toluene vapours. Figure 5.5(a) demonstrates a significant V_{th} shift to negative bias, by over 30 V, following exposure to acetone (solid red lines). Additionally, $I_{ds[min]}$ increased by two orders of magnitude, resulting in a subsequent reduction in $I_{on/off}$ from 10^5 to 10^3, as shown in Table 5.4. These changes were consistent with a notable decrease in the electrical resistance of the ZTO-ZTO film. After thermal treatment, $I_{on/off}$ was recovered by an order of magnitude (10^4), and V_{th} returned to positive bias (< 5 V), as indicated in Table 5.4.

Figure 5.5(b) shows that $I_{ds[min]}$ and, consequently, $I_{on/off} \approx 10^5$ of the ZTO-ZTO TFT were maintained after exposure to IPA vapour and subsequent recovery via heat treatment. A similar V_{th} shift to negative bias was observed, shifting from 2.41 V to −30.9 V, consistent with the acetone

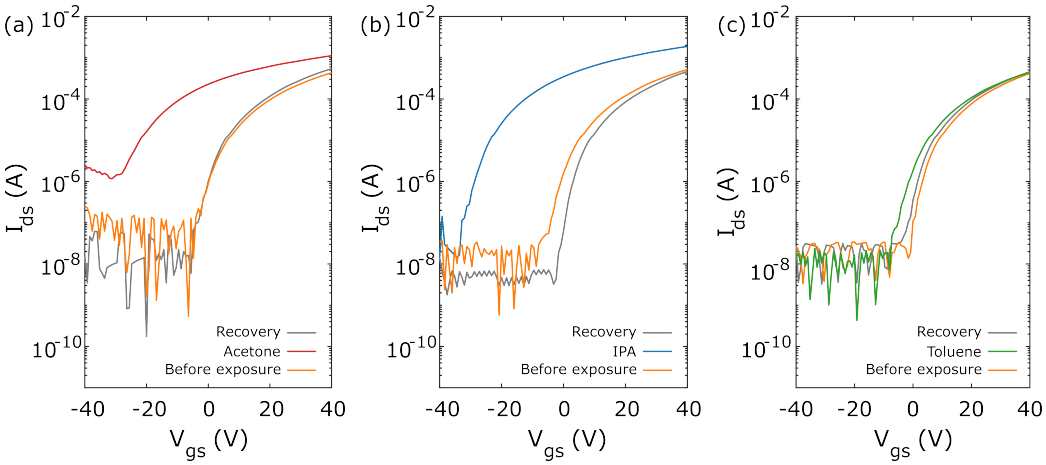

Figure 5.5: Transfer characteristics for the ZTO-ZTO TFTs treated at 500 °C in the saturation regime at $V_{ds} = 40$ V, $V_{gs} = -40$ V to 40 V following overnight exposure to (a) acetone, (b) IPA and (c) toluene vapours.

Table 5.4: $I_{on/off}$, μ, μ_{eff} and V_{th} of ZTO-ZTO TFTs before exposure, after exposure and recovery.

	$I_{on/off}$	μ ($cm^2\,V^{-1}\,s^{-1}$)	μ_{eff} ($cm^2\,V^{-1}\,s^{-1}$)	V_{th} (V)
As-prepared	10^5	3.49	3.31	0.30
Acetone	10^3	2.19	2.25	-34.4
Recovery	10^4	0.14	0.12	4.73
As-prepared	10^5	3.24	3.01	2.41
IPA	10^5	4.07	4.07	-30.9
Recovery	10^5	3.26	3.08	-0.40
As-prepared	10^5	5.04	4.55	1.05
Toluene	10^5	4.79	4.25	2.18
Recovery	10^5	4.55	4.13	-1.07

response. Despite the attractive electrical properties and amorphous morphology of the ZTO-ZTO TFT, a limited response was observed following exposure to toluene. As shown in Table 5.4, $I_{on/off}$, μ_{eff}, and V_{th} were maintained after exposure, with values of 10^5, $5\,cm^2\,V^{-1}\,s^{-1}$, and less than 2.5 V, respectively.

The calculated sensitivities, plotted in Figure 5.6, show that $S_{max} = 9,330$ at $V_{gs} = -2.40\,V$ following exposure to acetone, which was significantly higher compared to the ZTO-ZnO TFT ($S_{max} = 41.0$). Notably, the response was not distorted by the rising tail in the off-current, as observed in the ZTO-ZnO case. This result suggests that acetone favoured adsorption and desorption on the ZTO-ZTO film surface, likely due to its high V_O content. The high density of V_O in the ZTO-ZTO film acted as acceptor sites for oxygen ions under ambient conditions, resulting in the formation of a relatively thick depletion layer. In addition, the amorphous nature of the film promoted acetone adsorption. The observed increase in I_{off} following acetone exposure can therefore be interpreted using Equations 5.3.1 and 5.3.2: [15]

$$\ln(i) = \ln(i_0) + \ln\left(e^{\frac{eV}{mkT}} - 1\right), \tag{5.3.1}$$

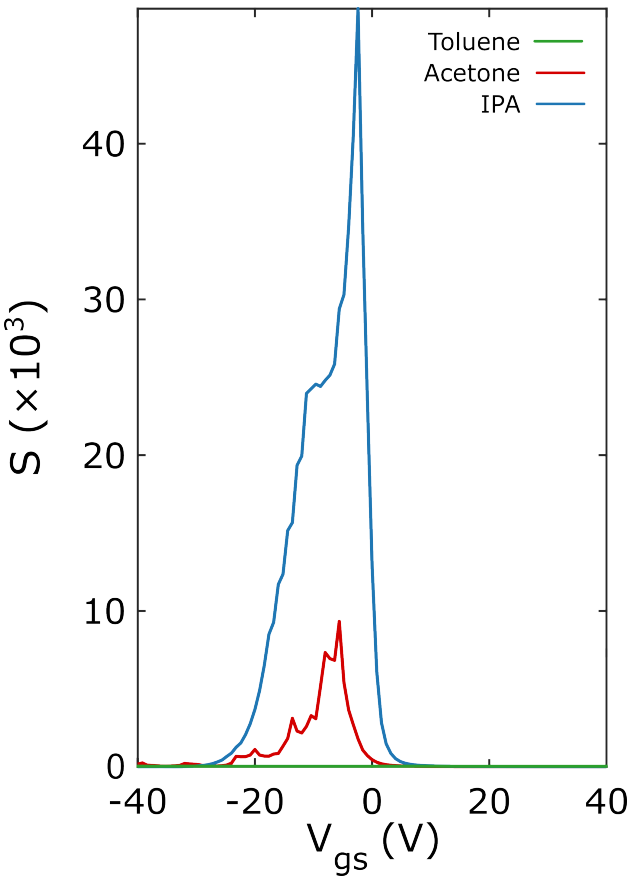

Figure 5.6: Calculated sensitivity of the ZTO-ZTO TFT following overnight exposure to toluene (green), acetone (red) and IPA (blue) vapours.

$$i_0(t) \propto n(t), \tag{5.3.2}$$

where $i_0(t)$ is the reverse saturation current and $n(t)$ represents the carrier density in the conduction band at a given time. Specifically, the redox interaction with acetone molecules generated additional free carriers, thereby increasing the charge density near both the valence band maximum and conduction band minimum. This process likely reduced the Schottky barrier height at the Al/ZTO interface, leading to the measured rise in I_{off}. [6,16,17] Support for this interpretation can be found in Kelvin probe studies reported in the literature, although a comprehensive investigation of this effect lies beyond the scope of the present work.

S_{max} was calculated to be $\approx 50,000$ at $-5.60\,\mathrm{V}$ for IPA, which is five times greater than the value obtained for acetone and remains within the

ideal low-voltage operating window. This markedly outperforms the ZTO-ZnO TFT, which exhibited a significantly lower S_{max} of 90.3. The enhanced sensitivity is attributed to the chemical environment of the ZTO-capped surface, particularly the higher proportion of M–OH states (11.4 %), which provide more specific adsorption sites for hydroxyl-containing analytes. As shown in Figure 5.6, toluene exhibited limited with the ZTO-capped surface – consistent with that described §5.3.1 – possibly due to the (i) low polarity of the methyl group ($-CH_3$), or (ii) larger size of the gas molecules.

5.3.3 ZTO-ZTO TFT Sensing vs. Channel Length

To confirm that the shortest channel length ($L = 80\,\mu m$) was the most responsive, L was increased to 100 µm and 120 µm, while the width (W) remained unchanged. The transfer characteristics are shown in Figures 5.7, 5.8 and 5.9 following exposure to acetone, IPA and toluene vapours, respectively, in comparison with the $L = 80\,\mu m$ configuration. At $L = 100\,\mu m$, Table 5.5 shows that V_{th} increased by 15 V and $I_{on/off}$ decreased by two orders of magnitude following exposure to acetone vapour (Figure 5.7, dashed

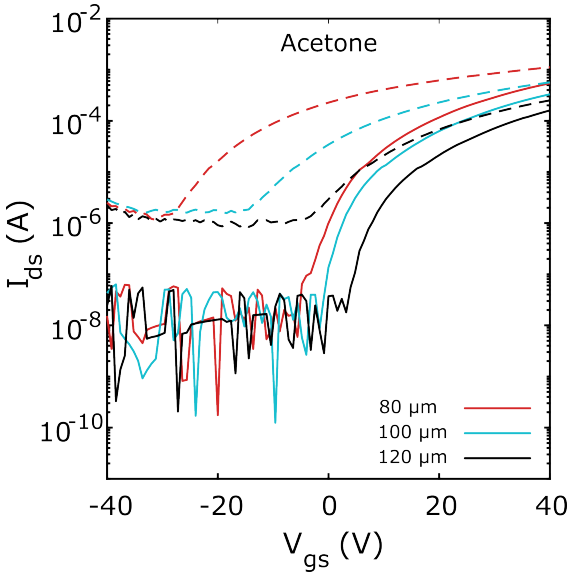

Figure 5.7: Transfer characteristics for the ZTO-ZTO TFTs in the saturation regime at $V_{ds} = 40\,V$, $V_{gs} = -40\,V$ to 40 V and $L = 80\,\mu m$ (red), 100 µm (cyan) and 120 µm (black). The dashed lines are after overnight exposure to acetone.

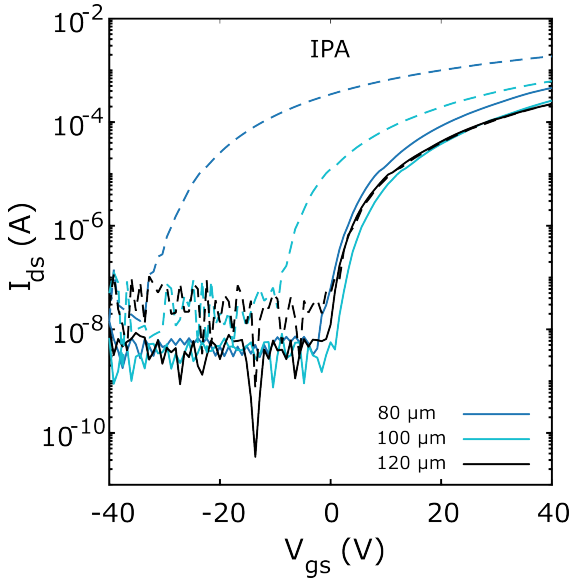

Figure 5.8: Transfer characteristics for the ZTO-ZTO TFTs in the saturation regime at $V_{ds} = 40\,\text{V}$, $V_{gs} = -40\,\text{V}$ to $40\,\text{V}$ and $L = 80\,\mu\text{m}$ (pale blue), $100\,\mu\text{m}$ (cyan) and $120\,\mu\text{m}$ (black). The dashed lines are after overnight exposure to IPA.

cyan lines). At $L = 120\,\mu\text{m}$, the increase in V_{th} from $4.5\,\text{V}$ to $-3.8\,\text{V}$ (listed in Table 5.5) was half of that observed at $L = 100\,\mu\text{m}$. These results confirm that $L = 80\,\mu\text{m}$ was the most sensitive to acetone vapours, as concluded in

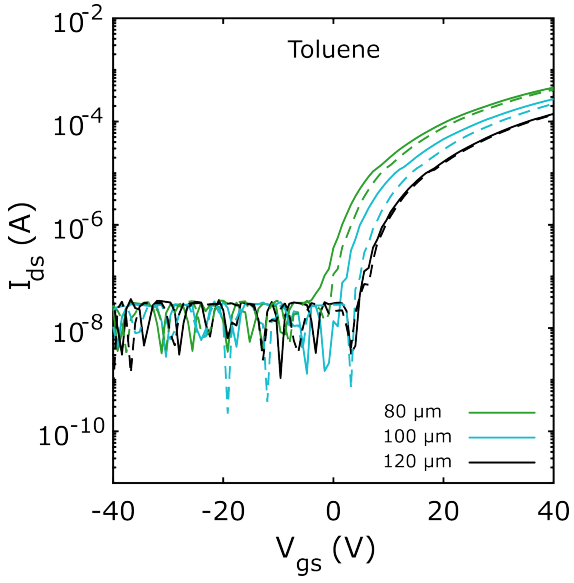

Figure 5.9: Transfer characteristics for the ZTO-ZTO TFTs in the saturation regime at $V_{ds} = 40\,\text{V}$, $V_{gs} = -40\,\text{V}$ to $40\,\text{V}$ and $L = 80\,\mu\text{m}$ (green), $100\,\mu\text{m}$ (cyan) and $120\,\mu\text{m}$ (black). The dashed lines are after overnight exposure to toluene.

Table 5.5: $I_{on/off}$, μ, μ_{eff} and V_{th} of ZTO-ZTO TFTs before exposure, after exposure and recovery, for $L = 100\,\mu m$ and $120\,\mu m$.

L (µm)		$I_{on/off}$	μ ($cm^2\,V^{-1}\,s^{-1}$)	μ_{eff} ($cm^2\,V^{-1}\,s^{-1}$)	V_{th} (V)
100	As-prepared	10^4	2.80	2.65	1.68
	Acetone	10^2	2.73	2.68	-13.1
	Recovery	10^4	2.24	2.06	2.33
	As-prepared	10^5	2.32	2.15	3.73
	IPA	10^5	3.99	3.80	-5.65
	Recovery	10^5	2.37	2.15	3.51
	As-prepared	10^4	3.22	2.84	2.99
	Toluene	10^4	2.68	2.27	4.41
	Recovery	10^4	3.02	2.68	2.34
120	As-prepared	10^3	1.74	1.55	4.48
	Acetone	10^1	2.11	2.00	-3.84
	Recovery	10^3	1.40	1.22	4.75
	As-prepared	10^4	2.35	2.22	2.04
	IPA	10^4	2.32	2.18	2.23
	Recovery	10^4	1.39	1.20	5.62
	As-prepared	10^4	1.72	1.44	4.80
	Toluene	10^4	1.67	1.89	4.99
	Recovery	10^4	1.64	1.36	4.95

Chapter 4.2.2, with the signal-to-noise ratio degrading as L increases due to higher channel resistance. After exposure to IPA vapour, Figure 5.8(a) shows that $I_{on/off}$ remained at 10^5, and V_{th} shifted left from 3.7 V to −5.7 V for $L = 100\,\mu m$. In contrast, the relative change in I_{ds} for $L = 120\,\mu m$ was minimal. Table 5.5 shows that V_{th} did not drop below 2 V and only increased to approximately 6 V after recovery. This suggests that the effect of increasing L was more significant following exposure to IPA vapour. In line with the results for $L = 80\,\mu m$, Figure 5.9 shows minimal changes in the transfer characteristics for both $L = 100\,\mu m$ and $L = 120\,\mu m$ after exposure to toluene vapours. Table 5.5 also reports minimal variations in $I_{on/off} \approx 10^4$, μ_{eff} ranging from $2\,cm^2\,V^{-1}\,s^{-1}$ to $3\,cm^2\,V^{-1}\,s^{-1}$, and $V_{th} < 5$ V after exposure and recovery.

Next, S was calculated from the transfer characteristics for $L = 100$

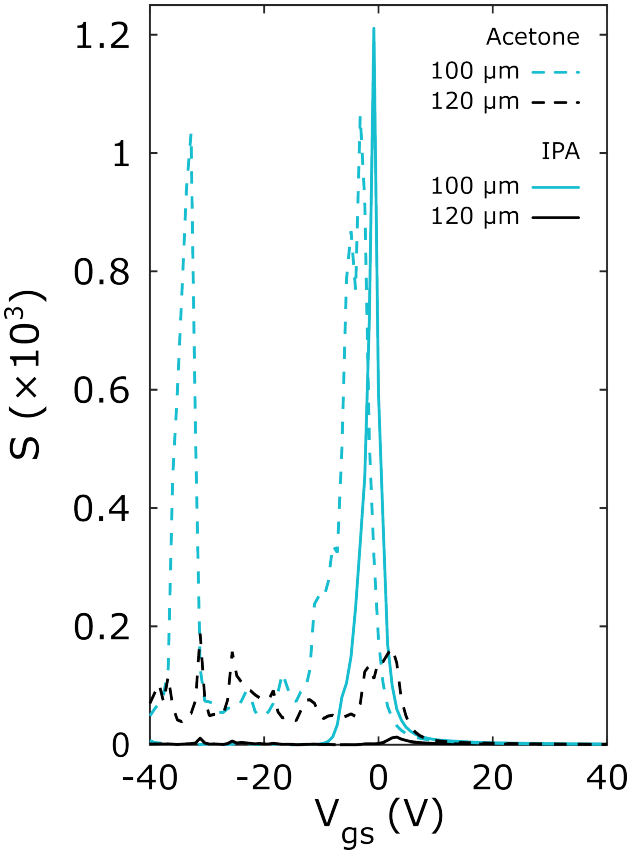

Figure 5.10: Calculated sensitivity following overnight exposure to acetone (dashed lines) and IPA (solid lines) vapours for $L = 100\,\mu m$ and $L = 120\,\mu m$.

µm and 120 µm using acetone and IPA only, as the toluene response was negligible. As shown in Figure 5.10, exposure to acetone resulted in $S_{max} \approx 1,000$ at $-0.8\,V$ for $L = 100\,\mu m$ – a tenfold decrease compared to $L = 80\,\mu m$ – due to the halved negative V_{th} shift, consistent with a less pronounced surface reduction and addition of electrons. This yielded a relative change in I_{ds} of approximately 10^2 at the gate bias corresponding to S_{max}. For $L = 120\,\mu m$, S_{max} further decreased to 164 at $2.4\,V$, with the signal becoming indistinguishable from the noise at $V_{gs} < 0$. In the case of IPA, although the V_{th} shift was less pronounced than for acetone, the ZTO-ZTO TFT exhibited slightly higher sensitivity to alcohol vapour, reaching $S_{max} \approx 1,200$ at $-0.8\,V$ for $L = 100\,\mu m$. These results confirm that the shortest channel length, $L = 80\,\mu m$, offered the most favourable W/L ratio for the TFT architecture used here and in Chapter 4, maximising both electronic performance and chemiresistive sensitivity.

5.3.4 Detection of Methanol Vapour

To highlight the exceptional performance of the ZTO-ZTO TFT sensors in detecting vapours containing hydroxyl groups, the device was exposed to methanol overnight, leveraging its high oxygen vacancy density and M-OH content. The ZTO-ZTO TFT with $L = 80\,\mu m$ was identified as the most suitable for VOC detection, as S was maximised following exposure to acetone and IPA, as discussed earlier. A key motivation for methanol detection is its association with poisoning outbreaks caused by the consumption of adulterated alcohol, which frequently overwhelms healthcare facilities in developing countries, leading to devastating consequences such as organ failure, blindness, and even death. [18, 19] Rapid detection for the screening of laced beverages is crucial and can be facilitated by measuring methanol concentration in human breath, which is approximately 0.4 ppm in healthy individuals. [20]

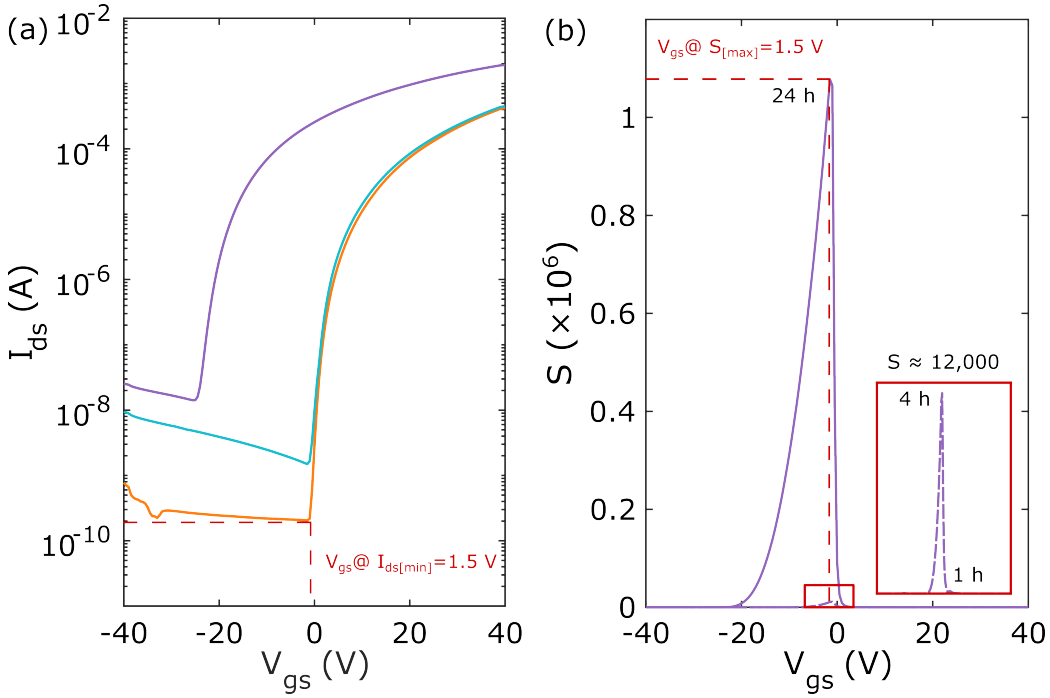

Figure 5.11: (a) Transfer characteristics for the ZTO-ZTO TFT in the saturation regime at $V_{ds} = 40\,V$, $V_{gs} = -40\,V$ to $40\,V$ and $L = 80\,\mu m$ following overnight exposure to methanol vapour and recovery with heat treatment (solid orange plot). (b) Calculated sensitivities following 1 hour, 4 hours and 24 hours exposure periods.

In this case, Figures 5.11(a) and (b) show that $I_{ds[min]}$ of the as-prepared ZTO-ZTO TFT (solid orange lines) was measured at $V_{gs} = -1.50\,\text{V}$, with maximum sensitivity ($S_{max} = 1.08 \times 10^6$) achieved at this point. The calculated responsivity after overnight exposure, shown in Figure 5.11(b) (24 h, solid purple lines), far exceeded that measured for acetone, IPA, and toluene vapours. The excellent $I_{on/off} > 10^7$ and low $V_{th} = 3.1\,\text{V}$ of the as-prepared TFT resulted in a difference in I_{ds} of 10^6 at the V_{gs} corresponding to S_{max}.

The electronic parameters of the as-prepared TFT, as well as after exposure and recovery with heat treatment, are summarised in Table 5.6. Since methanol adsorbed readily onto the ZTO-ZTO TFT, the recovery time was reduced from 1 h to 15 min. All key metrics returned to values close to those prior to exposure: $I_{on/off}$ between 10^6 and 10^7, $\mu_{eff} \approx 5\,\text{cm}^2\,\text{V}^{-1}\,\text{s}^{-1}$, and $V_{th} \approx 3\,\text{V}$. This indicates that the ZTO-ZTO TFT sensors demonstrated high reliability even after 24 hours of exposure, which is critical for this application.

The results presented thus far have demonstrated the calculated sensitivity following overnight exposure, ensuring that the solvent under test had fully evaporated and the TFT sensor was saturated with the vapour. To further evaluate the reliability and practical applicability of the ZTO-ZTO TFT sensor, Figure 5.12 illustrates its methanol response measured at different levels of a saturated atmosphere by varying the exposure duration from short (1 hour) to long (4 hours) and overnight (24 hours). The ZTO-ZTO

Table 5.6: $I_{on/off}$, μ, μ_{eff} and V_{th} of ZTO-ZTO TFTs before exposure and after exposure to methanol for 1 hour, 4 hours and 24 hours.

	$I_{on/off}$	μ ($\text{cm}^2\,\text{V}^{-1}\,\text{s}^{-1}$)	μ_{eff} ($\text{cm}^2\,\text{V}^{-1}\,\text{s}^{-1}$)	V_{th} (V)
As-prepared	10^7	5.21	4.66	3.14
Methanol (24 hours)	10^5	8.90	8.62	-23.3
Recovery	10^6	5.48	4.95	2.63
Methanol (4 hours)	10^5	2.04	2.87	-6.67
Recovery	10^6	1.71	1.45	4.86
Methanol (1 hour)	10^5	2.11	1.88	2.95

TFT was recovered with heat treatment for 15 min after each exposure cycle, as previously described (grey lines).

Notably, even after just 1 hour of exposure, a clear decrease in the resistance of the ZTO-ZTO film was observed, as evidenced by a promising V_{th} shift of $-1.9\,\mathrm{V}$, listed in Table 5.6 (lines 5–6). This shift resulted in a maximum sensitivity of $S_{max} < 400$ at $V_{gs} = -2.40\,\mathrm{V}$. The ZTO-ZTO TFT was more responsive ($S_{max} = 11,400$ at $V_{gs} = -1\,\mathrm{V}$) after exposure to methanol for 4 hours (Figure 5.11(b) inset, dashed purple lines) compared with overnight exposure to acetone ($S_{max} = 9{,}330$ at $V_{gs} = -2.40\,\mathrm{V}$). $I_{ds[min]}$ prior to V_{th} of the recovery curve following overnight exposure was at $V_{gs} = -1.50\,\mathrm{V}$, which correlated well with the position of S_{max}.

Finally, Figures 5.13(a)-(b) illustrate the responses of the ZTO-ZTO TFT to acetone, IPA, and methanol at fixed gate voltages ($V_{gs} = 15\,\mathrm{V}$, $25\,\mathrm{V}$, and

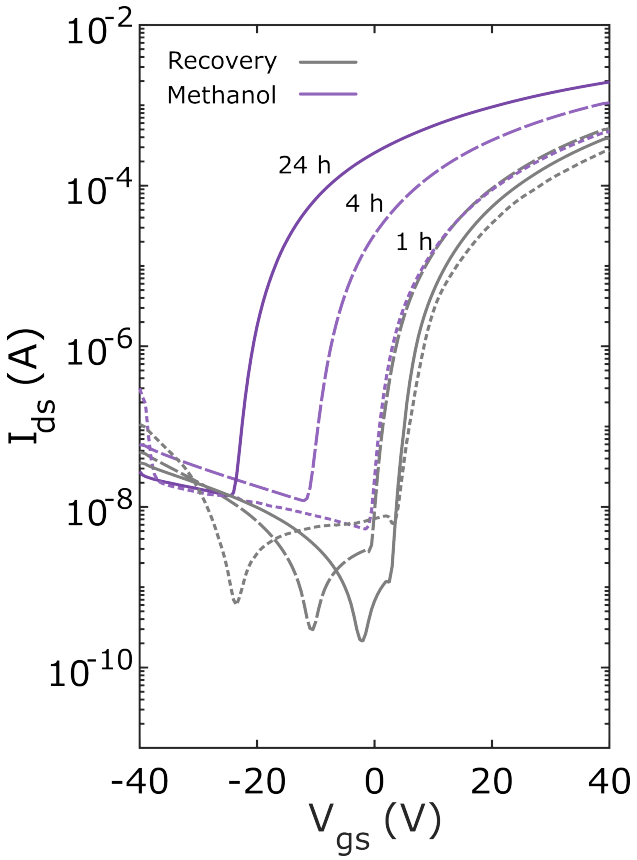

Figure 5.12: (a) Transfer characteristics for the ZTO-ZTO TFT in the saturation regime at $V_{ds} = 40\,\mathrm{V}$, $V_{gs} = -40\,\mathrm{V}$ to $40\,\mathrm{V}$ and $L = 80\,\mu\mathrm{m}$ following 1 hour, 4 hours and 24 hours exposure periods.

35 V) in both the linear and saturation regimes, with drain-source voltages of 10 V and 40 V, respectively. For reference, the calculated sensitivities, derived from the output characteristics in Figures 5.14(a)-(b), were evaluated before and after methanol exposure. In both regimes, sensitivity (S) was maximised as V_{gs} approached V_{th} of the as-prepared TFTs following exposure to oxygen-related VOCs. For acetone, S decreased with increasing V_{gs}, from 2.8 to 1.3 and 0.8 in the linear regime and from 5.8 to 2.5 and 1.4 in saturation. A similar trend was observed for IPA, where S dropped from 8.2 to 3.4 and 2.0 in the linear regime and from 16.6 to 6.7 and 2.7 in saturation. Methanol exhibited the highest sensitivity, decreasing from 16.0 to 4.8 and 2.7 in the linear regime and from 31.5 to 9.4 and 4.9 in saturation. These results confirm that the ZTO-ZTO TFTs were highly responsive to vapours containing hydroxyl groups, particularly methanol, with sensitivity enhanced in the saturation regime. This trend aligns with earlier observations for both single layer SnO_2 TFTs exposed to acetone and ZTO-ZnO TFTs exposed

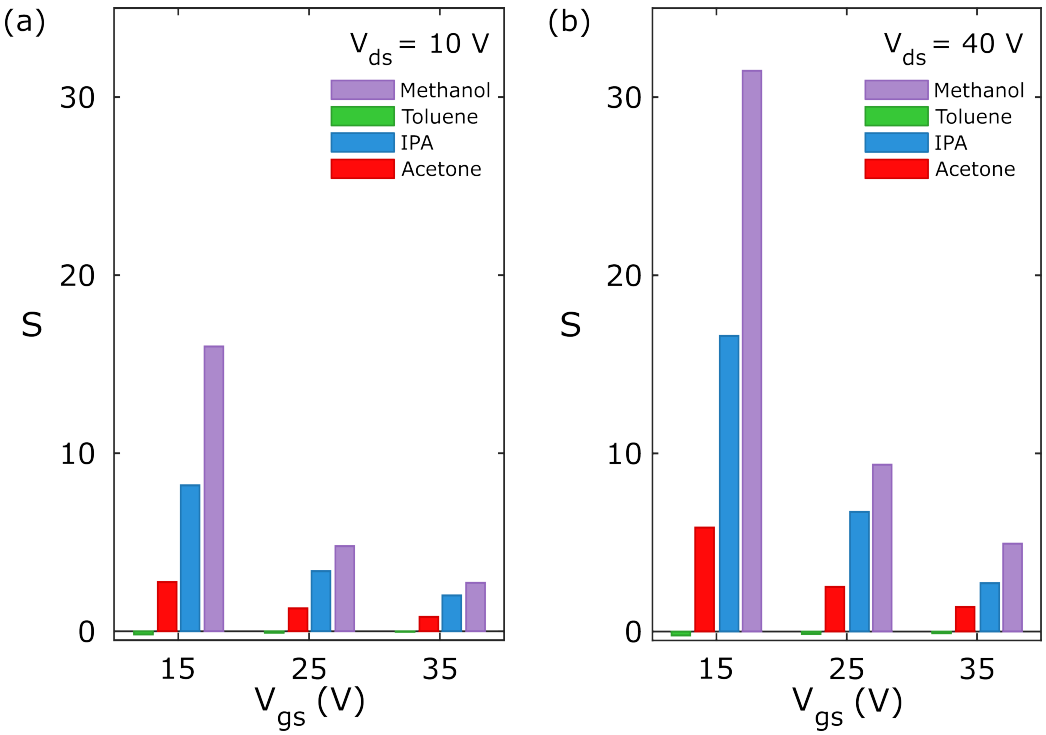

Figure 5.13: (a) Calculated sensitivity for ZTO-ZTO TFT following exposure to acetone, IPA, toluene, & methanol vapours (b) at fixed V_{gs} in the linear (V_{ds} = 10 V) and saturation regimes (V_{ds} = 40 V).

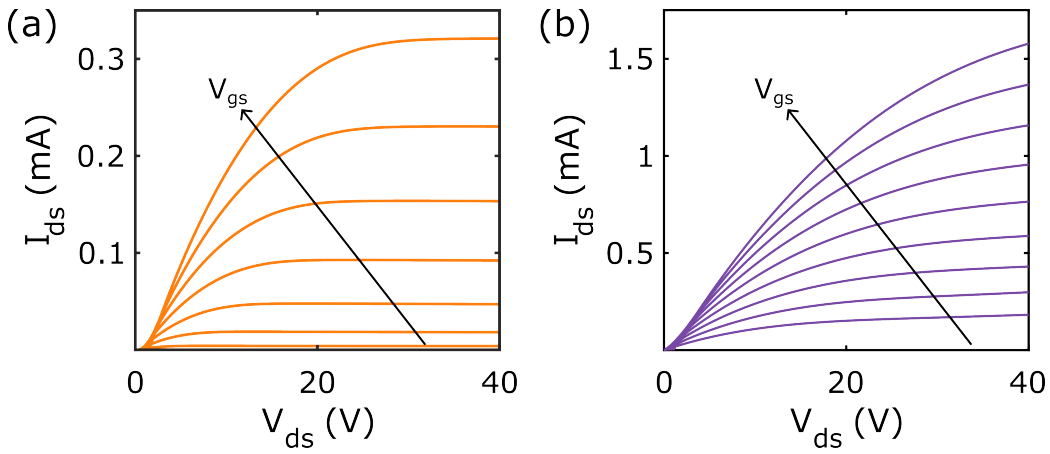

Figure 5.14: Output characteristics for the (a) as-prepared ZTO-ZTO TFT and (b) following exposure to methanol at $V_{ds}, V_{gs} = 0\,\text{V}$ to $40\,\text{V}$.

to IPA. The strong response is attributed to the high oxygen vacancy and M–OH contents, which provided specific adsorption sites. Methanol likely adsorbed more readily to the ZTO-ZTO TFT than IPA due to its lower vapour pressure, smaller size and lower molecular weight.

5.4 Summary

In summary, this Chapter has addressed the origin of the enhanced chemiresistive functionality of ZTO-based TFTs at low-voltage operation. The chemical environment heavily influenced the carrier transport properties of ZTO-based TFTs and can be tailored toward the detection of specific VOCs, ensuring that high specificity can be achieved for the diagnosis of life-threatening conditions by simple breath analysis.

Previously, the ZTO-ZnO TFT exhibited poor $I_{on/off} < 10^4$ and exceptionally low mobility ($\mu_{eff} \approx 0.1\,\text{cm}^2\,\text{V}^{-1}\,\text{s}^{-1}$), which minimised the relative change in I_{ds} after exposure to a selection of VOCs with different functional groups, specifically acetone, IPA and toluene. Its much rougher surface morphology and relatively low oxygen vacancy content (26.2 %) not only hindered carrier transport properties but chiefly the adsorption of these VOCs, which led to $S_{max} < 100$. Conversely, the ZTO-ZTO TFT achieved near-zero $V_{th} = 2.20\,\text{V}$ and excellent switching properties ($I_{on/off} > 10^7$) while maintaining

high mobility ($\mu_{eff} \approx 10\,\mathrm{cm^2\,V^{-1}\,s^{-1}}$). Its low surface roughness, superb Zn and Sn intermixing, high oxygen vacancy (31.2 %) and M-OH bonding (11.4 %) contents meant that this TFT was deemed an ideal chemiresistive sensor and subsequently underwent the same exposure tests. Qualitative analyses of both TFTs demonstrated high specificity to alcohol vapours at low-voltage operation. More importantly, the ZTO-ZTO TFT achieved $S_{max} = 1.08 \times 10^6$ following exposure to methanol, which was over two orders of magnitude greater than acetone. The difference in sensing characteristics suggested that ZTO-ZTO TFTs could achieve accurate cross-sensitivity to components in exhaled breath, with high responsivity at the required V_{gs}.

References

[1] J. Lee, Y. Choi, B. J. Park *et al.*, "Precise control of surface oxygen vacancies in ZnO nanoparticles for extremely high acetone sensing response," *J Adv Ceram*, vol. 11, no. 5, pp. 769–783, 2022.

[2] S. Ruzgar and M. Caglar, "The effect of Sn on electrical performance of zinc oxide based thin film transistor," *J Mater Sci: Mater Electron*, vol. 30, no. 1, pp. 485–490, 2019.

[3] M. Lei, L. Guo, C. Wang *et al.*, "Analysis of the valence state of tin in ZnSnOx thin-film transistors," *J Mater Sci: Mater Electron*, vol. 33, no. 32, pp. 24 785–24 793, 2022.

[4] G. Gordillo, L. C. Moreno, W. de la Cruz, and P. Teheran, "Preparation and characterization of SnO2 thin films deposited by spray pyrolysis from SnCl2 and SnCl4 precursors," *Thin Solid Films*, vol. 252, no. 1, pp. 61–66, 1994.

[5] L.-C. Liu, J.-S. Chen, J.-S. Jeng, and W.-Y. Chen, "Variation of Oxygen Deficiency in Solution-Processed Ultra-Thin Zinc-Tin Oxide Films to Their Transistor Characteristics," *ECS J. Solid State Sci. Technol.*, vol. 2, no. 4, p. Q59, 2013.

[6] H. Yuan, S. A. A. A. Aljneibi, J. Yuan *et al.*, "ZnO Nanosheets Abundant in Oxygen Vacancies Derived from Metal-Organic Frameworks for ppb-Level Gas Sensing," *Advanced Materials*, vol. 31, no. 11, p. 1807161, 2019.

[7] Z. Geng, X. Kong, W. Chen *et al.*, "Oxygen vacancies in zno nanosheets enhance co2 electrochemical reduction to co," *Angewandte Chemie International Edition*, vol. 57, no. 21, pp. 6054–6059, 2018.

[8] Q. Zhang, G. Xia, L. Li *et al.*, "High-performance Zinc-Tin-Oxide thin film transistors based on environment friendly solution process," *Current Applied Physics*, vol. 19, no. 2, pp. 174–181, 2019.

[9] Y. R. Denny, K. Lee, S. Seo *et al.*, "Electrical, electronic and optical properties of amorphous indium zinc tin oxide thin films," *Applied Surface Science*, vol. 315, pp. 454–458, 2014.

[10] Manju, M. Jain, S. Madas *et al.*, "Oxygen vacancies induced photoluminescence in $$\hbox {SrZnO}_2$$ nanophosphors probed by theoretical and experimental analysis," *Scientific Reports*, vol. 10, no. 1, p. 17364, 2020.

[11] C. Yim, M. Lee, W. Kim *et al.*, "Adsorption and desorption characteristics of alcohol vapors on a nanoporous ZIF-8 film investigated using silicon microcantilevers," *Chemical Communications*, vol. 51, no. 28, pp. 6168–6171, 2015.

[12] A. Mirzaei, J.-H. Kim, H. W. Kim, and S. S. Kim, "Resistive-based gas sensors for detection of benzene, toluene and xylene (BTX) gases: a review," *J. Mater. Chem. C*, vol. 6, no. 16, pp. 4342–4370, 2018.

[13] H. Hu, J. Zhu, F. Yang *et al.*, "A robust etb-type metal–organic framework showing polarity-exclusive adsorption of acetone over methanol for their azeotropic mixture," *Chem. Commun.*, vol. 55, no. 46, pp. 6495–6498, 2019.

[14] Y. Luo, Y. Lv, P. Kumar *et al.*, "Epitaxial growth: rapid synthesis of highly permeable and selective zeolite-T membranes," *J. Mater. Chem. A*, vol. 5, no. 34, pp. 17 828–17 832, 2017.

[15] M. Raees A, A. Alexander, A. B. Pillai *et al.*, "Sequential photoluminescence measurements to explore electron-trapping dynamics in slow photoresponse materials: Zinc oxide thin films as a model system," *Phys. Rev. Appl.*, vol. 19, p. 064034, Jun 2023.

[16] J. Wang, Z. Wang, B. Huang *et al.*, "Oxygen Vacancy Induced Band-Gap Narrowing and Enhanced Visible Light Photocatalytic Activity of ZnO," *ACS Appl. Mater. Interfaces*, vol. 4, no. 8, pp. 4024–4030, 2012.

[17] K. S. Kim, C. H. Ahn, S. H. Jung *et al.*, "Toward Adequate Operation of Amorphous Oxide Thin-Film Transistors for Low-Concentration Gas Detection," *ACS Appl. Mater. Interfaces*, vol. 10, no. 12, pp. 10 185–10 193, 2018.

[18] A. Mashallahi, M. Mohamadkhani, and A. Ostadtaghizadeh, "Methanol Poisoning Outbreaks in Southern Iran in 2018: A Lesson Learned," *Iran J Public Health*, vol. 50, no. 7, pp. 1502–1503, 2021.

[19] J. van den Broek, S. Abegg, S. E. Pratsinis, and A. T. Güntner, "Highly selective detection of methanol over ethanol by a handheld gas sensor," *Nat Commun*, vol. 10, no. 1, p. 4220, 2019.

[20] Z. Nekoukar, Z. Zakariaei, F. Taghizadeh *et al.*, "Methanol poisoning as a new world challenge: A review," *Annals of Medicine and Surgery*, vol. 66, p. 102445, 2021.

Chapter 6

Water-Gated Thin-Film Transistors

6.1 Chapter Overview

This chapter presents an alternative low-voltage transistor technology capable of detecting both positively and negatively charged aqueous species within a single architecture, further expanding the prospects for chemical sensing and medical diagnostics. To achieve this, two straightforward design strategies were implemented in the fabrication of ambipolar water-gated thin-film transistors (WG-TFTs). First, the individual performances of the organic p-type and n-type semiconductors were evaluated as unipolar WG-TFTs. Subsequently, their ambipolar behaviour was examined by blending the two components into a single active layer using a bulk heterojunction (BHJ) structure. The amphiphilic fullerene $PrC_{60}MA$ governed n-type trans-

port and was individually blended with one of two polymers – either P3HT or PCDTPT – to enable p-type transport. A full description of these materials was provided in Chapter 2.4.2. The blend composition, processing conditions, and thermal treatments were carefully controlled to tailor the morphology of the active layer, which was analysed using vapour phase infiltration (VPI) and water contact angle measurements. The performance of the blends depended not only on the polymer's influence on morphology but also on energy level alignment. While the impact of thermally-induced phase-separation on the performance of organic photovoltaics (OPVs) is well established, this work is the first to examine its adverse effects on the ambipolarity of WG-TFTs.

Secondly, bilayer and hybrid (organic/inorganic) WG-TFTs were investigated to eliminate the effects of thermally-induced phase-separation between organic materials. To achieve this, an organic p-type polymer was deposited onto an n-type metal oxide underlayer. Specifically, this configuration consisted of a ZnO underlayer with PCDTPT spin-coated on top to promote surface enrichment.

6.2 Organic WG-TFTs

WG-TFTs exhibit excellent environmental and electrochemical stability, along with high switching speeds – critical attributes for the reliable transfer of biological and chemical signals in systems relying on CMOS-like circuit architectures [1–5]. While individual p-type and n-type WG-TFTs based on the polymer P3HT and small molecule [6,6]-phenyl-C_{61}-butyric acid methyl ester (PCBM), respectively, have been reported for such applications [6, 7], reports on WG-TFTs exhibiting ambipolar behaviour i.e., capable of operating in both p-type and n-type modes under appropriate biasing conditions, remain limited. The integration of ambipolar WG-TFTs into interconnected networks offers a promising route to programmable logic circuits with polymorphic functionality. Such an approach could significantly reduce circuit

complexity, cut processing steps, and decrease fabrication costs relative to architectures based on separate unipolar TFTs for cation and anion detection. [8]

To achieve balanced ambipolar device performance, blends based on PCBM and P3HT – materials that have formed the foundation of OPV research and have since been adapted for organic TFTs (OTFTs) – offer a logical starting point for the fabrication of ambipolar WG-TFTs. By blending p-type and n-type materials into a single active layer, with each component responsible for transporting one type of charge carrier, this approach circumvents the need for complex synthesis of novel ambipolar materials. It also mitigates the inherent trade-off often encountered in single-material systems. A common limitation in such systems is asymmetrical charge transport, wherein the carrier mobility of one component is significantly higher than that of the other, resulting in predominantly unipolar operation [9,10]. To evaluate this strategy, the performance of stand-alone p- and n-type organic WG-TFTs was first investigated, followed by an assessment of their ambipolarity when incorporated into a BHJ channel.

6.2.1 P3HT WG- TFTs

Hereinafter, the WG-TFTs described adopted a top gate architecture (Figure 6.1(a)), and the source-drain geometries are detailed in Chapter 3.9.2. For unipolar p-type performance, the hole-transporting channel consisted of regioregular (RR) P3HT. In the following electrical characterisation, it was not possible to calculate μ_{eff} as the transfer characteristics in some cases were measured from a non-zero V_{gs}. Consequently, only μ was extracted. A detailed derivation of the calculation of μ_{eff} is provided in Chapter 3.10.

The P3HT WG-TFT exhibited p-type behaviour: clear linear and saturation regimes were observed in the output curves in the third quadrant, with $I_{ds[max]} = -1.50\,\mu\text{A}$ (Figure 6.1(a)). A double-layer capacitance of $3\,\mu\text{F}\,\text{cm}^{-2}$ at the water–organic semiconductor interface was assumed. This value was taken from the literature [1,11], in which the same concentration and solvent

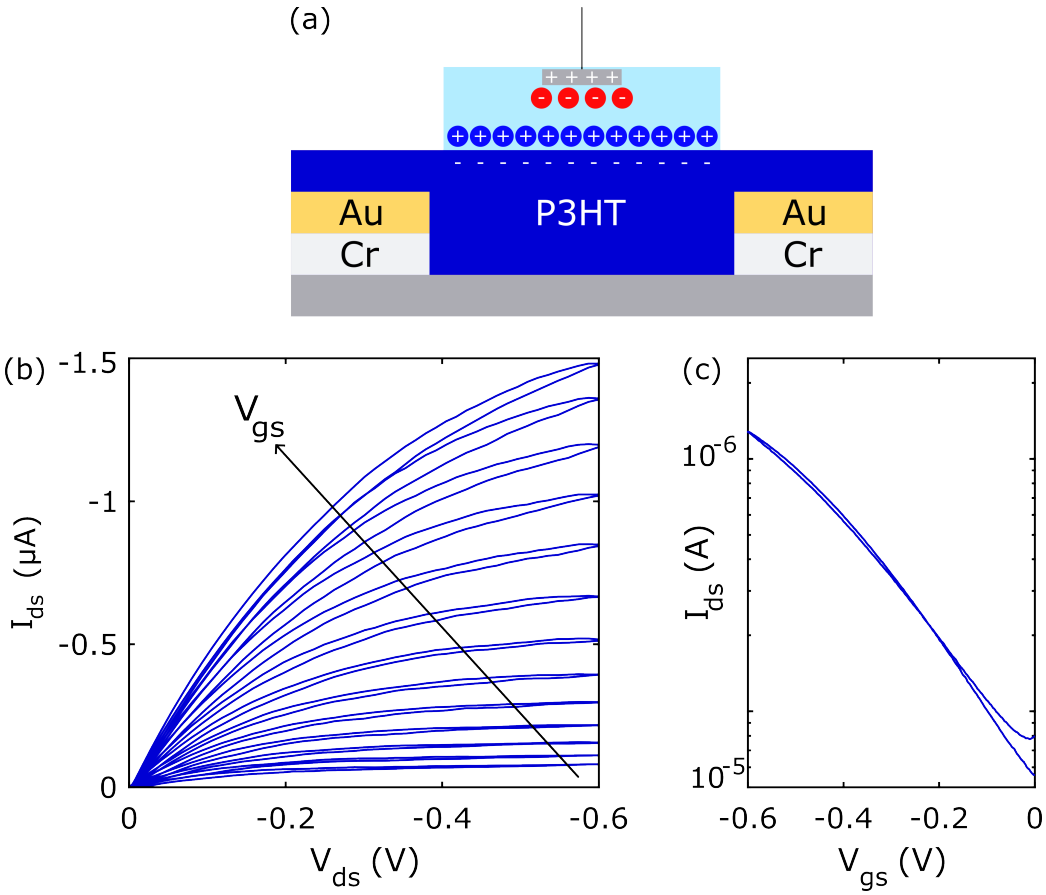

Figure 6.1: (a) Device schematic in p-type mode. (b) Output characteristics of thermally treated pristine P3HT WG-TFTs at $V_{ds}, V_{gs} = 0\,\mathrm{V}$ to $-0.6\,\mathrm{V}$. (c) Transfer characteristics at $V_{ds} = -0.6\,\mathrm{V}$ and $V_{gs} = 0\,\mathrm{V}$ to $-0.6\,\mathrm{V}$.

were used to dissolve the P3HT precursor, since a suitable impedance measurement setup was not available. In this work, it is further assumed that charge transport was governed solely by surface charge accumulation and that the channel was not doped through ion infiltration. However, this assumption could not be verified experimentally, as time-response measurements – in which rapid surface charging, typically observed in electrolyte-gated transistors, can be distinguished from the slower volumetric doping characteristic of OECT-dominated regimes – were not performed. [12]

The $I_{on/off}$, V_{th}, and μ were calculated from the transfer characteristics, shown in Figure 6.1(b), as 10^2, $-0.12\,\mathrm{V}$, and $0.04\,\mathrm{cm^2\,V^{-1}\,s^{-1}}$, respectively (see Table 6.1).

Table 6.1: $I_{on/off}$, μ, $I_{ds[max]}$ and V_{th} of organic WG-TFTs.

Material	Polarity	μ ($cm^2\,V^{-1}\,s^{-1}$)	$I_{on/off}$	V_{th} (V)	$I_{ds[max]}$ (µA)
P3HT	p	0.04	10^2	-0.12	-1.5
$PrC_{60}MA$	n	0.43	10^4	0.15	10.9

6.2.2 $PrC_{60}MA$ WG-TFTs

So far, the lack of suitable n-type organic materials has meant that the majority of WG-TFTs reported have operated as p-type devices. The first demonstration of n-type WG-TFTs was by Porrazzo *et al.*, [6] using two naphthalene diimide co-polymers and a soluble fullerene derivative. The highest I_{ds} values were measured with PCBM (1.1 µA at $V_{gs} = 0.8$ V), with a near-zero threshold voltage ($V_{th} = 0.18$ V). However, these devices required channel lengths in the order of a few microns to drive electron transport, which was only made possible through expensive lithographic processing.

Recently, amphiphilic fullerenes functionalised with ethylene glycol (EG) side chains have been shown to enhance electron transport in both OTFTs and organic electrochemical transistors (OECTs) due to their excellent self-assembly capabilities [13–15]. Hence, a fullerene derivative $PrC_{60}MA$ was used for n-type transport. Figure 6.2(a) shows the chemical structure of $PrC_{60}MA$, containing three EG side chains each with three oxygen repeating units. The impact of side-chain engineering on the $PrC_{60}MA$ film morphology is significant. The alternating fullerene moieties and polar CH_2CH_2O side chains induce spontaneous phase-separation, leading to a layered morphology. This behaviour promotes the crystallisation and alignment of $PrC_{60}MA$ molecules upon thermal annealing, consistent with observations in long-chain alkyl-substituted C_{60} derivatives, while avoiding the electron transport limitations typically associated with grain boundaries in PCBM films. [16–18] The improved structural order and creation of electron percolation pathways reduces the high W/L ratios typically required for n-type operation in PCBM channels. Additionally, the polarity of the EG side chains ensures good solu-

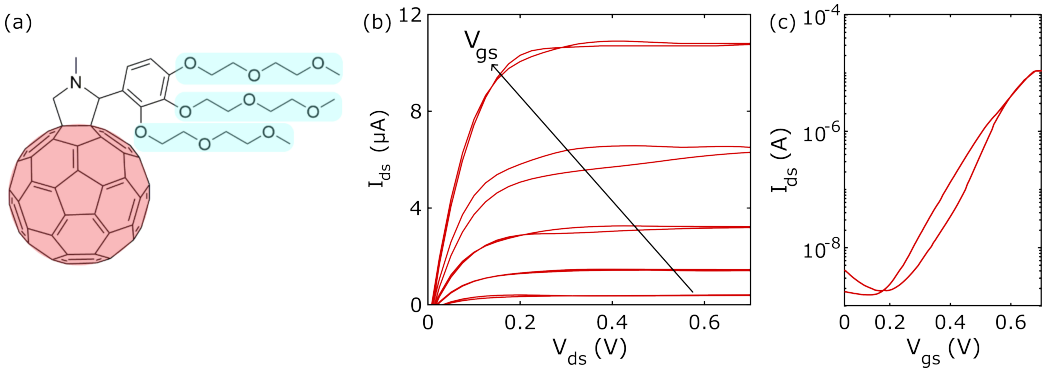

Figure 6.2: (a) Chemical structure of $PrC_{60}MA$. (b) Output characteristics thermally treated pristine $PrC_{60}MA$ WG-TFTs at $V_{ds}, V_{gs} = 0\,V$ to $0.7\,V$. (c) Transfer characteristics at $V_{ds} = -0.6\,V$ and $V_{gs} = 0\,V$ to $0.7\,V$.

bility in chloroform, making $PrC_{60}MA$ well suited for the solution-processing techniques employed here.

WG-TFTs operating in the n-type regime were fabricated using the same device architecture as Stein *et al.*, [14] but with DI water as the gating medium instead of the 0.1 M KCl aqueous electrolyte. The output characteristics, shown in Figure 6.2(b), reached $I_{ds[max]} = 10.9\,\mu A$. Assuming an identical double-layer capacitance of $3\,\mu F$ as discussed in §6.2, an impressive mobility of $\mu = 0.43\,cm^2\,V^{-1}\,s^{-1}$ was achieved, which far exceeded that obtained by Porrazzo *et al.*, with PCBM OFETs ($\mu = 0.008\,cm^2\,V^{-1}\,s^{-1}$). [6] Along with the high $I_{on/off} > 10^4$ and low $V_{th} = 0.15\,V$, as shown in Figure 6.2(c), this outstanding performance is inferred to stem from the formation of extended layered structures and efficient molecular packing, which is afforded by the presence of the EG side chains.

The electrical characterisation described thus far led to the development of a simple methodology to engineer balanced and ambipolar all-organic WG-TFTs, based on P3HT blended with $PrC_{60}MA$ for p- and n-type transport, respectively. The morphology of the active layer was crucial for achieving balanced ambipolarity and was controlled by adjusting the thermal treatments and blend ratios of the BHJ film, which will be discussed in the next section.

6.3 Ambipolar Blend-based Organic WG-TFTs

6.3.1 Water Contact Angle Measurements

During the spin coating of blend films, it is well documented that the component with the lowest surface energy tends to enrich the surface, while the other component segregates to the substrate [19–21]. This phase-separation could negatively impact the ambipolar performance of blend-based WG-TFTs, as they rely on the formation of an interdigitated network of p- and n-type domains at the film surface. Thus, water contact angle measurements were performed to qualitatively assess the surface energies of the $PrC_{60}MA$:P3HT blends. This technique was described in Chapter 3.8.

Water contact angle measurements were used to assess the wettability of the films by measuring the angle formed between a water droplet and the surface. A contact angle $\theta_w < 90°$ indicated a hydrophilic surface (higher surface energy), while $\theta_w > 90°$ signified a hydrophobic surface (lower surface energy). [12] The as-cast P3HT film exhibited poor wettability with a high contact angle of $\theta \approx 108°$ (Figure 6.3(a)), whereas the $PrC_{60}MA$ film showed good wettability with a much lower angle of $\theta \approx 67°$ (Figure 6.3(e)), consistent with previous studies of C_{60} thin films ($\theta \approx 72°$). [22] This difference suggests that P3HT has lower surface energy than $PrC_{60}MA$, likely due to its non-polar, hydrophobic alkyl side chains [20, 23]. In $PrC_{60}MA$:P3HT

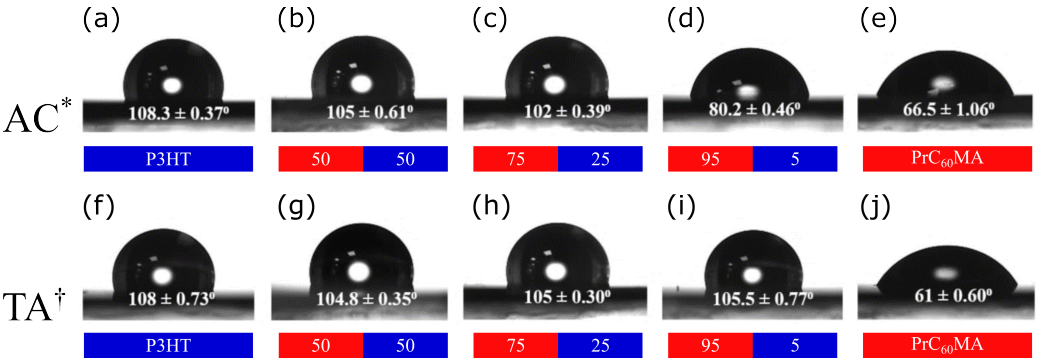

Figure 6.3: Contact angle measurements of the (a)-(e) as-cast (AC^*) and (f),(j) thermally annealed ($TA^\dagger$) pristine P3HT, $PrC_{60}MA$ and $PrC_{60}MA$:P3HT blend films with (b),(g) 50:50, (c),(h) 75:25 and (d),(i) 95:5 blend ratios.

blends, the contact angle decreased from $\theta \approx 105°$ at 50 % $PrC_{60}MA$ content to 102° and 80° at 75 % and 95 %, respectively (Figures 6.3(b)–(d)). This trend reflects the increasing hydrophilicity of the surface as the content of $PrC_{60}MA$ increases, demonstrating the role of its hydrophilic side chains in counteracting the fullerene core's inherent hydrophobicity.

These as-cast films were then thermally treated using the same methodology outlined in Chapter 3.9.2. The thermally treated P3HT film exhibited a contact angle of 108°, similar to that of the as-cast film (Figure 6.3(f)). In contrast, Figure 6.3(j) shows that the $PrC_{60}MA$ film became more hydrophilic upon thermal treatment, as evidenced by a decrease in contact angle to 61°, which indicated increased wetting. This may have been attributed to the reorganisation and better ordering of the $PrC_{60}MA$ films encouraged by thermal treatment.

Notably, for the blend films, the contact angle remained above 100° irrespective of $PrC_{60}MA$ content (Figures 6.3(g)-(i)). Even the 95:5 blend film exhibited a high contact angle of $\theta \approx 105.5°$ (Figure 6.3(i)), comparable to that of pristine P3HT, despite containing only a small fraction of the polymer. This behaviour contrasts with the as-cast blend films since increasing $PrC_{60}MA$ content resulted in a more hydrophilic surface. The differences in contact angle before and after thermal treatment suggest that heating induced a phase-separated bilayer structure. It is thus inferred that P3HT migrated to the water-organic semiconductor interface during thermal treatment, creating a more hydrophobic surface.

6.3.2 Vapour Phase Infiltration (VPI)

The pristine and blend films were then subjected to a VPI process to reveal their nanoscale morphology using SEM, through the *in-situ* deposition of diethylzinc (DEZ) vapours and subsequent conversion to ZnO (see Chapter 3.4). Visualising the different phases in organic films is generally challenging, as porous domains are not detectable by X-ray or electron diffraction methods. Organic films are additionally electron beam sensitive, meaning they

are easily damaged by electron irradiation, leading to degradation or even destruction of the sample during standard SEM or TEM analyses. [14, 20] Furthermore, the electrical characterisation of WG-TFTs does not account for the complexity of the blend morphology. However in VPI, the ZnO precursors selectively infiltrate the porous regions of blend films due to the working mechanism of atomic layer deposition, resulting in a Z-contrast detectable by cross-sectional SEM.

To begin, VPI was used to image pristine P3HT films, both as-cast and thermally treated. Precursor infiltration was strongly temperature-dependent. In the case of P3HT, the ZnO precursors readily infiltrated both the as-cast (Figure 6.4(a),(b)) and thermally treated (Figure 6.4(c),(d)) films, as evidenced by the strong bright contrast, due to its low transition temperature ($T_g = 12\,°C$). [21] High-magnification images of the as-cast and thermally treated samples (Figure 6.4(b),(d)) revealed that ZnO was evenly distributed, with particle sizes and spacing in the tens of nanometres. ZnO occupied a significant proportion of the film volume, suggesting substantial porosity, which aligned with previous studies on RR-P3HT of similar molecular weight and processing conditions. [21] These findings indicated that P3HT films, particularly in the as-cast state, exhibited a predominantly amorphous morphology and allowed precursor infiltration through these regions.

In contrast, it is well established that crystalline or ordered domains lack the free volume necessary for the precursor to infiltrate the film and hence

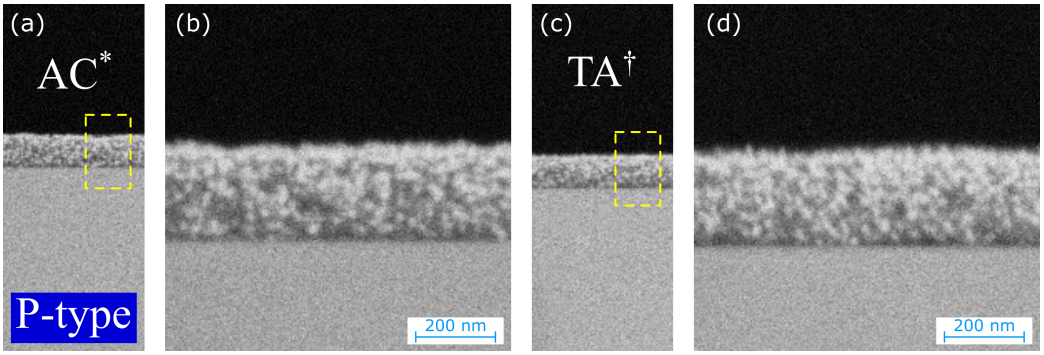

Figure 6.4: Cross-sectional analyses of the (a),(b) as-cast (AC^*) and (c),(d) thermally annealed ($TA^\dagger$) pristine P3HT films. (a),(c) Low- and (b),(d) high-magnification VPI images (yellow dashed square).

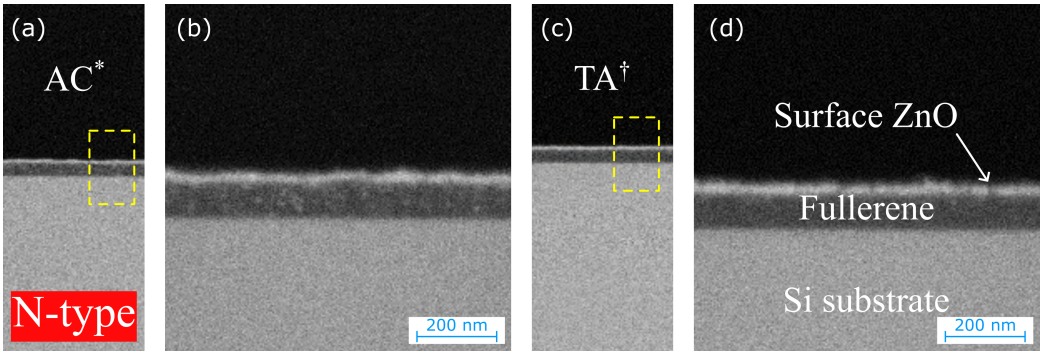

Figure 6.5: Cross-sectional analyses of the (a),(b) as-cast (AC^*) and (c),(d) thermally annealed ($TA^\dagger$) pristine $PrC_{60}MA$ films. (a),(c) Low- and (b),(d) high-magnification VPI images (yellow dashed square).

no metal oxide deposition occurs in their bulk. [24] As such, the ZnO precursors tended to accumulate on the surface of $PrC_{60}MA$ films with limited infiltration (Figure 6.5)(a),(b)), particularly for the thermally treated sample (Figure 6.5)(c),(d)). This suggests that $PrC_{60}MA$ was highly crystalline alike other fullerenes studied by Obuchovsky *et al.,* including $PC_{60}BM$, $PC_{70}BM$, BIS-PCBM and ICBA. [20,21] Since these materials possessed high T_g values of 120 °C, 160 °C, 145 °C and 168 °C, it was likely that $PrC_{60}MA$ had a T_g value way above the 60 °C used for the ALD process, as this has not been stated explicitly in the literature. Hence, ZnO was deposited only on the surface of the $PrC_{60}MA$ film and there was limited infiltration. This was in agreement with previous reports by Stein *et al.,* using an identical VPI process to image $PrC_{60}MA$ films. [14] Their grazing incidence wide angle X-ray scattering (GIWAXS) measurements showed well-defined diffraction spots, which supported that $PrC_{60}MA$ formed a highly crystalline morphology with a strong preferential orientation relative to the substrate.

Next, both as-cast and thermally treated $PrC_{60}MA$:P3HT blend films were imaged using VPI. As the images were acquired using back-scattered electrons (BSE), the bright domains correspond to regions of higher atomic density, specifically ZnO particles dispersed within the BHJ matrix. The diffusion of ALD precursors, and their subsequent *in situ* conversion to metal oxide, generally occurred in the porous regions of P3HT. As such, the location of ZnO domains after the ALD process was indicative of amorphous regions

in the original film that were not saturated with $PrC_{60}MA$.

The cross-sectional SEM images in Figure 6.6(a) and (b) show that ZnO particles are distributed throughout the as-cast BHJ with the highest fullerene content (95:5), although less densely than in pristine P3HT films due to the lower polymer concentration. This confirms a predominantly BHJ-like morphology, with some sub-surface ZnO deposition. Two distinct phases are observed: a brighter surface layer attributed to P3HT, and a darker bulk region containing bright ZnO-rich spots. A small number of dark spots are also present at the surface, consistent with increased hydrophilicity and enhanced wetting, as reflected by the reduced water contact angle (see Figure 6.3(d)). Importantly, connectivity between P3HT chains is preserved, with brighter domains forming percolation pathways critical for efficient hole transport.

Upon thermal treatment, the BHJ morphology underwent phase-separation, forming a structure clearly defined by two distinct layers, as shown in Figure 6.6(c) and (d). A thicker ZnO-rich layer accumulated at the film surface, corresponding to P3HT, indicating the formation of a bilayer channel due to thermally-induced phase-separation. This effect can be attributed to the significant difference in surface energies between the two components. The absence of ZnO-related bright spots in the film bulk suggests that $PrC_{60}MA$ preferentially occupied this region, particularly near the substrate–organic interface, thereby hindering ZnO deposition in those areas. This interpretation is supported by water contact angle measurements (Figure 6.3(i)), which

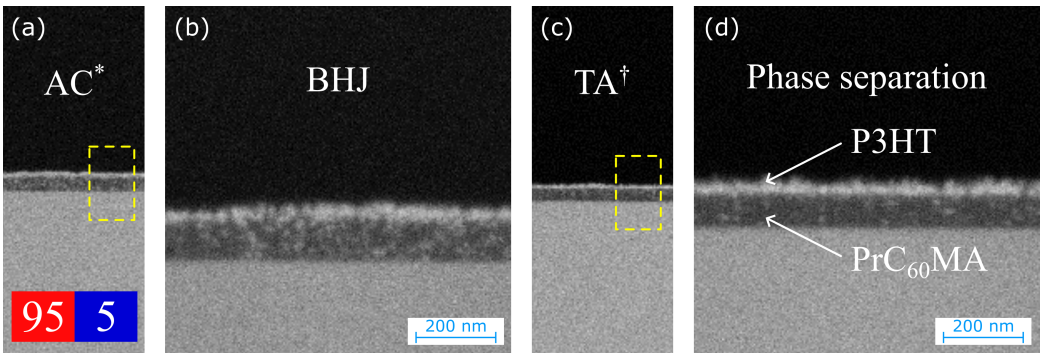

Figure 6.6: Cross-sectional analyses of the (a),(b) as-cast (AC^*) and (c),(d) thermally annealed ($TA^\dagger$) $PrC_{60}MA$:P3HT (95:5) BHJ films. (a),(c) Low- and (b),(d) high-magnification VPI images (yellow dashed square).

yielded values of $\theta > 90°$, indicating poor wetting and a hydrophobic surface composed predominantly of P3HT. Obuchovsky *et al.* also investigated the diffusion of ALD precursors in small molecule–polymer BHJ systems. They observed that phase-separation occurred in blends with PCBM contents above approximately 17 %, particularly when thermally treated, consistent with the behaviour of the blend films studied here [20]. Their findings suggested that the films comprised crystalline P3HT, intermixed P3HT:fullerene domains, and impenetrable, phase-separated fullerene aggregates. In this context, the fullerene competed with ALD precursors for occupancy of the amorphous domains in P3HT, reducing the free volume available for precursor diffusion.

The results presented in §6.2 demonstrated that both materials functioned effectively as stand-alone WG-TFTs. When blended, VPI images of the $PrC_{60}MA$:P3HT BHJ suggest that ambipolar behaviour would be more likely in the as-cast $PrC_{60}MA$-rich blend (95:5), in which both components appeared at the surface. In contrast, the thermally treated counterpart exhibited clear phase-separation into a bilayer channel, which would likely inhibit ambipolarity due to spatial segregation of the charge-transport pathways.

6.3.3 $PrC_{60}MA$:P3HT WG-TFTs

The WG-TFT BHJ channel was prepared as-cast and thermally treated for two compositions, 95:5 and 99:1, to examine the effect of high fullerene content and potential thermally-induced phase-separation on device performance. First, the 95:5 blend composition was studied, and the recorded ambipolar characteristics for as-cast WG-TFTs are shown in Figure 6.7. It is widely understood that semiconducting polymers, like P3HT, can be introduced in blends with extremely low content and still retain mobility in OFETs since the percolation threshold for hole transport is very low. [25, 26] The retainment of high μ upon blending typically results in large $I_{on/off}$, given that μ is proportional to I_{ds}. In this system, Figure 6.7(a) shows that $I_{on/off} > 10^2$ and $V_{th} = 0.01\,\mathrm{V}$, which were comparable to the P3HT WG-

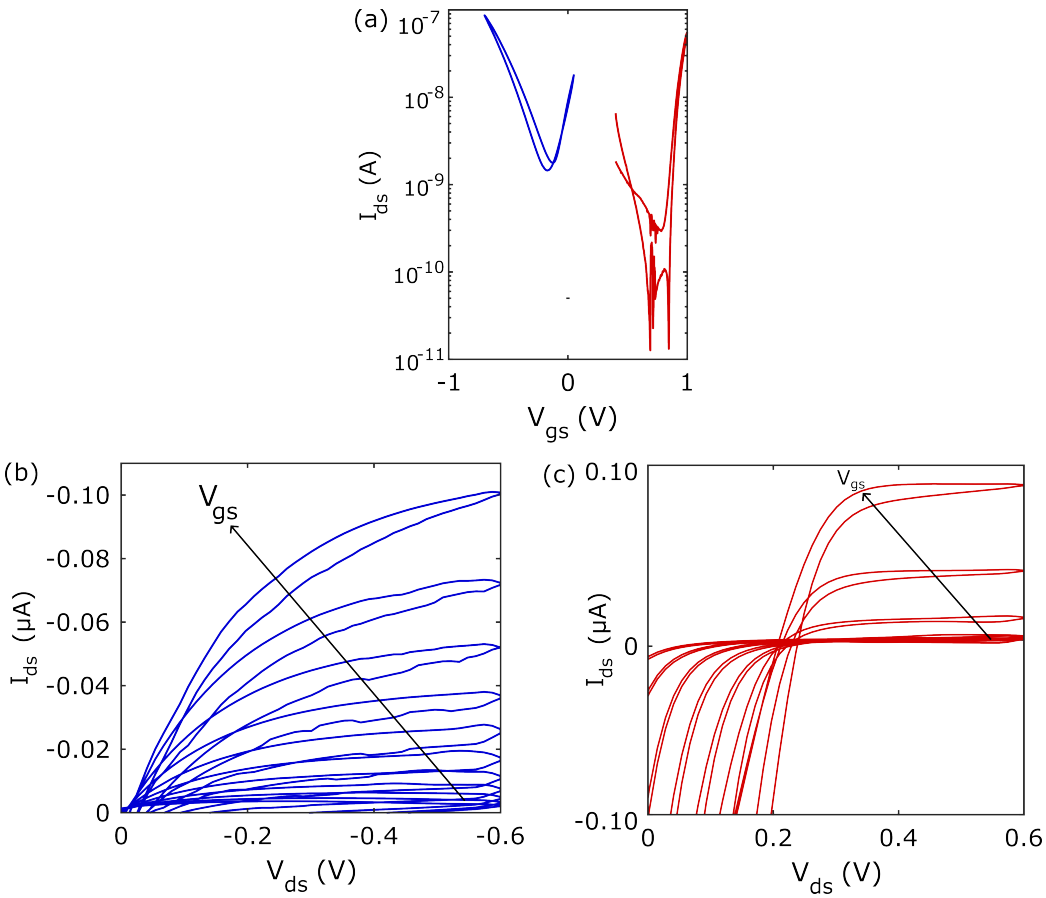

Figure 6.7: (a) Transfer characteristics for as-cast $PrC_{60}MA$:P3HT (95:5) BHJ WG-TFTs at $V_{ds} = -0.6\,V$ (blue curve), $V_{ds} = 0.6\,V$ (red curve) and $V_{gs} = -1\,V$ to $1\,V$. Output characteristics at (b) $V_{ds}, V_{gs} = 0\,V$ to $-0.6\,V$ and (c) $V_{ds}, V_{gs} = 0\,V$ to $0.6\,V$.

TFTs (10^2, $-0.12\,V$). Hole mobility was extracted from these transfer characteristics (solid blue lines) to be between $10^{-2} - 10^{-3}\,cm^2\,V^{-1}\,s^{-1}$. This may suggest that the double-layer capacitance decreased with the number of accessible monomer units as hole conduction was largely uninterrupted and thus unimpeded by the fullerene. Figure 6.7(b) also exhibits encouraging transistor behaviour in the p-type output curves, reaching $I_{ds[max]} = -0.01\,mA$.

Figure 6.7(c) shows distinct linear and saturation regimes in the output curves measured for the n-type regime. However, compared to the $PrC_{60}MA$ device, these were shifted by approximately $0.2\,V$ away from zero, and there was a significant drop in $I_{ds[max]}$ from $10.9\,mA$ to $0.01\,mA$ comparable to that achieved in p-type mode, due to high I_{gs}. This was likely caused by several compounding factors: (i) poor electron injection from Au to the LUMO

of $PrC_{60}MA$, (ii) overlap between the source-drain electrodes and the water droplet, and (iii) changes in the $PrC_{60}MA$ morphology upon blending. Regarding the latter point, Stein *et al.* reported that their blend film, comprising the p-type glycolated polymer p(g2T-TT) and $PrC_{60}MA$, had highly crystalline morphology, but this was significantly reduced relative to the pristine $PrC_{60}MA$ film. [14] While changes in lamellar stacking d-space were negligible, the coherence length of $PrC_{60}MA$, derived from their GIWAXS measurements, was reduced by 20 %. This decrease in coherence length and crystallinity lowered mobility and overall OECT performance upon blending with 5 wt % polymer. In this study, it is likely that the morphology of the $PrC_{60}MA$ portions of the blend was also negatively impacted, leading to inefficient n-type charge transport.

Here, the visible interpenetrating network and presence of the long P3HT polymer strands at the BHJ surface (Figure 6.6) likely obstructed the fullerene domains that provided efficient electron percolation pathways, giving rise to a significant reduction in electron mobility from $\mu = 0.43\,\mathrm{cm^2\,V^{-1}\,s^{-1}}$ to $0.003\,\mathrm{cm^2\,V^{-1}\,s^{-1}}$. V_{th} also shifted away from the V_{th} extracted for the $PrC_{60}MA$ WG-TFT from 0.15 V to 0.69 V, which suggests that the migration of positively charged ions in water and subsequent accumulation of electrons at the surface of the BHJ was more difficult with a blend film.

After thermal treatment, Figures 6.8(a)-(b) show unipolar p-type behaviour, that was improved relative to the as-cast device. This could be attributed to better crystallinity and ordering of polymer chains, as evidenced by the reduced hysteresis and lower contribution from I_{gs}. $I_{ds[max]}$ and μ increased to $-0.84\,\mu\mathrm{A}$ and $0.015\,\mathrm{cm^2\,V^{-1}\,s^{-1}}$, respectively, which were comparable to that achieved for the P3HT WG-TFT despite substantially less content (see Table 6.2). The near-zero $V_{th} < 0.1\,\mathrm{V}$ also suggests that the very thin layer of P3HT formed at the water-organic semiconductor interface was enough to turn the device on in p-type mode. Unsurprisingly, the transistor did not operate in the n-type regime (see Figure 6.8(c)) after thermal treatment as it was clear from the VPI images presented in Figures 6.6(b),

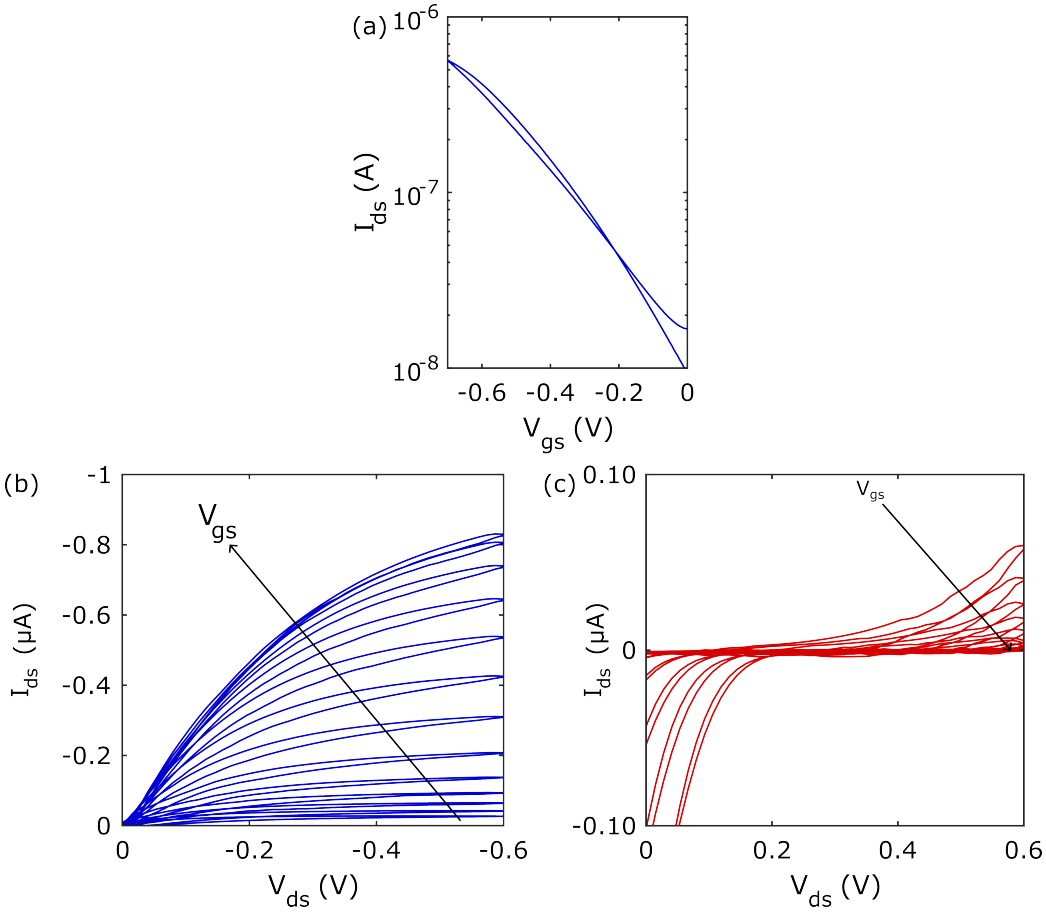

Figure 6.8: (a) Transfer characteristics for thermally treated $PrC_{60}MA$:P3HT (95:5) BHJ WG-TFTs at $V_{ds} = -0.6\,V$ and $V_{gs} = -1$ V to 1 V. Output characteristics at (b) $V_{ds}, V_{gs} = 0\,V$ to $-0.6\,V$ and (c) $V_{ds}, V_{gs} = 0\,V$ to $0.6\,V$.

(d) that $PrC_{60}MA$ phase-separated towards the substrate, which prevented the accumulation of electrons.

The observed ambipolar characteristics for the as-cast $PrC_{60}MA$:P3HT blend (95:5) prompted further investigation into the effect of even lower polymer content to ensure n-type mobility. BHJ films were prepared as-cast and

Table 6.2: $I_{on/off}$, μ, $I_{ds[max]}$ and V_{th} of $PrC_{60}MA$:P3HT (95:5) WG-TFTs

	Polarity	μ ($cm^2\,V^{-1}\,s^{-1}$)	$I_{on/off}$	V_{th} (V)	$I_{ds[max]}$ (µA)
As-cast	n	0.003	10^3	0.69	0.009
	p	0.002	10^2	-0.01	-0.10
Treated	p	0.02	10^2	-0.07	-0.84

thermally treated for a $PrC_{60M}A$:P3HT composition with 1 % P3HT content to examine the impact on transistor operation. The output characteristics shown in Figure 6.9(a)-(b) for the as-cast device reveal limited ambipolar behaviour, with transport primarily dominated by n-type conduction. This is attributed to the reduced P3HT content in the blend, limiting the extent of p-type transport. In the p-type regime, Figure 6.9(a) shows that the measured I_{ds} was in the nA range and dominated by I_{gs}, with large hysteresis observed in the forward and backward V_{ds} sweeps, preventing the formation of linear and saturation transistor regimes. Conversely, Figure 6.9(b) shows that $I_{ds[max]}$ in the n-type regime increased from 0.009 µA to 0.26 µA and μ improved by an order of magnitude to 0.03 $cm^2\,V^{-1}\,s^{-1}$ compared to the as-cast blend film with 95 % $PrC_{60}MA$ content. V_{th} also approached 1 V, suggesting that even a 1 % polymer addition still impeded the accumulation of electrons.

Figure 6.9(c) demonstrates a dramatic improvement in hole transport upon thermal treatment, with $I_{ds[max]}$ reaching −0.21 µA after turning on at $V_{th} = -0.35$ V, relative to the as-cast film with identical composition. However, $I_{ds[max]}$ decreased from −0.84 µA to −0.21 µA, which was only a quarter of that measured for the thermally-treated blend film with 5 % P3HT content. V_{th} also increased from −0.07 V to −0.35 V. This suggests a decrease in double-layer capacitance, as fewer monomer units became accessible, and hole mobility was reduced by an order of magnitude to 0.003 $cm^2\,V^{-1}\,s^{-1}$. This reduction in mobility was likely due to the breakup of the hole percolation network formed by interconnecting polymer chains, as the presence of more fullerene domains weakened their connectivity.

Meanwhile, Figure 6.9(d) shows that n-type performance completely degraded, similar to the behaviour observed for the 95:5 composition. This aligns with the formation of a thermally-induced bilayer, where a very thin of P3HT dominated the film surface. Consequently, increasing the fullerene content did not enhance I_{ds} compared to more dilute fullerene conditions. [27] The lack of accessible $PrC_{60}MA$ at the surface prevented effective electron

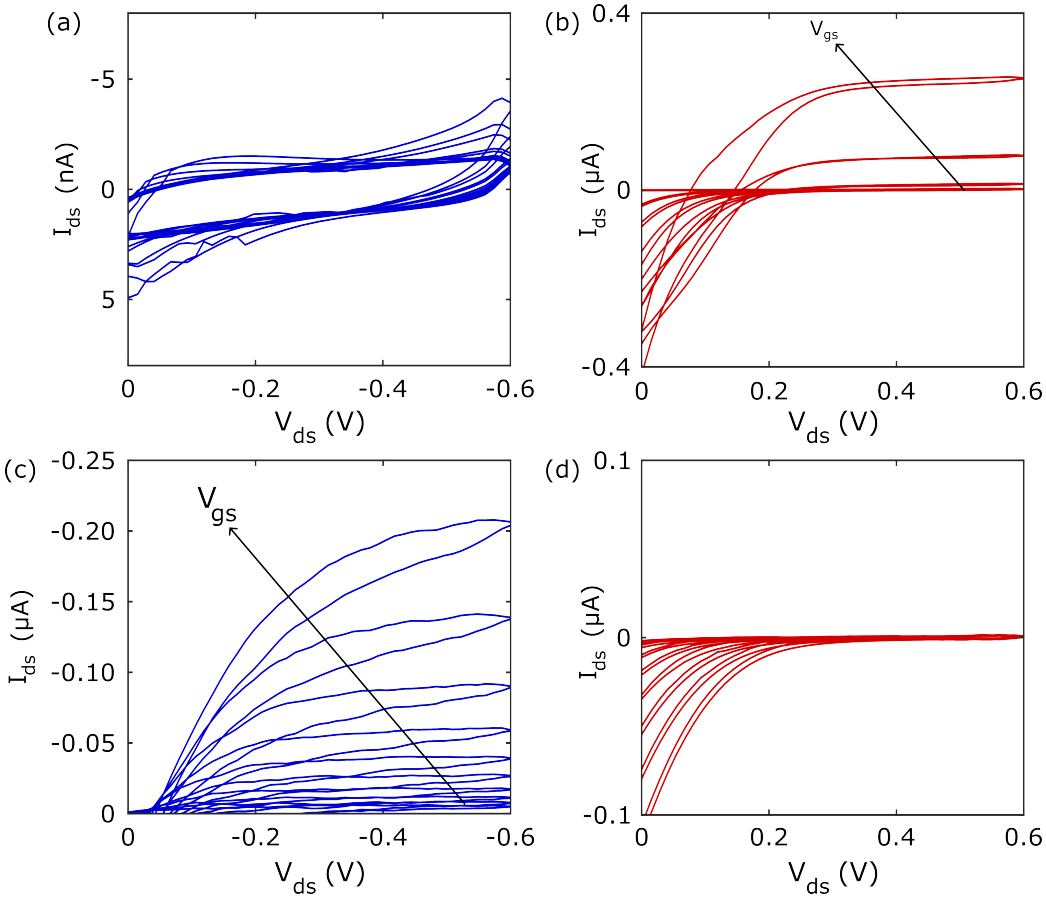

Figure 6.9: Output characteristics for (a),(b) as-cast and (c),(d) thermally treated $PrC_{60}MA$:P3HT (99:1) BHJ WG-TFTs at (a),(c) $V_{ds}, V_{gs} = 0\,\text{V}$ to $-0.6\,\text{V}$ and (b),(d) $V_{ds}, V_{gs} = 0\,\text{V}$ to $0.6\,\text{V}$.

accumulation, further limiting n-type transport. The electrical parameters extracted for the as-cast and thermally treated $PrC_{60}MA$:P3HT (99:1) WG-TFTs are summarised in Table 6.3.

The best-performing ambipolar $PrC_{60}MA$:P3HT WG-TFTs had a 95:5 composition ratio, with 5 % P3HT, and the BHJ channel was studied in its as-cast form after deposition. However, n-type performance declined upon blending, primarily due to a significant reduction in extracted mobility from

Table 6.3: $I_{on/off}$, μ, $I_{ds[max]}$ and V_{th} of $PrC_{60}MA$:P3HT (99:1) WG-TFTs

	Polarity	μ ($\text{cm}^2\,\text{V}^{-1}\,\text{s}^{-1}$)	$I_{on/off}$	V_{th} (V)	$I_{ds[max]}$ (µA)
As-cast	n	0.03	10^3	0.76	0.26
Treated	p	0.003	10^2	-0.35	-0.21

$\mu = 0.43\,\mathrm{cm^2\,V^{-1}\,s^{-1}}$ to $0.003\,\mathrm{cm^2\,V^{-1}\,s^{-1}}$, along with a V_{th} shift from 0.15 V to 0.69 V, compared to the $PrC_{60}MA$ WG-TFT. This ambipolar behaviour significantly degraded upon thermal treatment, leading to unipolar p-type operation despite the high $PrC_{60}MA$ content. This was attributed to the formation of a thermally-induced bilayer, where a thin layer of P3HT dominated the film surface. The morphological changes were further confirmed in a 99:1 composition with just 1 % P3HT content, reinforcing the impact of thermal treatment on phase-separation and charge transport characteristics.

To investigate the impact of a reduced number of EG side chains on the ambipolar performance of P3HT blend-based WG-TFTs, PTEG−1 was used instead of $PrC_{60}MA$ for n-type transport (see Figure 6.10). Similar to $PrC_{60M}A$, PTEG−1 is also a fullerene derivative but with just on hydrophilic triethylene glycol type side chain. [28] The blend-based WG-TFT contained 95 % PTEG−1 and only the thermally treated WG-TFTs are shown in this case, as the as-cast devices did not turn on in either regime. However, unipolar p-type performance was observed with thermal treatment, albeit inferior to that of the thermally treated $PrC_{60}MA$:P3HT WG-TFT with the same composition, reaching $I_{ds[max]} = -0.05\,\mu A$. This suggests that the components were too intimately mixed to form efficient percolation paths, as evidenced by the large hysteresis and noise present. In general, fullerenes

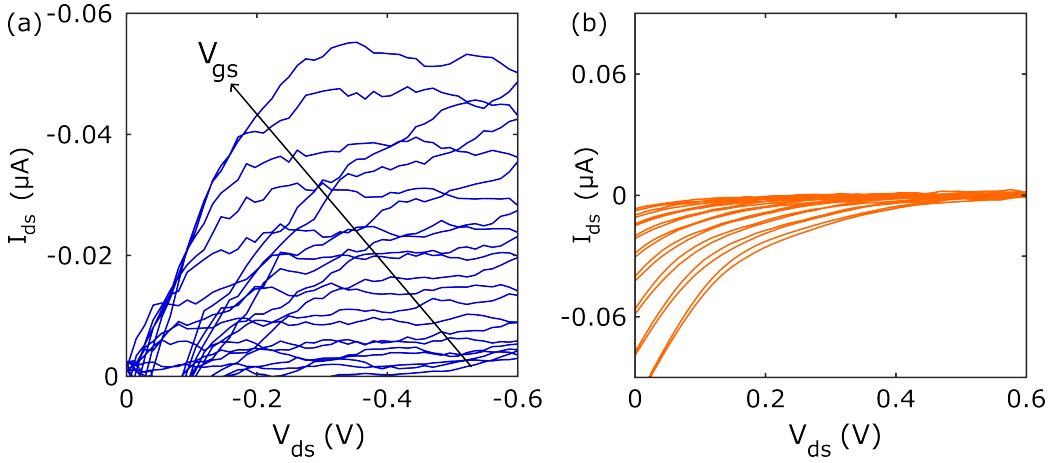

Figure 6.10: Output characteristics for thermally treated PTEG-1:P3HT (95:5) BHJ WG-TFTs at (a) $V_{ds}, V_{gs} = 0\,\mathrm{V}$ to $-0.6\,\mathrm{V}$ and (b) $V_{ds}, V_{gs} = 0\,\mathrm{V}$ to $0.6\,\mathrm{V}$.

adopt tetragonal packing with the side-chains facing one another. Dong *et al.* found that PTEG−1 exhibited a lower degree of orientation compared to other fullerenes with more oxygen repeating units on the single EG side chain. [13] Therefore, the poor performance observed here was inferred to result from reduced interlayer spacing and thus smaller unit cell of PTEG−1 relative to $PrC_{60}MA$ due steric effects. The higher number of EG side chains likely resulted in better packing made possible by the additional freedom provided by the larger unit cell. This led to a greater $\pi - \pi$ orbital overlap, responsible for the good mobility values exhibited by these molecules. [13]

6.3.4 $PrC_{60}MA$:PCDTPT WG-TFTs

Next, an alternative semiconductor, PCDTPT, was studied for p-type operation, as this co-polymer has been shown to possess superior $\pi-\pi$ stacking and ease of polymerization, leading to high mobility and promising stability. [29] Like P3HT, PCDTPT is primarily hydrophobic; however, strong electronic delocalization between the donor and acceptor units enhances hole transport along the PCDTPT chain, while orbital interactions reduce the gap between the HOMO and LUMO, which is thought to improve ambipolar conduction (see Figure 6.11(a) for its chemical structure). Its porous nature has also been shown to support the operation of ion-gated transistors fabricated on flexible substrates. [30] However, the successful operation of WG-TFTs was not guaranteed due to the significantly lower ion concentration in DI water and differences in charge distribution compared to the ion-gel, where $[HCO_3^-] = [H^+] = 10^{-7}\,M$ [31]. The output characteristics recorded for the PCDTPT WG-TFT achieved $I_{ds[max]} = -10.3\,\mu A$ at $V_{ds} = -0.8\,V$ and $V_{gs} = -1\,V$ (see Figure 6.11(b)). Table 6.4 shows that high $\mu \approx 0.3\,cm^2\,V^{-1}\,s^{-1}$, $I_{on/off} > 10^3$, and near-zero $V_{th} = -0.08\,V$ were extracted from the transfer characteristics plotted in Figure 6.11(c), which champion over those listed for P3HT in Table 6.1 ($\mu = 0.04\,cm^2\,V^{-1}\,s^{-1}$, $I_{on/off} > 10^2$, and $V_{th} = -0.12\,V$).

To enhance the ambipolar characteristics of the WG-TFTs discussed in §6.3.3, PCDTPT was blended with $PrC_{60}MA$ following the same 95:5 compo-

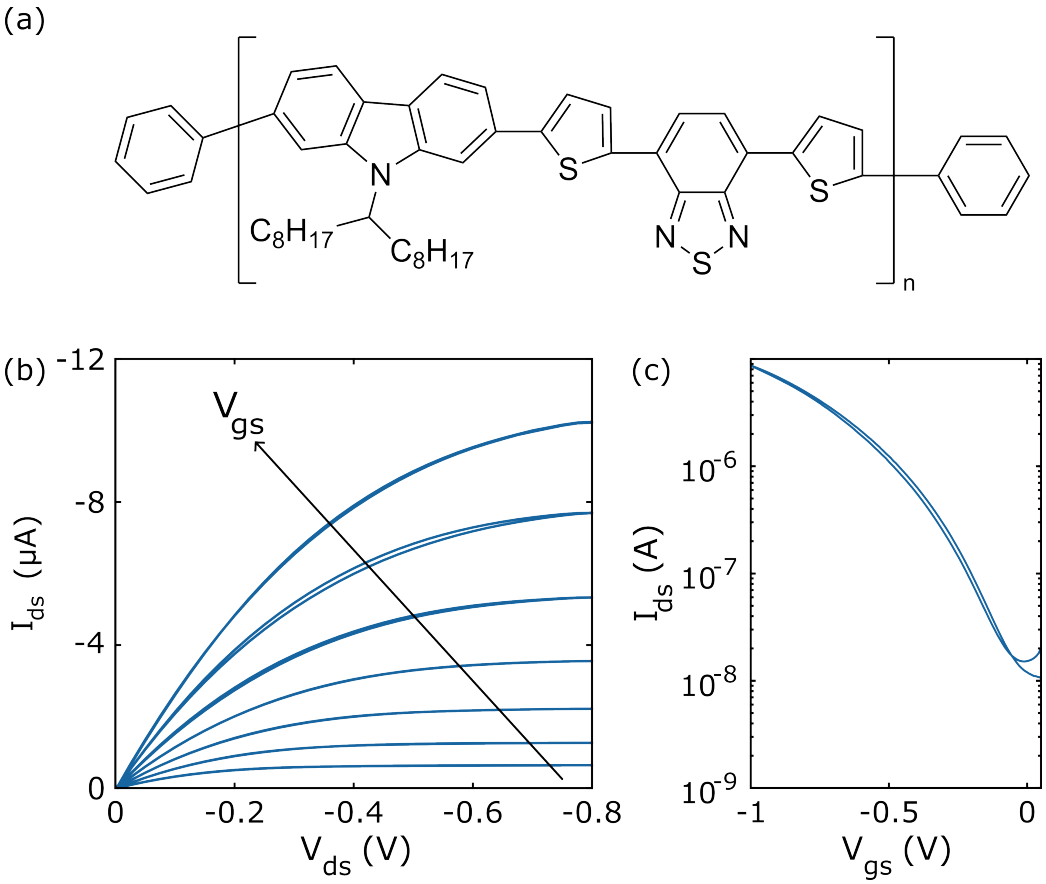

Figure 6.11: (a) Chemical structure of PCDTPT. (b) Output characteristics thermally treated pristine PCDTPT WG-TFTs at $V_{ds}, V_{gs} = 0\,\text{V}$ to $-0.8\,\text{V}$. (c) Transfer characteristics at $V_{ds} = -0.8\,\text{V}$ and $V_{gs} = 0.05\,\text{V}$ to $-1\,\text{V}$.

sition with high fullerene content. Starting with the as-cast WG-TFT, unipolar n-type operation was observed in both the transfer and output (Figures 6.12(a) & (c)) characteristics, with a stable current drive reaching $I_{ds[max]}$ just under 0.5 µA. Nonetheless, Figure 6.12(a) also reveals significant hysteresis for $V_{gs} > 0$, which was reflected in the output curves that were shifted by 0.4 V from $V_{gs}, V_{ds} = 0\,\text{V}$. In contrast, Figure 6.12(b) shows limited p-type operation, as little to no field effect was observed with increasing V_{gs}. This suggests that the polymer chains were unable to self-organise and form

Table 6.4: $I_{on/off}$, μ, $I_{ds[max]}$ and V_{th} of PCDTPT WG-TFTs.

Material	Polarity	μ ($\text{cm}^2\,\text{V}^{-1}\,\text{s}^{-1}$)	$I_{on/off}$	V_{th} (V)	$I_{ds[max]}$ (µA)
PCDTPT	p	0.29	10^3	-0.08	-10.3

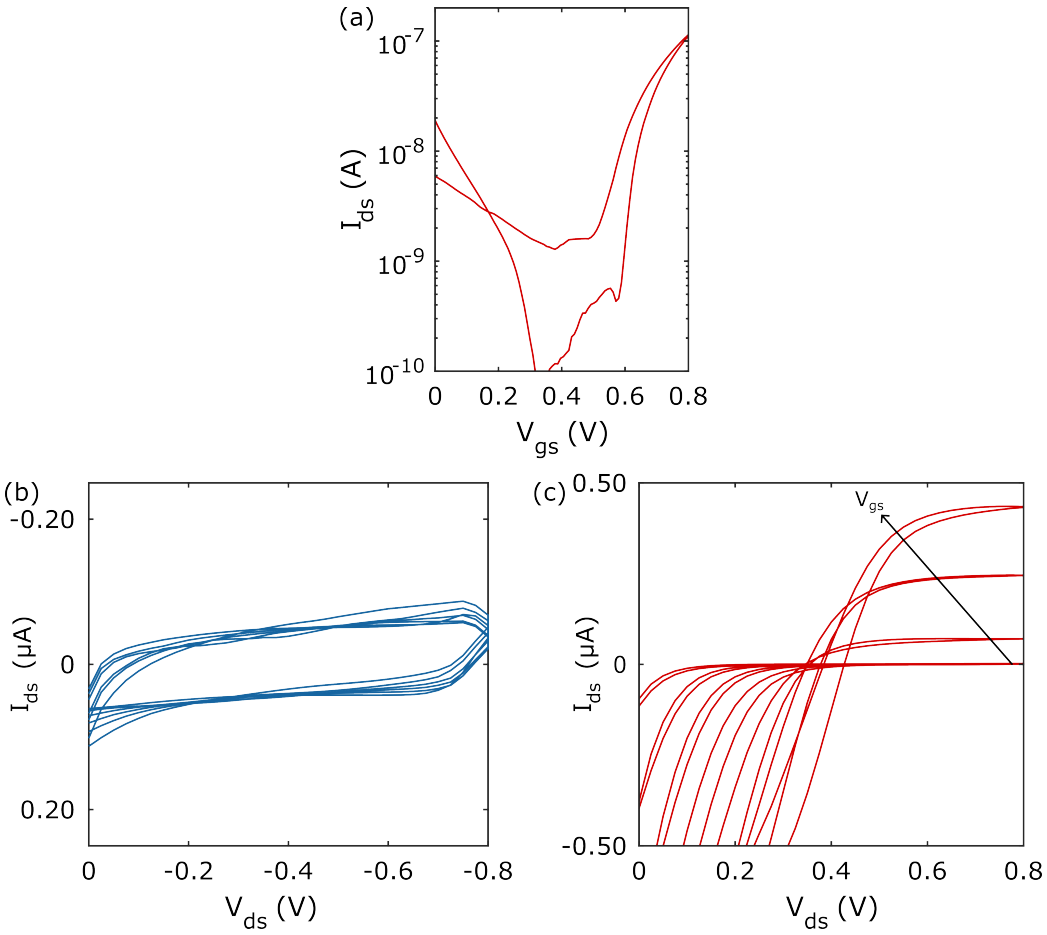

Figure 6.12: (a) Transfer characteristics for as-cast $PrC_{60}MA$:PCDTPT (95:5) BHJ WG-TFTs WG-TFTs at $V_{ds} = 0.8\,V$ and $V_{gs} = -1\,V$ to $1\,V$. Output characteristics at (b) $V_{ds}, V_{gs} = 0\,V$ to $-0.8\,V$ and (c) $V_{ds}, V_{gs} = 0\,V$ to $0.8\,V$.

hole-percolation networks at the BHJ surface when the film was left at room temperature to allow the solvent to evaporate slowly.

Ambipolar behaviour was observed after thermal treatment, however, the presence of $PrC_{60}MA$ in the blend likely contributed to unintentional doping of the polymer film, as electrons from $PrC_{60}MA$ reduced the hole current, leading to an overall decrease in I_{ds} for p-type mode. The V-shape of the light-blue transfer curve in Figure 6.13(a), characteristic of ambipolar OSCs, meant that PCDTPT struggled to reach a well-defined off-state, resulting in $I_{on_{off}} \approx 10^2$. The reduction in mobility from $\mu \approx 0.3\,cm^2\,V^{-1}\,s^{-1}$ to $0.04\,cm^2\,V^{-1}\,s^{-1}$, relative to the pristine PCDTPT WG-TFT, was expected and aligned with the rule of mixtures, which assumed

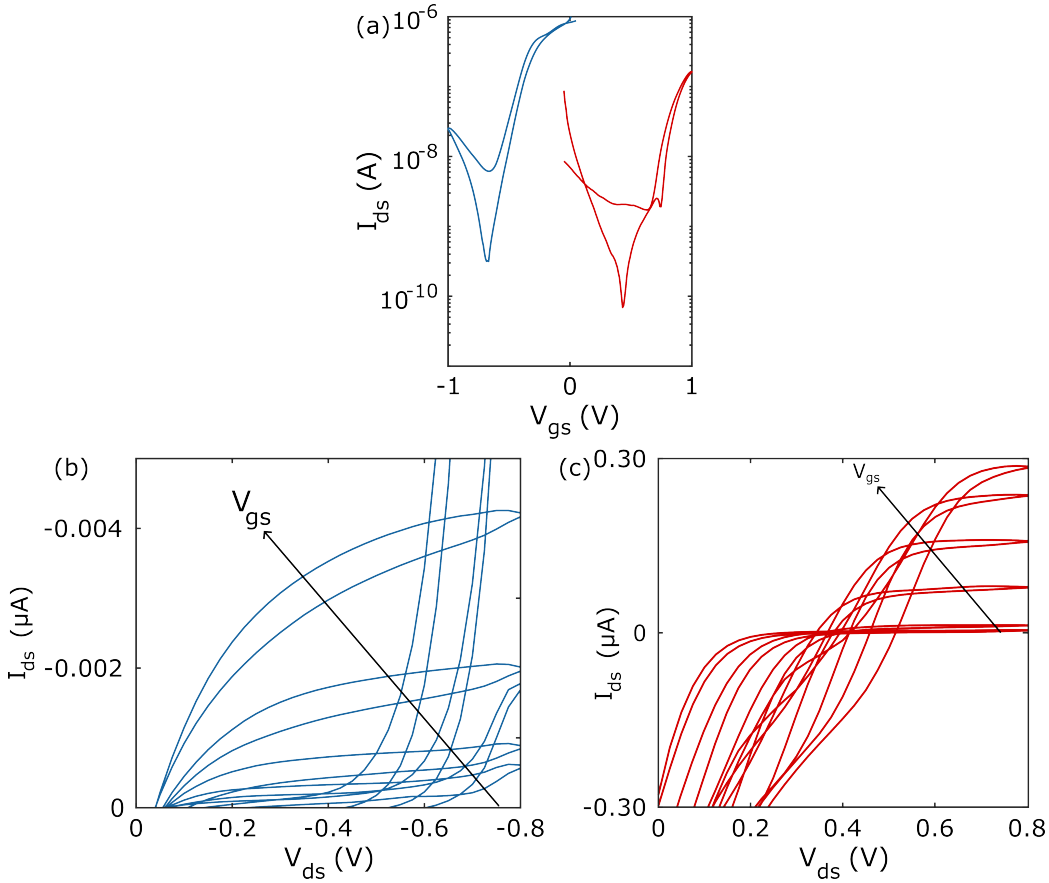

Figure 6.13: (a) Transfer characteristics for thermally treated $PrC_{60}MA$:PCDTPT (95:5) BHJ WG-TFTs at $V_{ds} = -0.8\,V$ (blue curve), $V_{ds} = 0.8\,V$ (red curve) and $V_{gs} = -1\,V$ to $1\,V$. Output characteristics at (b) $V_{ds}, V_{gs} = 0\,V$ to $-0.8\,V$ and (c) $V_{ds}, V_{gs} = 0\,V$ to $0.8\,V$.

that p-type operation would be adversely affected by reducing the content of PCDTPT to 5 %. However, this hole mobility still outperformed that of both the as-cast ($0.002\,cm^2\,V^{-1}\,s^{-1}$) and thermally treated ($0.02\,cm^2\,V^{-1}\,s^{-1}$) $PrC_{60}MA$:P3HT WG-TFTs, likely due to the enhanced structural order of hole-percolation networks and improved $\pi - \pi$ stacking.

Figure 6.13(b) shows a clear modulation of I_{ds} with steps in V_{gs}. As shown in Table 6.5, I_{ds} remained in the nA range ($I_{ds[max]} = 0.004\,\mu A$), although the output curves were smooth and largely noise-free. Additionally, diode-like tails were observed for $V_{gs} < V_{th} < -0.83\,V$, potentially arising from the intrinsic ambipolarity of PCDTPT.

Moving on to the n-type regime, Figure 6.13(c) shows that high I_{gs} caused a shift of approximately $0.05\,V$ in V_{ds} as V_{gs} was incremented. This re-

Table 6.5: $I_{on/off}$, μ, $I_{ds[max]}$ and V_{th} of $PrC_{60}MA$:PCDTPT (95:5) WG-TFTs

	Polarity	μ ($cm^2\,V^{-1}\,s^{-1}$)	$I_{on/off}$	V_{th} (V)	$I_{ds[max]}$ (µA)
As-cast	n	0.05	10^3	0.54	0.43
Treated	n	0.02	10^3	0.58	0.28
	p	0.04	10^2	-0.83	-0.004

sulted in less defined linear and saturation regimes as V_{gs}, V_{ds} approached 1 V. Nonetheless, key performance metrics such as $I_{on/off} = 10^3$, $V_{th} \approx 0.05\,V$, and $\mu = 0.02\,cm^2\,V^{-1}\,s^{-1}$ and $0.05\,cm^2\,V^{-1}\,s^{-1}$ remained largely consistent before and after thermal treatment, respectively. These results suggest a clear difference in the blend morphology between the P3HT and PCDTPT systems. The degree of thermally-induced phase-separation was likely much less than that observed with the P3HT blend. Instead, thermal treatment encouraged the ordering of the polymer to govern hole-transport while retaining connectivity between the fullerene domains at the film surface, enabling the ambipolar performance of the BHJ WG-TFT.

Given the limited p-type conduction and reduced phase separation observed in comparison to the P3HT blends, the PCDTPT content was increased from 5 % to 10 %. Only thermally treated films were considered for further investigation due to the poor performance of the as-cast films. Interestingly, both n-type and p-type performance improved with the higher PCDTPT content. A decrease in V_{th} by 0.2 V in the transfer characteristics (Figure 6.14(a)), relative to the 5 % blend, likely resulted from a higher density of longer monomer units at the water–organic interface, leading to increased double-layer capacitance. This is consistent with the p-type output characteristics in Figure 6.14(b), which show that at negative gate bias, $I_{ds[max]}$ increased by several orders of magnitude – from the nanoampere to the microampere scale ($-0.16\,\mu A$). The significant increase in I_{ds} suggests more efficient hole accumulation at the film surface. As shown in Table 6.6, the hole mobility and $I_{on/off}$ ratio remained unchanged at $0.03\,cm^2\,V^{-1}\,s^{-1}$ and 10^1, respectively, for both 5 % and 10 % PCDTPT content, indicating

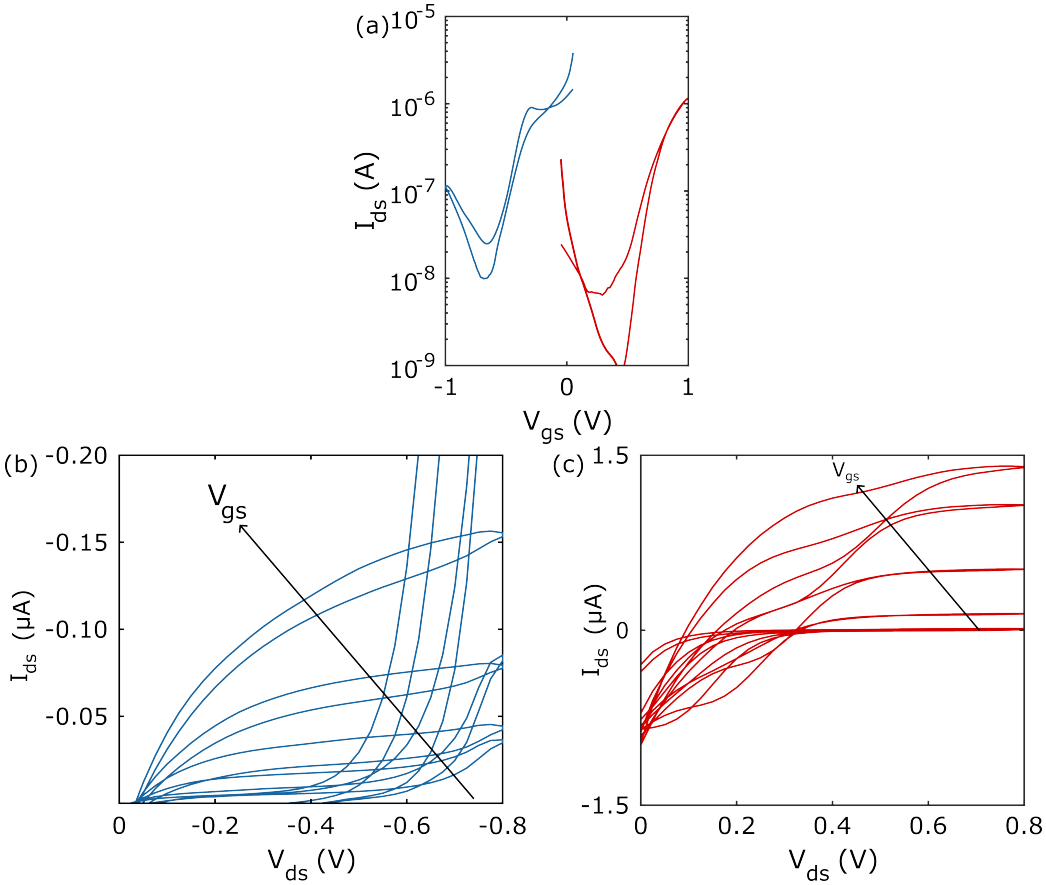

Figure 6.14: (a) Transfer characteristics for thermally treated $PrC_{60}MA$:PCDTPT (90:10) BHJ WG-TFTs at $V_{ds} = -0.8\,V$ (light blue curve), $V_{ds} = 0.8\,V$ (red curve) and $V_{gs} = -1\,V$ to $1\,V$. Output characteristics at (b) $V_{ds}, V_{gs} = 0\,V$ to $-0.8\,V$ and (c) $V_{ds}, V_{gs} = 0\,V$ to $0.8\,V$.

a low percolation threshold for hole transport.

Moreover, the identification of the linear and saturation regimes in the n-type polarity was significantly easier. Figure 6.14(c) shows that the channel was saturated from around $V_{ds} = 0.4\,V$ despite the large hysteresis at $V_{gs} = 1$ V. There was remarkable field-effect, evidenced by $\mu = 0.19\,cm^2\,V^{-1}\,s^{-1}$ and $I_{on/off} > 10^3$, which suggests that it was easier for electrons to accumulate at the water-semiconductor interface with this blend composition.

The improvement in both n- and p-type performance went against the rule of mixtures, which assumed that n-type operation particularly would be adversely affected by reducing the content of $PrC_{60}MA$. In the photovoltaic field, it has been shown that the donor polymer can provide a bridge for electron transport across the crystalline domains of small molecular acceptors

Table 6.6: $I_{on/off}$, μ, $I_{ds[max]}$ and V_{th} of thermally treated $PrC_{60}MA$:PCDTPT (90:10) WG-TFTs

Polarity	μ ($cm^2\,V^{-1}\,s^{-1}$)	$I_{on/off}$	V_{th} (V)	$I_{ds[max]}$ (µA)
n	0.19	10^3	0.53	1.5
p	0.03	10^1	-0.64	-0.16

rather than isolate the electron percolation pathways. [32] This can happen because, for these systems, the LUMO offset is small. Figure 6.15 suggests that the LUMO of PCDTPT is lower than that of P3HT, estimated to be $\approx -3.7\,eV$ and $-3.2\,eV$, respectively. [33, 34] The LUMO of $PrC_{60}MA$ was listed as $-3.9\,eV$ in the study conducted by Stein *et al.,* [14] therefore, it could have been possible for electrons to hop between the n- and p-type materials employed here. It is clear that electrons became more mobile assisted by polymer addition as mobility was five times higher than that achieved with the previous blend composition.

Compared to the ambipolar performance of the as-cast blend system with

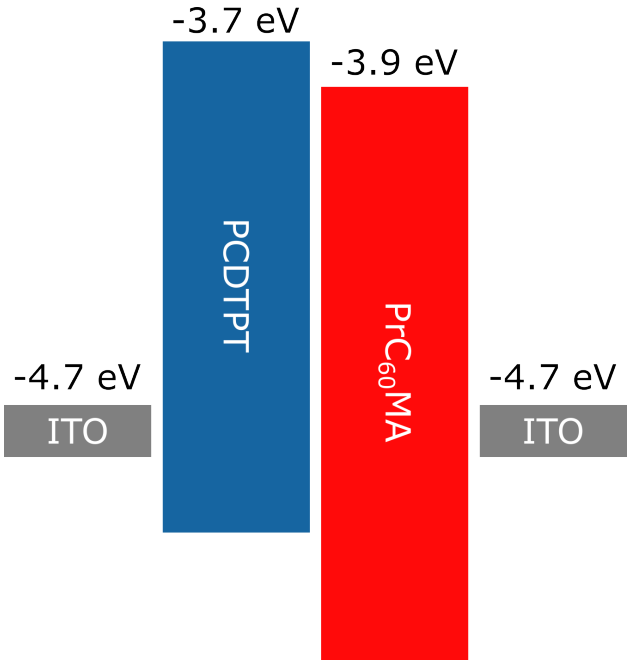

Figure 6.15: Band diagram illustrating the LUMO of PCDTPT and $PrC_{60}MA$. The work function of the source-drain ITO contacts are also shown.

5 % P3HT content, the PCDTPT blend may have exhibited significantly reduced phase-separation, as ambipolarity only developed after thermal treatment for the same blend composition. In the p-type regime, PCDTPT did not outperform P3HT, unlike in pristine p-type WG-TFTs, as $I_{ds[max]}$ dropped by two orders of magnitude from $-0.10\,\mu A$ to $-0.004\,\mu A$, despite an improvement in mobility from $0.002\,cm^2\,V^{-1}\,s^{-1}$ to $0.04\,cm^2\,V^{-1}\,s^{-1}$. This reduction was likely due to the intrinsic ambipolarity of PCDTPT and the contribution of mobile electrons upon switching the polarity of V_{ds} and V_{gs}.

Unlike the P3HT blends, n-type performance was less adversely affected by blending with PCDTPT. In this case, $I_{ds[max]}$ increased threefold to 0.28 µA, while the electron mobility improved from $0.003\,cm^2\,V^{-1}\,s^{-1}$ to 0.02 $cm^2\,V^{-1}\,s^{-1}$. Given that thermally treated $PrC_{60}MA$:PCDTPT TFTs with a 95:5 composition exhibited minimal phase-separation, the PCDTPT content was subsequently increased to 10 %. This adjustment yielded the best-performing blend-based ambipolar device in this study. In the p-type regime, mobility remained stable, and a lower threshold voltage ($V_{th} = -0.64\,V$) was achieved in comparison to the equivalent blend with half the PCDTPT content. Furthermore, the device reached $I_{ds[max]} = -0.10\,\mu A$, surpassing the optimal P3HT blend. However, this came at the slight expense of the switching capability of the WG-TFT, which decreased by an order of magnitude (10^1). In addition, n-type performance was further enhanced, achieving the highest $I_{ds[max]} = 1.5\,\mu A$, $\mu = 0.19\,cm^2\,V^{-1}\,s^{-1}$, and the lowest $V_{th} = 0.53\,V$ among the blend-based WG-TFTs studied here.

Despite the ambipolar character exhibited by the P3HT and PCDTPT blend WG-TFTs, achieving this required careful engineering of the BHJ microstructure. Additionally, all measurements displayed clear hysteresis, which could contribute to rapid device degradation and long-term instability. The mismatch between the work function of the Au source-drain electrodes and LUMO of $PrC_{60}MA$ also caused large offset in the n-type output characteristics from $V_{gs}, V_{ds} = 0\,V$.

6.4 Ambipolar ZnO-based WG-TFTs

An innovative design strategy inspired by OPVs was adopted for ambipolar WG-TFTs involving a bilayer channel to help combat the morphological changes associated with thermally-induced phase-separation and impact on device ambipolarity. A key challenge associated with solution-processed bilayer OPVs is choosing a suitable pair of orthogonal solvents to ensure that the surface morphology of the first layer is unchanged following the deposition and thermal treatment of the second. The operation of these devices requires a sharp, well-defined interface between the two layers to allow for efficient charge transfer. [35]

To prevent chemical intermixing ZnO, previously employed in Chapter 4 as an electron-transporting TFT, was introduced as the underlayer to govern n-type transport, while PCDTPT was spin-coated on top of ZnO for p-type transport. Furthermore, Figure 6.16 shows that ZnO possesses a wide bandgap, which meant that the electron injection barrier from ITO to its conduction band was reduced by $\approx 0.5\,\text{eV}$, in comparison to the LUMO

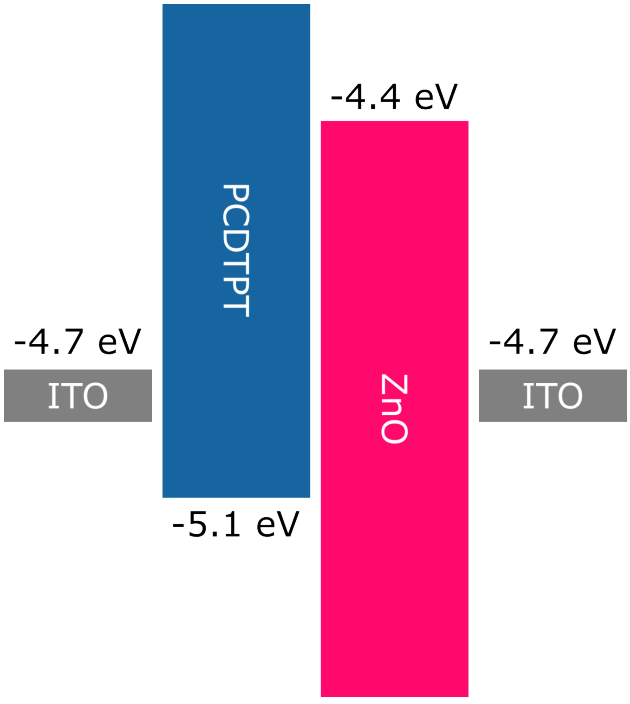

Figure 6.16: Band diagram illustrating the LUMO of ZnO. The work function of the source-drain ITO contacts are also shown.

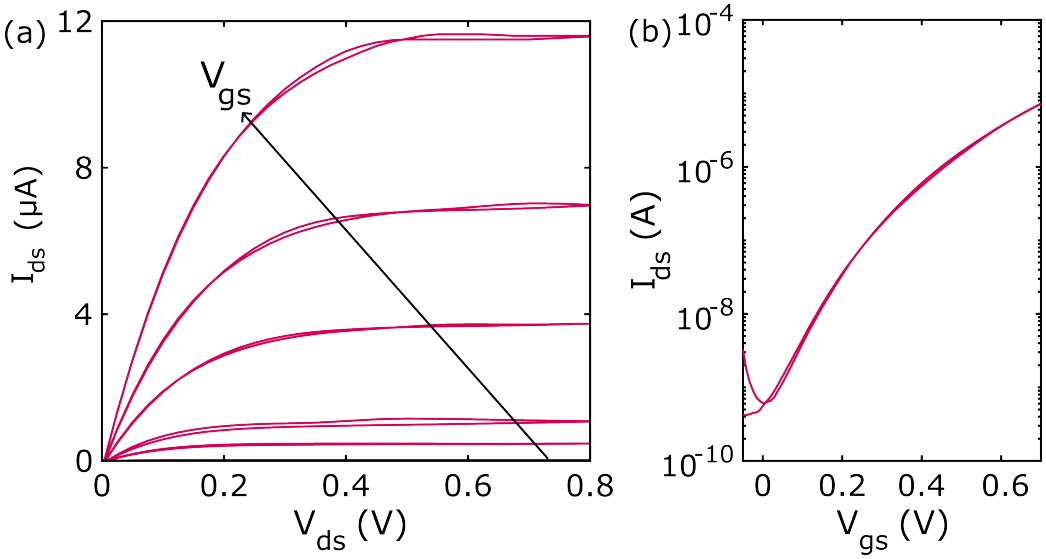

Figure 6.17: (a) Output characteristics thermally treated pristine ZnO WG-TFTs at $V_{ds}, V_{gs} = 0\,\text{V}$ to $0.8\,\text{V}$. (b) Transfer characteristics at $V_{ds} = 0.8\,\text{V}$ and $V_{gs} = -0.05\,\text{V}$ to $0.7\,\text{V}$.

of $PrC_{60}MA$. First, the performance of a ZnO WG-FET was assessed and Figure 6.17(a) shows that this led to excellent n-type performance in the first quadrant: I_{ds} was modulated well by positive increments of V_{gs}, attaining a maximum value of $11.7\,\mu\text{A}$ and I_{gs} was minimised evidenced by the sharp turn-on at $V_{gs}, V_{ds} = 0\,\text{V}$. The forward and backwards sweeps in both the transfer and output characteristics were well-matched with very little hysteresis. This suggests that the rougher surface morphology imaged in the previous Chapter 4 assisted the preferential movement of positively charged ions and electrons at the water-inorganic semiconductor interface to achieve superb switching from the off-state and charge carrier mobility, comparable with a conventional TFT architectures analysed in Chapter 4 ($I_{on/off} > 10^5$, $\mu = 0.62\,\text{cm}^2\,\text{V}^{-1}\,\text{s}^{-1}$).

The best-performing p-type polymer from §6.2.1, PCDTPT, was deposited atop ZnO and thermally treated using the same methodology outlined in Chapter 3 to achieve ambipolarity. Bilayer films were prepared by spin-coating and annealing ZnO as the underlayer under ambient conditions, followed by deposition and thermal treatment of PCDTPT in a glovebox. The inverse architecture was unsuitable due to the aggressive solvent used

to dissolve $ZnCl_2$ and the high-temperature processing required for ZnO, both incompatible with PCDTPT. Figure 6.18 demonstrates ambipolar behaviour in this hybrid (organic/inorganic) WG-TFT for the first time. The much higher mobility of ZnO ensured that n-type operation was largely unaffected by the addition of PCDTPT, as the transfer curves plotted in Figure 6.18(a) (solid pink lines) had minimal hysteresis, turning on at $V_{th} < 0.25\,\mathrm{V}$. $I_{on/ff}$ and μ also remained high at 10^4 and $0.2\,\mathrm{cm^2\,V^{-1}\,s^{-1}}$, respectively. In fact, the ambipolar nature of PCDTPT likely assisted electron accumulation at the water-organic semiconductor interface. Alike the PCDTPT-based blend system, the light blue transfer curve exhibited a similar tail prior to $V_{th} = -0.51\,\mathrm{V}$ due to the high density of electrons generated and low-lying

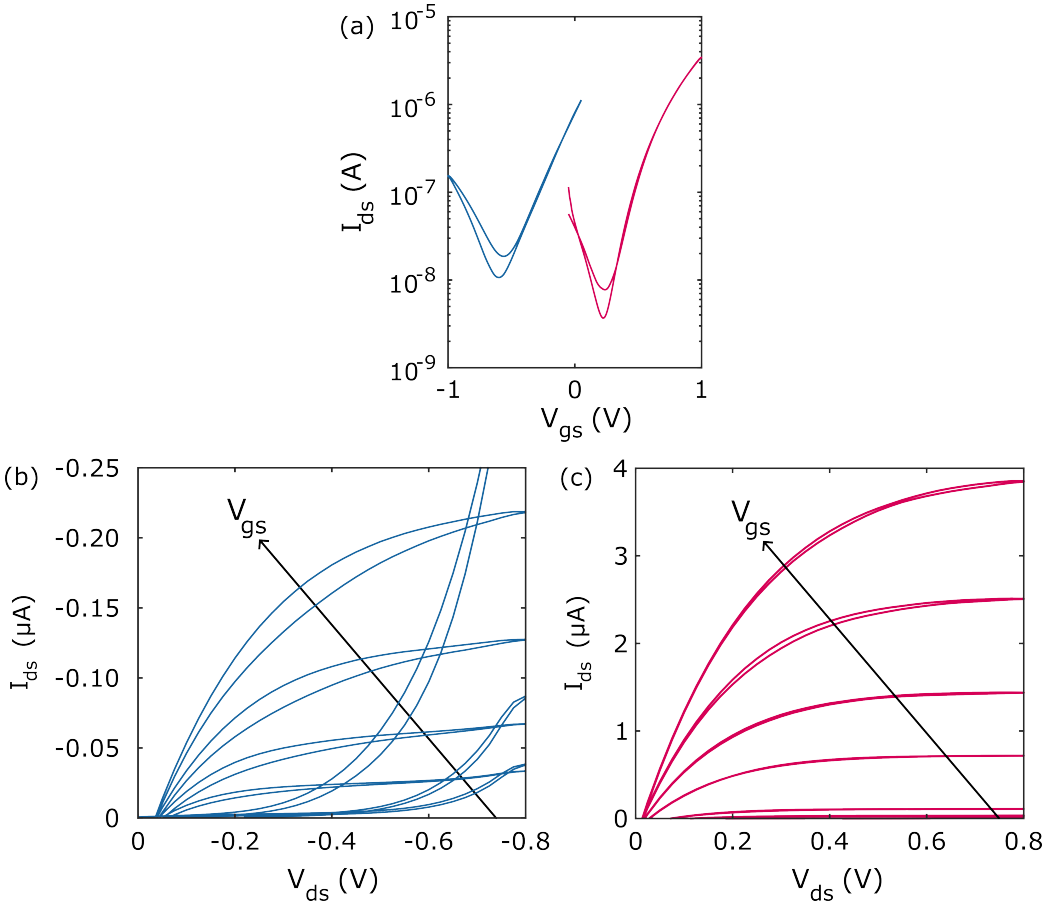

Figure 6.18: (a) Transfer characteristics for ZnO-PCDTPT bilayer WG-TFT at $V_{ds} = -0.8\,\mathrm{V}$ (light blue curve), $V_{ds} = 0.8\,\mathrm{V}$ (pink curve) and $V_{gs} = -1\,\mathrm{V}$ to $1\,\mathrm{V}$. Output characteristics at (b) $V_{ds}, V_{gs} = 0\,\mathrm{V}$ to $-0.8\,\mathrm{V}$ and (c) $V_{ds}, V_{gs} = 0\,\mathrm{V}$ to $0.8\,\mathrm{V}$.

Table 6.7: $I_{on/off}$, μ, $I_{ds[max]}$ and V_{th} of ZnO-based WG-TFTs

Material	Polarity	μ ($cm^2\,V^{-1}\,s^{-1}$)	$I_{on/off}$	V_{th} (V)	$I_{ds[max]}$ (µA)
ZnO	n	0.62	10^5	0.13	11.7
ZnO-PCDTPT	n	0.15	10^4	0.24	3.9
	p	0.02	10^1	-0.51	-0.22

LUMO of PCDTPT, which reduced $I_{on/off}$ to 10^1.

The p- and n- type output curves (Figures 6.18(b)-(c)) were slightly offset from $V_{ds}, V_{gs} = 0\,V$, attributed to the slow ion dynamics in water as the gate polarity switched during measurements. [27] Nonetheless, as shown in Table 6.7, the $I_{ds[max]}$ outperformed previous blend-based WG-TFTs, reaching $-0.22\,\mu A$ and $3.9\,\mu A$ for the p- and n-type modes, respectively – compared to $-0.16\,\mu A$ and $1.5\,\mu A$ for $PrC_{60}MA$:PCDTPT blend films.

Finally, to demonstrate the feasibility of the symmetrical performance for circuitry, inverters (NOT logic gates) built using two interconnected PCDTPT and ZnO WG-TFTs as each transistor exhibited low hysteresis

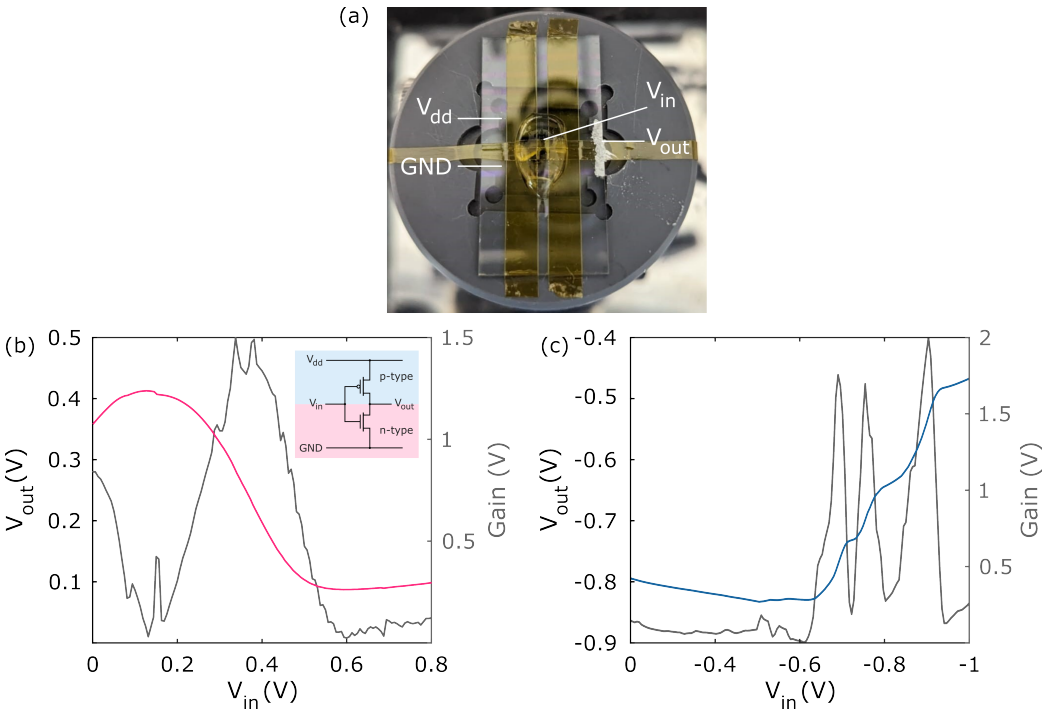

Figure 6.19: (a) Annotated wiring schematic. (b) VTC characteristics with calculated gain for the n- and (c) p-type regimes.

and similar $I_{ds[max]} > 10\,\mu A$. The wiring schematic is illustrated by Figure 6.19(a) and $V_{dd} = \pm 0.7\,V$ depending on n- or p-type operation. The limit for V_{in} was selected to be the same as the V_{gs} sweep of the pristine WG-TFTs presented in Figures 6.11(c) and 6.17(b). Figures 6.19(b) and (c) show that the voltage step occurred at $\frac{V_{dd}}{2}$, given that the V_{th} of the PCDTPT ($-0.08\,V$) and ZnO ($0.13\,V$) WG-TFTs were symmetrical near $V_{gs} = 0\,V$.

Reasonable gains were recorded in the n- and p- regimes, reaching a peak at 1.5 V. It is important to note that while this configuration showed promise for the realisation of ambipolar inverters using a single device, the voltage transfer characteristics (VTC) were still not ideal compared to traditional CMOS inverters. The fact that the ambipolar transistors shown in Figure 6.18(b), particularly in p-type mode, struggled to switch off caused a Z-shape in the VTC which in turn, translated to higher static power consumption and lower static noise margins. Nonetheless, the unique tunability of the systems presented in this Chapter opens up exciting avenues for the employment of ambipolar WG-TFT circuitry.

6.5 Summary

In summary, this Chapter has demonstrated two viable methodologies with a broad matrix of tunable parameter to achieve ambipolar WG-TFTs. The former employed a small molecule:polymer BHJ channel based on $PrC_{60}MA$ blended with either P3HT or PCDTPT for n- and p-type operation, respectively. The BHJ-like morphology of the as-cast P3HT:$PrC_{60}MA$ film with 5 % P3HT content governed ambipolar performance. After thermal treatment, this transitioned to unipolar p-type behaviour due to thermally-induced phase-separation. In contrast, the degree of phase-separation was markedly reduced with the PCDTPT blend as ambipolarity was observed only after thermal treatment. In fact, both n- and p-type transport were improved upon by doubling PCDTPT content from 5 % to 10 %, as the lower LUMO of PCDTPT allowed electrons to hop between p- and n-type regions.

The second strategy employed a hybrid bilayer channel, which outperformed that achieved by the former. The novel combination of the inorganic n-type metal oxide, ZnO, with PCDTPT as the capping layer, achieved low hysteresis and relatively balanced ambipolarity. Their performance as individual WG-TFTs also facilitated the fabrication of an inverter, which was a stepping stone for advanced CMOS-like circuit design required for sensing applications.

References

[1] L. Kergoat *et al.*, "A water-gate organic field-effect transistor," *Adv. Mater.*, vol. 22, pp. 2565–2569, 2010.

[2] R. Picca *et al.*, "A study on the stability of water-gated organic field-effect-transistors based on a commercial p-type polymer," *Front. Chem.*, vol. 7, p. 667, 2019.

[3] R. Porrazzo *et al.*, "Field-effect and capacitive properties of water-gated transistors based on polythiophene derivatives," *APL Mater*, vol. 3, p. 014905, 2015.

[4] L. Kergoat *et al.*, "Dna detection with a water-gated organic field-effect transistor," *Organic Electronics*, vol. 13, pp. 1–6, 2012.

[5] R. Porrazzo *et al.*, "Improving mobility and electrochemical stability of a water-gated polymer field-effect transistor," *Organic Electronics*, vol. 15, pp. 2126–2134, 2014.

[6] ——, "Water-gated n-type organic field-effect transistors for complementary integrated circuits operating in an aqueous environment," *ACS Omega*, vol. 2, pp. 1–10, 2017.

[7] H. Xu *et al.*, "An organic water-gated ambipolar transistor with a bulk heterojunction active layer for stable and tunable photodetection," *Appl. Phys. Lett.*, vol. 109, p. 213301, 2016.

[8] P. Harikesh *et al.*, "Organic electrochemical neurons and synapses with ion mediated spiking," *Nat. Commun.*, vol. 13, p. 901, 2022.

[9] E. J. Meijer *et al.*, "Solution-processed ambipolar organic field-effect transistors and inverters," *Nature Materials*, vol. 2, pp. 678–682, 2003.

[10] M. Dang *et al.*, "P3ht:pcbm, best seller in polymer photovoltaic research," *Adv. Mater.*, vol. 23, pp. 3597–3602, 2011.

[11] R. Furlan de Oliveira *et al.*, "Water-gated organic transistors on polyethylene naphthalate films," *Flex. Print. Electron.*, vol. 1, p. 025005, 2016.

[12] S. Simotko, Y. Yadav, and G. L. Frey, "A Blending Approach for Dual Surface and Bulk Functionality in Organic Transistors," *Advanced Electronic Materials*, vol. n/a, no. n/a, p. 2500085, 2025.

[13] J. Dong *et al.*, "Fullerene derivatives with oligoethylene–glycol side chains: an investigation on the origin of their outstanding transport properties," *J. Mater. Chem. C*, vol. 9, pp. 16 217–16 225, 2021.

[14] E. Stein, O. Nahor, M. Stolov *et al.*, "Ambipolar blend-based organic electrochemical transistors and inverters," *Nature Communications*, vol. 13, no. 1, p. 5548, 2022.

[15] J. Liu, L. Qiu, G. Portale *et al.*, "Side-chain effects on N-type organic thermoelectrics: A case study of fullerene derivatives," *Nano Energy*, vol. 52, pp. 183–191, 2018.

[16] M. Chikamatsu, S. Nagamatsu, Y. Yoshida *et al.*, "Solution-processed n-type organic thin-film transistors with high field-effect mobility," *Applied Physics Letters*, vol. 87, no. 20, p. 203504, 2005.

[17] F. K.-C. Leung, F. Ishiwari, T. Kajitani *et al.*, "Supramolecular Scaffold for Tailoring the Two-Dimensional Assembly of Functional Molecular Units into Organic Thin Films," *Journal of the American Chemical Society*, vol. 138, no. 36, pp. 11 727–11 733, 2016.

[18] M. Chikamatsu, A. Itakura, Y. Yoshida *et al.*, "Correlation of molecular structure, packing motif and thin-film transistor characteristics of solution-processed n-type organic semiconductors based on dodecyl-substituted C60 derivatives," *Journal of Photochemistry and Photobiology A: Chemistry*, vol. 182, no. 3, pp. 245–249, 2006.

[19] W. Ma, J. R. Tumbleston, L. Ye *et al.*, "Quantification of Nano- and Mesoscale Phase Separation and Relation to Donor and Acceptor Quantum Efficiency, Jsc, and FF in Polymer:Fullerene Solar Cells," *Advanced Materials*, vol. 26, no. 25, pp. 4234–4241, 2014.

[20] S. Obuchovsky, M. Levin, A. Levitsky, and G. L. Frey, "Morphology visualization of P3HT:Fullerene blends by using subsurface atomic layer deposition," *Organic Electronics*, vol. 49, pp. 234–241, 2017.

[21] S. Obuchovsky, B. Shamieh, I. Deckman *et al.*, "Harnessing ald to directly map the morphology of organic photovoltaic bulk heterojunctions," *Solar Energy Materials and Solar Cells*, vol. 143, pp. 280–283, 2015.

[22] Ren, Yang, and Zhao, "Preparation and Tribological Studies of C60 Thin Film Chemisorbed on a Functional Polymer Surface," *Langmuir*, vol. 20, no. 9, pp. 3601–3605, 2004.

[23] N. Schmerl and G. Andersson, "A layered structure at the surface of P3HT /PCBM blends," *Physical Chemistry Chemical Physics*, vol. 13, no. 33, pp. 14 993–15 002, 2011.

[24] C. Z. Leng and M. D. Losego, "Vapor phase infiltration (VPI) for transforming polymers into organic–inorganic hybrid materials: a critical review of current progress and future challenges," *Mater. Horiz.*, vol. 4, no. 5, pp. 747–771.

[25] L. Qiu, X. Wang, W. H. Lee *et al.*, "Organic Thin-Film Transistors Based on Blends of Poly(3-hexylthiophene) and Polystyrene with a Solubility-Induced Low Percolation Threshold," *Chemistry of Materials*, vol. 21, no. 19, pp. 4380–4386, 2009.

[26] M. J. Ford, M. Wang, S. N. Patel *et al.*, "High Mobility Organic Field-Effect Transistors from Majority Insulator Blends," *Chemistry of Materials*, vol. 28, no. 5, pp. 1256–1260, 2016.

[27] E. Stein, S. Simotko, Y. Yadav *et al.*, "Synergistic effects in ambipolar blends of mixed ionic–electronic conductors," *Materials Horizons*, 2025.

[28] J. Liu, L. Qiu, G. Portale *et al.*, "N-Type Organic Thermoelectrics: Improved Power Factor by Tailoring Host-Dopant Miscibility," *Advanced Materials*, vol. 29, p. 1701641, 2017.

[29] M. Ford *et al.*, "Acceptor percolation determines how electron-accepting additives modify transport of ambipolar polymer organic field-effect transistors," *ACS Nano*, vol. 12, p. 7134–7140, 2018.

[30] M. Azimi, A. Subramanian, N. A. Roslan, and F. Cicoira, "Flexible organic ion-gated transistors with low operating voltage and light-sensing application," *Journal of Physics: Materials*, vol. 4, no. 2, p. 024001, 2021.

[31] L. Kergoat, L. Herlogsson, D. Braga *et al.*, "A Water-Gate Organic Field-Effect Transistor," *Advanced materials (Deerfield Beach, Fla.)*, vol. 22, pp. 2565–9, 2010.

[32] H. Yin, L.-K. Ma, Y. Wang *et al.*, "Donor polymer can assist electron transport in bulk heterojunction blends with small energetic offsets," *Advanced Materials*, vol. 31, no. 44, p. 1903998, 2019.

[33] M. J. Ford, M. Wang, H. Phan *et al.*, "Fullerene additives convert ambipolar transport to p-type transport while improving the operational stability of organic thin film transistors," *Advanced Functional Materials*, vol. 26, no. 25, pp. 4472–4480, 2016.

[34] G. Acar, M. J. Iqbal, and M. U. Chaudhry, "Large area emission in p-type polymer-based light-emitting field-effect transistors by incorporating charge injection interlayers," *Materials*, vol. 14, no. 4, 2021.

[35] R. Lin, Y. Wang, Q. Lu *et al.*, "All-perovskite tandem solar cells with 3D/3D bilayer perovskite heterojunction," *Nature*, vol. 620, no. 7976, pp. 994–1000, 2023.

Chapter 7

Conclusions

7.1 Chapters & Contributions Summary

Chapter 4 began with the fabrication and characterisation of single layer SnO_2 TFTs for both electronic and chemiresistive functionality. Surface crystallisation – evidenced by AFM and XRD analyses – significantly enhanced device performance as the annealing temperature increased from 350 °C to 450 °C. The TFT annealed at 450 °C exhibited a stronger chemiresistive response to acetone vapour across the entire bias range compared to the device treated at 350 °C, owing to the improved surface crystallinity. This enhancement likely promoted acetone adsorption at nanoscale surface features, resulting in a greater change in $I_{on/off}$ upon exposure.

Subsequently, the electrical performance of the metal oxide TFTs was improved through the stacking of ZTO-based films. The addition of a ZnO capping layer substantially influenced the crystalline and morphological properties of the material systems. While the ZTO-capped TFTs demonstrated enhanced electrical performance, the ZnO-capped variant exhibited the growth of ZnO particles that increased surface roughness and degraded source-drain contact quality. Taking this into account, the bilayer ZTO-capped TFT

achieved a $V_{th} = 2.20\,\mathrm{V}$, an excellent $I_{on/off} = 10^7$ and $\mu_{eff} \approx 10\,\mathrm{cm\,V^{-1}\,s^{-1}}$. Similarly, the trilayer ZTO-capped TFT yielded $V_{th} = -1.74\,\mathrm{V}$, $I_{on/off} = 10^6$ and the second-highest mobility at $\mu_{eff} \approx 3\,\mathrm{cm\,V^{-1}\,s^{-1}}$. Their low surface roughness ($< 1\,\mathrm{nm}$) and high Sn content – with Sn/Zn ratios of 0.75 and 1.04 for the bilayer and trilayer devices, respectively – contributed to their strong current driveability.

Chapter 5 addressed the origin of the enhanced chemiresistive functionality of ZTO-based TFTs at low-voltage operation. The chemical environment heavily influenced the carrier transport properties of ZTO-based TFTs and can be tailored toward the detection of specific VOCs, ensuring that high specificity can be achieved for the diagnosis of life-threatening conditions by simple breath analysis.

Previously, the bilayer ZnO-capped TFT exhibited poor $I_{on/off} < 10^4$ and exceptionally low mobility ($\mu_{eff} \approx 0.1\,\mathrm{cm^2\,V^{-1}\,s^{-1}}$), which minimised the relative change in I_{ds} after exposure to a selection of VOCs with different functional groups, specifically acetone, IPA and toluene. Its much rougher surface morphology and relatively low oxygen vacancy content (26.2 %) not only hindered carrier transport properties but chiefly the adsorption and desorption of these VOCs under test, which led to $S_{max} < 100$. Conversely, the bilayer ZTO-capped TFT achieved near-zero $V_{th} = 2.20\,\mathrm{V}$ and excellent switching properties ($I_{on/off} > 10^7$) while maintaining high mobility ($\mu_{eff} \approx 10\,\mathrm{cm^2\,V^{-1}\,s^{-1}}$). Its low surface roughness, superb Zn and Sn intermixing, high oxygen vacancy (31.2 %) and M-OH bonding (11.4 %) contents meant that this TFT was deemed an ideal chemiresistive sensor and subsequently underwent the same exposure tests. Qualitative analyses of both TFTs demonstrated high specificity to alcohol vapours at low-voltage operation. More importantly, the bilayer ZTO-capped TFT achieved $S_{max} = 1.08 \times 10^6$ following exposure to methanol, which was over two orders of magnitude greater than acetone. The difference in sensing characteristics suggested that these TFTs could achieve accurate cross-sensitivity toward exhaled breath containing multiple gases and high responsivity at the V_{gs}

required for a battery-driven chemiresistive gas sensor.

Chapter 6 presented two viable methodologies with a broad matrix of tunable parameter to achieve low-voltage ambipolar WG-TFTs. The former employed a small molecule:polymer BHJ channel based on $PrC_{60}MA$ blended with either P3HT or PCDTPT for n- and p-type operation, respectively. The BHJ-like morphology of the as-cast P3HT:$PrC_{60}MA$ film with 5 % P3HT content governed ambipolar performance. After thermal treatment, this transitioned to unipolar p-type behaviour due to thermally-induced phase separation. In contrast, the degree of phase separation was markedly reduced with the PCDTPT blend as ambipolarity was observed only after thermal treatment. In fact, both n- and p-type transport were improved upon by doubling PCDTPT content from 5 % to 10 %, as the lower LUMO of PCDTPT allowed electrons to hop between p- and n-type regions.

The second strategy employed a hybrid bilayer channel, which outperformed that achieved by the former. The novel combination of the inorganic n-type metal oxide, ZnO, with PCDTPT as the capping layer, achieved low hysteresis and relatively balanced ambipolarity. Their performance as individual WG-TFTs also facilitated the fabrication of an inverter, which was a stepping stone for advanced CMOS-like circuit design required for sensing applications.

7.2 Thesis Conclusion

This work has established a blueprint for the scalable design of solution-processed thin-film devices aimed at medical diagnostics. Two complementary sensing strategies were developed: ZTO-based chemiresistive detectors VOCs and ambipolar WG-TFTs for the detection of aqueous biomarkers. Together, these platforms enable simultaneous, multimodal analysis of breath and saliva, producing diagnostic signatures with enhanced specificity and reliability.

In particular, detailed characterisation of their transistor and chemiresis-

tive behaviours revealed the fundamental sensing modalities that underpin their performance. These insights not only guided device optimisation but also laid the groundwork for future quantitative analyses and widespread adoption of stacked ZTO-based TFTs for exhaled breath analysis.

Overall, this research contributes to the growing field of point-of-care electronics by demonstrating how thin-film device engineering, informed by materials science and electronic design, can be harnessed for non-invasive, scalable diagnostics.

7.3 Further Work & Recommendations

The versatility of the solution-processing techniques employed in this thesis opens up numerous avenues for future research. For the multilayer TFTs, future work could explore the characterisation of alternative stacked material systems, such as all-ZnO bilayer and trilayer configurations (e.g., ZnO–ZnO or ZnO–ZnO–ZnO), as well as all-ZTO trilayers (e.g., ZTO–ZTO–ZTO), with a focus on their electronic and chemiresistive functionalities. In terms of precursor preparation, zinc acetate dihydrate ($Zn(CH_3COO)_2{\cdot}2H_2O$) could be used to reduce the processing temperature of ZnO thin films and suppress the formation of nanoparticles, which have previously hindered the performance of ZnO-based TFTs. Alternative deposition techniques, such as sputtering or ALD, could also be employed to enable precise control over film thickness and the Zn-to-Sn stoichiometric ratio in ZTO layers. Finally, time-resolved photoluminescence spectroscopy could offer valuable insights into charge trapping and de-trapping mechanisms, as well as their associated rate constants.

Regarding chemiresistive sensing, the current qualitative study could be expanded into a quantitative analysis of the multilayer TFTs' gas response. Establishing a clear correlation between electrical performance and vapour concentration would enable direct comparison of key sensing parameters – such as limit of detection, response time and recovery time – with literature benchmarks. This would require a dedicated experimental setup incorporat-

ing a mass flow controller. Furthermore, Kelvin probe measurements could provide deeper insight into the sensing mechanism by revealing work function and Fermi level shifts upon exposure, and relating these to the observed rise in I_{off}.

As for the WG-TFTs discussed in this thesis, further analysis of the crystallinity of the all-organic blends – for example, using GIWAXS – would provide valuable insight into the connectivity of electron and hole percolation pathways and orientation of the polymer and small molecule. Morphological characterisation of PCDTPT-based BHJs, such as those processed via VPI, would also be beneficial to compare the extent of thermally-induced phase-separation with the P3HT-based BHJs already studied. A compelling extension of this work could involve using the same ALD parameters applied in VPI to fabricate WG-TFTs with hybrid BHJs that incorporate ZnO nanoparticles dispersed in an amorphous polymer matrix.

Finally, an alternative solution-processed transistor technology with strong potential for remote chemical sensing is the LEFET. LEFETs integrate transistor logic with the light-emission capabilities of OLEDs, enabling dual electronic and optical functionality within a single device. This integration has the potential to simplify circuit design in advanced sensing and display applications. Crucially, LEFETs allow simultaneous monitoring of both electrical

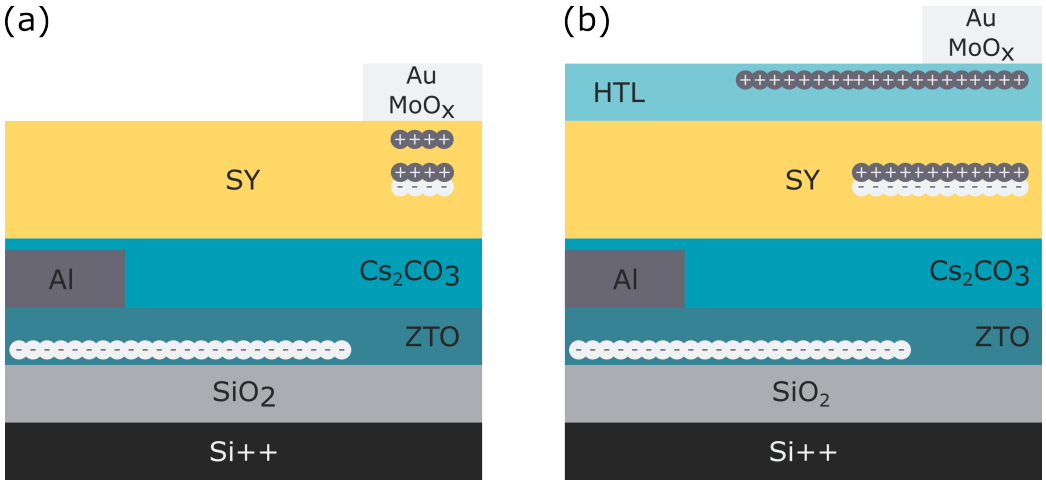

Figure 7.1: Device schematic of (a) SY-only hybrid LEFET and (b) with additional HTL layer.

and optical responses, offering an additional layer of sensitivity and diagnostic insight. A preliminary study explored the incorporation of an additional hole transport layer (HTL) – specifically poly(triarylamine) (PTAA) and poly(N-vinylcarbazole) (PVK) – to enhance hole injection into the emissive layer (see Figure 7.1). This approach aimed to improve brightness and, consequently, the external quantum efficiency (EQE) of hybrid LEFETs, paving the way for power-efficient sensor platforms. ZTO was employed as the electron transport layer and super yellow (SY) as the emissive material. Transfer characteristics for both SY-only and SY-HTL devices are shown in Figure 7.2.

Electrons were injected from the Al source electrode into the ZTO layer. To facilitate this process, the work function of the source electrode was

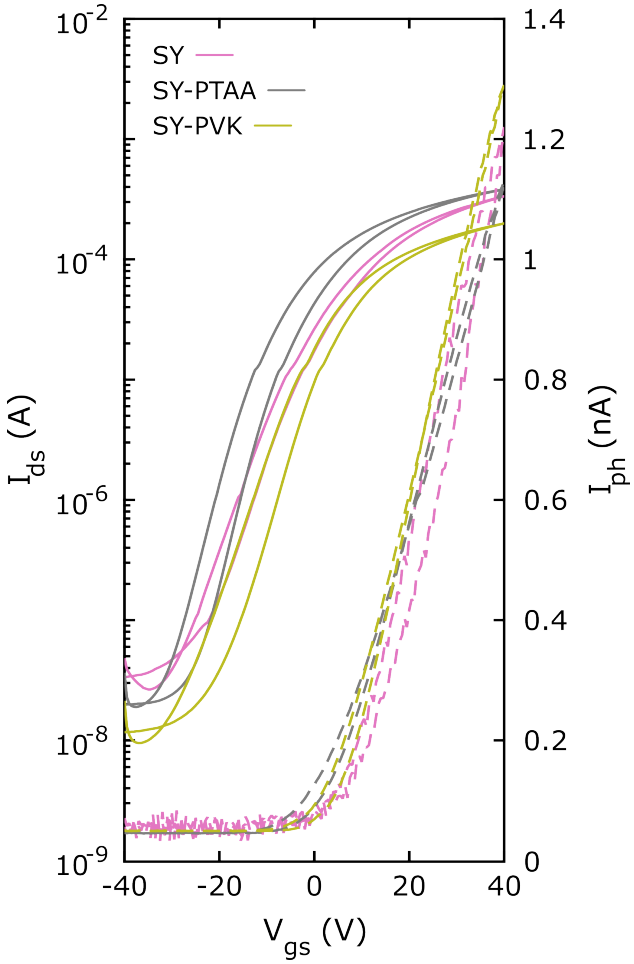

Figure 7.2: Transfer characteristics in the saturation regime at $V_{ds} = 40\,\mathrm{V}$ and $V_{gs} = -40\,\mathrm{V}$ to $40\,\mathrm{V}$ for SY-only and SY–HTL LEFETs.

modified to $-3.7\,\text{eV}$ using a Cs_2CO_3 interlayer, effectively reducing the injection barrier between the ZTO conduction band and the LUMO of SY ($-2.9\,\text{eV}$). Simultaneously, holes were injected from the MoO_x/Au drain electrode ($-5.3\,\text{eV}$) into the HTL, where they subsequently recombined with electrons within the channel to produce light emission. Uniform electroluminescence was observed across the semi-transparent MoO_x/Au drain area at a gate bias of approximately $V_{gs} = 0$, with spatial stability maintained throughout operation. The use of a staggered electrode geometry improved charge injection, while the Cs_2CO_3 interfacial layer contributed to consistent, gate-independent light emission. The addition of the HTL did not noticeably alter I_{ds}, indicating that charge transport remained dominated by the electron mobility in ZTO. Although qualitative trends were established, quantitative evaluation of brightness and EQE requires dedicated instrumentation and testing procedures that were beyond the scope of this thesis.